Growth of semiconductor layers studied by spot profile analysing low energy electron diffraction

Michael Horn-von Hoegen*

Universität Hannover, Institut für Festkörperphysik, Appelstr. 2, D-30167 Hannover, Germany

Received July 20, 1998, accepted March 23, 1999

Abstract. The universal capabilities of high resolution spot profile analysis low energy electron diffraction for in situ studies of surface morphology and surface defects will be discussed and demonstrated. The position of the diffraction spots is used to determine lateral lattice constants, step heights and the strain state of heterosystems with a precision of 0.02Å. With the knowledge of the spot profile we could determine island and domain size distributions - even during deposition - and correlation functions of arbitrary surface defects. The variation of the spot profile with electron energy allows the evaluation of the 3dim. reciprocal space. With this the power spectrum of surface roughness, facet orientation, or step morphology of flat and vicinal surfaces could be completely characterised.

Contents

1. Introduction

Electron diffraction is one of the first and one of the most successful surface science techniques ever invented. For more than 50 years it has been the only and dominant method to study the structure and morphology of two dimensional plane surfaces. The extreme surface sensitivity of electrons with energies in the range of 50 to 200 eV is one of the reasons for this success. With the electrons wavelength of the order of inter atomic distances

$$\lambda(\text{Å}) = \sqrt{150.4/E(\text{eV})} \quad (1.1)$$

the atomic arrangement in the surface unit cells is accessible for the measurement. For metals and most semiconductors electrons are a non-destructive probe. And finally, electron are easy to generate, to deflect, to focus, and to detect.

From its invention in 1927 by Davison and Germer [1] until today a vast variety of very different techniques and extremely sophisticated applications have been developed. Low energy electron diffraction (LEED) has been developed [2-5] to an easy to use 120° or 180° optical screen detector for standard applications [6], as determination of crystalline quality, size of unit cells, or type of reconstruction [7,8]. For a review of the early years of LEED studies see the papers from Bauer [9] and Ertl [10]. Backview LEED allows easier access to the LEED pattern, however, instead of the sample

---

* e-mail: horn-von-hoegen@uni-due.de
Present address: Universität Duisburg-Essen, Experimentalphysik, Lotharstr. 1, D-47048 Duisburg, Germany

holder nowadays always the shadow of the electron gun is depicted in any published LEED pattern.

For structure analysis of atomic positions in the surface unit cell IV-LEED has been developed with an accuracy of less than a few hundreds Å [11-16]. Determination of complex surface structures has been automated [17]. Anisotropic vibration amplitudes could be determined [18]. Diffuse LEED is used to determine the binding site geometry of non periodic adsorbates [19,20]. A holographic LEED analysis allows the direct determination of atomic sites on the surface by holographic reconstruction from the diffraction pattern [15,21]. Even low-energy positron diffraction has been employed for structure analysis [22].

Gracing incidence of the electrons enhances the surface sensitivity in reflection high energy electron diffraction (RHEED), which is used in almost any crystal growth chamber as in-situ monitoring technique to study the growth during deposition [23-25]. The periodic RHEED intensity oscillations are a well known example for the observation of a layer-by-layer mode in a crystal growth experiment [26-29].

Beside the intensity of the diffraction spots also the profile and position contains important information about the surface morphology which can be analysed by Spot Profile Analysing LEED (SPA-LEED) [30-54]. The key for this high resolution technique are a fine focus electron gun, an electrostatic deflection unit and a channeltron single electron detector [55-58]. Determination of lattice parameters or size of unit cell is possible with an accuracy of up to 0.02 Å. Due to the high coherence of the electron beam morphological features up to 2000Å size (the transfer width) could be detected. Using SPA-RHEED allows a transfer width of up to 15000Å [59-63].

Very recent developments combine electron loss spectroscopy with LEED for high resolution studies of electron loss spectra in reciprocal space (ELS-LEED) [64-70]. Here the profile of the energy loss peak allows to determine the depth of a dipole active layer or interface [71].

With the invention and discovery of scanning tunnelling microscopy (STM) by Binnig and Rohrer in 1981 [72] an atomically resolved image of almost any conducting surface became possible. STM and all other scanning probe techniques took a tremendous rise both as standard as well as advanced surface science technique. With all the very persuasive "real" images of surfaces obtained by STM we have to ask the critical question about the advantages and relevance of electron diffraction techniques.

One major advantage of diffraction techniques as a non contact probe is accessibility of the sample for material deposition or adsorption without restrictions of the measurement or the deposition process. This is the reason for the huge success of RHEED as in-situ in-vivo growth monitoring technique in molecular beam epitaxy (MBE). The grazing incidence leaves plenty of space for all evaporators. Without shadowing part of the surface (by the tip as in scanning probe techniques) uniform films could be grown and simultaneously monitored at any deposition rate without interfering with the growth process.

Due to principle reasons diffraction techniques are not sensitive for lateral shifts of the sample position during changes of the sample temperature. Changes from room temperature up to very high temperatures does not affect the diffraction spot positions (except for a contraction of the LEED pattern due to thermal expansion of the crystal).

Accurate atomic structure analysis is still only possible by diffraction with electrons (IV-LEED) or x-rays (surface x-ray diffraction techniques). An elemental analysis is also usually not possible by STM or tunnelling spectroscopy.

Any diffraction technique allows to measure inter atomic distances with high accuracy by a simple angle determination of the position of the diffraction spots. This can be used for the determination of lateral or vertical lattice constants. The Laue condition sets the correlation between atomic distances and diffraction angles [73]. No calibration is necessary for the determination of atomic distances.

This of course also holds for low energy electron diffraction as will be shown throughout this paper. With the high surface sensitivity of electrons lattice constants and variations of surface layer distances are easily accessible even during deposition. This kind of measurements is especially important for the study of lattice mismatched heteroepitaxial material systems.

With the same principle also the parameters of rough surface morphology are easy to determine: The orientation of facet planes is unambiguously and exactly known from the position of the corresponding spots in reciprocal space. Average values for lateral and vertical roughness parameters (terrace width distribution $P(\Gamma)$and the asperity height Δ or the layer distribution p_h, respectively) are obtained for large surface areas.

Using a typical spot size of the order of a mm^2 with the inherent disadvantage of a non local probe (any diffraction technique is principally a non local probe!) provides average information of surface morphology for representative surface areas. LEED in combination with a scanning probe technique as STM for the characterisation of the local morphological arrangement will therefore provide a very extensive and complete description of surface morphology.

The electron current density on the sample is of the order of 1...10^{-3} A/m^2, i.e. 6...8 orders of magnitude lower than in an STM experiment. This extreme low electron density minimises any electron stimulated desorption, current effects or field induced effects on the surface morphology.

This paper will review the potent capabilities of modern high resolution spot profile analysis in LEED for the determination of surface morphology using a commercial SPA-LEED instrument. In order to keep the limits of this review it will be restricted to group IV semiconductors without restriction of the generality of spot profile analysis. The same principles of evaluation of the spot profiles in the framework of kinematic approximation is possible for all other material systems.

This review will start with a short description of the theory, the contrast mechanism, and the various possible morphological features which could be observed by LEED. The analysis of vertical and lateral roughness parameters will be presented. In the experimental part we demonstrate examples for each of these surface defects together with a thorough description of the analysis.

A closer look to the SPA-LEED and the experimental set-up follows. The main requirements for high resolution electron diffraction experiments will be addressed. The different scattering geometries using normal and grazing incidence will be described. A correct analysis of spot profiles is based on the accurate knowledge of spot position in the 3-dim. reciprocal space, when scanning the diffraction pattern by rocking the Ewald sphere.

The experimental section will start in chapter 4 with the homoepitaxial growth of Si(111). The layer-by-layer growth mode has been studied for different temperatures and deposition rates in chapter 4.1 and 4.2. Applying a Venables type nucleation theory a surface defect mediated heterogeneous nucleation at superstructure domain boundaries was concluded. The complicate initial stage of growth is described in chapter 4.3 by a complete roughness analysis for different sub- and monolayer coverages.

We show in chapter 4.4, that in the presence of atomic hydrogen as a surfactant the growth mode is completely modified. At temperatures below 480°C the growing Si film exhibits an increasing surface roughness together with an increasing number of bulk defects which finally lead to an amorphous Si film. Above 500°C the facet formation instead of layer-by-layer growth is observed: the existence of adsorbed atomic hydrogen changes the surface free energy of the growing Si(111) surface and favours the formation of facets. The evolution of the large scale roughness of this faceted surface has been presented for the first time in chapter 4.5 employing electron diffraction close to a Bragg condition.

Ge growth on Si(001) is studied in chapter 5 in presence of the surfactants As and Sb. The surfactant hinders 3D-cluster formation of Ge on Si(001) even at temperatures as high as 800°C. However, the Ge surface is not smooth, but exhibits a pronounced micro roughness on a nm scale in order to relief strain by partial relaxation towards its own bulk lattice constant (chapter 5.1). We show in chapter 5.2 that the roughness parameters are almost independent on the growth temperature, i.e. this rough surface is energetically most favourable. The enlarged surface free energy due to the increases surface area is out balanced by the strong decrease of Ge film strain. The residual tetragonal distortion of the Ge film is observed in a vertical shift of the 3D-Bragg conditions. The variation of the layer distances in the rough Ge film becomes apparent in an increased broadening of the 3D-Bragg conditions with $K_\perp$.

Above 700°C the Ge film forms cones with a uniform size distribution which cover the entire surface (chapter 5.4). Depending on the surfactant coverage, i.e. surface free energy, the shape of the cones could be reversibly changed from pyramids composed of (105) facets via the cones to pyramids composed of (117) facets. The in-vivo study of this reversible transition presented in chapter 5.5 is only possible with this electron diffraction technique.

With further increasing Ge film thickness on Si(001) dislocations are also introduced, however, in an irregular manner and show up as mosaic spread of the entire LEED pattern (chapter 5.6).

Very different mechanism of strain relief are presented in chapter 6 in a in situ in vivo SPA-LEED study for surfactant mediated deposition of Ge on Si(111). During the coherent stage of hetero epitaxial growth the formation of a micro rough surface allows very effective strain relief by elastic deformation of the Ge film towards its bulk lattice constant. This effect is observed in a continuous change of both the vertical and lateral lattice constant. The formation of distinct (113) facets for surfactant mediated growth of 8 atomic monolayers Ge on Si(111) is observed (chapter 6.1).

The next is the plastic stage of strain relief, i.e. the introduction of dislocations (chapter 6.2). On Si(111) the formation of a periodic array of dislocations, completely confined to the Ge/Si interface, has been observed for the first time. The strain fields surrounding each dislocation results in a weak, quasi periodic undulation of the surface, which acts as a 2-dim. phase grid for electrons. This causes (as in light optics) the splitting of each fundamental LEED spot into a periodic array of satellite spots. This allowed for the first time to follow the formation and completion of a lattice matching interfacial dislocation network, though it is buried by a Ge layer with a thickness of more than 3 nm (thus exceeding the escape depth of electrons by a factor of more than 10!).

The intensity of the satellite spots was used to determine the shape of the surface undulation, i.e. to determine the exact geometry of the interfacial dislocation network during its formation (chapter 6.3).

The diffraction pattern from vicinal and faceted surfaces will be demonstrated in chapter 7 by noble metal induced faceting of regular stepped Si(001). The spot splitting reveal the average terrace width and step height. The motion of the spots with electron energy is used to determine the miscut of the surface or the orientation of facets. The kinetics of the transition from step train to facets is easily followed during the metal adsorption by SPA-LEED.

2. Theory

2.1. Kinematic Approximation

The diffraction from surfaces may be described as sum of electron wave functions scattered from the initial wave vector $\mathbf{k}_i$ of the incoming electron to the final wave vector $\mathbf{k}_f$ by all surface atoms at positions $\mathbf{r}(\mathbf{n})$

$$\Psi(\mathbf{K},\mathbf{k}_i)=\sum_n f(\mathbf{n},\mathbf{K},\mathbf{k}_i)\,e^{i\mathbf{K}\mathbf{r}(\mathbf{n})} \tag{2.1}$$

where $\mathbf{K}=\mathbf{k}_i-\mathbf{k}_f$ is the scattering vector and $f(\mathbf{n},\mathbf{K},\mathbf{k}_i)$ the structure factor which depends both on the initial $\mathbf{k}_\mathrm{i}$ and final electron wave vector $\mathbf{k}_\mathrm{f}$. The structure factor combines the electron wave coming from the surface atom at $\mathbf{r}(\mathbf{n})$ and all underlying atoms in the column perpendicular to the surface.

The diffraction phenomena with the diffraction spot intensity

$$I(\mathbf{K},\mathbf{k}_i)=\left|\Psi(\mathbf{K},\mathbf{k}_i)\right|^2$$
$$=\sum_{n,m} f(\mathbf{n},\mathbf{K},\mathbf{k}_i)\,f^*(\mathbf{m},\mathbf{K},\mathbf{k}_i)e^{i\mathbf{K}(\mathbf{r}(\mathbf{n})-\mathbf{r}(\mathbf{m}))} \tag{2.2}$$

are mainly determined by the scattering cross section, i.e. the values of the structure factor $f(\mathbf{n},\mathbf{K},\mathbf{k}_i)$. Two extreme cases could be distinguished:

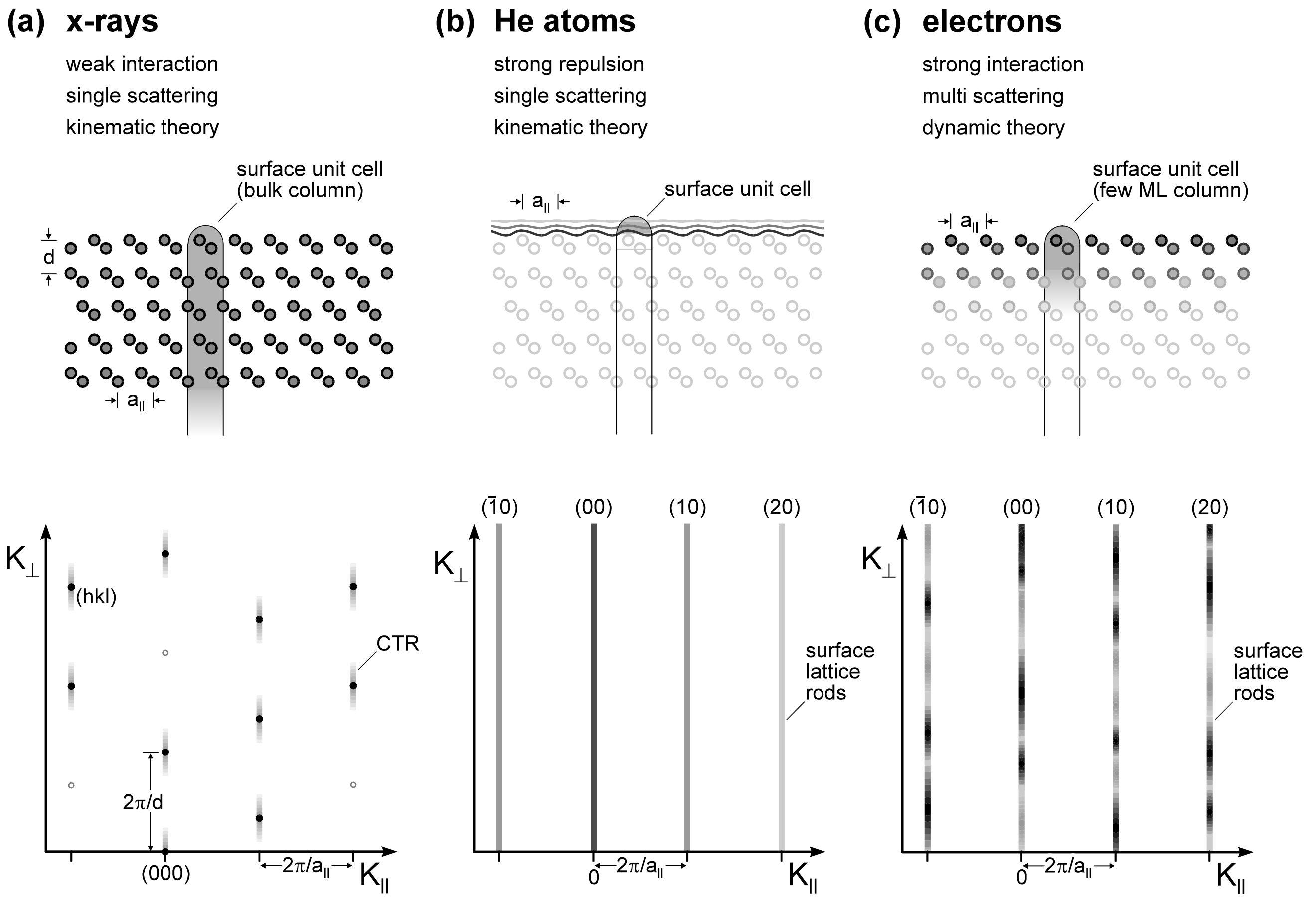

Fig. 2.1 Surface diffraction with x-rays, He-atoms, and electrons. Shown are the most dominant property of each of the probes, the interaction depth with the surface and bulk, and the resulting structure of reciprocal space. For these examples a group IV (111) surface with diamond lattice structure has been chosen. This determines the Bragg positions and sets also the condition for the disappearance of some of the x-ray diffraction spots: the (002), the (222) and $22\bar{2}$ are forbidden due to the atomic position in the bulk unit cell. The 3dim. Bragg positions are be of special importance for the electron diffraction from rough surfaces.

First, the weak interaction of x-rays with matter, penetrating µm underneath the surface. The small cross section allows to describe the interaction as single scattering process using kinematic scattering theory. As a consequence of the large number of contributing crystal layers $f(\mathbf{n},\mathbf{K},\mathbf{k}_i)$ is strongly modulated with $\mathbf{K}$ (Bragg conditions perpendicular to the surface). The resulting reciprocal lattice is sketched in Fig. 2.1(a). The 3-dim. periodicity of the single crystal causes the well defined Bragg conditions for diffraction: constructive interference of all x-rays scattered from all lattice planes and marked by dots in Fig. 2.1(a). The position of the Bragg conditions is determined by the structure of the bulk lattice (and therefore also by the structure of atomic steps at surfaces, i.e. the translational vector from a terrace to an adjacent terrace separated by an atomic step).

The infinite periodicity parallel to the surface results in extremely well defined reciprocal lattice vectors $\mathbf{K}_{\|}$. The half infinite extension of the crystal (with the surface as boundary in z-direction) and the still finite penetration depth of the x-rays relaxes the Bragg condition in $\mathbf{K}_{\perp}$. The intensity is not only confined to the 3dim. Bragg conditions, but also smeared out perpendicular to the surface between the Bragg conditions. These crystal truncation rods (CTRs) are used to obtain information about surface morphology [74,75] and structure [76-80] with x-ray diffraction.

The second case is the strong interaction of neutral He atoms with matter resulting in an extreme surface sensitivity with the repulsion of He atoms well above the surface [81-84]. The complete absence of a periodic scattering potential perpendicular to the surface cancels any selection rule for $\mathbf{K}_{\perp}$. Because any value is possible the reciprocal lattice consists of vertical lattice rods perpendicular to the surface, as sketched in Fig. 2.1(b). Only the very first layer of atoms contributes to the structure factor $f(\mathbf{n},\mathbf{K},\mathbf{k}_i)$. As a direct consequence this factor does not show a drastic dependence on $\mathbf{k}_i$ and $\mathbf{k}_f$.

Electrons in a LEED or RHEED experiment are elastically scattered within a depth of only a few atomic layers due to strong electron-electron interaction. The lack of a well defined periodicity perpendicular to the surface also relaxes the selection rule for $\mathbf{K}_{\perp}$: almost any value of $\mathbf{K}_{\perp}$ is possible. The reciprocal lattice in a LEED experiment is well described by a periodic arrangement of lattice rods, too, as shown in Fig. 2.1(c).

The finite penetration depth of the electrons together with the dominant multi scattering effects influences the intensity along the lattice rods via the structure factor $f(\mathbf{n},\mathbf{K},\mathbf{k}_i)$ as function of initial $\mathbf{k}_i$ and final scattering vector $\mathbf{k}_f$ [85].

With all atoms on perfect lattice sites (thermal vibration may already be described by a Debye Waller factor and will not be considered in the moment without restriction of generality)

$$\mathbf{r}(\mathbf{n}) = r(n_x + n_y) = \mathbf{a}_x n_x + \mathbf{a}_y n_y + \mathbf{d}_z h(\mathbf{n}) \quad (2.3a)$$

Here $\mathbf{a}_x$ and $\mathbf{a}_y$ are the unit vectors parallel to the surface, $\mathbf{n} = (n_x, n_y)$ describes the position of a unit cell. The surface morphology is now described by $\mathbf{d}_z h(\mathbf{n})$, with the height function $h(\mathbf{n})$ for the unit cell at position $\mathbf{n}$ and the step translational vector $\mathbf{d}_z$.

With such a rough surface the equation for the intensity (2.2) could be rearranged. For simplicity reasons this will be done for a square lattice, with the vertical translational vector $\mathbf{d}_z$ perpendicular to the surface and a layer distance *d*. The lattice positions are given by

$$\mathbf{r}(\mathbf{n}) = a_0 \mathbf{n} + \mathbf{d}_z h(\mathbf{n}) \quad (2.3b)$$

with a_0 the surface lattice constant. The intensity results as

$$I(\mathbf{K},\mathbf{k}_i) = \sum_n \Big\langle f(\mathbf{n}+\mathbf{m},\mathbf{K},\mathbf{k}_i)\, f^*(\mathbf{m},\mathbf{K},\mathbf{k}_i) \times e^{idK_\perp(h(\mathbf{n}+\mathbf{m})-h(\mathbf{m}))} \Big\rangle_{\mathbf{m}} e^{iaK_\parallel \mathbf{n}} \quad (2.4)$$

The brackets $\langle\ \rangle_{\mathbf{m}}$ denote averaging with respect to **m**. Here it becomes obvious, that morphological and structural information are intermixed. The intensity depends both on the surface morphology (i.e. the arrangement of unit cells) and the structure factor of scattering (i.e. the arrangement of atoms in the unit cell).

Dynamic LEED theory is necessary to describe the dependence between geometric atomic structure in the unit cell (which is the entire column of all bulk atoms underneath the surface unit cell) and the intensity $I(\mathbf{K},\mathbf{k}_i)$ of the diffraction spots as function of electron energy and incidence angle. This whole field of atomic structure determination by IV-LEED for smooth and homogeneous surfaces will be addressed by K. Heinz in this series of reviews.

Due to simplicity reasons the kinematic approximation is also used for the spot profile analysis of rough or stepped surfaces. Moritz et al. [86] and Pendry et al. [87] have discussed multiple scattering effects of disordered surfaces. However, up to now it is still too complicated to consider different structure factors $f(\mathbf{n},\mathbf{K},\mathbf{k}_i)$ for diffraction from disordered step edges of rough surfaces.

All structure factors are replaced by their spatial average

$$f = f(\mathbf{K},\mathbf{k}_i) = \big\langle f(\mathbf{n},\mathbf{K},\mathbf{k}_i) \big\rangle_{\mathbf{n}} \quad (2.5a)$$

independent on the site of a particular unit cell and the arrangement of the neighbouring unit cells. This approximation is strictly valid for a smooth and flat surface. However, small deviations may be expected at crystal positions without translational symmetry, i.e. at step edges. Considering the unit cell columns just at the step edge, it becomes clear, that the surrounding atomic configurations are different as shown in Fig. 2.2. Electrons scattered directly from below or from above the step edge undergo different structure factors. Due to the very limited electron penetration depth of less than 5Å only such a small band around a step edge may show up a different structure factor. Electrons scattered from unit cells further away than 5Å from the step edge are simply insensitive to it and exhibit all the same structure factor *f*. Therefore this approximation is the better, the larger the separation between steps. With decreasing step density also the areas with a different structure factor decreases and therefore also their influence to the spot profile.

The intensity splits up

$$I(\mathbf{K},\mathbf{k}_i) = F(\mathbf{K},\mathbf{k}_i)\, G(\mathbf{K}) \quad (2.6)$$

into the dynamical form factor, which depends on initial and final wave vector

$$F(\mathbf{K},\mathbf{k}_i) = \left| f(\mathbf{K},\mathbf{k}_i) \right|^2 \quad (2.5b)$$

and the well known lattice factor, which is only determined by the surface morphology and scattering vector **K**

$$\begin{aligned} G(\mathbf{K}) &= \frac{1}{2\pi} \sum_n \Big\langle e^{idK_\perp(h(\mathbf{n}+\mathbf{m})-h(\mathbf{m}))} \Big\rangle e^{iaK_\parallel \mathbf{n}} \\ &= \frac{1}{2\pi} \left| \sum_n e^{iaK_\parallel \mathbf{n}}\, e^{idK_\perp h(\mathbf{n})} \right|^2 \end{aligned} \quad (2.7a)$$

The lattice factor $G(\mathbf{K})$ does not modify the integral intensity of the spots (as the structure factor does), it influences the intensity distribution in reciprocal space. A perfect smooth, flat surface shows up with perfectly sharp diffraction spots, which are only instrumentally broadened. However, any deviation from a perfect translational symmetry - as a step edge or an island - results in a redistribution of intensity from the sharp fundamental diffraction spots (reflecting long range order) into diffuse intensity between the LEED spots [88,89]. For a rough surface a spot broadening (chapter 2.2), for a regular step train a spot splitting (chapter 2.4.1), and for facets new fundamental spots (chapter 2.4.2) are observed [33,34].

The total intensity of the diffuse and peaked part of a particular spot i,j is conserved and normalised to 1 by the number *N* of surface unit cells and is independent on the surface morphology $h(\mathbf{n})$ and independent on $K_\perp$:

$$\int_{Bz} d\mathbf{K}_\parallel G_{ij}(\mathbf{K}) = 1 \quad (2.8a)$$

This is of very special importance for the spot profile analysis and is essential for the practical data evaluation.

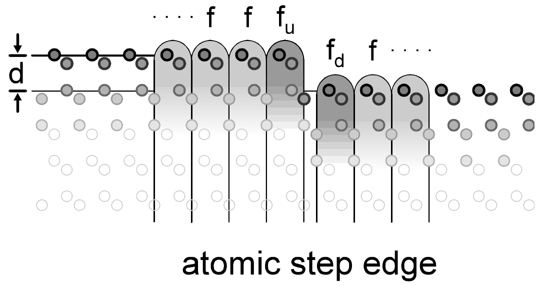

Fig. 2.2 At a step edge the structure factor *f* deviates from its average value. *fu* and *fd* may show different scattering amplitudes and scattering phases.

The lattice factor $G_{ij}(\mathbf{K})$ is obtained from the intensity $I_{ij}(\mathbf{K})$ of LEED spot i,j. The absolute value of the spot intensity is not evaluated, only the variation of the spot profile with **K**. The lattice factor $G_{ij}(\mathbf{K})$ is obtained by normalisation of the experimentally measured intensity profile $I_{ij}(\mathbf{K})$ with the total integral intensity of the spot i,j

$$\begin{aligned}\frac{I_{ij}(\mathbf{K})}{\int d\mathbf{K}_{\parallel} I_{ij}(\mathbf{K}_{\parallel})} &= \frac{F(\mathbf{K},\mathbf{k}_i)G(\mathbf{K})}{\int_{BZ} d\mathbf{K}_{\parallel} F(\mathbf{K},\mathbf{k}_i)G(\mathbf{K})} \\ &\cong \frac{F(\mathbf{K},\mathbf{k}_i)G(\mathbf{K})}{\bar{F}_{ij}(\mathbf{k}_i)\int_{BZ} d\mathbf{K}_{\parallel} G(\mathbf{K})} \\ &= \frac{F(\mathbf{K},\mathbf{k}_i)G(\mathbf{K})}{\bar{F}_{ij}(\mathbf{k}_i)} \\ &\cong G(\mathbf{K}) \end{aligned} \qquad (2.8b)$$

This intensity profile is also modulated by the dependence of the dynamic form factor $F(\mathbf{K},\mathbf{k}_i)$ on the electron energy E, the angle of incidence φ of the electron beam and the scattering vector **K**. Recording a spot profile usually only the scattering vector **K** is varied. For the analysis it is usually assumed, that the variation of $F(\mathbf{K},\mathbf{k}_i)$ with **K** is much smoother than those of the lattice factor $G_{ij}(\mathbf{K})$, i.e. that $F(\mathbf{K},\mathbf{k}_i)=\bar{F}_{ij}(\mathbf{k}_i)$ is constant with respect to **K** around the spot i,j in reciprocal space, where diffuse intensity is observed.

This approximation is the better, the larger the observed morphological features are, because the diffuse intensity will be confined to a smaller region around the spot i,j . We obtain the same result as for the discussion of equation (2.5b): the kinematic approximation works best for large morphological structures. However, the observation of such large structures requires a high resolution instrument.

Nevertheless, experimental results reveal strong evidence for a smooth and good-natured behaviour of $F(\mathbf{K},\mathbf{k}_i)$ on energy and initial and final electron wave vector [90]. Dynamic LEED theory typically predicts a weak variation of $F(\mathbf{K},\mathbf{k}_i)$ with scattering vector **K** [91]. Important is the penetration and interaction depth of electrons in the crystal which is limited to about 5Å. This gives a reciprocal length, i.e. a value $\delta k \approx 2\pi/5$Å for which strong changes of intensity are expected. With IV-LEED strong changes of intensity are also observed for changes of the order of $\delta k \approx 1 Å^{-1}$.

Of special importance are conditions, when the structure factor equals zero: the different scattering amplitudes from all atoms of the unit cell annihilates each other (complete destructive interference). Small changes of the initial or final wave vector will immediately disturb the cancellation: intensity is observed and may strongly vary by orders of magnitude for small variations of the scattering vector **K**. This effect does not happen for strong intensity conditions, when the scattering amplitudes of most atoms of the unit cell interfere constructively. Changes of the energy and scattering vectors will also affect this situation and may also modify the intensity. However, the relative changes of the structure factor with **K** or $\mathbf{k}_i$ will be small, and will only become large, when the structure factor varies strongly or is close to zero.

The lattice factor could also be expressed by the absolute square of the two dimensional Fourier transform

$$G(\mathbf{K}) = \frac{1}{2\pi}\left|\sum_n e^{ia\mathbf{K}_{\parallel}\mathbf{n}}\ \phi(K_{\perp},\mathbf{n})\right|^2 \qquad (2.7b)$$

of the surface phase function

$$\phi(K_{\perp},\mathbf{n}) = e^{idK_{\perp}h(\mathbf{n})} \qquad (2.9a)$$

This equation highlights the maximum obtainable morphological information: The surface height function $h(\mathbf{n})$ is on principal not accessible, only its projection on the unit circle of complex numbers could be determined! Due to the modulo properties of the complex exponential with 2π this causes some ambiguous results if the spot profile is determined only for a single value of $K_{\perp}$. For an unambiguous determination of the surface morphology $h(\mathbf{n})$ the lattice factor $G(\mathbf{K})$ must be known for different values of $K_{\perp}$.

The scattering phase S replaces the vertical scattering vector as dimensionless value (independent on the particular material system)

$$S = K_{\perp}d/2\pi \qquad (2.10a)$$

$$\phi(S,\mathbf{n}) = e^{i2\pi S h(\mathbf{n})} \qquad (2.9b)$$

The scattering phase S describes the phase difference in numbers of electron wavelength $\lambda_{\mathrm{electron}}$ when electrons are scattered from adjacent terraces with a height difference of one atomic step d as sketched in Fig. 2.3 :

$$\lambda_{\mathrm{electron}} = \left(h^2/2m_e eE\right)^{-1/2} \qquad (2.11a)$$

Electrons interfere constructively for integer values of S, i.e. the Bragg or "in-phase" condition of scattering. For this conditions they are not sensitive to any surface roughness.

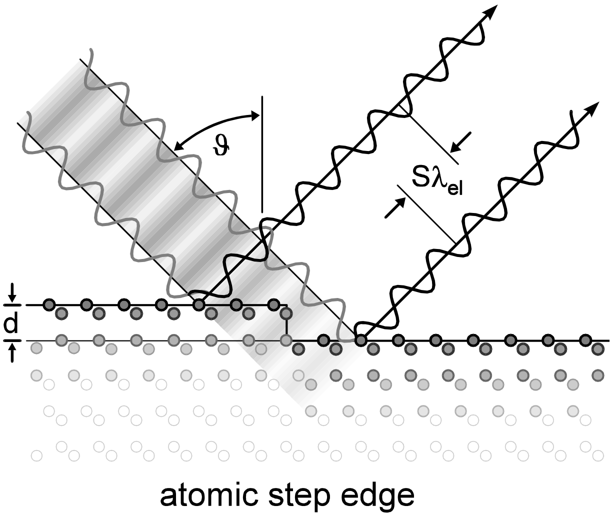

Fig 2.3 Phase contrast at a step edge: Electrons scattered from terraces separated by a single atomic step interfere with a phase difference of $2\pi S$, i.e. a path difference given by the product of the scattering phase S and the electron wavelength λ. For half integer values of S the electrons interfere destructively and the sharp LEED spot disappears. For integer values of S the interference is constructive and the electrons are insensitive to surface roughness.

Therefore a sharp LEED spot is expected for electrons with an energy corresponding to a Bragg condition.

For the "out-of-phase" or anti-Bragg condition the electrons interfere destructively and are most sensitive to surface roughness. Of course the electrons are not annihilated from the sharp LEED spot, but redistributed into a diffuse part surrounding the sharp spot. The shape or profile of such a broadened spot is determined by the lattice factor $G(\mathbf{K})$.

For the (00)-spot, i.e $\mathbf{K}_{\|} = 0$, and an arbitrary incidence angle φ the scattering phase S depends as follows on electron wavelength

$$S = 2\,d\cos\vartheta\,/\,\lambda_{\text{electron}} \tag{2.10b}$$

or electron energy

$$S = 2\,d\cos\vartheta\sqrt{E(\text{eV})/150.4} \tag{2.11b}$$

Depending on the geometric structure of the step, i.e. the translational vector across a step between adjacent terraces, the phase condition S may be ambiguous [31]. On Si(001) steps with different translational vectors are present (S_A and S_B type steps with a translational vector rotated by 90° with respect to each other). As a result the "in-phase" and "out-of-phase" conditions for the (10)-type lattice rods are not well defined: At the in-phase condition for S_A steps the terraces separated by an S_B step scatter in an "out-of-phase" condition! These "in-phase" and "out-of-phase" conditions for diffraction at a rough surface are identical with the 3-dim. Bragg conditions: The geometric step structure becomes apparent in the Bragg positions.

Though the electrons gain energy during the scattering process due to the inner potential V_0 of the crystal, the interference conditions described by the scattering phase S are not affected! Each electron undergoes the same constant phase shift due to the inner potential.

Therefore the accurate and absolute determination of vertical layer distances is possible for a rough surface via the position of the "in-phase" conditions, i.e. the 3dim. Bragg conditions [33,34,92-96].

2.2. Rough Surfaces

The lattice factor from a perfect surface is given by a sum of δ-functions

$$G_{\text{ideal}}(\mathbf{K}) = \sum_{i,j} \delta\Big(\mathbf{K}_{\|} - \frac{2\pi}{a_0}(i,j)\Big) \tag{2.12}$$

and produces sharp LEED spots, which are only instrumentally broadened as sketched in Fig. 2.4(a). The finite angular and/or energy resolution due to physical limits of the instrument sets a minimum experimental width of the spots.

Any deviations from such a perfect surface will now redistribute intensity from these sharp spots to diffuse intensity in the Brillouinzone. This may happen either by small displacements of the atoms from their lattice site as for uncorrelated thermal motion of the atoms (chapter 2.7) or point defects at the surface. As a result the uniform background in the brillouinzone increases on the expense of the intensity of the LEED spots.

In the following part, however, we will consider morphological defects with all atoms on lattice sites. As a consequence the structure factor and the LEED pattern is periodic with $K_\perp$ or the scattering phase S: The observed spot profiles should be identical for same deviations δS

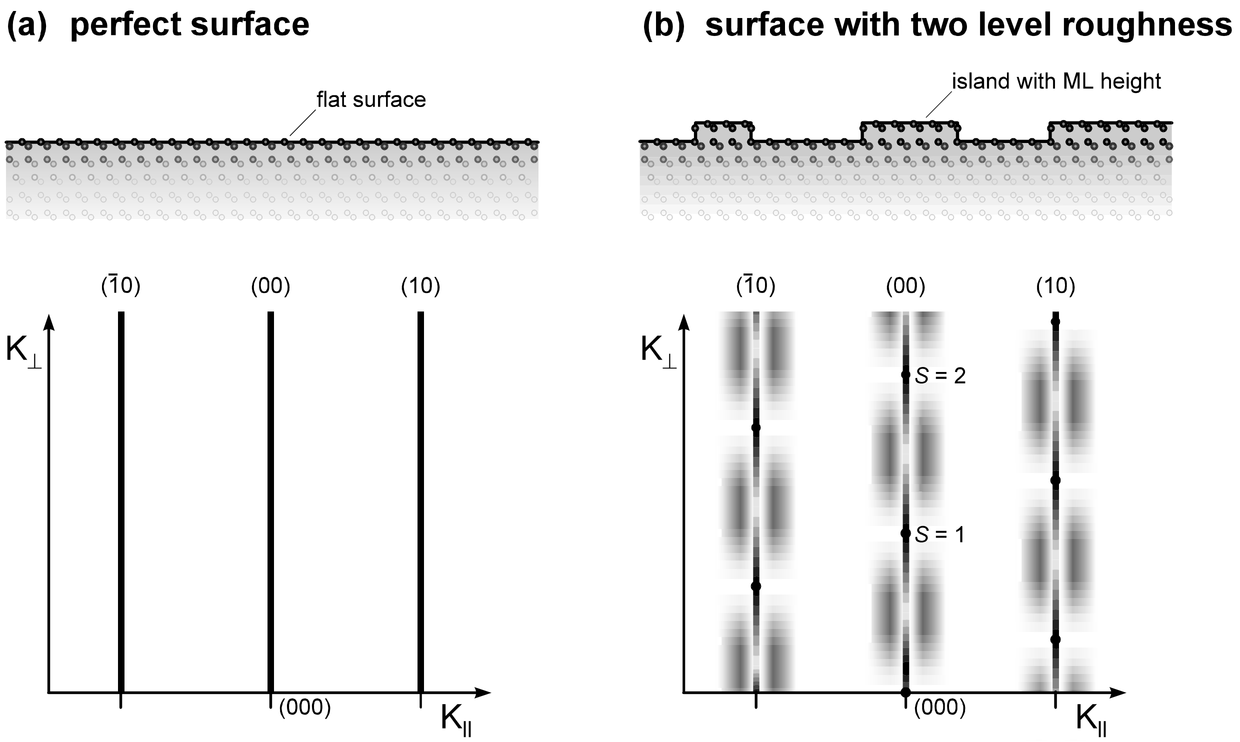

Fig 2.4 Diffraction rods from (a) a perfect surface: spots show only the instrumental broadening. Spot profile does not change as function of vertical scattering vector $K_\perp$. The diffraction rods from a rough surface with two levels (b) show diffuse intensity for most energies. The spots are sharp without broadened part at the "in-phase" condition, i.e. the 3-dim. Bragg conditions.

from Bragg conditions independent on the order of the fundamental spot. Even more, the lattice factor has a point symmetry in reciprocal space with respect to 3dim. Bragg conditions. For reversible surfaces (the surface morphology could not be distinguished after reflection at a plane perpendicular to the surface) the lattice factor has an additional mirror symmetry with the mirror plane along the lattice rod.

2.2.1 Two level system

The simplest example is a rough surface of just two layers as sketched in Fig. 2.4(b). The 2-dim. islands of average width $\overline{\Gamma}$ are separated by single atomic steps of height *d*.

The LEED spots consist of a sharp central spike $I_0(K_\perp)$ due to the long range order of the substrate and a diffuse part $I_{diff}(\mathbf{K}_\|, K_\perp)$. The central spike is given by the constructive part of interference of electrons scattered from upper and lower levels of the surface [97]. Its intensity depends on the coverage θ_1 in the first layer (i.e. the fraction of scatterers in this layer)

$$G_{00}(\mathbf{K}_{\|}=0,S)=G_{\text{ideal}}(1-2\theta_1(1-\theta_1)(1-\cos 2\pi S)) \quad (2.13a)$$

and oscillates with a cosine function of the scattering phase *S* as sketched in Fig. 2.4(b) and 2.5. For "in-phase" condition with *S* equal to integer values *n* the intensity is the same as for a perfect smooth surface and all intensity is confined to the central spike: The electrons are insensitive to surface roughness. The diffraction is - at least partly - destructive for all other scattering conditions: The central spike intensity is reduced. For $\theta_1 = 1/2$ (half of a complete layer)

$$G_{00}(\mathbf{K}_\|=0,S)=G_{\text{ideal}}(1/2-\cos^2(2\pi S)) \quad (2.13b)$$

and "out-of-phase" condition $S = n + 1/2$ the interference from electrons scattered from the islands and from the substrate is completely destructive and the central spike vanishes! The parabolic dependence on the coverage θ_1

$$G_{00}(\mathbf{K}_\|=0,S=n+\tfrac{1}{2})=G_{\text{ideal}}4(\theta_1-\tfrac{1}{2})^2 \quad (2.13c)$$

is the reason for the periodic intensity oscillations during expitaxial growth [56,98-104].

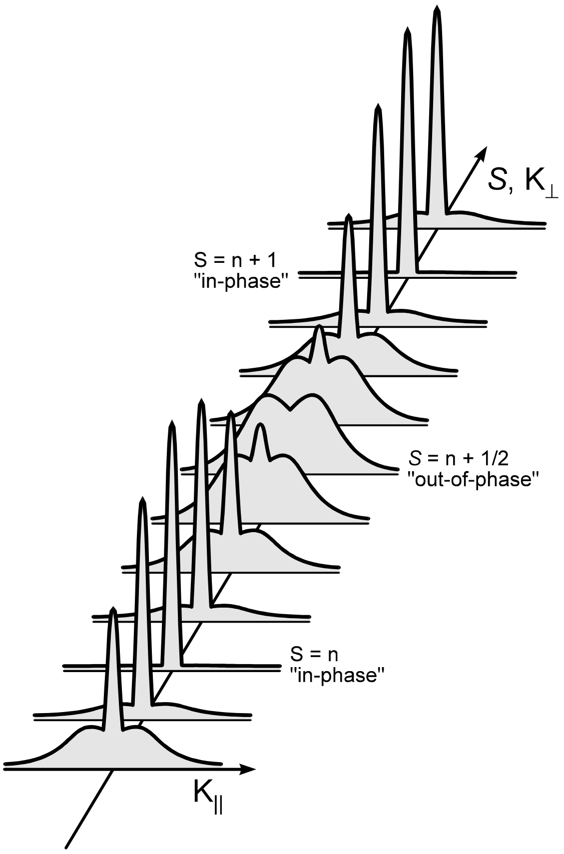

Fig 2.5 Principal behaviour of the spot profile as a function of vertical scattering vector $K_\perp$ or scattering phase *S* for a rough surface consisting of two layers. The profile consists of two contributions: a sharp central spike and a diffuse part determined by the terrace width distribution. At "in-phase" conditions the electrons are insensitive to the surface roughness due to constructive interference from all scattered electrons. Only the sharp central spike is visible. At "out-of-phase" condition with destructive interference for electrons scattered from different levels the diffuse part is maximum. For 1/2 ML conditions the central spike vanishes.

The intensity of the diffuse part of the profile oscillates in anti-phase to the central spike, i.e. the total intensity is conserved

$$G_{\text{diff}}(\mathbf{K}_\|,S)=\Phi_{\text{diff}}(\mathbf{K}_\|)2\theta_1(1-\theta_1)(1-\cos 2\pi S) \quad (2.14)$$

$$\int_{Bz} d\mathbf{K}_\| \Phi_{\text{diff}}(\mathbf{K}_\|) = 1 \quad (2.15a)$$

$$\int_{Bz} d\mathbf{K}_\| G_{\text{ideal}}(\mathbf{K}) = 1 \quad (2.15b)$$

It is important to note, that for a two-level system the profile of the diffuse intensity does not depend on the vertical scattering vector $K_\perp$ or scattering phase *S* [97]. The normalised shape of the diffuse part $\Phi_{\text{diff}}(\mathbf{K}_\|)$ is determined by the terrace width distribution $P(\Gamma)$: A geometric terrace width distribution with an average terrcace width $\overline{\Gamma}$ of non interacting steps results for 1-dim. problems in a Lorentzian profile [35,97]

$$\Phi_{\text{diff}}(\mathbf{K}_\|)=\frac{1}{2}\frac{\kappa}{(\kappa^2+K_\|^2)} \quad (2.16a)$$

of the diffuse part of the profile with $\kappa = 2/\overline{\Gamma}$. The average terrace width $\overline{\Gamma}$ could be derived from the full-width at half-maxima (FWHM) of the diffuse part of the profile $\overline{\Gamma} = 4/FWHM$. An mean terrace width $\overline{\Gamma} = 10$ unit cells results in a broadening of ~ 6.4% of the length of the surface Brillouin zone (100%Bz corresponds to the distance between fundamental spots of the substrate).

A more regular arrangement of islands (or steps as will be discussed in section 2.4.1) will manifest in sharper satellite peaks with a separation close to $\Delta K_\| = 2\pi/\overline{\Gamma}$ as discussed in [35,105].

Isotropic 2-dim. islands with a geometric terrace width distribution results in a Lorentzian with exponent 3/2 [106]

$$\Phi_{\text{diff}}(\mathbf{K}_\|)=\frac{\kappa}{2}(\kappa^2+K_\|^2)^{-\frac{3}{2}} \quad (2.16b)$$

Anisotropic islands sizes and the 2-dim LEED pattern have been tried to describe by a Markovian approach for rough surfaces [107-109].

More general cases for terrace width distributions and the resulting spot profile could be found in the literature [35,110-119]. The "domain matrix method" allows the combination of arbitrarily composed surface morphologies [120]. For the special case of non interacting single steps Busch found an algorithm to directly determine the 1-dim. terrace width distribution $P(\Gamma)$ from the measured intensity profile [121].

2-dim. intensity profiles could be analysed within a 1-im. algorithm using the integral projection of the profile onto one axis. The resulting profile is determined by the 1-dim. terrace width distribution [122].

2.2.2 Multi level system

With increasing vertical roughness the situation becomes more complex. The vertical roughness, i.e. the layer distribution p_h, determines the variation of the central spike with $\mathbf{K}_\perp$.

The lattice factor $G_{00}(\mathbf{K}_\parallel, S)$ for $\mathbf{K}_\parallel = 0$ is simply given by the Fourier transform of the projection of all surface scatterers onto the z-axis: the fraction of visible surface atoms $p_h = \theta_h - \theta_{h+1}$ or unit cells in the level h

$$
\begin{aligned}
G\left(\mathbf{K}_\parallel = 0, S\right) &= \left| \sum_n e^{ia\mathbf{K}_\parallel \mathbf{n}} e^{i \quad 2\pi Sh(\mathbf{n})} \right|^2 \\
&= \left| \sum_n e^{i \quad 2\pi Sh(\mathbf{n})} \right|^2 \\
&= \left| \sum_h p_h \cos(2\pi Sh) \right|^2 \\
&= \sum_h \sum_l p_l \, p_{h+l} \cos(2\pi Sh) \\
&= \sum_h C_h \cos(2\pi Sh)
\end{aligned}
\qquad (2.17)
$$

and will in the following be described as $G(S)$. The vertical height correlation is defined as

$$
\begin{aligned}
C_h &= \sum_l p_l \, p_{h+l} \\
&= \frac{1}{2\pi} \int_{-\pi}^{+\pi} dS \, G(S) \cos(2\pi Sh)
\end{aligned}
\qquad (2.18)
$$

and can be obtained by a Fourier transform from the normalised central spike intensity, i.e. the lattice factor $G(S)$, via the Eq. (2.8b).

As for the lateral pair correlation, the vertical height correlation provides the most extensive information in a diffraction experiment. It is therefore only for a two-level system possible, to unambiguously determine the probabilities p_h, without determination of the coverages θ_0 and θ_1. There are two sets of possible values. Using a diffraction technique, it is not possible to determine which is the upper and lower level: the phase information is lost!

A principal sketch of the $G(S)$ curve is shown in Fig. 2.7. The peaks corresponds to the "in-phase-condition" at the Bragg positions of diffraction: All electrons constructively interfere, i.e. "in-phase". Increasing roughness adds terms with higher frequencies to the shape of the $G(S)$ curve, i.e., $(4\pi S)$, $(6\pi S)$, $(8\pi S)$ terms as arguments for the cosine. This results in sharper peaks of the $G(S)$ curve. The behaviour is similar to the optical transmission properties of a Fabry Perot interferometer: the more layers contribute to the LEED pattern (the rougher the surface is), the sharper is

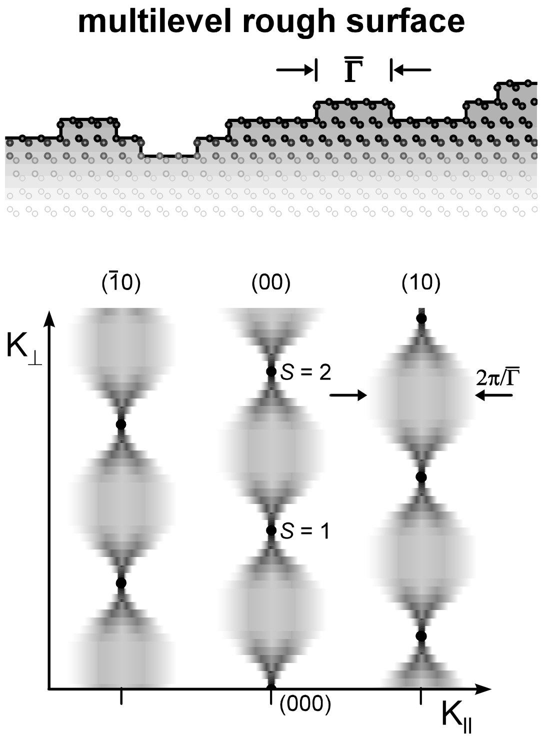

Fig 2.6 Principal behaviour of the spot profile as a function of vertical scattering vector $K_\perp$ or scattering phase S for a rough surface consisting of an infinite number of layers. The profile consists no longer of two contributions: due to the infinite roughness on large length scales only the diffuse part remains. A sharp central spike is only observed at the exact Bragg condition. The varying width of the profile reflects the varying sensitivity - as function of ΔS - of the electrons for the different length scales of surface roughness. For simple models describing the surface roughness a cosine behaviour for the FWHM of the profile is expected.

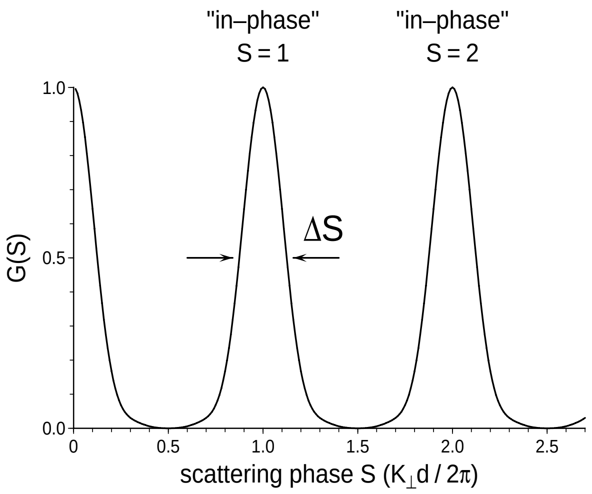

Fig 2.7 Normalised central spike intensity $G(S)$ of the LEED profile as function of scattering phase S, i.e. the square root of energy. At the "in-phase" conditions with constructive interference all intensity is in the central spike confined. From the FWHM of the $G(S)$ curve around the "in-phase" conditions the asperity height Δ, i.e. the rms. value of vertical roughness is determined.

the $G(S)$ peak! In the limit of infinite roughness this will result in the existence of a 3-dim. central spike only around the Bragg conditions, as well known for bulk x-ray diffraction!

For more than two existing levels on the surface, generally more than one set of $\{p_h\}$ exists as solution for the equation system Eq.(2.18).

In an epitaxial growth experiment the total deposited amount

$$\theta_{\text{total}} = \sum_{h=1}^{H} h\, p_h \tag{2.19}$$

sets another boundary condition and reduces the possible sets of $\{p_h\}$. $\{p_h\}$ is determined by fitting the resulting $G(S)$ curve to the experimental values of the normalised central spike intensity using a least square method.

For symmetric layer distributions $p_h = p_{-h}$ an analytical solution is possible. The values p_h have to be real and it follows for the Fourier transform:

$$F\{p_h\} = F\{p_{-h}\} = F^*\{p_h\} \tag{2.20}$$

The lattice factor $G(S)$ is:

$$\begin{aligned} G(S) &= F\{p_h\}\cdot F^*\{p_h\} \\ &= F^2\{p_h\} \end{aligned} \tag{2.21}$$

$$\begin{aligned} p_h &= F^{-1}\left\{\sqrt{G(S)}\right\} \\ &= \frac{1}{2\pi}\int_{-\pi}^{+\pi} \pm\sqrt{G(S)}\cos(2\pi Sh)\,dS \end{aligned} \tag{2.22}$$

The sign of the square root has to be chosen in such a way, that the resulting function has a smooth slope at the zeros of the $G(S)$ curve. The maximum number of zeros of the $G(S)$ curve is given by the number of layers.

The resulting function is the only existing symmetric set $\{p_h\}$ for a measured $G(S)$ curve. It should be noted, that not every measured $G(S)$ curve has such a simple solution. A lattice factor $G(S)$ resulting from an asymmetric set $\{p_h\}$ produces negative or complex values for some p_h when this method is used. Although $G(S)$ is always symmetric with respect to Bragg conditions or the deviations δS from Bragg conditions, negative or complex values of p_h point to asymmetries in the layer distribution.

Following Wollschläger [123] the asperity height, i.e. the rms. value of the vertical roughness

$$\begin{aligned} \Delta^2 &= d^2\left[\left\langle h^2(\mathbf{m})\right\rangle - \left\langle h(\mathbf{m})\right\rangle^2\right] \\ &= d^2 \sum_{l,h>0} h^2 p_l\, p_{l+h} \end{aligned} \tag{2.23}$$

could be determined by the slope of the G(S)-curve at the in-phase condition. Any further information about the special set $\{p_h\}$ is not achievable. A Gaussian shape is assumed for the G(S)-curve as approximation close to the in-phase condition:

$$G(S) \approx e^{-\Delta^2 (2\pi\,\delta S)^2} \tag{2.24}$$

with δS as deviation of the scattering phase S from the next integer value. This allows the easy estimation of the roughness Δ (in values of the layer distances d) via the full width at half maximum G(S)-curve. The diffraction for non-Gaussian rough surfaces has been studied by Lu et al.[124].

The $G(S)$-curve provides another important information: the vertical layer distance d could be derived from the distance δS between the in-phase conditions:

$$d = 2\pi\delta S / k_{\perp} \tag{2.25}$$

This information could only be obtained for a rough surface, since it is necessary to accurately determine the "in-phase" or "out-of-phase" conditions of scattering [94,95,125]. This is possible with higher accuracy when the $G(S)$-curve is experimentally determined over more than one period. In contrast to He atom scatteringa Smoluchowski smoothening effect, which misleads to a smaller layer distance [126] has not been observed [92].

Especially for pseudomorphic strained heteroepitaxial systems the knowledge of the layer distance d is of special importance [127] concerning the strain relief mechanism via tetragonal distortion of the hetero film [96].

Beside the strong variations of the central spike intensity also the width and shape of the diffuse part of the spot profile varies with the scattering phase S for multi-level systems. Following the descriptions by Pukite, Lent, and Cohen [117] partial lateral pair correlation functions are modulated with $\cos(2\pi Sh)$ for all possible height differences h. Fourier transformation results in a spot profile whith a shape depending on the scattering condition.

Assuming a surface which consists of an unlimited number of surface layers and identical terrace width distribution in any layer a cosine behaviour follows for the FWHM of the profile as function of S

$$FWHM = (\pi\xi)^{-1}(1-\cos 2\pi S) \tag{2.26}$$

with ξ as the average terrace width [117]. Such a rough surface no longer exhibits a central spike: only for the "in-phase" condition all electrons scatter constructively. On such an infinite rough surface exists for any scattering condition always two terraces (on a large length scale) which interfere destructively, i.e. the central spike is erased.

The short scale size distribution (here the terrace width distribution) could be obtained from the profile "out-of-phase" condition. Due to the modulo π property of the exponential for $S = n + \frac{1}{2}$. All even levels interfere with an amplitude of 1, all odd levels with an amplitude of -1. The resulting spot profile is determined by the projection of all even levels into one layer and all odd levels into a second layer. This "out-of-phase" projection of the entire surface roughness on to a two level system is sketched in Fig. 2.8.

2.2.3 Power spectrum

The complementary information about the long wavelength roughness on large scales could be obtained from the profile close to the Bragg condition, i.e. the "in-phase" condition. More precisely: the power spectrum of the surface roughness is available for rough surfaces with finite roughness as sketched in Fig. 2.9.

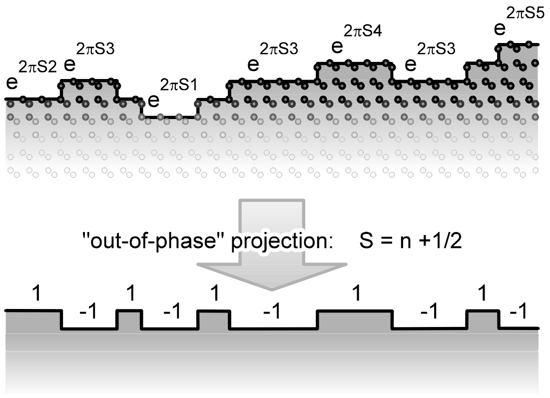

Fig 2.8 "Out-of-phase" projection of a multi level rough surface on to a two level system. At the anti Bragg condition both surfaces could not be distinguished from the LEED pattern.

Using Eq.(2.7b) and Eq.(2.9b) in a 1-dim. description the amplitude of the diffracted electron wave is determined by the surface height function:

$$A(S,k)=\int dxe^{ikx}e^{i2\pi \quad S \quad h(x)} \tag{2.27}$$

For $S=n+\delta S$, i.e. a diffraction condition close to a Bragg condition, the exponential could be expanded in a Taylor series

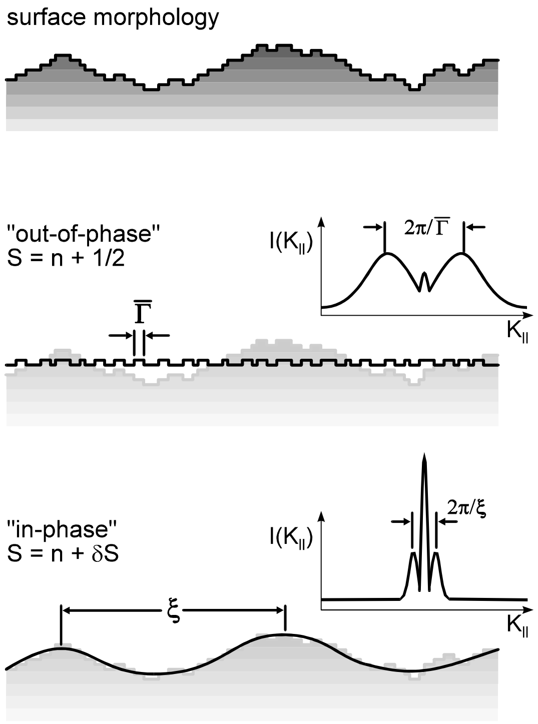

Fig 2.9 The wide spot profile of a multi level rough surface at the "out-of-phase" condition reflects the terrace width distribution ("out-of-phase" projection). Close to the "in-phase" condition the spot profile is determined by the large scale roughness ξ of the surface. Atomic steps are no longer seen. The spot profile has a width of 2π/ξ which is much narrower than at the "out-of-phase" condition.

$$\begin{aligned}A(S,k)=\int dxe^{ikx}&(1+2\pi i\delta Sh(x)\\&-2\pi^2\delta S^2h^2(x)+O(\delta S^3))\end{aligned}\quad . \tag{2.28}$$

The range of validity of this approximation could be expressed by

$$2\pi\delta Sh_{\max}<\frac{\pi}{2} \tag{2.29a}$$

with the maximum height difference $h_{\max}$. This sets an upper limit for $h_{\max}$ and restricts the following procedure to surfaces with finite roughness! In Fig. 2.10 a surface height profile is shown together with the real part of the resulting phase function $\phi(S,x)=e^{i2\pi Sh(x)}$. For small values of δS the correlation length ξ_ϕ of the phase function $\phi(S,x)$ is identical with the correlation length ξ of the surface height function $h(x)$. With increasing deviations from the Bragg condition δS the monotone dependence from height function $h(x)$ to phase function $\phi(S,x)$ is lost and the correlation length of the phase function ξ_ϕ decreases (finally to the average terrace width $\overline{\Gamma}$ at the "out-of-phase" condition): The spot profile becomes broader as sketched in Fig. 2.9!

The measured intensity $I(S,k)=\left|A(S,k)\right|^2$ is

$$\begin{aligned}I(S,k)=\int dx\int dx'e^{ik(x-x')}&(1+2\pi i\delta Sh(x)\\&-2\pi^2\delta S^2h^2(x)-2\pi i\delta Sh(x')\\&-2\pi^2\delta S^2h^2(x')+4\pi^2\delta S^2h(x)h(x'))\end{aligned}\quad . \tag{2.30}$$

Substitution $x\rightarrow x+x'$ results in

$$\begin{aligned}I(S,k)=\int dxe^{ikx}\int dx'&(1+2\pi i\delta Sh(x+x')-2\pi i\delta Sh(x')\\&-2\pi^2\delta S^2h^2(x+x')-2\pi^2\delta S^2h^2(x')\\&+4\pi^2\delta S^2h(x+x')h(x'))\end{aligned} \tag{2.31}$$

and allows averaging with respect to x' of all terms

$$\begin{aligned}I(S,k)=\int dxe^{ikx}&(1+2\pi i\delta S\left\langle h(x+x')\right\rangle_{x'}-2\pi i\delta S\left\langle h(x')\right\rangle_{x'}\\&-2\pi^2\delta S^2\left\langle h^2(x+x')\right\rangle_{x'}-2\pi^2\delta S^2\left\langle h^2(x')\right\rangle_{x'}\\&+4\pi^2\delta S^2\left\langle h(x+x')h(x')\right\rangle_{x'})\end{aligned} \tag{2.32}$$

All averaging terms as $\left\langle h(x')\right\rangle_{x'}$, could be set to zero, because of the free choice of the origin of $h(x)$. This holds also for $\left\langle h(x+x')\right\rangle_{x'}$, because the average $\left\langle\ \right\rangle_{x'}$ is independent on the origin in x'.

$$\begin{aligned}I(S,k)=\int dxe^{ikx}&(1-4\pi^2\delta S^2\left\langle h^2(x')\right\rangle_{x'}\\&+4\pi^2\delta S^2\left\langle h(x+x')h(x')\right\rangle_{x'})\end{aligned} \tag{2.33}$$

Using Eq.(23) with $\left\langle h(x)\right\rangle_x=0$ allows to replace $\left\langle h^2(x)\right\rangle_x$ by the asperity height Δ and results in

$$I(S,k)=(1-4\pi^2\delta S^2\Delta^2)\delta(k)+4\pi^2\delta S^2P(k) \tag{2.34}$$

with the power spectrum

$$P(k)=\int dxe^{ikx}\left\langle h(x+x')h(x')\right\rangle_{x'} \tag{2.35}$$

The resulting spot profile consists of the central spike described by the δ-function, which decreases proportional to

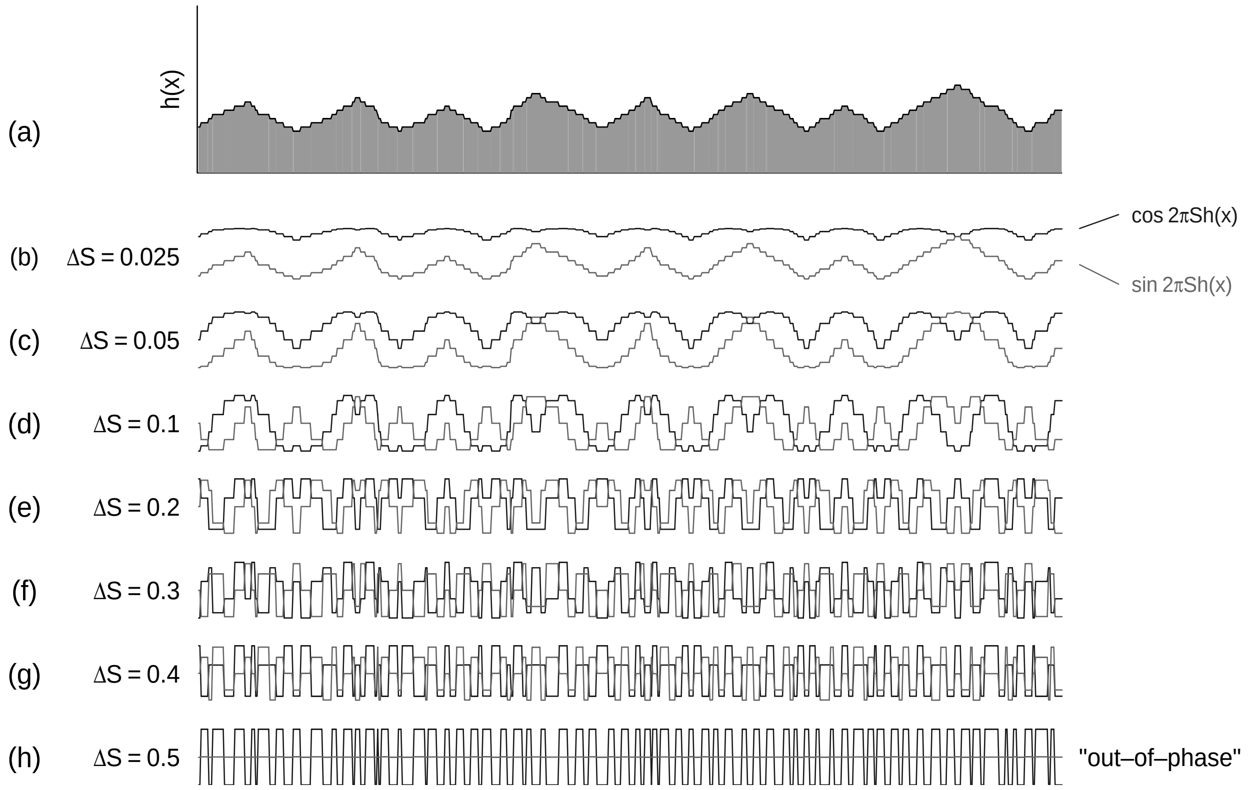

Fig 2.10 (a) 1-dim. height function h(x) of a rough surface. (b-i) Phase transformation cos(h(x)) and sin(h(x)) of the height function for various scattering phases S. (b) is close to in-phase condition, the phase transformation reproduces almost exactly the height function. With decreasing deviations from the in-phase condition the height information h(x) gets distorted and becomes ambiguous. Due to the oscillatory behaviour of the sin and cos function the large-scale roughness information is already lost at (d). At the out-of-phase condition (i) only the short scale information of the terrace width distribution p(Γ)remains.

$\delta S^2 \Delta^2$ as already used for the vertical roughness analysis in Eq.(2.24). The asperity height Δ - as measure of the surface roughness - may now be used to set the range of validity for the Taylor expansion:

$$\delta S < \frac{1}{\sqrt{8}\pi\Delta} \qquad (2.29b)$$

The diffuse part of the profile is described by the power spectrum of the surface roughness and its intensity increases proportional to δS^2. It should be noted, that for $2\pi\delta S h_{\max} < \pi / 2$ the diffuse part of the spot profile does not change its shape, only its intensity!

Describing the rough surface $h(x)$ by a Fourier series

$$h(x) = \int dk H(k) e^{-ikx} \ . \qquad (2.36)$$

allows to rewrite the second term of Eq.(intensity)

$$\begin{aligned} \langle h(x+x')h(x')\rangle_{x'} &= \left\langle \int dk \int dk' H(k) H(k') e^{-ik(x+x')} e^{-ik'x'} \right\rangle_{x'} \\ &= \int dk \int dk' H(k) H(k') e^{-ikx} \left\langle e^{-i(k+k')x'} \right\rangle_{x'} \\ &= \int dk H(k) H(-k) e^{-ikx} \end{aligned}$$

The power spectrum $P(k)$ is therefore given by

$$\begin{aligned} P(k) &= \int dx e^{ikx} \int dk H(k) H(-k) e^{-ikx} \\ &= H(k) H(-k) \\ &= |H(k)|^2 \end{aligned} \qquad (2.38)$$

the square of the Fourier transform of the surface height function.

The interpretation of the spot profile for all other intermediate interference conditions between "in-phase" and "out-of-phase" condition is more complicated. The ambiguity of the projection of the height function onto the phase function ("out-of-phase" projection) causes the smooth transition of a spot profile determined by the power spectrum to the much wider profile reflecting the terrace width distribution as sketched in Fig. 2.9.

Only with a high resolution instrument the diffuse intensity close to the "in-phase" condition could be detected and the spot profile resolved. Using a low resolution LEED the weak diffuse intensity would be outshined by the strong intensity of the central spike.

2.3. Form factor

The spot profile may not only be affected by the surface morphology but also by variations of the structure of form factor of scattering. Here we will not address deviations from the kinematic theory as for instance variations of the structure factor at step edges (see also chapter 7). The case of two alternating terrace structure factors on adjacent terraces on a vicinal Si(001) surface has been described by Martin et al. [128].

If we consider an inhomogeneous surface - as adsorbate islands on a substrate - different structure factors are present and will cause a broadening of the fundamental spots also at the Bragg conditions [129,130]. If a reconstruction with a

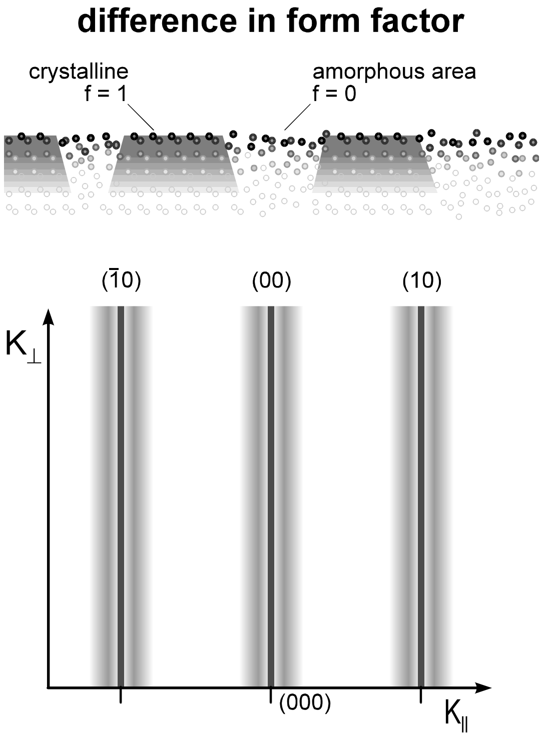

Fig 2.12 Diffraction pattern from a partially amorphous surface. Only the crystalline areas contribute to the diffraction spots. The amorphous areas scatter to a uniform background. The diffraction pattern could be understood as diffraction from a partially blind mirror.

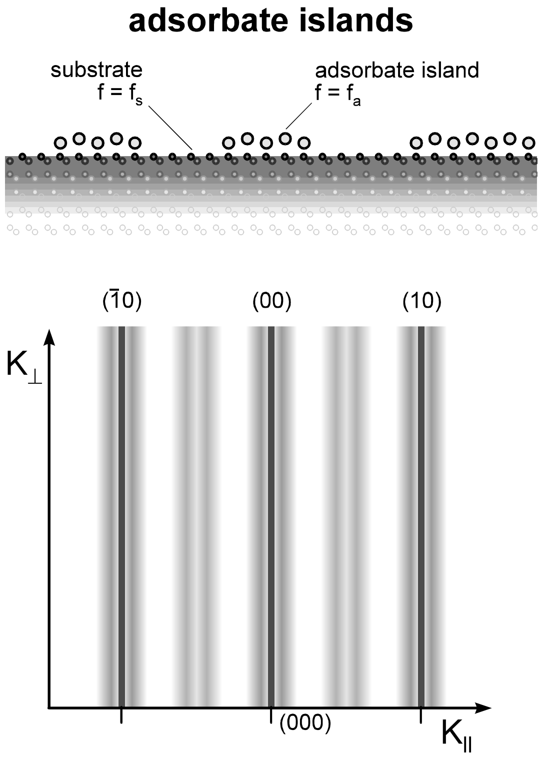

Fig 2.11 Diffraction pattern from a surface with adsorbate island with a different unit mesh or reconstruction than the substrate and two different form factors of scattering.

different unit mesh is present, also the reconstruction spots are broadened and reflect only their own island size distribution [131]. Considering the spot profile of one particular reconstruction spot the structure factor could therefore be set either equal one for the area exhibiting that reconstruction or zero for all other areas. The problem could be described as diffraction from a partly blind mirror as sketched in Fig. 2.11 and Fig.2.12.

If the long range order for the reconstruction is conserved (due to overgrowth of a reconstructed substrate by islands) the profile of the reconstruction spot will consist of a central spike and a diffuse part. The spot profile does not change with the vertical scattering vector, because no steps are involved! Even at "in-phase" conditions $S = n$ the intensity ratio between central spike and diffuse part is constant and does not depend on S [131]! The integral intensity of the reconstruction spot is proportional to the area Θ_{rec} covered with the reconstruction:

$$\int_{total} I_{rec} = \Theta_{rec} \tag{2.39}$$

The intensity of the central spike is given by the absolute square of the diffraction amplitude, i.e. shows a parabolic decay with Θ_{rec}:

$$\int_{centralspike} I_{rec} = \Theta_{rec}^2 \tag{2.40}$$

Here the profile of the spot is simply given by the absolute square of the Fourier transform of the area covered with the reconstruction.

This description holds also for the diffraction from a partly amorphous or disordered layer as sketched in Fig. 2.12. In this case the total intensity of the fundamental spots reveal the still single crystalline surface areas [132,133].

2.4. Non-reversible surfaces

Up to now only reversible surfaces has been considered. Non-reversible surface morphologies as vicinal faces or facets results in diffraction profiles with reduced symmetry; only the point symmetry with respect to Bragg conditions remains.

2.4.1 Regular step train

The influence of regular arranged steps on the LEED pattern has been discussed since the 70th by Germer and Mac Rae [134] and Park and Farnsworth [135]. The first thorough LEED analysis is given by Schwoebel et al. [136]. The diffraction pattern of a vicinal could easily be constructed following the procedure given by Henzler [30,31,33,34]: in real space a regular stepped surface can be constructed by the convolution of a widely spaced super lattice with one single terrace. The periodicity of the superlattice is given by the separation between individual steps with an orientation normal to the vicinal surface, i.e. inclined with respect to the low index surface.

Using the convolution theorem the diffraction pattern is given by the multiplication of the Fourier transform of the super lattice with the Fourier transform of one single terrace. The first is a periodic array of rods, normal to the vicinal surface and a separation given by $\Delta k = 2\pi / Na_0$ with the terrace width $\Gamma = Na_0$. This term determines the position of

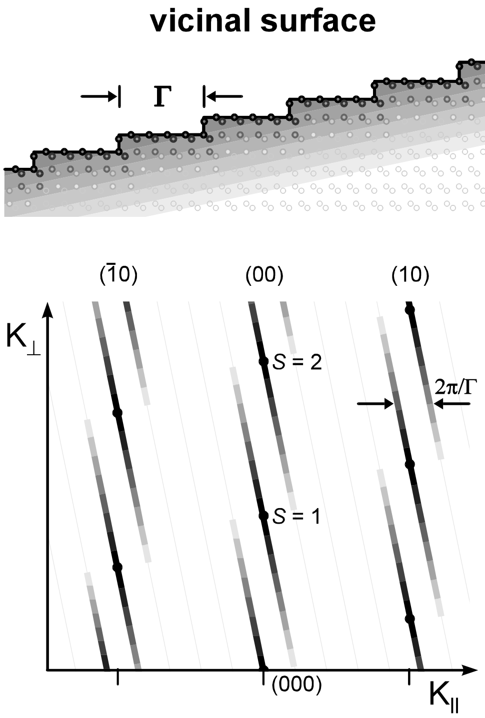

Fig 2.13 Diffraction pattern from a vicinal surface with a regular step train. All LEED spots show a spot splitting due to the linear phase grid of steps. The spots move in accordance to the inclination of the vicinal surface.

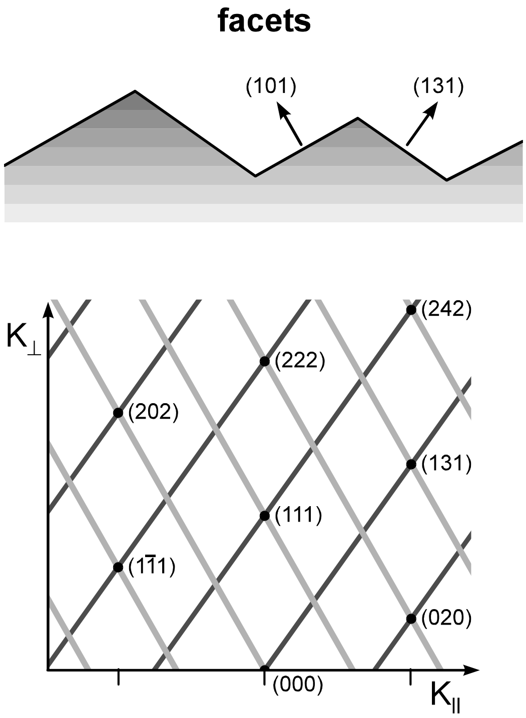

Fig 2.14 Diffraction pattern from a surface with low index facets. Each facet contributes with a complete set of diffraction rods to the pattern. All spots move with electron energy with respect to the macroscopic surface of the sample.

the spots. The whole pattern is now dominated by the periodicity of the steps: All fundamental spots split up into spots with a separation inversely proportional to the terrace width as shown in Fig. 2.13. This phenomenon has been observed in a variety of studies on semiconductors and metals [137-140].

The second term modulates the intensity of the rods. The Fourier transform of one single terrace of width Γ is the multi slit interference function

$$A(k) = \frac{\sin^2\left(\frac{N}{2}ka_0\right)}{\sin^2\left(\frac{1}{2}ka_0\right)} \qquad (2.41)$$

Because this expression is peaked around $k = 2\pi/a_0$ the diffraction spots of a vicinal surface are only intense close to the positions where normal spots of a flat surface would be expected. In general, the split spots have non-equivalent intensities except for the exact "out-of-phase" condition. Within kinematic scattering theory the intensity is given by Eq.(60) and typically only two intense spots are expected. The intensity of any other rod is strongly reduced due to the strong decline of Eq.(60) for $k > 2\pi/Na_0$. Deviations from the kinematic scattering theory - as variations of the form factor at a step edge (see Fig. 2.30a) - manifest in significant intensity of higher order split spots (see also results in chapter 7)

The inclination of the vicinal surface (or facet) could easily be determined by the motion of the split spots in reciprocal space as function of vertical scattering vector $K_\perp$ or scattering phase *S*. Those lattice rods intersect the fundamental rods of a flat surface at the Bragg conditions. Here electrons interfere "in-phase": they are insensitive to the steps of the surface. Intersection of the fundamental lattice rods at anti-Bragg conditions reflects the existence of double steps (also the terrace width is doubled).

Disordered step trains causes a characteristic broadening of the split spots, which may additionally depend on the scattering phase *S* [105,119,141].

2.4.2 Facets

The description of the diffraction pattern of facets is mostly identical with a vicinal surface. Facets could be defined as very dense and very regular step trains. The orientation could be described by low value Miller indices. The single terrace of a facet is that narrow, that it should no longer be considered as composed of steps and terraces. As a consequence of Eq.(60) the facet rods have strong intensity all over the Brillouinzone: The intensity of the facets is not only confined to the vicinity of the fundamental spots. Even more, the relative intensity of the facet spots as function of electron energy could not be described by Eq.(60) but requires a full dynamical calculation as for any other low index surface, too.

The transition in the description of the diffraction pattern from a regular step train to a facet is smoothly. However, experimentally there are some strong hints for the formation of a facet instead of a regular step train: A facet is usually characterised by a minimum of surface free energy due to the formation of an energetically favourable surface structure. This is very often accompanied by the formation of a reconstruction along the inclination direction. This reconstruction stabilizes the facet and is not observed for a step train. Due to the sharp minimum of surface free energy a surface may develop only very few possible and well defined facet orientation. Whereas a step strain may smoothly vary its inclination because the surface free energy also increases smoothly with increasing step density.

2.5. Lattice constants

A change of lateral lattice constant during hetero epitaxial growth is much better measurable than the vertical layer distance: only the measurement of the distance between fundamental spots is necessary [142]. The diffraction spots are much sharper in parallel direction than in the perpendicular direction. For a perfect flat surface the width of the spots are only broadened by the instrument.

With increasing order of the fundamental spots the deviation of the spot positions increases linearly with the difference in lattice constant as sketched in Fig. 2.15(a). Multiscattering events in the substrate and in an adlayer may additionally help to measure changes of the lateral lattice constant with superior accuracy [143-145]. The continuous shift of a compressed Pb layer on Cu has been determined with an absolute accuracy of 0.02 Å [146]! The Relaxation of an InAs film on GaAs has been studied with RHEED [147].

However, when for an weakly bonded adlayer the position of the atoms is determined by a Markov process, i.e. the inter atomic distance (not the displacements!) varies randomly around an average value, long range order of the atomic distances is no longer conserved. This results in the total loss of a sharp central spike for all spots except the (00) spot which is not sensitive for lateral displacements. The fundamental spots are broadened as sketched in Fig. 2.15(b). The profile is determined by the inter atomic distance distribution of the adlayer. For a true Markovian chain (no correlation between neighboured distances) the FWHM of the spots increases proportional to the square of the order of the spot [105,119,148].

Periodic small displacements of unit cells or atoms from their mean position - as observed for surface undulations caused by interfacial dislocation arrays - cause a spot splitting of all fundamental spots [Fig. 2.15(c)] inversely proportional to the average distance between the dislocations [93,149,150]. The intensity of the satellite spots is determined by the geometry of the surface undulation [151].

The (00) spot is only sensitive to the vertical component of the undulation because the lateral scattering vector $\mathbf{K}_{||}$ is zero. With increasing scattering phase *S* the electrons become more and more sensitive to the weak height undulation. The higher order fundamental spots are sensitive to the lateral displacements, too. If the surface exhibits a reconstruction those spots also show a splitting into periodic satellite spots.

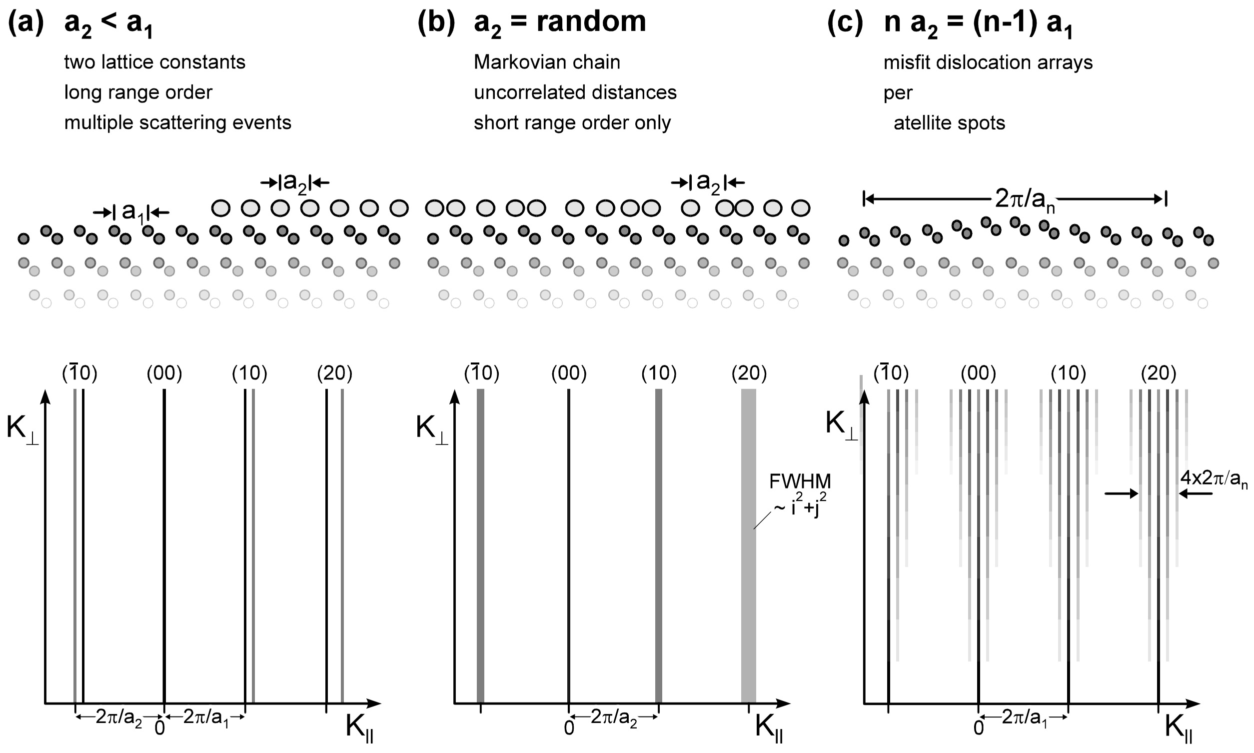

Fig 2.15 Displacements of atoms or unit cells from their periodic position results in different scattering phenomena: (a) Two different lattice constants become apparent through different positions of the high order fundamental spots. Long range order is conserved. Uncorrellated thermal motion of the atoms causes an increase of the homogeneous background on the expense of the spot intensity. (b) Random distances in a weakly bonded adlayer have no long range order: Only short range order is conserved. The (00) spot remains sharp, all other spots are broadened. The FWHM increases with the square of the order i,j of the spots. (c) A periodic displacement of the atoms or unit cells from their mean position - as caused by a periodic interfacial dislocation network - results in a spot splitting of all fundamental and superstructure spots in an array of satellite spots. The surface height undulation acts as 1- or 2-dim. phase grid for electrons.

Because the displacements of the unit cells are not integer values but small fractions of the lateral and vertical lattice constant the diffraction pattern is no longer periodic with respect to Bragg positions. Also the point symmetry with respect to Bragg conditions is lost.

For small displacements and small scattering vector S the electron wave function could be expanded in a Taylor expansion:

$$\begin{aligned} A(S,\mathbf{K}_{\|}) &= \int d\mathbf{r} e^{i\mathbf{K}_{\|}\mathbf{r}} e^{i2\pi \quad S \quad h(\mathbf{r})} \\ &= \int d\mathbf{r} e^{i\mathbf{K}_{\|}\mathbf{r}} \left(1 + 2\pi i S h(\mathbf{r}) - 2\pi^2 S^2 h^2(\mathbf{r})\right) \end{aligned} \qquad (2.42)$$

The vertical component of the 2-dim. surface height undulation $h(\mathbf{r})$ is expressed by a Fourier series

$$h(\mathbf{r}) = \sum_{p,q} D_{p,q} \sin\left(\frac{2\pi}{a_{net}}(x,y)\mathbf{r} + \Phi_{p,q}\right) \qquad (2.43)$$

with the Fourier amplitudes $D_{p,q}$ and phases $\Phi_{p,q}$. The periodicity length of the height undulation is expressed by a_{net}. Exploiting Eq.(42) and (43) under the condition $2\pi S \Delta h < 1$ results in a parabolic intensity behaviour for the satellite spots $I_{sat_{i,j}}$ with the scattering phase S:

$$I_{sat_{i,j}} = 4\pi^2 S^2 D_{i,j}^2 \qquad (2.44)$$

The total intensity of the (00) spot is conserved on the expense of the central spike

$$I_{00} = 1 - 4\pi^2 S^2 \sum_{i,j} D_{i,j}^2 \qquad (2.45)$$

The values $D_{j,l}$ could directly be derived from the slope of the square root of the satellite intensity $I_{sat_{i,j}}$ for very low electron energies. The behaviour for higher values of S is much more complicated and thoroughly addressed in the literature [151].

2.6. Bulk defects

Beside the morphological defects at surfaces also bulk defects have a strong influence on the diffraction pattern. Characteristic is the complete lack of any periodicity in the pattern along the direction of vertical scattering vector.

A typical example for such defects are small angle mosaics: The bulk of the sample consists of crystallites connected by small angle grain boundaries. The diffraction pattern must be constructed by the incoherent sum of the single crystal patterns of each of the crystallites. Because the normal orientation of the crystallites are inclined by small angles, also the diffraction rods follow this misorientation. The incoherent sum results in a spot broadening proportional to the vertical scattering vector $\mathbf{K}_{\perp}$. As a result the spots are sharp only for very low electron energies. Assuming a Gaussian distribution with a standard deviation of σ_{mosaic} for the misorientation of the crystallites the mosaic spread results in a width of the spots of

$$FWHM_{mosaic} = \sigma K_{\perp} \qquad (2.46)$$

Therefore already a small average misorientation causes significant broadening of the spots. As a consequence high resolution diffraction measurements are no longer possible!

2.7. Thermal diffuse scattering

Beside the static defects and morphological surface features also thermal motion of the atoms influence the LEED pattern and the spot profiles [152,153]. Phonon scattering affects both the energy and the momentum of the electrons. Because the energy changes are of the order of only few 10 meV (quasi-elastic scattering) those electrons could not be discriminated from the purely elastic scattered electrons when using a conventional 4 grid LEED optics or a conventional SPA-LEED.

Though the change of energy is small, the accompanied change of momentum, however, could easily be of the order of the Brillouinzone and therefore could not be neglected: the spot profile is affected by the thermal motion of the atoms.

The thermal motion of the atoms is described by $\mathbf{r}(\mathbf{n},t) = \mathbf{r}(\mathbf{n}) + \mathbf{u}(\mathbf{n},t)$. If the thermal displacement $\mathbf{u}(\mathbf{n},t)$ of an atom $\mathbf{n}$ from its mena position $\mathbf{r}(\mathbf{n})$ is small with respect to the lattice constant, the thermal diffuse scattering could be described in the framework of kinematic theory:

$$\begin{aligned} \langle G(\mathbf{K},t)\rangle_t &= \frac{1}{2\pi}\sum_n\sum_m \left\langle e^{i\mathbf{K}(\mathbf{r}(\mathbf{n}+\mathbf{m},t)-\mathbf{r}(\mathbf{m},t))}\right\rangle \\ &= \frac{1}{2\pi}\sum_n\sum_m \left\langle e^{i\mathbf{K}(\mathbf{u}(\mathbf{n}+\mathbf{m},t)-\mathbf{u}(\mathbf{m},t))}\right\rangle e^{ia\mathbf{K}\mathbf{n}} \end{aligned} \qquad (2.47)$$

The brackets $\langle\ \rangle$ denote the time average. With small thermal displacements $\mathbf{u}(\mathbf{n},t)$ we additonally can assume a motion in a harmonic potential. This allows to split the

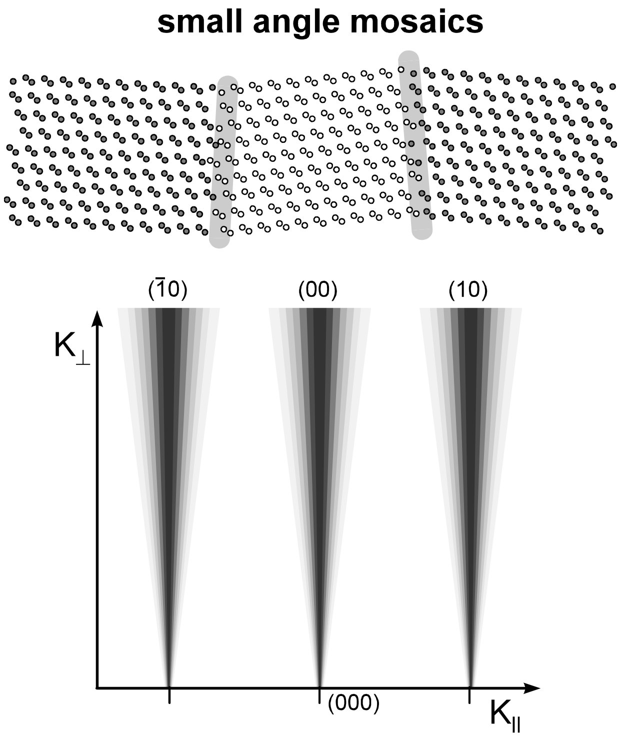

Fig 2.16 Small angle mosaics cause a spread of all diffraction rods. The mosaic spread increases linear with the vertical scattering vector . Each of the small crystallites contributes with one set of arbitrarily oriented diffraction rods to the pattern.

lattice factor into a zero-phonon, an one-phonon, and a multi phonon contribution [153-155] :

$$\langle G(\mathbf{K},t)\rangle = \langle G_0(\mathbf{K},t)\rangle + \langle G_1(\mathbf{K},t)\rangle + \langle G_m(\mathbf{K},t)\rangle \qquad (2.48)$$

In the Debye approximation the three contributions could be formulated independent on the details of the phonon spectrum. The zero phonon contribution $\langle G_0(\mathbf{K},t)\rangle_t$ are the purely elastic scattered electrons without momentum transfer to a phonon. The diffraction pattern for a perfect surface is described by δ-functions

$$\langle G_0(\mathbf{K},t)\rangle \propto e^{-2M}\delta(\mathbf{K}_\parallel - \mathbf{G}_\parallel) \qquad (2.49)$$

which are damped [152] by the Debye Waller factor e^{-2M} which is defined by

$$2M = \langle \mathbf{Ku}\rangle^2 = 1/3|\mathbf{K}|^2\langle \mathbf{u}^2\rangle \qquad (2.50)$$

with $\langle \mathbf{u}^2\rangle$ the mean square oscillation amplitude in the case of isotropic thermal motion of the atom. For an anisotropic surface phonon mode the projection along the direction of the scattering vector **K** has to considered.

The elastically diffracted intensity $\langle G_0(\mathbf{K},t)\rangle$ decreases exponentially with the electron energy E ~ K^2 and the temperature T because the mean square oscillation amplitude $\langle \mathbf{u}^2\rangle$ shows a linear dependence with temperature [156]:

$$\langle \mathbf{u}^2\rangle = \frac{3\hbar^2 T}{m k_B \Theta^2_{D,surf}} \qquad (2.51)$$

The surface Debye temperature $\Theta_{D,surf}$ is usually smaller than the bulk Deybe temperature [152]. Anisotropic vibrational motion of the surface atoms may additionally cause different Deybe Waller factors for different integral order spots.

The multi phonon contribution $\langle G_m(\mathbf{K},t)\rangle$ is described by a constant thermal diffuse background.

$$\langle G_m(\mathbf{K},t)\rangle \propto e^{-2M}(e^{2M}-1-2M) \qquad (2.52)$$

independent on the scattering vector. For high temperatures the LEED pattern is dominated by this contribution.

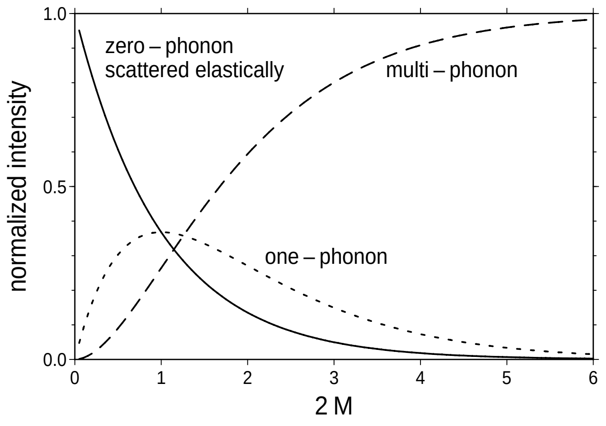

Fig 2.17 Temperature dependence of thermal diffuse scattering. The solid line represents the elastically scattered Bragg peak. With increasing temperature the phonon scattering events increases. At high temperatures multi phonon processes dominate and electrons are scattered to a constant diffuse background.

Only the one-phonon contribution $\langle G_1(\mathbf{K},t)\rangle$ shows a dependence on the scattering vector [153,154,157]:

$$\langle G_1(\mathbf{K},t)\rangle \propto 2M\,e^{-2M}\frac{1}{|\mathbf{K}_\parallel - \mathbf{G}_\parallel|} \qquad (2.53)$$

which has to be corrected for larger $\mathbf{K}_\parallel$ because the electron diffarction from surfaces has no Bragg conditions perpendicular to the surface. Phonons with any possible $q_\perp$ contribute to the one phono loss processes [154]:

$$\langle G_1(\mathbf{K},t)\rangle \propto 2Me^{-2M}\frac{1}{|\mathbf{K}_\parallel - \mathbf{G}_\parallel|}\arctan\frac{\pi/a}{|\mathbf{K}_\parallel - \mathbf{G}_\parallel|} \qquad (2.54)$$

Fig. 2.17 shows the intensity of these three contributions as function of 2*M*, i.e. of temperature *T* or electron energy *E*. The intensity of the diffraction spots decreases with the Debye Waller factor. The one phonon contribution is significant for low temperatures and causes a spot broadening. For higher temperatures the multi phonon processes become dominant and is apparant in the constant thermal diffuse background as shown in the simulated spot profiles in Fig. 2.18. Using a high resolution instrument the elastically diffracted central spike is always the dominant feature of the spot profile.

Using a combinied high resolution electron energy loss spectrometer SPA-LEED [64] the one-phonon, the multi-phonon, and elastic scattering for Al(111) throughout the Brillouin zone could be separated [70]. With the high energy resolution of 4 meV it was possible to measure the dispersion of the acoustic surface phonons. The spot braodening due to the one-phonon losses (see Eq. 54) was experimentally confirmed.

This thorough analysis highlights the necessity to consider spot profile broadening by thrmal diffuse scattering, i.e. especially the one-phonon contribution. The simplest way to do so is to include the arctan(π/$K_\parallel$a)/$K_\parallel$

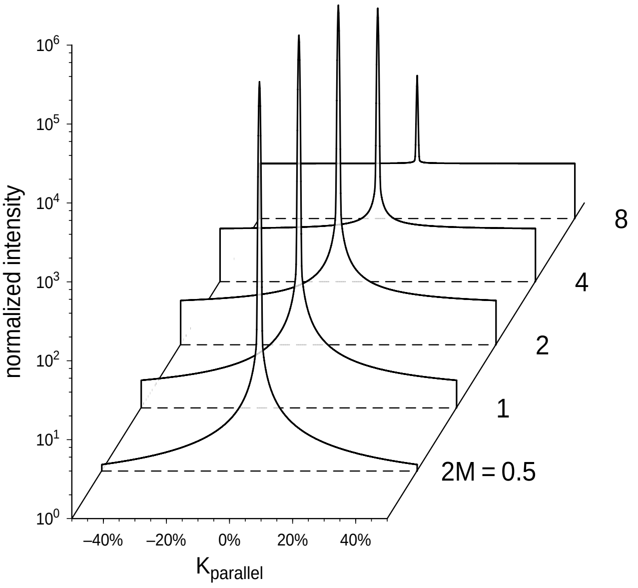

Fig 2.18 Effect of thermal diffuse scattering on the LEED pattern for different values of the Debye-Waller factor. Spot profiles are simulated for an instrument with a transfer width of 200 unit meshes and are shown in a logarithmic intensity scale.

broadening due to the one-phonon contribution into the instrumental response function. The instrumental profile has to be measured for the well prepared initial surface prior to the experiment at the appropriate temperature. Any changes of the profile during an experiment (at constant temperatur) could then be correctly obtained by a deconvolution of the measured profile with the instrumental response function [70].

3. Instrumentation

Spot profile analysing LEED requires high resolution diffraction: the instrumental broadening of the spots limits the possible applications. This restriction is described by the transfer width of the instrument which defines the maximum surface area from which electrons interfere coherently [158-161]. Only features smaller than the coherence length could be observed. The dependence of the transferwith on the size of the electron source and detector, on the angular and energetical distribution of the electrons is discussed in detail already in the litertaure [25,162-164]. As already mentioned in the theoretical description, the kinematic approximation works best the larger the morphological features at the surface.

3.1. Normal incidence

A SPA-LEED is composed of four major parts: a fine focus electron gun, an entrance lens close to the sample, an electrostatic or magnetic deflection unit, and a small aperture in fornt of a single electron channeltron detector. The commercial type SPA-LEEDs also have a screen for visual inspection of the LEED pattern.

High resolution could only be obtained by a small spot size, i.e. a fine focus electron gun at low electron beam current condition. Typical current settings range from 50 pA for a well prepared Si(111) surface up to 500 nA for visual inspection with low resolution. Electron energies could vary from 5 to 500 eV.

The electron beam is not focused on the sample but onto the detector. In the SPA-LEED this is a 100-300µm aperture in front of a channeltron detector. The highest resolution is obtained with the use of the entrance lens of the SPA-LEED, directly in front of the sample. Both the incident electron beam as the diffraction pattern are passing the lens which provides a 1:1 image of the electrons cross over in the electron gun on to the detector. This 1:1 imaging condition causes a very small focus of only 200 - 300 µm in the detector plane. In order to keep the spherical aberrations of the lens as low as possible, the beam size on the sample should be reduced using the einzel lens in the electron gun.

A further reduction of the spherical aberrations could be obtained with a magnetic lens which is integrated into the electrostatic entrance lens [165]. An additional advantage of the magnetic entrance lens is its insensitivity to the shape of the sample and sample holder. The potentials of the electrostatic entrance lens are affected due to the punch through effect of the electrostatic field. The focus properties depend on the lateral sample position and the rotational orientation of the sample holder. Using the magnetic lens allows any sample position. Image rotation and the square root dependence of the lens current on the electron energy are disadvantages of the magnetic lens.

The width of the focused electron beam in the detector plane determines the instrumental response function and the transfer width of the instrument

$$T = \frac{\Delta k}{k_{01}} a_0 \tag{3.1}$$

with Δk the FWHM of the beam, k_{01} the distance between fundamental spots and a_0 the atomic row distance at the surface. In order to measure the instrumental response function it is on principal necessary to use an ideal crystal without any steps, bulk defects or adsorbates. A sample cut from a well oriented Si(111) wafer at an "in-phase" condition comes very close to this ideal case (for instance 96 eV for normal incidence) .

A further important requirement is a large dynamic range for the measurement of electron intensities. With increasing transfer width also the FWHM of the central spike of the LEED spots decreases while its integral intensity stays constant. This results in a strongly enhanced peak intensity. The diffuse intensity of the spots and the background intensity is not affected: the signal to noise ratio in a SPA-LEED system could be enhanced by a factor of 200 compared to a standard 4-grid LEED optics. For a well prepared Si surface a ratio of peak to background intensity up to 100000 could be observed at room temperature.

This requires an electron detector with a dynamic range of more than 10^6. The solution is a single electron channeltron detector with a maximum count rate of more than 10^6 counts/s with a dark count rate of less than 0.1 count/s.

A retarding field analyser is mounted between the apperature and the channeltron in order to reflect inelastic scattered electrons. The typical cut-off characteristics of $\Delta E \sim 1$ eV is determined by the energetical width of the electron beam and the analyser properties. Electrons with phonon losses or gains could not be discriminated with this energy resolution. Nevertheless the inelastic background is strongly reduced by a factor of 2...5 when using the discriminator.

With a single electron detector it is, however, necessary to record the entire LEED pattern in a scanning mode. In the SPA-LEED electrostatic deflection plates are used to continuously vary the angle of incidence of the electron beam in all directions at the sample position as shown in Fig.3.1. A second set of deflection plates with opposite polarity keep the electron beam position on the sample constant independent on the angle of incident. The deflection plates are arranged as sets of two octopoles in order to minimise field inhomogeneities in x and y direction.

The diffracted electrons which are recorded by the channeltron detector follow almost the time reversed path of the incident electrons because the detector is located very close to the electron gun. Scanning the incident angle of the electron beam results in a simultaneous variation of the angle under which diffracted electrons from the surface are recorded. This variation of both the incident and the exit angle of the electrons results in a very special scanning mode in reciprocal space as sketched in Fig. 3.2

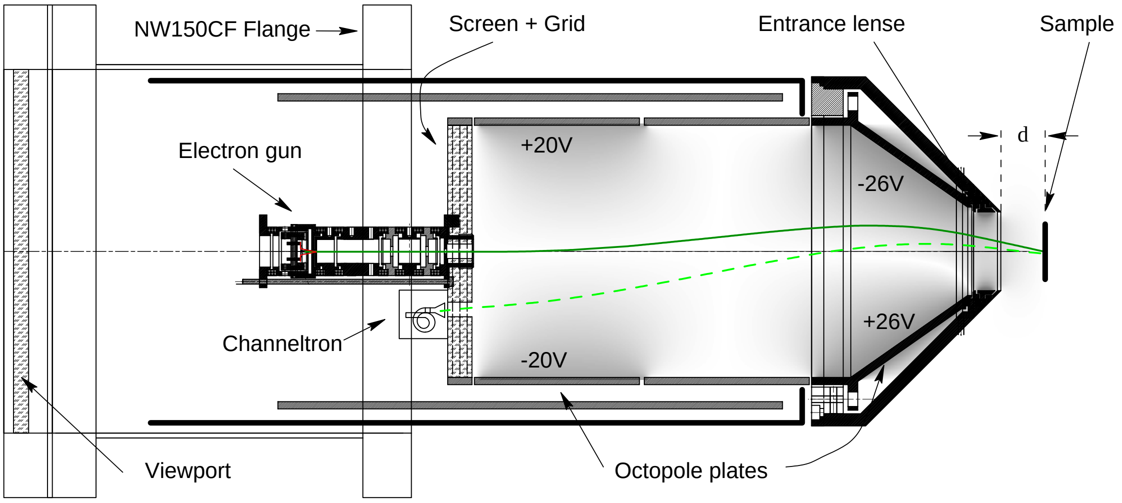

Fig. 3.1 Horizontal cut through a 3rd generation SPA-LEED with conical shape (prototype based on a commercial SPA-LEED from Omicron). Shown are the electron gun, the channeltron detector, the electrostatic deflection unit, the entrance lens and the sample in a position with distance d. The potential of the electrostatic deflection field is shown in a grey scale representation. The path for the incident electron beam and the path of those electrons which are recorded in the detector are shown. During scanning the spot position on the sample stays constant.

The angle between incident and final scattering vector stays constant (and is determined by the geometric angle between gun and detector - here 7°). While the incident angle is changed, the Ewald sphere is rotated around the origin of reciprocal space. As a result the recorded diffraction pattern follows not the Ewald sphere (as for a 4-grid LEED optics) but a sphere with the origin at (000) and twice the diameter of the Ewald sphere. This scanning mode has two advantages compared with a 4-grid LEED optics. The variations of $K_\perp$ with $K_\parallel$ for large parallel scattering vectors are a factor 2 smaller

$$k_\perp = k_{\perp 0} - \frac{\mathbf{K}_\parallel^{\;2}}{k_{\perp 0}} \qquad (3.2)$$

than for the Ewald sphere. A larger area of reciprocal space is on principle accessible to the measurement. Due to the limitations of the electrostatic deflection unit the usable detection area is limited to an angle variation of ±18° which corresponds on a Si(111) surface to an area of six surface Brillouinzones at an electron energy of 77 eV as shown in Fig. 3.2.

Small barrel distortions of the image are caused by non-linearities of the deflection unit and should be corrected afterwards by remapping the recorded LEED pattern.

Further requirements for high resolution electron diffraction are absence of magnetic and electrostatic ac-stray fields, which would sweep the electron beam with 50 or 60 Hz. For the typical data acquisition times this result in unpredictable spot broadening or intensity oscillations. Due

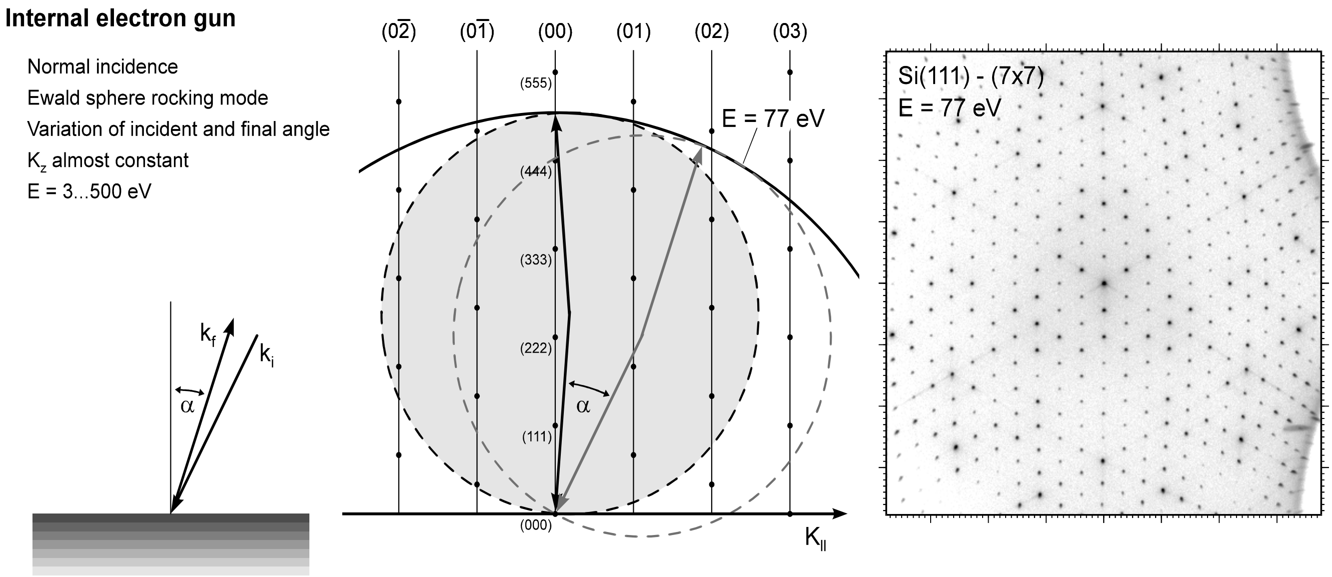

Fig. 3.2 Diffraction geometry in reciprocal space for the SPA-LEED internal electron gun. Both the angle of the incident electron beam and of the diffraction pattern are varied continuously in order to record the LEED pattern. The relative angle between incident and final scattering vector stays constant As a result the recorded diffraction pattern is described by the envelope of the rocking Ewald sphere, i.e. a sphere centred at the origin of the reciprocal space and a diameter twice the size of the Ewald sphere. Typical electron energy is 30 - 120 eV.

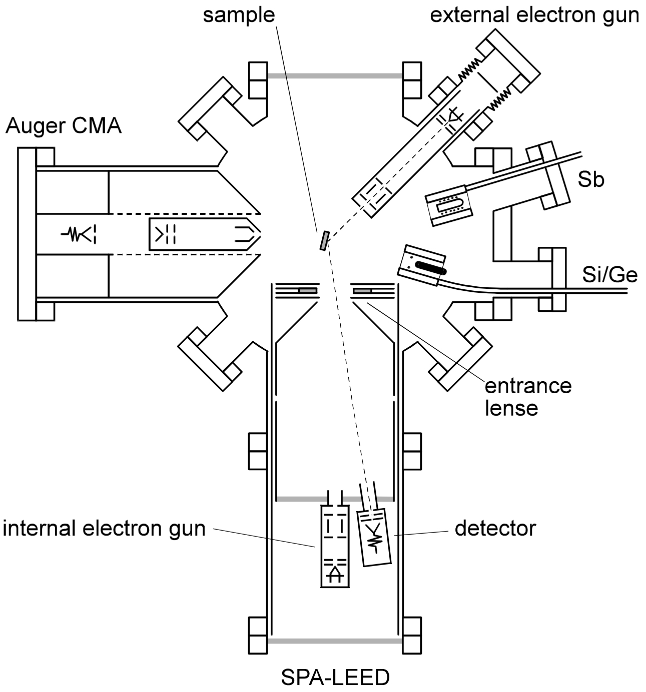

Fig. 3.3 Experimental set-up for the in-situ in-vivo experiments during adsorption and/or deposition using a second, external electron gun in a RHEED like geometry. Ge or Si deposition is now possible perpendicular to the sample surface resulting in homogeneous film thickness. At the same time surfactants could be co-evaporated. Shown is a cylindrical shaped 2nd generation SPA-LEED with bent deflection plates.

to the same reason mechanical vibration has to be avoided. The SPA-LEED is not that sensitive to constant magnetic and/or electrostatic stray fields which usually only cause a shift of the spots without changes of the spot profile or the intensity. The Bragg conditions, however, could be changed by a few eV due to small changes of the incident angle of the electron beam (see also Eq. 11b,c).

3.2. Grazing incidence

In order to perform in-situ in-vivo measurements during adsorption or crystal growth experiments a second "external" electron gun is used as shown in Fig.3.3 with the principal sketch of the apparatus. A small focus is obtained by a large back focal length resulting in a small image of the cross over on the channeltron apperture.

An incident angle of ~65° for the electron beam leaves plenty of space in front of the sample for evaporators. The geometry is similar to a RHEED experiment with a larger grazing angle of ~25° as shown in Fig.3.4. An additional advantage is the increased k-space resolution $\Delta K_x / K_{01}$ along the grazing incidence direction

$$\frac{\Delta K_x}{K_{01}} = \frac{1}{\cos\vartheta}\frac{\Delta K_y}{K_{01}} \qquad (3.3)$$

compared with the resolution in the y-direction. Transfer widths of more than 200nm have been obtained on Si surfaces. A disadvantage is the strong distortion of the LEED pattern due to the grazing projection of the diffraction rods on to the Ewald sphere (see Fig.3.4). The spots are located on the so called Laue circles. For spot profiles along K_x the vertical scattering vector $K_\perp$ varies strongly

$$K_\perp = K_{\perp 0} - K_x \tan\vartheta \qquad (3.4)$$

which must be taken into account for the analysis.

Recording a LEED pattern using the external electron gun the angle of incidence of the electrons is not changed. Therefore the diffraction pattern follows the Ewald sphere and the accessible area of reciprocal space is much smaller (see Fig. 3.4).

The typical electron energy ranges from 60 to 200 eV. This results in a small vertical scattering vector (grazing incidence). Therefore the Debye Waller factor is small: a LEED pattern with sufficient signal to background ratio could easily be recorded up to high sample temperatures.

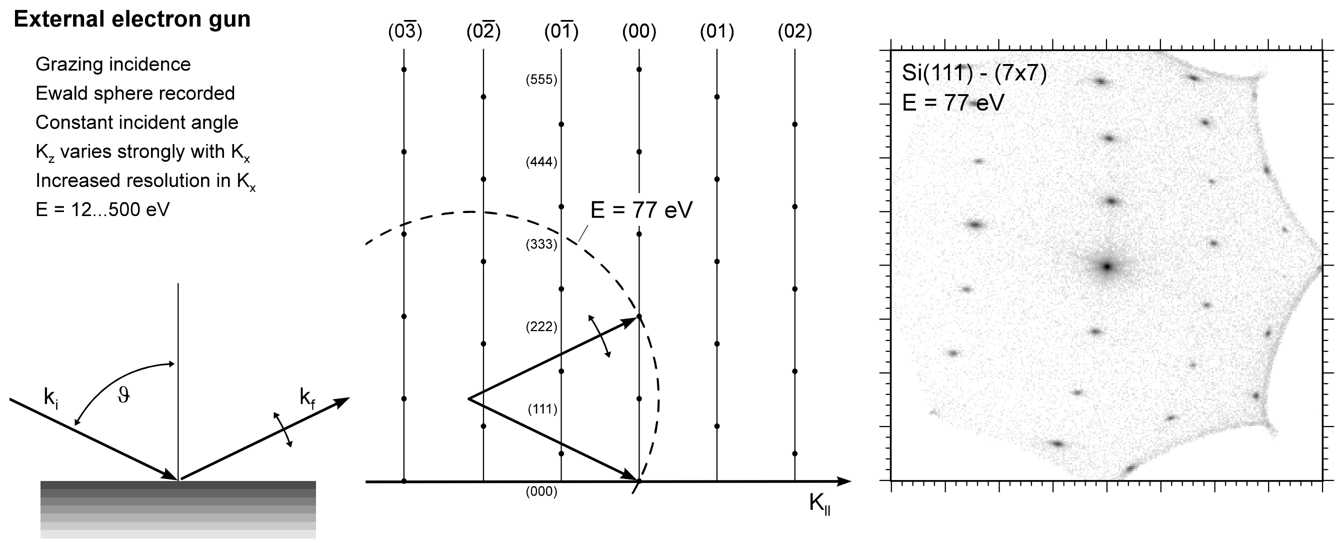

Fig. 3.4 Diffraction geometry in reciprocal space with the external electron gun. Experimental set-up for the in-situ in-vivo experiments during adsorption and/or deposition using a second electron gun in a RHEED like geometry. Typical electron energy is 100 eV. Angle of incident electron beam is fixed. The diffraction pattern is scanned and follows the Ewald sphere. The LEED pattern is distorted du to the grazing incidence of ~25°.

3.3. Real Space Mode

Synchronising the deflection voltages of rear and front oktopole (using a multiple switch) the electron beam is scanned over the sample and the entrance lens of the SPA-LEED. By recording elastic and secondary electrons with the channeltron detector it is possible to obtain an image of the sample. Due to the electron beam diameter of ~0.5mm the SPA-LEED works in this mode as a low resolution high distance scanning electron microscope.

Nevertheless there are two big advantages using this mode. First it is possible to check the electron spot position on the sample. The centre of the real space image as shown in Fig. 3.50 (with an u-shaped Si(111) sample, the sample holder and the inner parts of the entrance lens) corresponds to the spot position in the LEED mode. Second from the resolution in this image the diameter of the electron beam on the sample could be determined and optimised. The smaller the diameter in the entrance lens, the smaller are the spherical aberrations of the lens and the higher is the resolution of the SPA-LEED.

Surprisingly a (7×7) diffraction pattern appears in the image of the sample surface. For each of the spots the Laue condition is fulfilled during the real space imaging mode: electrons are elastically diffracted directly towards the channeltron.

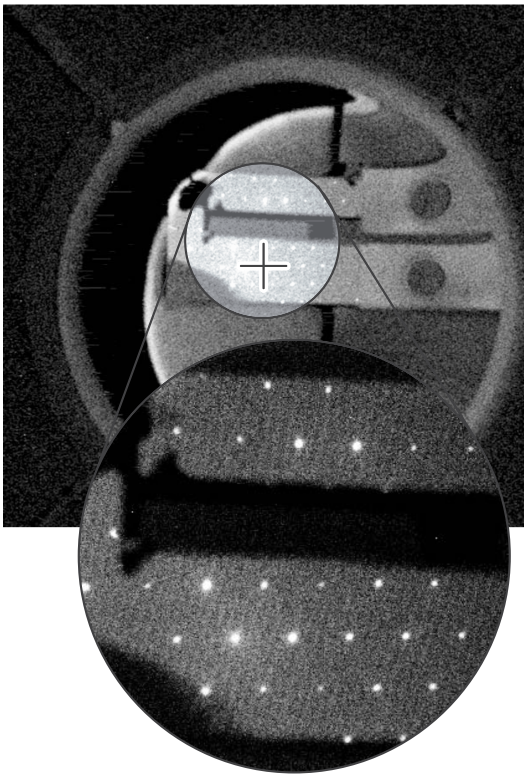

Fig. 3.5 Real space image of the sample, sample holder, and inner parts of the entrance lens obtained with the low resolution long distance scanning electron microscopy mode. The voltages of the deflection plates are synchronised and the electron beam is scanned over the sample. Electrons are detected with the built- in channeltron. The bright regular arranged spots are observed, when the scattering condition for the (7×7) reconstruction is fulfilled. Oxide covered areas appear dark.

4. Si(111) Homoepitaxial Growth

4.1 Intensity oscillations

We will starte the experimental part of this review with the homoepitaxial growth of Si(111). This is an ideal system to demonstrate various capabilities of high resolution diffraction for in-situ studies of surface morphology during deposition.

The bare substrate shows a (7×7) reconstruction as already shown in Fig. 3.2. For temperatures above 300°C Si grows in a 2-dim layer mode as revealed by periodic intensity oscillations of the central spike of the (00) spot as function of coverage. The origin of the oscillations is the periodic completion of the surface layers during deposition together with the destructive interference of electrons scattered from adjacent terraces [56,98-101]. The oscillation period shown in Fig. 4.1 correspond to the deposition of two atomic monolayers, i.e. one bilayer of Si (1BL = 15.7×10^{14} Si cm^{-2}). Due to their stacking sequence (111) surfaces of Si and Ge always grow in a bilayer fashion [101,166-170].

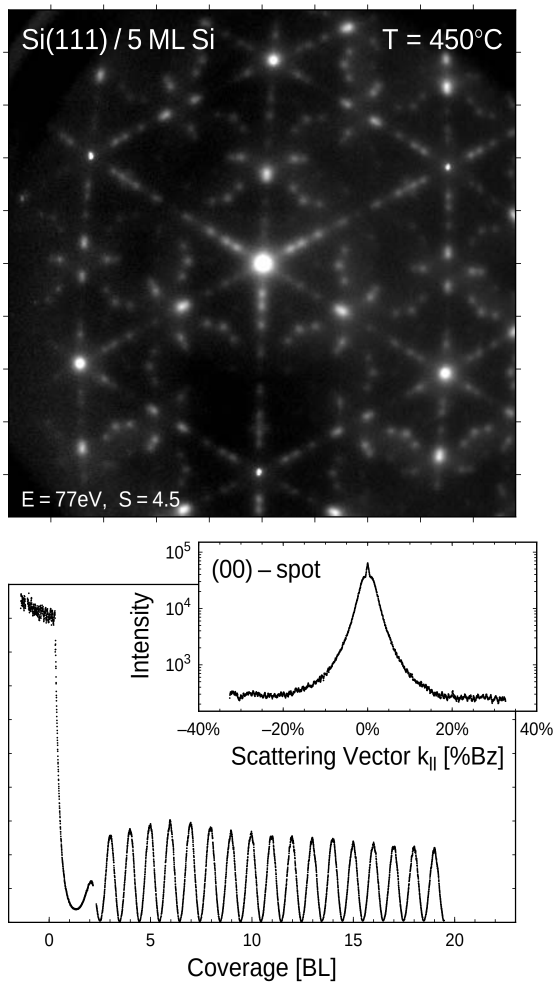

Fig. 4.1 LEED pattern after deposition of 5 ML of Si on Si(111) at 450°C. Due to the low deposition temperature both (7×7) and (5×5) reconstruction domains are present. The spots are strongly broadened. The constant intensity oscillations in the lower plot exhibit a 2-dim. layer growth mode without kinetic roughening. The spot profile of the (00) at "out-of-phase" condition shows the broadening due to surface roughness.

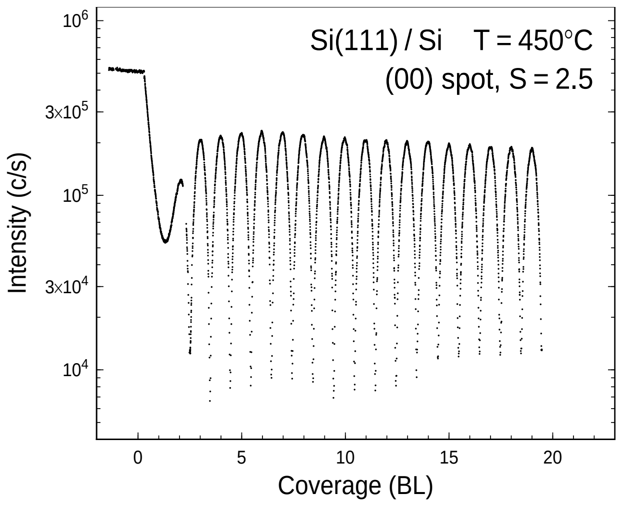

Fig. 4.2 (00)-spot intensity oscillations in a logarithmic scale. The very pronounced minima of the oscillations with a dynamic range of 1:100 reflects a zero passage of the scattering amplitude. The sample must be extremely uniform over the size of the electron beam and the "out-of-phase" condition must be exactly be fulfilled to show this phenomena.

From the intensity oscillations some important growth features can be concluded. The initial stage of growth for the first 2 to 3 BLs differs from the steady state behaviour beyond deposition of 3 BLs. The constant amplitude of the intensity oscillations reflects the absence of kinetic roughening of the growth front. For a perfect layer-by-layer growth mode parabola like, peaked oscillation maxima would be expected which have to show the same intensity than the bare surface. Here the intensity of the oscillations, however, is significantly lower and the maxima are rounded which is explained by the nucleation of a new layer before the previous layer is complete.

The central spike almost vanishes for the half monolayer condition. The large dynamic range of the variation of the central spike intensity of more than 100 could be seen best in Fig. 4.2 in a logarithmic plot of the intensity. The remaining intensity at the minima of the oscillations is caused by the diffuse part of the spot.

This very pronounced decrease of the central spike intensity to almost zero verifies the chemical and morphological uniformity of the illuminated area of the sample. Because the diameter of the electron beam is of the order of mm^2 this could be considered as a representative area of the surface. Any deviations from the half monolayer condition (due to inhomogeneous deposition) would result in the presence of a central spike at the oscillation minima. This condition requires to mount the Si evaporator normal to the surface of the sample. Deposition under off normal conditions would result in a wedge shaped Si layer. The incoherent sum of the coherent diffraction patterns would show a damped beat of the oscillations.

Figure 4.3 shows that not only the central spike intensity oscillates, but also the intensity and profile of the diffuse intensity. The total intensity of the spot is almost constant. The variation of the spot profile reflects the change of terrace width distribution during the complete cycle of nucleation and completion of one bilayer. At half coverage condition the diffuse intensity shows a "Henzler"-ring indicating a terrace width distribution with a dominant terrace length.

The oscillations of the central spike intensity could not only be used for the determination of the number of deposited layers. With Eq.(17) and (18) the intensity of the central spike is given by the partial coverages $p_h = \theta_h - \theta_{h+1}$ in the different levels [101].

An intensity measurement at the "out-of-phase" condition together with the boundary condition of the totally deposited amount $\theta_{total} = \theta_1 + \theta_2 + \ldots$ allows the determination of the coverage in three different surface layers during growth. The central spike intensity for such a three level system is

$$G(\theta, S = \tfrac{1}{2}) = (p_0 - p_1 - p_2)^2 \tag{4.1}$$

with $\boldsymbol{p}_0$ the visible fraction of the lowest layer and $\boldsymbol{p}_1$

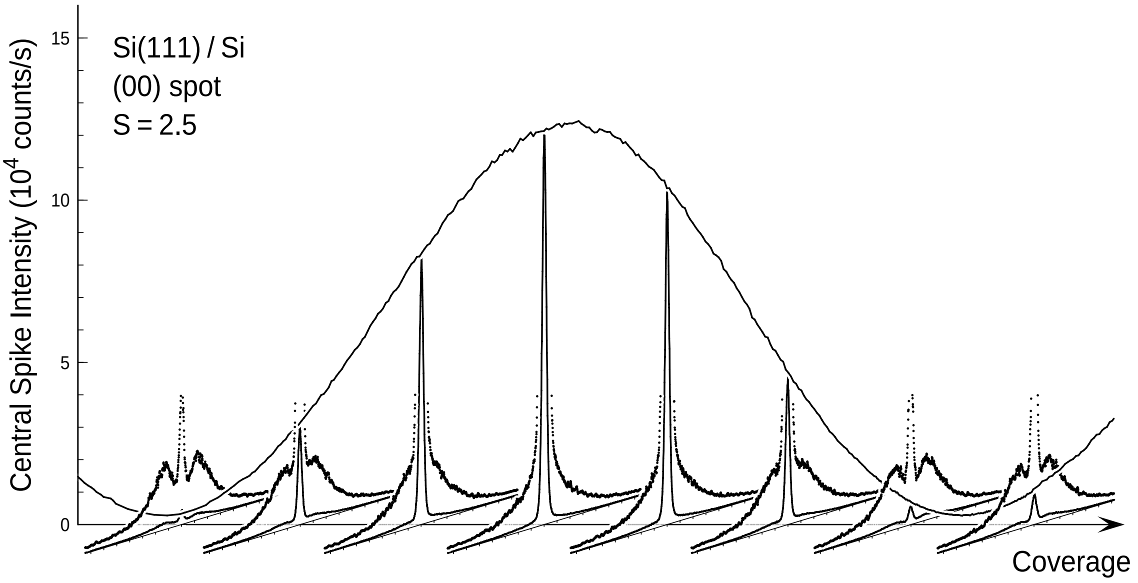

Fig. 4.3 (00) spot profiles during one oscillation period. The shape of the profile also varies periodically. The total intensity of central spike and diffuse part is conserved during deposition.

and $\boldsymbol{p}_2 = \theta_2$ the visible fraction in the top layers. Using the normalisation $1 = p_0 + p_1 + p_2$ we obtain

$$p_1 = \tfrac{1}{2} \pm \tfrac{1}{2}\sqrt{G(\theta, S = \tfrac{1}{2})} \tag{4.2}$$

The sign of the square root has to be changed for every zero passage. Conservation of the total deposited coverage allows the determination of the remaining values

$$p_2 = \frac{\theta_{total} - p_1}{2} \tag{4.3}$$

$$p_0 = 1 - p_1 - p_2 \tag{4.4}$$

Fig. 4.4 shows two examples for such an evaluation: the layer-by-layer intensity oscillations for Si homoepitaxial growth in the presence of a monolayer of Sb for two different temperatures. The Sb monolayer acts as surfactant floating on the growth front without significant incorporation. In contrast to experiments without Sb a weak kinetic roughening is observed: the amplitude of the oscillations decreases with coverage.

The topmost graph shows the normalised central spike intensity during deposition. The partial coverages $p_h = \theta_h - \theta_{h+1}$ are derived from the square root of the intensity and are shown in the middle plot. In order to apply this algorithm for such a steady state growth the index of the levels must be reduced by 1 when the lowest level is complete $p_{i+1} \to p_i$. This is done for every minima of the intensity oscillations (zero passage of $G(\theta, S = \frac{1}{2})$). For that condition only two levels are present, with the top layer half filled. The lower curves in the middle plot gives the resulting partial coverages p_0 and p_2, respectively. Now it is possible to follow the evolution of each layer from its nucleation until it is completely covered by the next layer. Finally the coverages θ_h of the different levels is plotted in the lower plot.

Growth at 700°C shows almost a perfect layer-by-layer behaviour (dashed lines). We observe the nucleation of a new layer before the previous layer is complete. This behaviour is responsible for the rounded peaks of the intensity maxima.

Using the LEED intensity oscillations at a second electron energy, i.e. a scattering phase $S = n \pm 1/4$, allows to unambiguously determine the layer distribution for a 4-level system. This will be demonstrated in chapter 4.3 for the initial stage of growth for this system.

4.2 Temperature and flux dependence

The homoepitaxial growth of Si(111) depends strongly on temperature. Below 250°C the film quality degrades with thickness and results in non crystalline amorphous layers. A strong damping and decrease of the intensity of the LEED specular spot has been observed [169]. The LEED pattern completely vanishes.

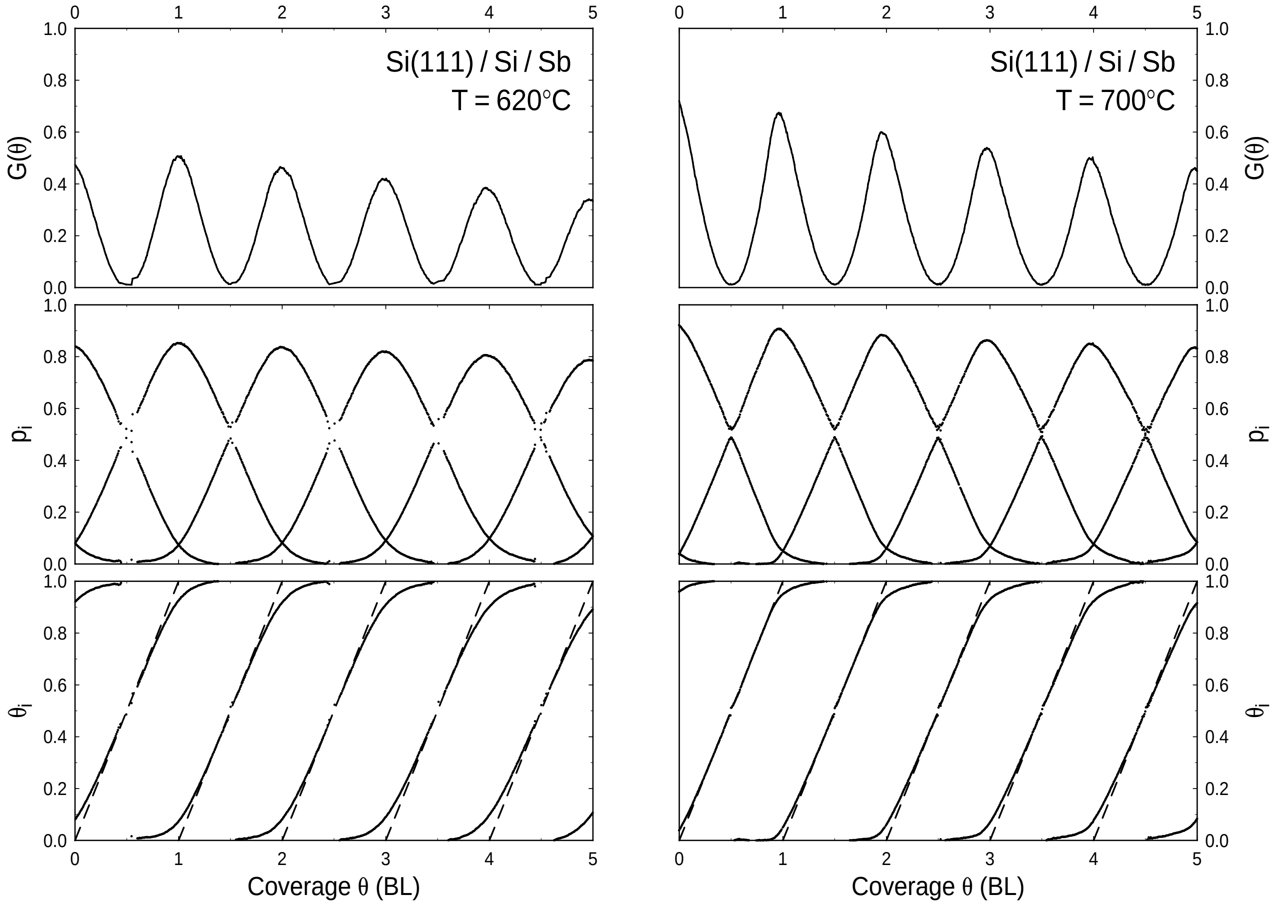

Fig. 4.4 Homoepitaxial growth of Si(111) in the presence of Sb as surfactant shows almost perfect layer-by-layer growth behaviour. The coverage in the different layers could be determined during growth from the central spike intensity at "out-of-phase" condition. The proposed model (see text) is valid for up to three simultaneously visible surface levels.

In the temperature range between 250°C and 600°C the mobility of the Si adatoms is high enough to form single crystalline films. The growth front is rough; a 2-dim. layer growth mode is observed in pronounced LEED and RHEED oscillations [101,170,171]. The surface is highly defected: a mixture of (7×7)- and (5×5)-reconstruction domains has been observed [101,172]. Minor (3×3)- or (9×9)-domains are also present. Nucleation is observed at domain boundaries. The (5×5)-is a smaller and metastable version of the famous DAS (7×7)-reconstruction. It is observed for low temperature growth or during annealing of a cleaved Si(111)-(2×1) surface [173].

Above 600°C a step flow growth mode is observed. All Si atoms are that mobile to be trapped at step edges, which propagate over the surface. Only a (7×7)-reconstruction is observed. LEED and RHEED experiments show no intensity oscillations [171].

The LEED pattern shown in Fig. 4.10 after deposition of 11.5 BLs shows the above mentioned mixture of broadened (7×7)- and (5×5)-spots. The width and relative intensity of the superstructure spots as well as the width of the fundamental spots depends on the kinetics, especially on growth temperature and deposition rate. With increasing temperature all spots become much sharper and the intensity of the (7×7)-spots increases on the expense of the (5×5)-spots as shown in Fig. 4.5 and 4.6. The very broad spots in Fig 4.5(a) reflect the small size of the superstructure domains at 475°C. Very weak (5×5) reconstruction spots could be observed up to temperatures of 630°C (using a deposition rate of ~1ML/min). Above 630°C the (5×5) reconstruction is vanished, only the stable (7×7) remains. At lower temperatures the intensity of the (5×5)-spots is stronger than those of the (7×7)-spots. Interpreting this as dominant formation of (5×5) reconstruction would be a hint

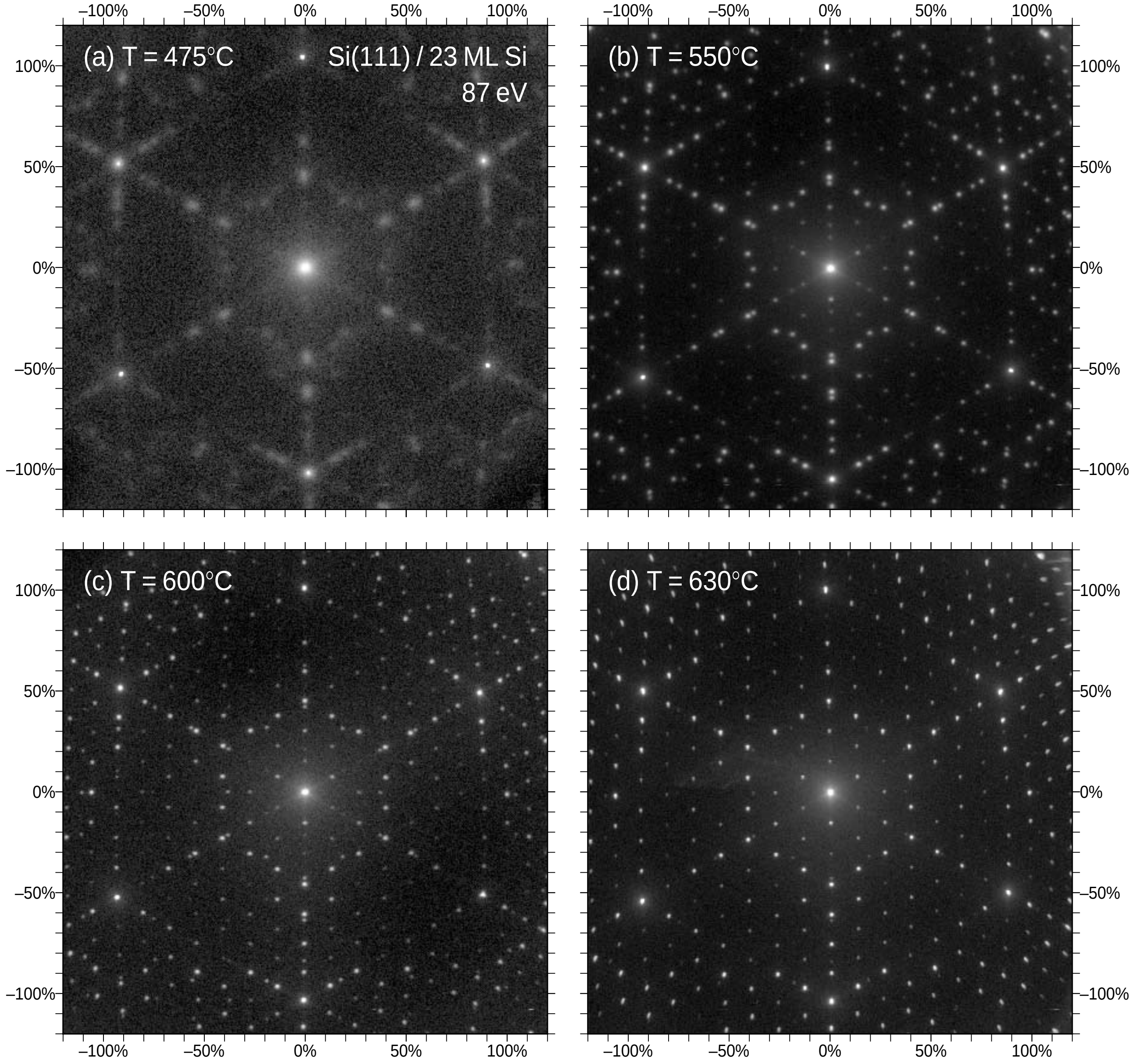

Fig. 4.5 LEED patterns after growth of 23 ML of Si on Si(111) at 87 eV using a logarithmic intensity scale with a dynamic of 1:1000. (a) Growth at 475°C results in broad superstructure spots. The (5×5)- and (7×7)-spot could not be distinguished. (b) The (5×5)- and (7×7)-spots are seen much better after growth at 550°C; they are, however, still broadened. (c) The spots are sharp. The intensity of the (5×5)-spots is decreased. (d) Very weak (5×5)-spots are detectable up to 630°C.

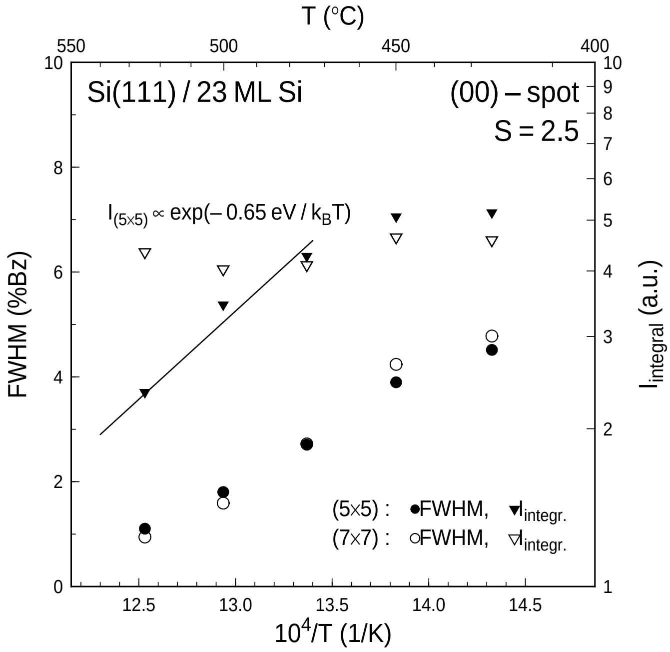

Fig. 4.6 Temperature dependence of the FWHM and intensity of the (7×7) and (5×5) superstructure spots after deposition of 11.5 BLs of Si. The width decreases strongly with temperature. For higher temperatures the (7×7) becomes the dominant reconstruction.

for a larger kinetic barrier for the formation of (7×7) unit cells.

Fig. 4.7 shows the influence of growth temperature on the intensity oscillations of the (00)-spot during deposition of the first 11.5 BLs. The growth proceeds in a layer-by-layer mode with bilayer period.

The electron energy has been chosen as an "out-of-phase condition" where electrons scattered from neighboured terraces interfere destructively. The maxima of the oscillations reflect the completion of a bilayer with the constructive interference of most of the electrons.

For half of a complete bilayer coverage, however, the vanishing of the central spike of the (00)-spot is observed in the minima of the intensity oscillations. Only the broadened part of the (00)-spot remains (the total intensity of the LEED spot is conserved, independent on the surface morphology and causes the remaining intensity).

This zero passage of the amplitude (only 0.1% of the (00)-spot intensity remains in the central spike at the minima) can only occur for the exact out-of-phase condition and reflects a very uniform sample preparation and a homogeneous coverage of the deposited film.

The first intensity maximum occurs at first at a coverage of 2 BL as also reported by other authors [166,174]. This behaviour is caused by the preferred growth on top of the already grown islands. The second bilayer grows almost as fast as the first bilayer [101]. For low total coverages this is only possible if the diffusion length is much larger than the average island separation, because very small islands have already a double bilayer height [175,176] at low coverages.

The surface grows in a steady state mode without any trace of kinetic roughening for increasing coverage as seen in the constant height of the oscillation maxima. This is only possible without generation of bulk defects. The oscillation amplitude is also almost independent of the temperature of growth and points to an almost constant vertical roughness. Thus the diffusion of the deposited adatoms across steps is kinetically not hindered for this temperature range. Even more, we observe a preferential filling of the lowest levels during layer-by-layer growth [101]. This and the constant amplitude with coverage emphasises the absence of a diffusion barrier (Schwoebel Ehrlich step edge barrier) across step edges for Si(111).

With increasing temperature the intensity in the minima of the oscillations raises more and more which is caused by the diffuse part of the (00)-spot. Figure 4.8 shows spot profiles immediately measured after deposition of 23~ML of Si with a rate of 1.0~ML/min. The central spike at $\mathbf{K}_{\|} = 0$ is clearly seen. The broadening becomes sharper and more

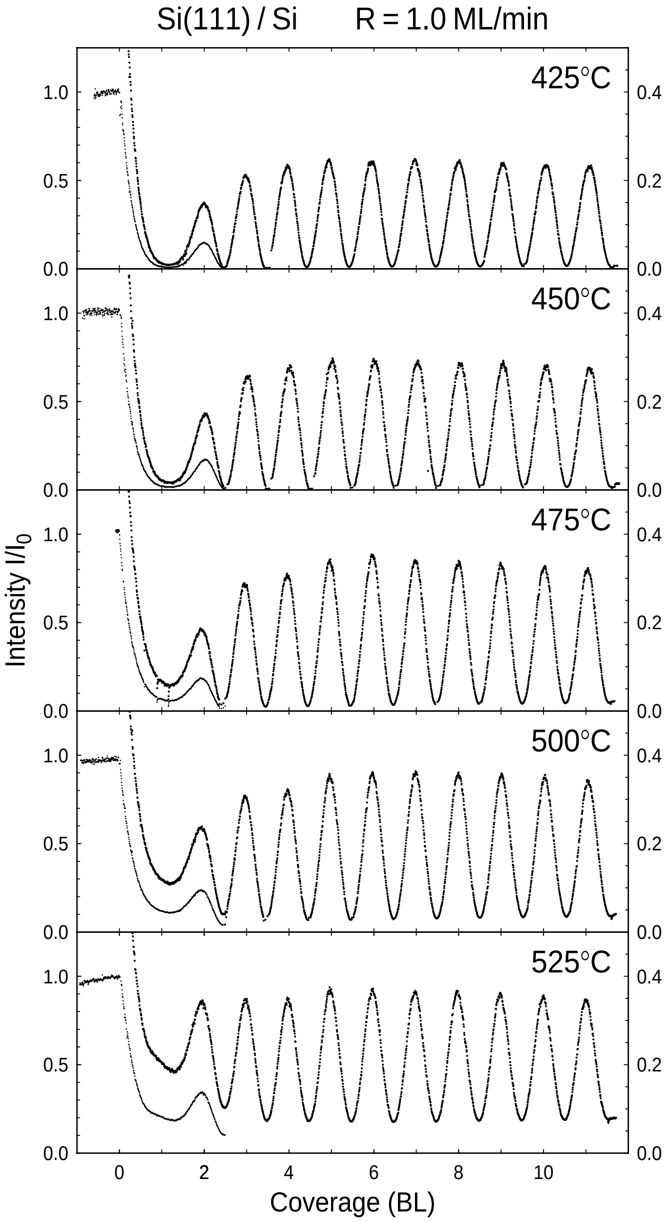

Fig. 4.7 Bilayer intensity oscillations of the (00)-spot during deposition reflect the epitaxial growth. The growth in double bilayer high islands on the perfect (7×7) substrate is apparent in the lack of the first intensity maximum at 1 BL coverage. The almost constant oscillation amplitude reflects the vertical roughness being independent on the temperature of growth. The oscillations are enhanced by a factor 2.5 (labels on the right axis).

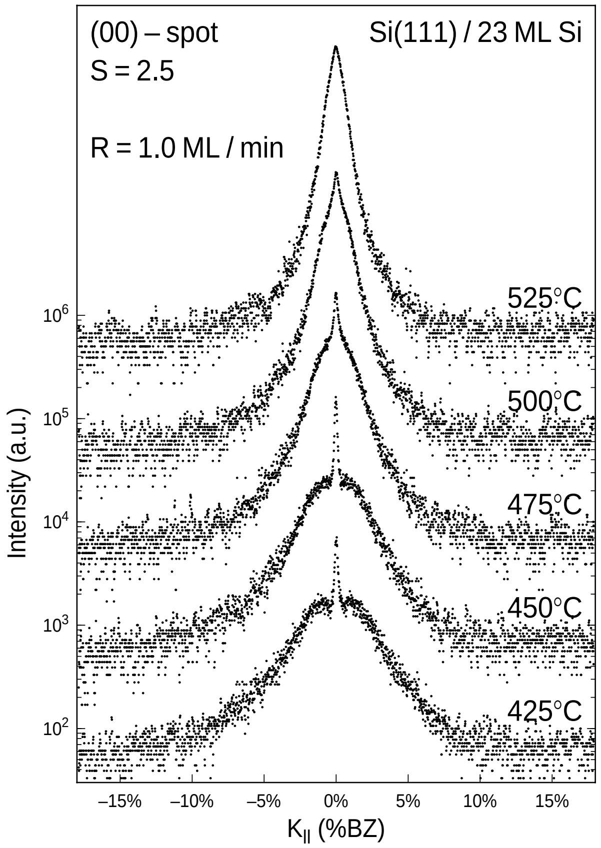

Fig. 4.8 LEED (00)-spot profiles immediately after growth of 23~ML of coverage at different temperatures. The small central spike at reflects the deviations from the exact half coverage condition. With increasing temperature the broadened part of the (00)-spot becomes narrower and more intense (the total intensity in the (00)-spot, however, is conserved).

intense at higher temperatures which reflects the increasing size of the terraces or islands.

The average terrace width is now derived from the spot profiles [121,129] and plotted in Fig. 4.9. An activation energy of 0.64±0.05eV is derived from the Arrhenius plot of the terrace length. If the island density is estimated roughly as the reciprocal square of this value - an activation energy of 1.28eV results for that magnitude.

Instead of changing the temperature it is also possible to vary the deposition rate *R* at constant temperature in order to become further insight into the island nucleation process. The intensity oscillations for the change of deposition rate *R* are very similar to those shown in Fig. 4.7.

We therefore only show in Fig. 4.10 the spot profiles after growth of 23~ML of Si at a constant temperature of 450°C at varying rates *R*. These profiles have almost the same shape as those shown in Fig. 4.8, where the temperature has been changed at constant flux. For growth above 500°C we observe exactly the same shape for the spot profiles. As a conclusion: it does not matter for the growth if the deposition rate is changed or the temperature of growth - both variations cause the same changes of surface morphology.

In Fig. 4.11 the average terrace width as function of the deposition rate is plotted in a double logarithmic scale for a growth temperature of 450°C and 500°C respectively. The change of terrace width is only small compared with the flux

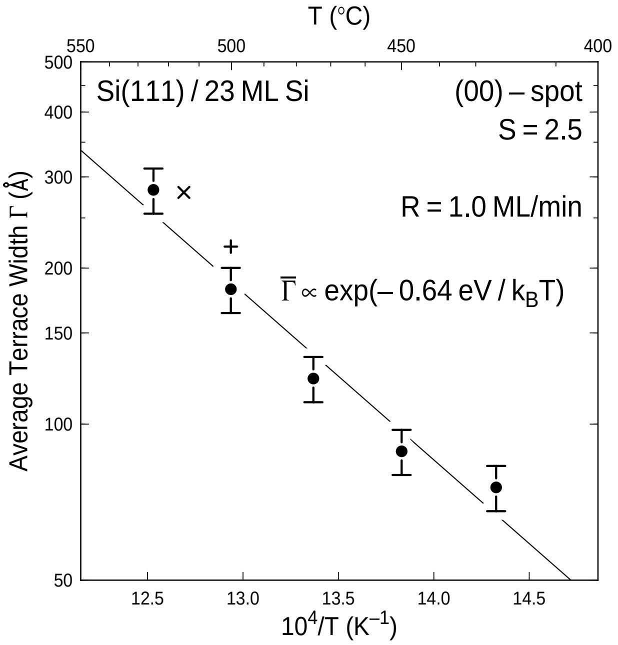

Fig. 4.9 Arrhenius plot of the average terrace width derived from the (00)-spot profiles shown in Fig. 4.8. A constant deposition rate of 1.0 BL/min was used. The two crosses are from Ref.[175] and [176] for nucleation on the perfect Si(111)-(7×7) surface.

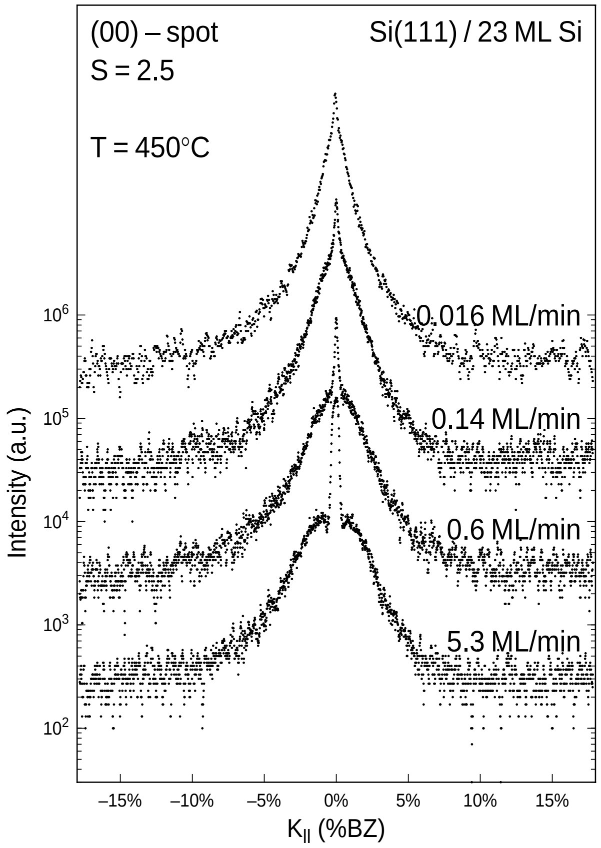

Fig. 4.10 LEED (00)-spot profiles immediately after growth of 23 ML of coverage at constant temperature and different deposition rates *R*. With increasing rate *R* the broadened part of the (00)-spot becomes wider. The shape of the profiles is very similar to those in Fig. 4.8.

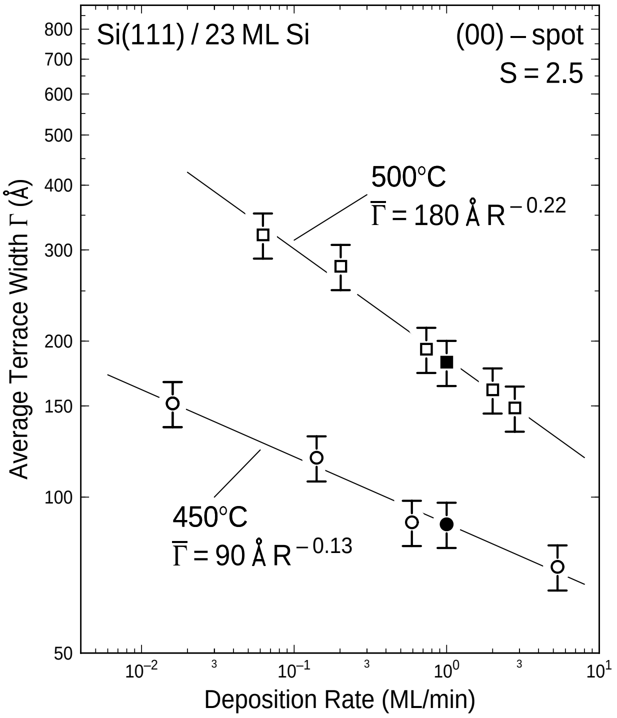

Fig. 4.11 Double logarithmic plot of the average terrace width at constant temperature as function of the deposition rate *R*. The values are derived from the (00)-spot profiles shown in Fig. 4.10. The exponent of the slope depends on the temperature. Solid data points are taken from Fig. 4.8.

variation of almost three orders of magnitude. The exponential dependence on the deposition rate *R* is clearly seen for both temperatures. The slope, however, is much weaker for the lower temperature of 450°C. For temperatures of 47°C and 525°C we have also observed an exponent of about 0.22 (data points not shown).

Following Venables theory [177] for complete condensation and homogenous nucleation the dependence of island density *n* on flux and temperature could be expressed by

$$n(T,R) \propto R^{i^*/(i^*+2)} \exp \frac{(E_{i^*} + i^* E_d)}{(i^*+2) k_b T} \qquad (4.5)$$

with the diffusion energy E_d, the number *ix* of atoms in the critical nucleus, the total energy E_{ix} of the critical cluster. This solution is exact only for perfect substrates without defects. A critical nucleus i^X of one atom would result in an exponent of -1/6 and a critical nucleus i^X of two atoms in an exponent of -1/4 for the dependence of the average terrace size on the deposition rate *R*. For the island density (which is usually plotted) an exponent of 1/3 or 1/2 respectively results. The change in the number of atoms for the critical cluster i^X should also influence the slope of the exponential function in Fig. 4.9 as shown in equation (1). This change of slope has been observed experimentally in Ref. [170].

In contrast to these small values of i^X of only one or two atoms for the steady state regime values of $i^X > 5$ are observed for nucleation on perfect (7×7) surfaces [175,176]. This difference obviously results from the different nucleation mechanism: the first as heterogeneous nucleation at linear surface defects with a stable cluster of only one or two atoms and the second as homogeneous nucleation on the defect free surface with a larger critical nucleus.

As soon as a stable island is nucleated it acts as sink for the mobile adatoms in the surrounding area which are captured at the island edges [178,179]. This decreases the density of mobile adatoms in the surrounding area which inhibits the nucleation of another island. The average area associated with each island (i.e. the inverse island density) depends on the adatom diffusion length and therefore has the character of homogeneous nucleation. If the number of surface defects increase more nucleation sites would be provided, however, the first island nucleated inhibits the nucleation of further in the surrounding area. This is the mechanism why we do not observe a a continuous increase of the surface defect density during growth. If the density of surface defects is too low, again homogeneous nucleation occur as on the perfect (7×7).

Assuming a size of the critical nucleus $i^X = 1$ an exponent of 1/3 results for the island density as function of deposition rate *R*. This model also predicts identical surface morphology for either changes of the temperature of growth or variations of the deposition rate [178,179].

4.3 Initial stage of growth

The initial stage of Si homoepitaxial growth shows a different behaviour than the steady state 2-dim layer growth mode. As already shown in Figs. 4.1 and 4.7 the steady oscillations start with a delay of one to two bilayers [101,166,170,174]. This must be explained by a very special surface morphology because it is extremly unlikely, that the sticking coefficient of Si is not equal one at this low growth temperatures.

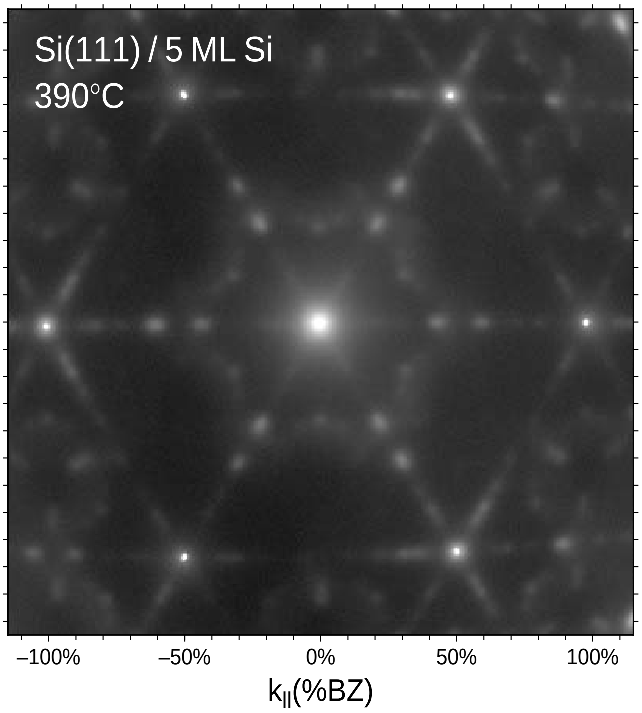

Fig. 4.12 The LEED pattern after deposition of 5 ML Si at 390°C on Si(111) shows a strongly broadened mixture of (5×5) and (7×7) spots. Sharp central spikes of the fundamental spots indicate epitaxial growth without bulk defects.

In order to study the surface roughness, i.e. the coverage θ_h in the different layers in detail the deposition has been interrupted at 1.25 BL of coverage and the temperature was quenched. The LEED pattern in Fig. 4.12 again shows the mixture between (7×7)- and (5×5)-spots which are strongly broadened.

Spot profiles of the (00) spot have been recorded with the external electron gun for various different energies corresponding to a range of scattering phase $S = 2.5 \ldots 4.1$. The shape of the profiles strongly depends on the scattering condition as shown in Fig. 4.13. At "in-phase" conditions only the sharp central spike remains, at "out-of-phase"

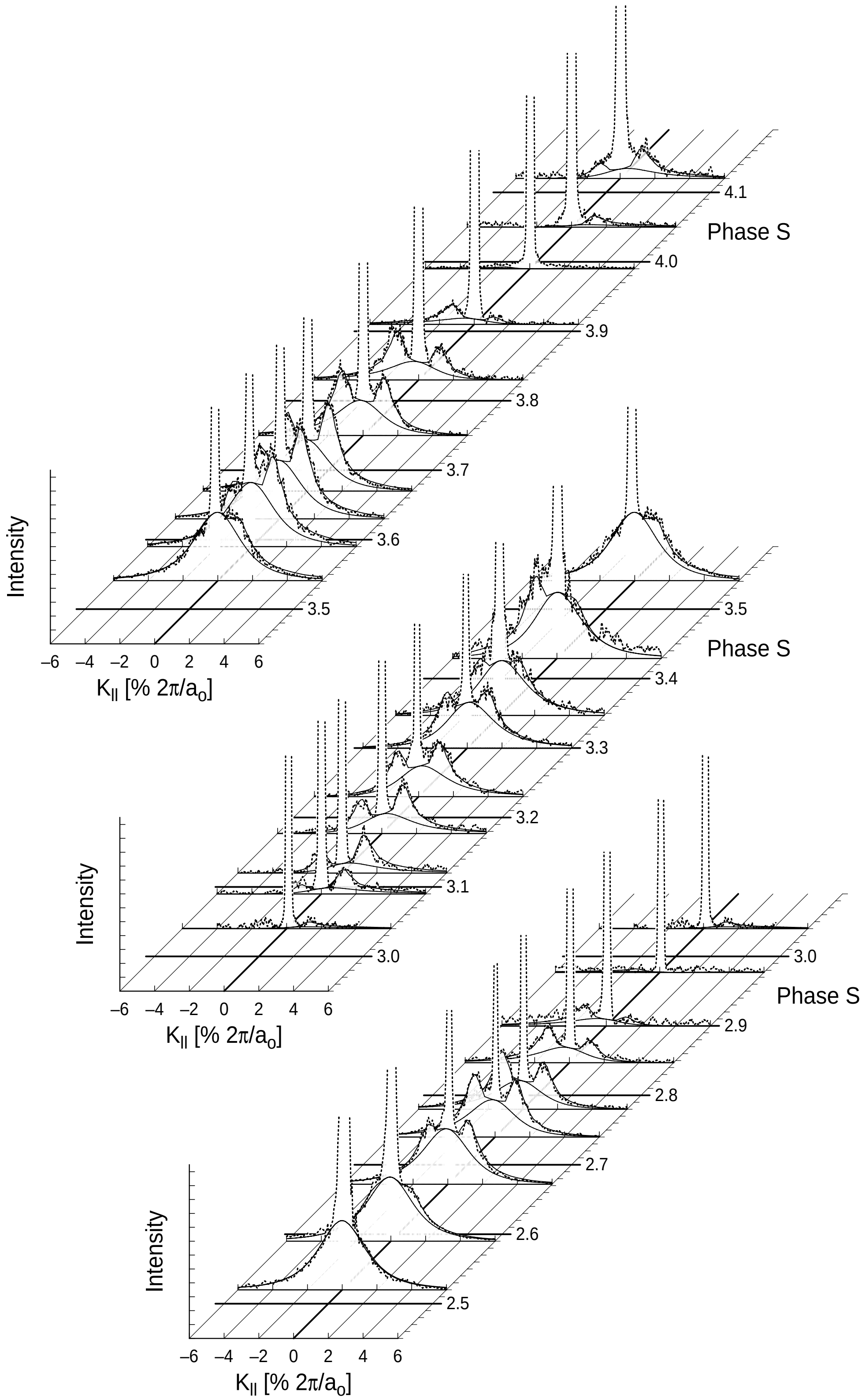

Fig. 4.13 (00) spot profiles after deposition of 1.25 BL of Si for various electron scattering conditions obtained with the external electron gun. The shape of the spot profile varies periodically with the scattering phase *S*. For "out-of-phase" conditions a Lorentzian shaped profile is observed. For "out-of-phase" conditions for double bilayer steps a Henzler ring is also seen. At "in-phase" conditions only the sharp central spike remains.

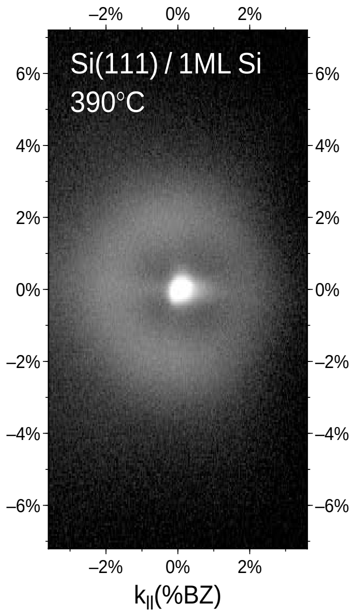

Fig. 4.14 A Henzler ring around the (00) spot. This diffuse intensity is caused by surface roughness with a well defined average terrace width. The central spike is clearly visible. The pattern has been recorded with the external electron gun and corrected for image distortions.

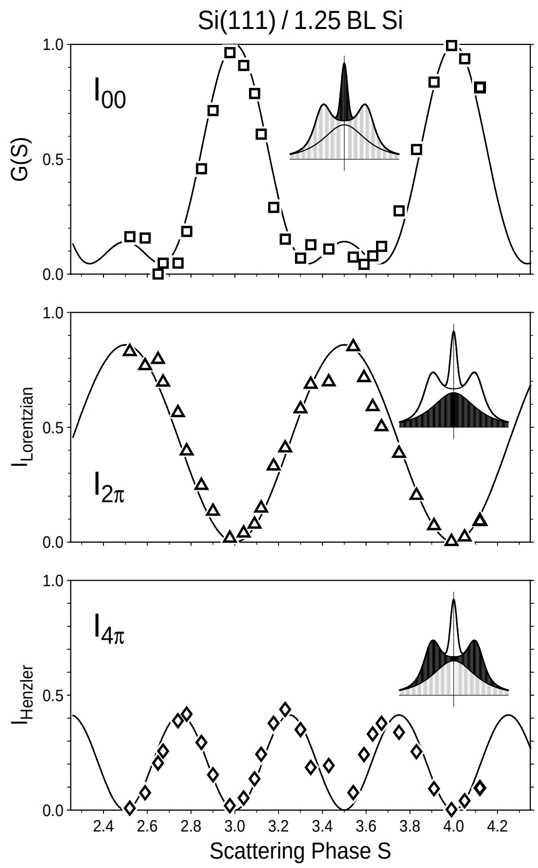

Fig. 4.15 Relative normalised integral intensities of the central spike (top), the Lorentzian shaped diffuse intensity (middle), and the Henzler ring diffuse intensity (bottom) as function of scattering phase S. The diffuse intensities vary periodically with the cosine of $2\pi s$ or with $4\pi s$, respectively.

conditions a Lorentzian shaped diffuse intensity is observed. At intermediate scattering conditions well defined peaks arise originating from a Henzler ring around the (00) spot as shown in Fig. 4.14. This peaks are most pronounced at "out-of-phase" scattering conditions for double bilayer step heights $S = n \pm \frac{1}{4}$.

The profiles are not symmetric with respect to $\mathbf{K}_{||}$. This behaviour is caused by the special diffraction geometry for the external electron gun. When K_x is recorded, $K_\perp$ also is strongly varied as already shown in Fig. 3.4. As a consequence the value of the scattering phase S changes significantly during a measured spot profile. The external gun has been used for these measurements due to its higher resolution.

The spot profile of the (00) spot could be described for any scattering phase S by only three components: a sharp central spike, a Lorentzian shaped component and a Henzler ring. Fig. 4.15 shows the relative integral intensities of each of those three components as function of scattering condition. Both diffuse components show a cosine dependence on the scattering phase S. The Lorentzian part varies with $\cos 2\pi S$. The Henzler ring varies with $\cos 4\pi S$ which already reflects diffraction from a three level system [117]. This component is vanished at the "out-of-phase" conditions. The central spike variation $G(S)$ is a combination of both components and reflects the layer distribution or vertical roughness (see Eq. 17 and 18).

From the amplitudes of the cosine functions vertical height correlations $C_1 =$ and $C_2 =$ are derived. Together with the knowledge of the total coverage $\theta_{total} = 1.25\,\text{BL}$ a coverage of $\theta_1 = 0.778\,\text{BL}$ and $\theta_2 = 0.466\,\text{BL}$ in the first and second layer results. The uncovered part of the substrate is $p_h = 0.222$. The solid lines in Fig. 4.15 show the expected behaviour for the above estimated coverages.

The surprisingly low value of $p_1 = 0.312$ is explained by Si islands which exhibit a two bilayer height as sketched in Fig. 4.16. The occurrence of even higher islands has been reported for this system [169].

Usually only the variation of the central spike intensity could be measured and the $G(S)$ curve has to be fitted to this curve. In this special case it was possible to additionally determine the intensity variations of two components of the diffuse intensity due to their very special shape.

This two components of the diffuse intensity are plotted in Fig. 4.17 in a logarithmic intensity scale. The Lorentzian shaped part reflects the terrace width distribution of the "out-of-phase" projection, i.e. short terrace length. At

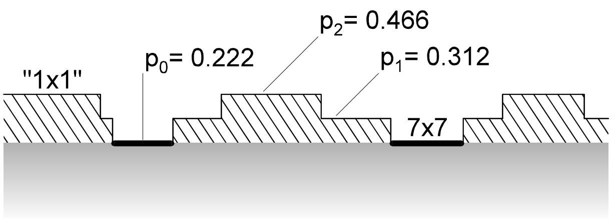

Fig. 4.16 Sketch of the layer distribution after Si deposition of 1.25 BL. Part of the substrate $p_0 = 0.222$ is still uncovered and exhibits a perfect (7×7) reconstruction with long range order. The Si islands show a highly disordered mixture of various reconstructions denoted as "1×1".

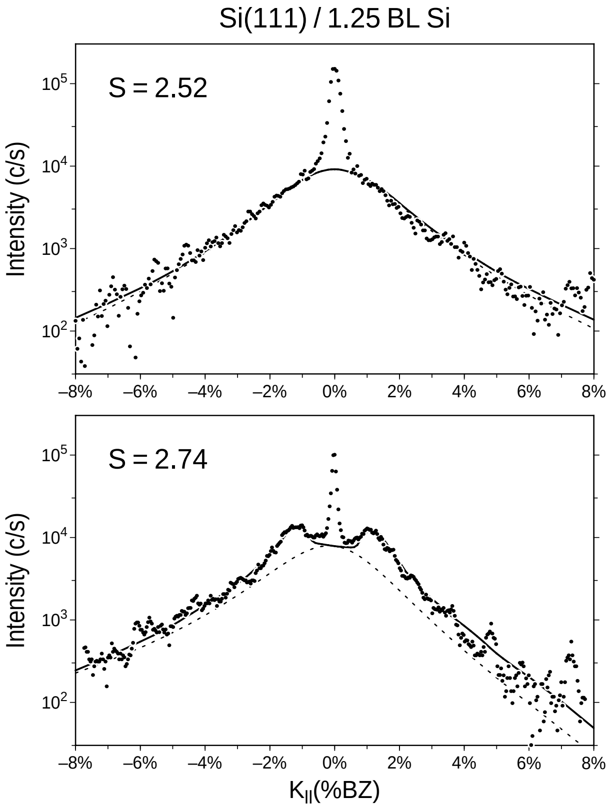

Fig. 4.17 Shape of the diffuse intensity for "out-of-phase" condition $S = 2.52$ (top) and "out-of-phase" condition for double bilayer steps $S = 2.74$ (bottom) in a logarithmic intensity scale.

$S = n \pm \frac{1}{4}$ conditions the separation between islands of two bilayer height is dominant in the diffraction pattern.

The highly disordered reconstruction on the grown Si islands has a special influence on the spot profile of the (7×7) reconstruction spots. Only the (7×7) reconstruction of the substrate exhibits long range order. The only contribution to the central spike of the (7×7) spots results from the remaining visible areas of the substrate. Due to the lack of a vertical interference condition the central spike intensity of the (7×7) spots shows no $\mathbf{K}_\perp$ dependence. The $G(S)$ curve of the (7×7) spot has a constant value as shown in Fig. 4.18.

This preference of multiple bilayer high islands during the initial stage of growth is explained in terms of surface free energy: the deposited Si does not like to wet a perfect Si(111)-(7×7) substrate. The surface of the Si islands exhibit a very high surface defect density as domain boundaries between different reconstrcutions or anti-phase translational domain boundaries [172] as seen in Fig 4.12.

The large number of surface defects in the deposited Si layer results in a higher surface free energy which causes a Volmer Weber growth mode (islanding). This mode is additionally supported by kinetics. Si atoms do not nucleate on the perfect (7×7)-reconstruction: there are no favourable binding sites. The size of the critical nucleus $i^* = 5 \ldots 7$ is large [175,176] compared with the nucleation at linear surface defects [170]. Therefore mobile adatoms preferentially grow at step edges of already nucleated islands or on top of those islands at domain boundaries. This interpretation is confirmed by STM studies [175,176].

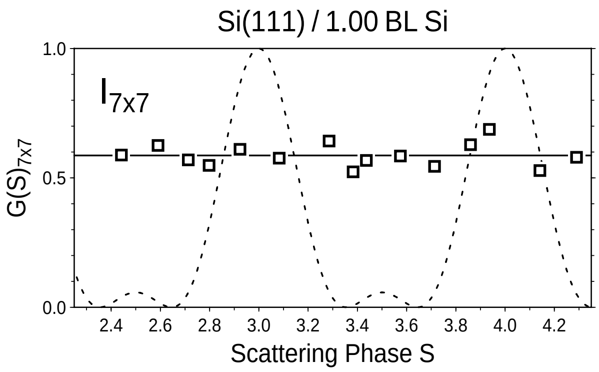

Fig. 4.18 Normalised central spike intensity of one of the (7×7) spots. The $G(S)$ curve does not depend on the scattering condition. The dashed line shows the behaviour for the (00) spot.

In chapter 4.1 the oscillating intensity of the central spike has been used to determine the evolution of the different levels during the steady state growth. In the following we will demonstrate how to expand the model for the description of four simultaneously growing layers [122].

The necessary information is obtained from a measurement of the central spike intensity for $S = n \pm \frac{1}{2}$ and $S = n \pm \frac{1}{4}$. Using Eq.(25) The intensities are determined by

$$G(\theta, S = \tfrac{1}{2}) = \left| p_0 - p_1 + p_2 - p_3 \right|^2 \tag{4.6}$$

$$\begin{aligned} G(\theta, S = \tfrac{1}{4}) &= \left| p_0 + ip_1 - p_2 - ip_3 \right|^2 \\ &= (p_0 - p_2)^2 + (p_1 - p_3)^2 \end{aligned} \tag{4.7}$$

the partial coverages p_h during deposition. Using the normalisation results in

$$p_1 = \underbrace{\frac{1 \pm \sqrt{G(\theta, S = \frac{1}{2})}}{2}}_{a} - p_3 \tag{4.8}$$

$$p_0 = \underbrace{\frac{1 \mp \sqrt{G(\theta, S = \frac{1}{2})}}{2}}_{b} - p_2 \tag{4.9}$$

with $a + b = 1$. Replacing p_0 and p_1 in Eq. 4.7 by Eq. 4.8 and 4.9 and using

$$2p_2 = \theta - p_1 - 3p_3 = \theta - a - 2p_3 \tag{4.10}$$

results in an expression for p_3 as function of $G(\theta, S = \frac{1}{4})$:

$$\begin{aligned} G(\theta, S = \tfrac{1}{4}) &= (b - \theta + a + 2p_3)^2 + (a - 2p_3)^2 \\ &= 2\left[(2p_3 + \frac{c-a}{2})^2 + \frac{c^2 + a^2}{2} - \frac{(c-a)^2}{4} \right] \end{aligned} \tag{4.11}$$

with $c = a + b - \theta = 1 - \theta$. Finally we obtain an expression for all p_h:

$$p_3 = \frac{1}{2}\left[\frac{a-c}{2} \pm \sqrt{\frac{G(\theta, S = \frac{1}{4})}{2} - \frac{(c+a)^2}{4}} \right] \tag{4.12}$$

$$p_2 = \frac{1}{2}[\theta - a - 2p_3] \tag{4.13}$$

$$p_1 = a - p_3 \tag{4.14}$$

$$p_0 = b - p_2 = 1 - p_1 - p_2 - p_3 \tag{4.15}$$

Four sets of solutions are possible depending on the choice of the sign of the square root functions. The boundary condition for $\theta_{total} = 0$ (here $p_0 = 1$ $p_1 = p_2 = p_3 = 0$) selects the one set of solutions. The sign of a changes for every zero passage of $G(\theta, S = \frac{1}{2})$. The sign in Eq.(4.8) changes whenever

$$G(\theta, S = \tfrac{1}{4}) = (2 - 2\theta + 1 \pm G(\theta, S = \tfrac{1}{2}))^2 \tag{4.16}$$

is fulfilled.

We will use the initial stage of growth at 400°C in order to demonstrate an analysis of the layer evolution in the framework of the above described algorithm. The coverage of up to four visible layers could be determined.

The upper plot of Fig. 4.19 shows the central spike intensity for two different scattering ($S = 2.5$ and $S = 2.75$) conditions. The intensity has been simultaneously measured using a chopping modus for two electron energies. The integral intensity for both scattering conditions is normalised to 1. Steady state oscillations set in beyond a coverage of 3 BL.

The middle plot shows the resulting partial coverages p_h. The resulting coverages θ_h are plotted in the lower graph of Fig. 4.19. The measured intensities do not give a meaningful solution for p_h (of a four level system) in the coverage range from 1.8...2.4 BL.

Most remarkable is the almost identical coverage in the first and second layer during the deposition of the first two BLs. During this stage of growth all islands exhibit a double bilayer height. The diffraction with $S = 2.5$ at "out-of-phase" condition for single bilayer steps is insensitive to this growth mode. Electrons scattered from double bilayer high islands interfere constructively with electrons scattered from

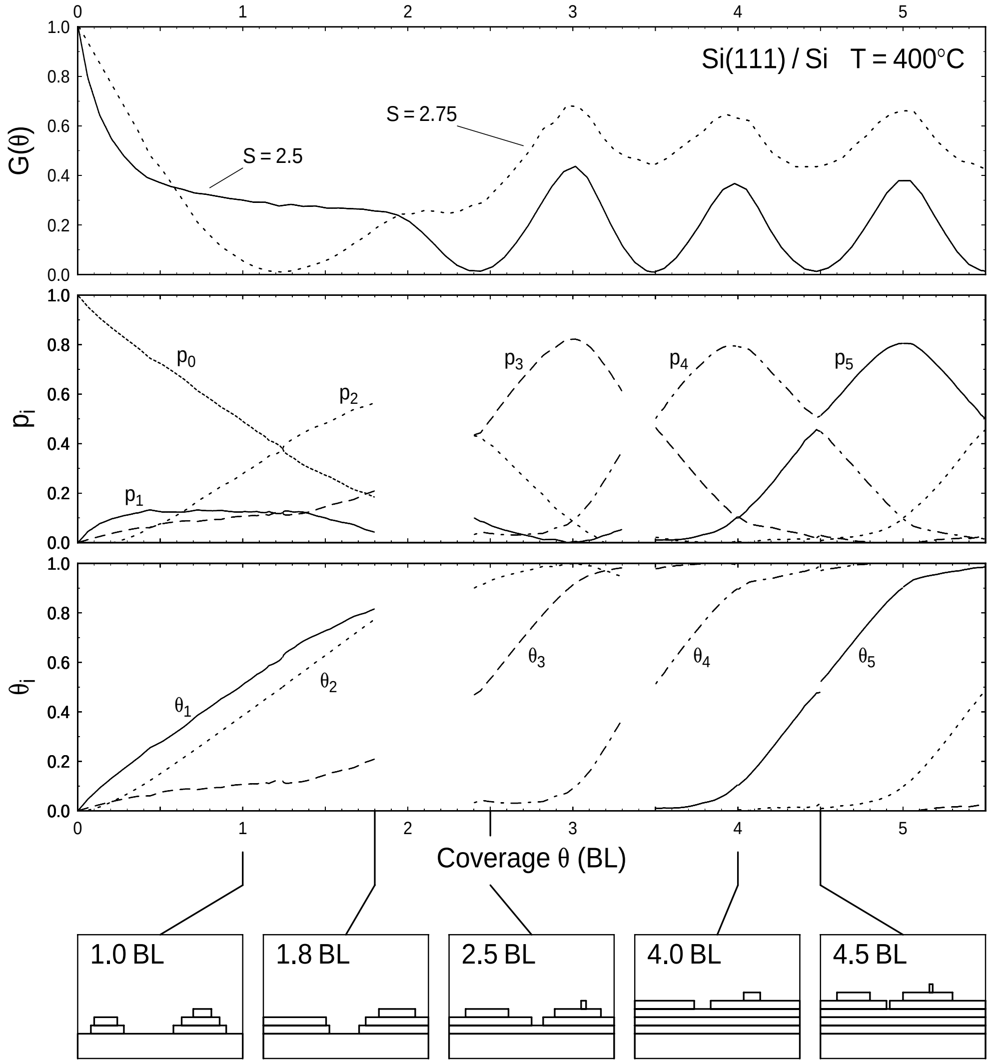

Fig. 4.19 (a) Normalized central spike intensity of the (00) spot during the first 5 BL of Si homoepitaxial growth on Si(111) for two different scattering conditions S = 2.5 and S = 2.75. Steady state behaviour with oscillations is seen beyond 3 BL. Almost zero intenisty in the minima is observed only for the "out-of-phase" condition S = 2.5. (b) Evolution of the partial coverages p_i in the different visible layers. During the initial stage up to four layers are simultaneously present at the growth front. (c) Evolution of the coverages Θ_i in the different visible layers. The first layers grow in a double bilayer fashion: both Θ_1 and Θ_2 grow with the same rate! For higher coverages the typical layer-by-layer growth mode is observed. The small insets below the plots show a typical distribution of the deposited amount. The surface shows a maximum roughness at Θ = 1.8 BL.

the substrate: from 0.5 to 2 BL the central spike intensity shows only little variation.

At the "out-of-phase" condition for double bilayer step heights with $S = 2.75$ the electrons scattered from islands and substrate interfere destructively, i.e. the diffraction is most sensitive to this special kind of surface roughness. Accordingly the central spike intensity shows a parabola like behaviour as function of coverage θ_{total}. The first Si layers do not grow in a layer-by-layer mode but in a double-bilayer mode! The visible area of the substrate decreases almost linear with $p_0 \cong 1 - \theta_{total}/2$.

Beyond 2.5 BL of coverage the substrate is finally covered and the growth proceeds in a 2-dim. layer growth mode. Nucleation of a new layer sets in before the previous layer is complete. This steady state growth regime could be described within a three level system.

The minimum of the intensity for $S = 2.75$ indicates the maximum roughness of the growth front. The increasing value of $G(\theta, S = \frac{1}{4})$ for higher coverages reflects a much smoother growth during the steady state regime.

4.4 H as surfactant

The termination of a semiconductor surface by an adsorbate can dramatically influence the surface morphology. The surface free energy, the mobility of diffusing adatoms and their nucleation behaviour, i.e. size of critical nucleus i^x or binding energy, is affected. Such a surface active species (surfactant) strongly decreases the surface free energy by saturating the semiconductor dangling bonds which causes the very efficient segregation of the surfactant and the incorporation of the growing species. This manipulation of surface properties is of critical importance during homo- and heteroepitaxial crystal growth.

Here we will demonstrate how a ML of adsorbed Hydrogen changes the equilibrium surface during Si(111) homoepitaxial growth. The growth mode changes from layer-by-layer to a faceting of the entire surface [180-182]. The complete disappearance of all planar (111)-areas, the formation of well developed facets with orientations ranging from (113) to (779) ("hill-and-valley" structure) is explained by a change of the surface free energy during Si deposition and H termination of the surface: The energetically more favourable orientations develop during growth [182].

Adsorption of H without deposition of Si passivates the surface by saturation of the dangling bonds. This changes the equilibrium surface reconstruction of the (111) surface from a (7×7) to a (1×1) [183,184].

Si(111) was grown at 520°C under a constant flux of atomic Hydrogen (2×10^{14} H atoms cm^{-2} s^{-1} at a background pressure of 5×10^{-7} mbar) compensating H desorption. The change of surface morphology is directly evident in the

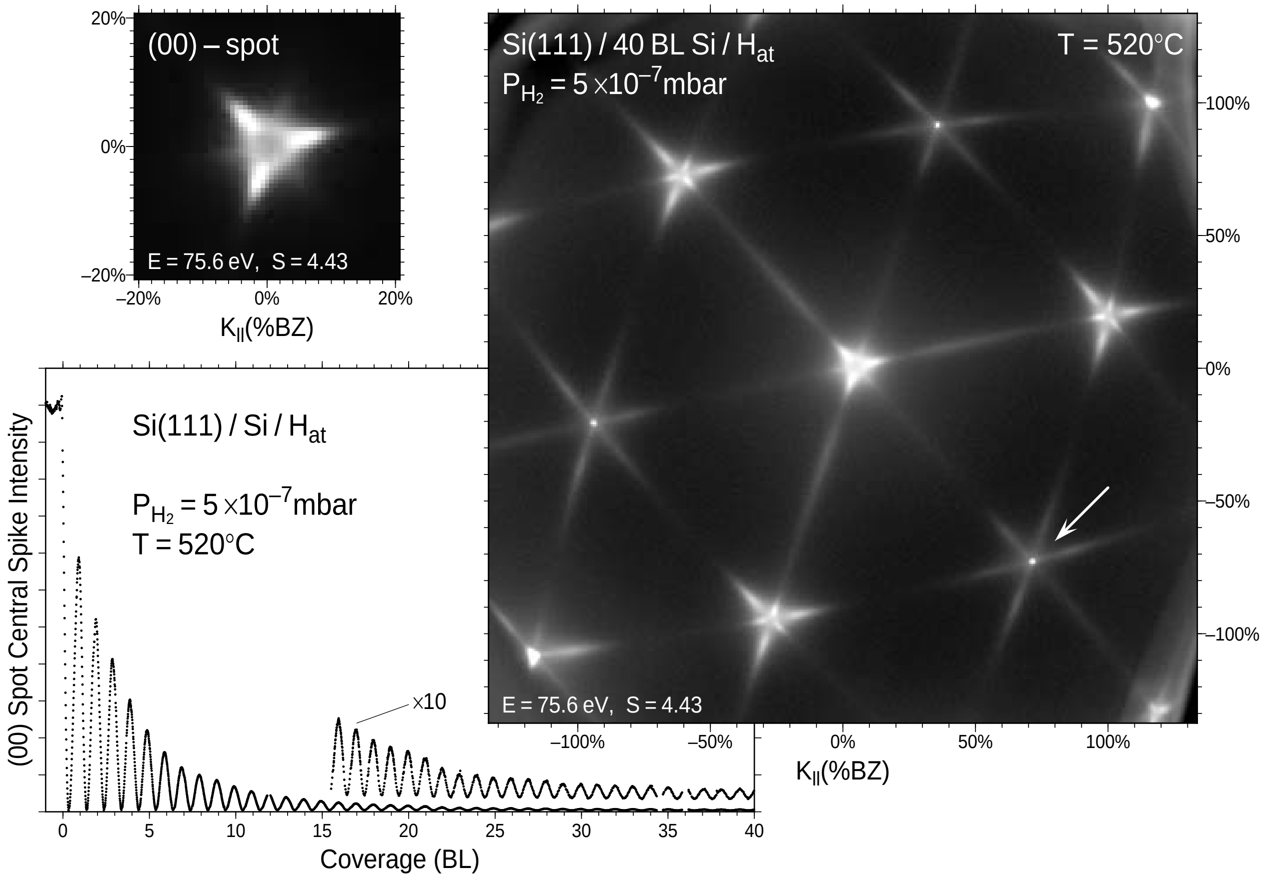

Fig. 4.20 Exponentially decaying LEED intensity oscillations reflects a built-up of surface roughness during epitaxial growth. After deposition of 40 BL Si all integer order spots in the LEED pattern were split into star like shaped facet spots (shown right in a logarithmic intensity to grey scale representation). Sharp central spikes at three integral order spot positions (arrow) reflects excellent epitaxial growth without formation of stacking faults. The complete lack of the (00) spot central spike (left pattern in a linear intensity representation) indicates that the whole surface is completely covered by facets.

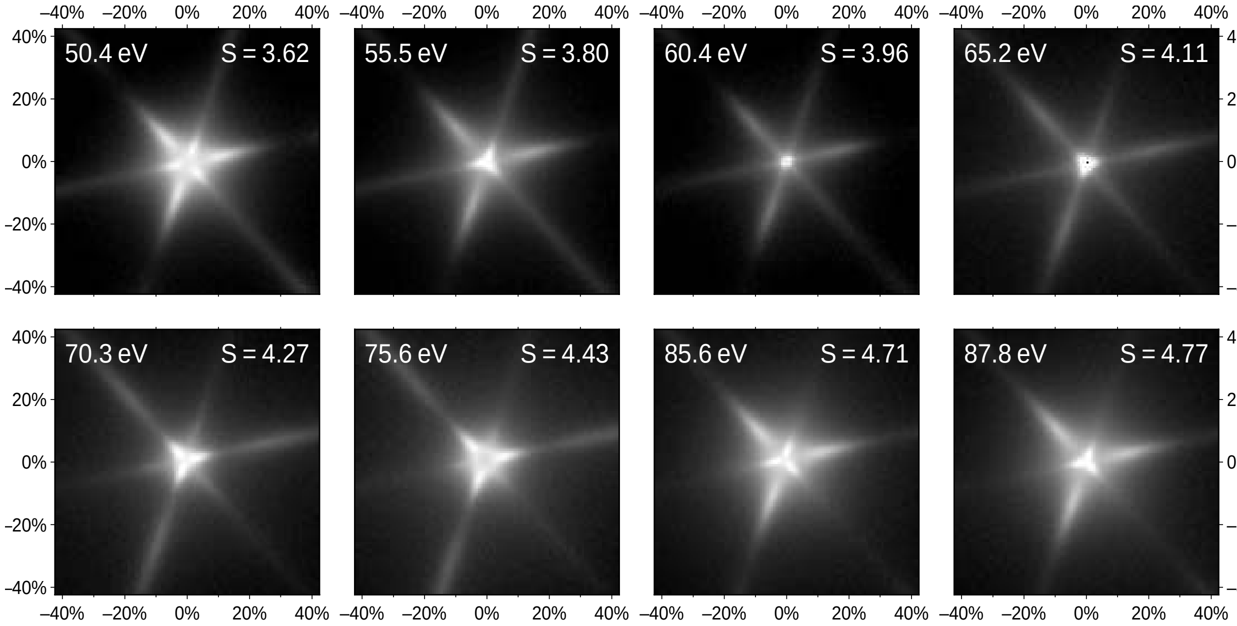

Fig. 4.21 LEED pattern of the (00) spot as function of electron energy. The motion of the facet spots along the fundamental directions is clearly visible. At the "in-phase" condition one bright sharp spot remain together with weak facet spot of the neighboured facet rods. The length of the facet spots increases linear with the separation to the centre of the (00) spot. This reflects rough and irregular facets.

LEED pattern shown in Fig. 4.20 after deposition of 40 BL of Si: all fundamental spots exhibit a star like shape with a threefold symmetry. The appearance of sharp central spikes at three integral order spot positions (arrow) reflects excellent epitaxial growth without formation of stacking faults (which would produce six fold symmetric LEED patterns).

The shape of those threefold "stars" varies with electron energy as shown in Fig. 4.21. Depending on the scattering condition, the elongated spots (which form a "star") move towards or away from the central spikes. The position in reciprocal space of one set of those spots is plotted in Fig. 4.22 as function of the vertical scattering vector $\mathbf{K}_{\perp}$. The linear dependence of the spot position on the vertical scattering vector identifies them as facet spots (see chapter 2.4.2) with an average facet plane orientation of [557]. The facets are composed of dihydride-terminated steps in [-1-12] direction. The width of the ovals in Fig. 4.22 corresponds to the intensity of the spots. The length of the ovals reflects the extension of the spots in reciprocal space. The facet spots become much broader with increasing distance from the integral order spot positions (also clearly seen in Fig. 4.20). This behaviour indicates the formation of an irregular step train, i.e. not well ordered facets.

The steps, however, are straight according to the narrow shape of the facet spots, which points to an increased mobility of the deposited Si along the step edge. From the finite width of the facet spots close to the Bragg conditions, an average size of the facets of ~100Å is estimated for this film with 40 BL coverage (see chapter 2.2.3 Powerspectrum). The complete lack of the (00)-spot central spike at the out-of-phase or anti-Bragg condition (see inset of Fig. 4.20) indicates that the entire surface is completely covered by facets, without any remaining planar (111)-face. We would like to emphasise that the adsorption of atomic H without Si deposition does not produce facets at the surface, even at temperatures up to 650°C and H fluxes of 10 ML/s.

The build-up of surface roughness is also apparent in the strong (and initially exponential) damping of the corresponding intensity oscillations of the (00) spot during Si deposition. Also the initial stage of growth is different from those on the bare Si(111)-(7×7) surface. The oscillations start immediately without delay of one or two BL. The first intensity maxima are higher than for growth on the bare surface which reflects a much smoother initial stage

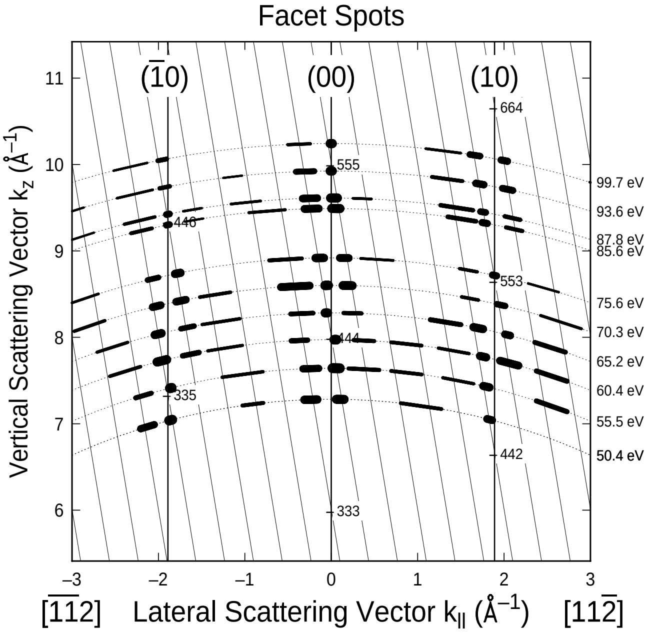

Fig. 4.22 The motion of facet spots in reciprocal space on rods perpendicular to the facet plane. The mean facet orientation of [557] is plotted with thin lines. The width of the ovals corresponds to the intensity, the length to the extension of the spots in reciprocal space.

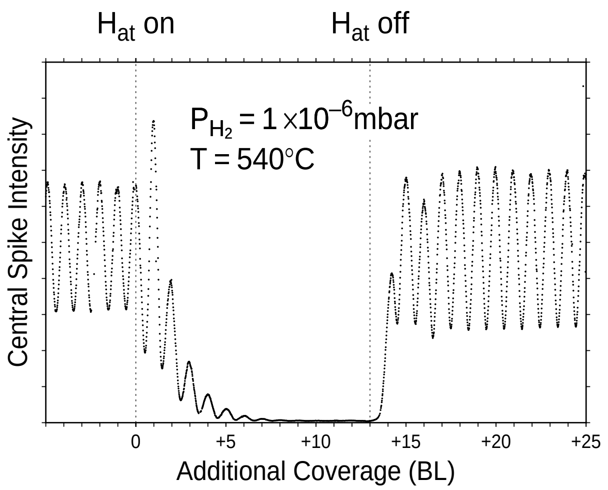

Fig. 4.23 (00) spot intensity oscillations reflects the Si growth behaviour before, during H adsorption, and after H desorption at 540°C. The exponential decay after H adsorption is caused by the build-up of surface roughness due to faceting. After H desorption the surface smoothens and the undamped LEED intensity oscillations immediately recover again.

of growth: the first layer growth almost in a perfect layer-by-layer mode.

Figure 4.23 shows the growth behaviour before and during H adsorption, and after H desorption at 540°C. The left part of the curve shows the undamped oscillations of steady state Si growth on the bare surface (Si has been deposited with 1 BL/min). H termination (a rough estimation for the H flux yields 0.5 ML/s) results in a strong damping of the oscillations which decrease exponentially.

Because the period of oscillation stays constant during H exposure, we can conclude that all deposited Si atoms are immediately incorporated into the adsorbate layer and stick to the surface (and do not desorb again). Due to the same reasons any H related etching processes can also be excluded.

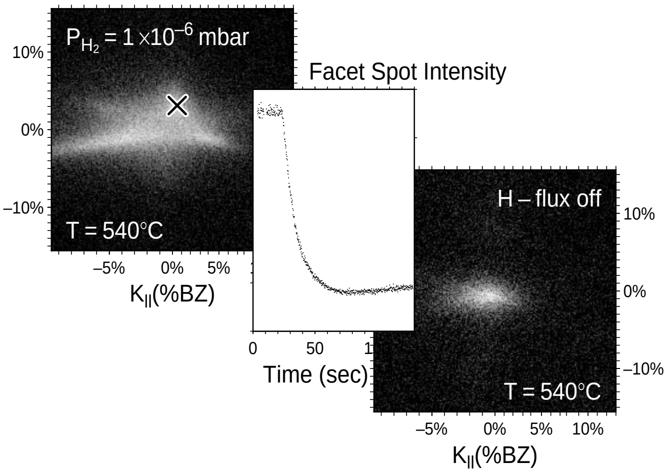

Fig. 4.24 Decomposition of the facets is monitored by the intensity of one of the facet spots (marked by a cross). Left LEED pattern has been taken before switching off the atomic H. The right LEED pattern is taken after desorption of the H monolayer. The surface has smoothed and only a slightly broadened (00) spot remains. The LEED patterns are distorted due to the use of the external electron gun.

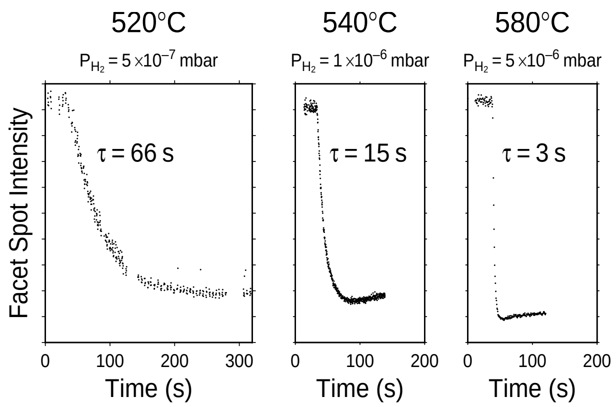

Fig. 4.25 Temperature dependence of the decay of the facets upon H desorption. The intensity of one of the facet spots has been recorded. The time constant of decay varies between 66 and 3 s.

After deposition of 13 additional BLs of Si the H flux has been turned off and the undamped LEED intensity oscillations of the steady state mode recovers almost immediately. The LEED pattern shows a mixture of (7×7)- and (5×5)-spots, which is typical for growth on the bare Si(111) surface.

Obviously the H is desorbed. First, this shows that any form of contamination originating from the H source can be excluded as the reason for faceting. Secondly, there is no generation of bulk defects as observed for growth below 500°C [181].

After interruption of the Si deposition the facets are stable under continuous H flux. Although the driving force for the faceting (the deposition of Si atoms) is no longer present, the diffusion of Si from sub-adsorbate sites seems to be kinetically hindered due to the strength of the H-Si bond with a binding energy of 3.1 eV [185-187].

A minimum flux of atomic H is necessary for the onset of faceting and stabilisation of the facets. This minimum flux depends on the temperature of growth and compensates for H desorption. A value roughly twice the critical value has been chosen for the experiments.

The decomposition of the facets upon desorption of the H monolayer proves that the facets are a phase stabilised by the adsorbate. This process has been monitored during H desorption by the intensity decay of one of the facet spots as shown in Fig. 4.24. The LEED pattern shows a very weak mixture of (7×7)- and (5×5)-spots, indicating the desorption of the H monolayer

Figure 4.25 shows this exponential decay of facet spot intensity for various temperatures after the H flux has been turned off. Increasing the temperature by only 60°C yields a change of the decay time constant τ by a factor of 20. Considering the decay as an activated process, an energy of $E_a = 2.3\,\text{eV}$ and a pre-exponential factor of $\nu_0 = 10^{13}\,\text{s}^{-1}$ results as plotted in Fig. 4.26.

From the excellent agreement with parameters found in the literature [186] we conclude the desorption of H is the dominant process in the decomposition of the facets. The smoothing of the facets is driven by Si diffusion, which can not be the limiting process and must happen on a much faster time scale.

Chemical vapour deposition (CVD) of disilane at high fluxes (flooding the chamber, $p_{\mathrm{Si_2H_6}} > 1\times10^{-4}\,\mathrm{mbar}$) results in identical LEED patterns. Triangular pyramids have also been observed for CVD by scanning tunnelling microscopy [180]. The faceting is therefore independent of the adsorption and reaction processes of the disilane to Si-H. During CVD Si-H radicals are present at the surface [188].

With increasing H coverage the mobility seems to be strongly reduced (a transition from layer-by-layer growth or step propagation to faceting is also observed) resulting in a super saturation of Si-H radicals.

During CVD the Si growth is intimately connected to the ad- and desorption of H. In our experiment we were able to independently adjust the Si and H fluxes which has offered the variety of experiments presented here.

The decomposition of the planar (111)-surface and the formation of facets is thus explained in terms of an adatom gas induced increase of the free energy of the low index

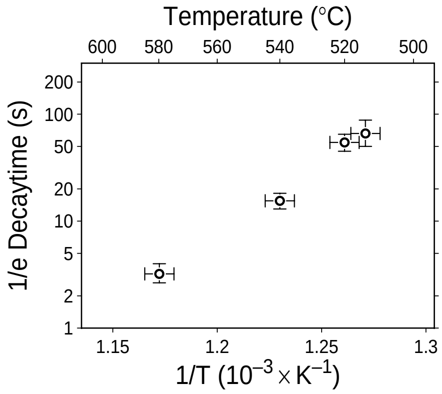

Fig. 4.26 Time constants of the facet decay in an Ahrrenius plot. Assuming an activated process a characteristic energy of $E_a = 2.3$ eV and a pre exponential factor of $\nu_0 = 10^{13}\mathrm{s}^{-1}$ results.

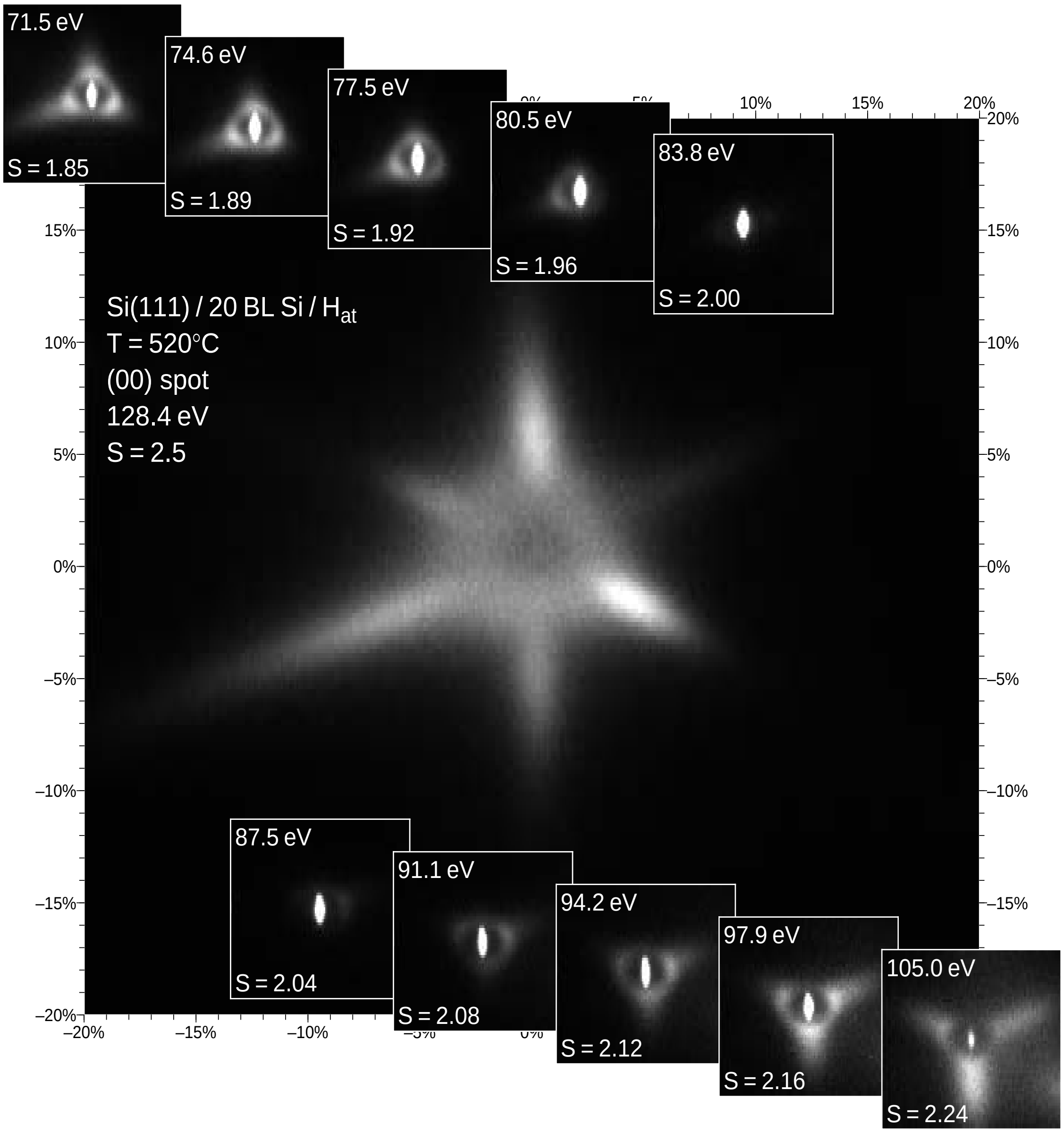

Fig. 4.27 Central large image: the star like LEED pattern of the (00) spot for "out-of-phase" condition reflects the facet formation at the surface. The smaller images show the variation of the (00)-spot close to the "in-phase" condition. The central region surrounding the central spike always lacks any intensity.

surface: It is very likely that the ideally H terminated Si(111) surface still has the lowest free energy. Only by the additional deposition of Si atoms the surface energy increases, because the Si atoms could not occupy regular lattice sites and remain as supersaturated lattice gas of weakly bonded Si mono-hydrides as for CVD [188]. We argue that the mobility of these mono-hydrides is reduced, because they are embedded in the H layer, which is strongly bonded with 3.1 eV [185-187].

At step edges the geometry and the strength of the H-Si bond is different and the weakly bonded mono-hydrides could easier exchange with the H and occupy regular binding sites to the Si substrate without generation of defects as observed for lower growth temperatures [170,184]. Under these conditions (together with the reduction of mobility) only the formation of steps strongly reduces the number of Si-H mono-hydrides and thus lowers the surface free energy. This reduction of the surface free energy is the precondition for the decomposition of the planar surface into a "hill-and-valley" structure [189].

It is, however, also possible that the faceted surface could be thermodynamically stable in the H environment. Then the driving force for faceting may be to maximise the number of Si-H bonds without much reduction in Si-Si bonds. In this case kinetic barriers might prevent the spontaneous faceting of the (111) surface.

4.5 Large scale roughness

Up to now we have considered surface roughness only on an atomic scale, i.e. the determination of an average terrace width or the inclination angle of facets. This information was obtained from the spot profile at the "out-of-phase" condition or from the average motion of facet spots in reciprocal space. From these measurements, however, the large scale morphology could not be deduced: the long scale roughness or the size of the facets do not have an effect on the shape of the profile at the "out-of-phase" condition or on the mean position of a facet spot. The problem arises from the modulo properties of the complex exponential function. The resulting "out-of-phase" projection of all surface levels to only two levels has already been sketched in Fig. 2.8.

In this section we will demonstrate how the large scale surface morphology, i.e. size of facets or the correlation length ξ of extended surface roughness over many levels, could be obtained from the fine structure of the spot profile close to the Bragg condition. In the range of kinematic approximation electrons are insensitive to any kind of (single crystalline) surface roughness at the "in-phase" condition. For small deviations from the "in-phase" condition [see Eq.(2.29)] part of the electrons already interfere destructively resulting in diffuse intensity.

Close to the "in-phase" condition the complex exponential function could be linearised. Following Eqs.(2.27 - 38) the spot profile could be approximated by the absolute square of the Fourier transform of the surface morphology: the power spectrum of the surface roughness could be obtained.

This kind of evaluation will be demonstrated for Si(111) homoepitaxial growth under the presence of a monolayer of

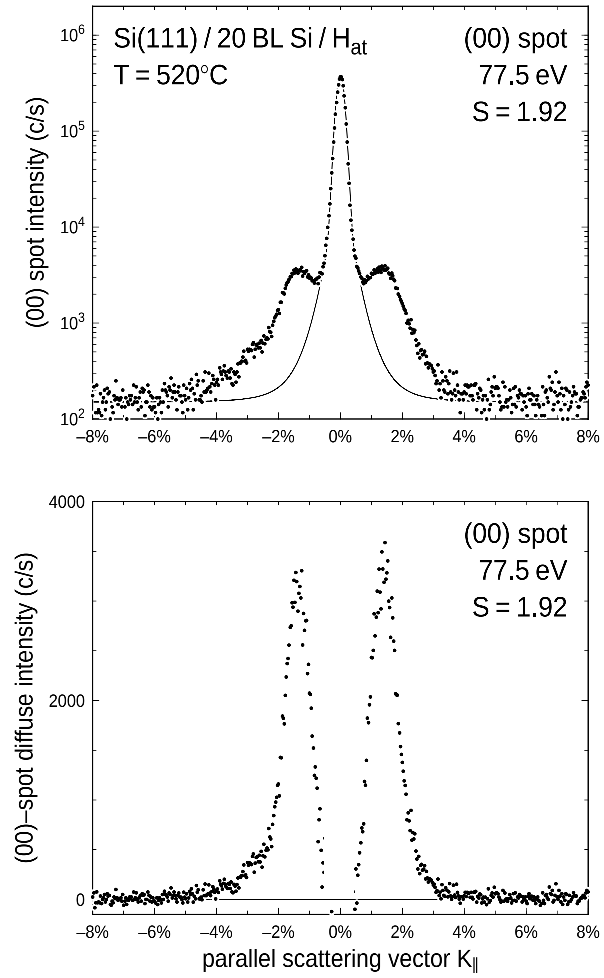

Fig. 4.28 The upper plot shows the (00) spot profile close to the "in-phase" condition for S = 1.92 or 77.5 eV. The shoulders due to the diffuse intensity with maxima a 1.4%BZ are clearly visible. The solid line represents the instrumental response function obtained at the "in-phase" condition at 83.8 eV. The lower plot shows the diffuse intensity after subtraction of the central spike and a constant background. The sharp peaks at ±1.4%BZ reflects the average facet size.

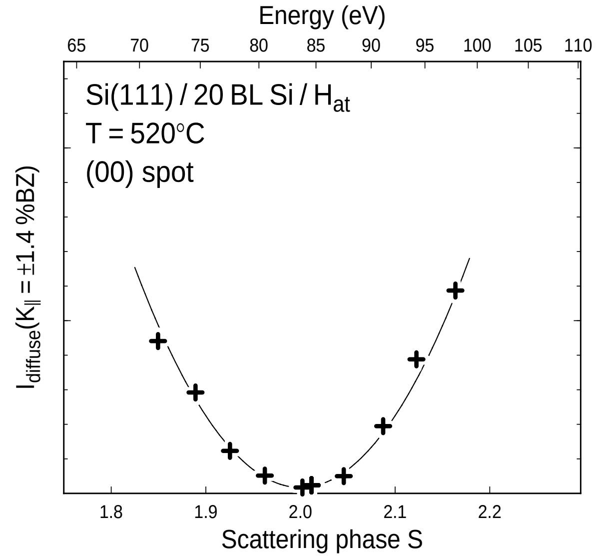

Fig. 4.29 Peak intensity of the diffuse part of the spot profile shown in Fig. 4.28 as function of scattering phase S. The parabolic behaviour reflects the range of validity for the approximation used for this analysis.

adsorbed Hydrogen. In the last section it has been shown, that the surface develop triangular mounds composed of facets with a mean orientation of (557). The large image of Fig. 4.27 shows the (00) spot at "out-of-phase" condition $S = 2.5$ at 128.4 eV. In order to obtain the heighest possible resolution the external electron gun with 65° incident angle has been used for this measurements. The LEED patterns have been remapped in order to correct for image distortions. The star like shape of the spot profile reflects the disordered facets as already shown in Figs. 4.20 and 4.21.

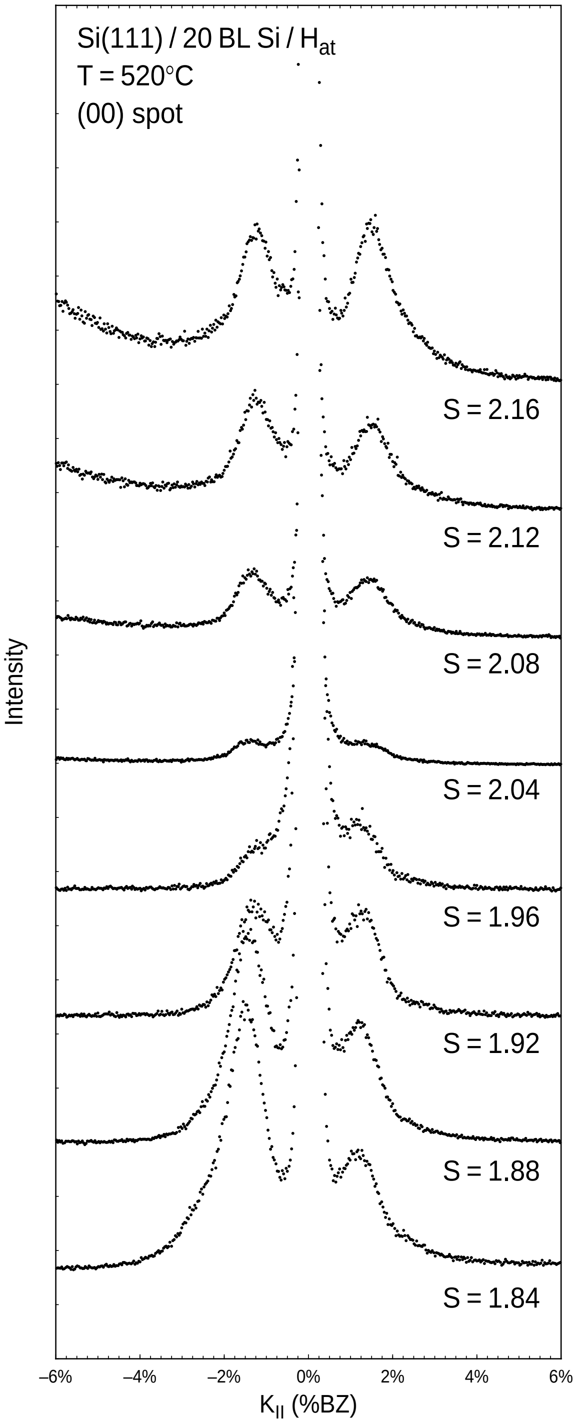

Fig. 4.30 (00) spot profiles close to the "in-phase" condition. The diffuse intensity disappears for $S = 2.00$. The position of the peaks of the diffuse intensity is almost independent on the scattering condition.

The small insets in Fig. 4.27 show the fine structure of the (00) spot for various energies close to the Bragg or "in-phase" condition of diffraction at $S = 2.00$ at 83.8 eV. The $\mathbf{K}_{||}$ scale is the same as for the large image. At "in-phase" condition only the sharp central spike is visible with a FWHM of 0.2 %BZ, corresponding to a transfer width of ~1500 Å. The elongated shape of the spot is due to the image corrections of the LEED patterns obtained with the external electron gun (see also chapter 3.2).

With decreasing deviations from the exact "in-phase" condition diffuse intensity becomes apparent around the central spike. The striking feature is the complete lack of intensity directly around the central spike. Even when elongated facet spots are present (visible at $S = 1.85$ or $S = 2.24$) the area surrounding the central spike shows no intensity. This pronounced intensity cut-off for parallel scattering vectors $\Delta\mathbf{K}_{||} / \mathbf{K}_{\perp} < 1\%\mathrm{BZ}$ is caused by the lack of surface features with a size larger than $\xi > 2\pi/\Delta\mathbf{K}_{||}$, i.e. the largest occurring wavelength in the power spectrum of the surface roughness.

In the upper part of Fig. 4.28 the spot profile at 77.5 eV corresponding to a scattering phase $S = 1.92$ is shown. The solid represents the instrumental response function obtained at from the spot profile at "in-phase" condition. The weak shoulders of diffuse intensity are clearly seen. Here the absolute requirement of a high resolution diffraction instrument becomes obvious. Weak diffuse intensity has to be distinguished and clearly separated from the very intense central spike which irradiates any diffuse intensity in the direct vicinity.

In the lower part of Fig. 4.28 the central spike and the constant background has been subtracted from the measured spot profile and only the diffuse intensity is plotted. The sharp maxima at $\Delta\mathbf{K}_{||} / \mathbf{K}_{\perp} = \pm 1.4\%\mathrm{BZ}$ reflects the typical size of the facets at the surface.

According to Eq.(2.34) the intensity of this diffuse part of the spot profile should be proportional to S^2. This is proved in Fig. 4.29 where the normalised peak intensity of the diffuse part at $\Delta\mathbf{K}_{||} / \mathbf{K}_{\perp} = \pm 1.4\%\mathrm{BZ}$ is plotted as function of scattering phase S. The parabolic behaviour with

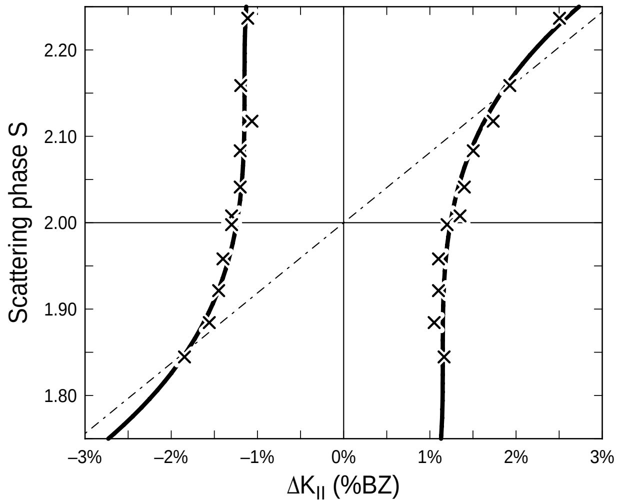

Fig. 4.31 Position of the maxima of the diffuse intensity as function of scattering phase S. The maxima of the diffuse intensity close to the facet rod (dashed line) is shifted towards the facet rod.

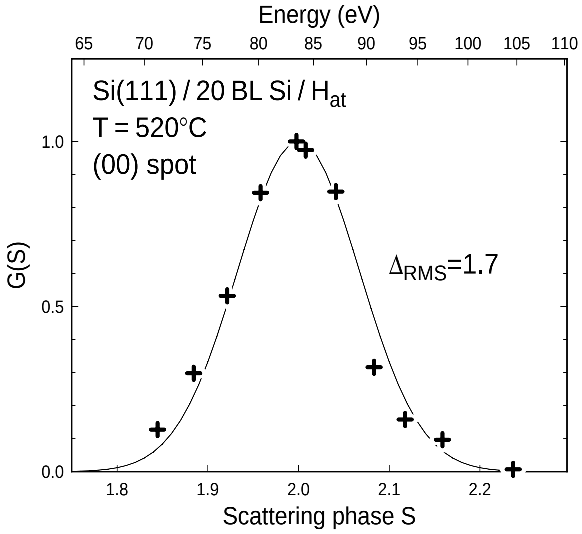

Fig. 4.32 A G(S) analysis reflects the extended roughness of the surface: the central spike is only visible close to the "in-phase" condition. From the FWHM of the peak of the G(S) curve an rms. value of the roughness of Δ=1.7 atomic layers is deduced.

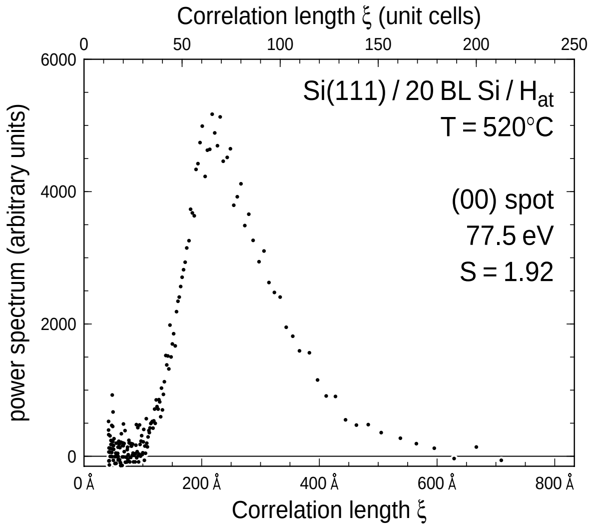

Fig. 4.33 Power spectrum of the surface roughness as function of correlation length ξ. The cut-off for large ξ reflects the finite size of the facets which form triangular pyramids on the surface.

S is clearly seen and reflects the increasing sensitivity of the electrons for the surface morphology.

Following Eq.(2.34) the shape of the diffuse part is determined by the power spectrum and should be independent of the scattering phase *S* (within the limits of Eq.(2.29), i.e. for small deviations from the Bragg condition $S = n$). The spot profiles of the (00) spot are shown in Fig. 4.30 as function of scattering phase *S*. The sharp maxima at $\Delta\mathbf{K}_{\parallel}$ / $\mathbf{K}_{\perp}$ = ± 1.4%BZ are clearly seen for all profiles without significant changes of the shape. The left -right asymmetry of the diffuse intensity is caused by the special diffraction conditions using the external electron gun, see also Eq.(3.04). Due to the gracing incidence of 25° $\mathbf{K}_{\perp}$ varies strongly with $\mathbf{K}_{\parallel}$ which causes this additional variation of intensity.

With increasing deviations from the "in-phase" condition (for $S < 1.9$ or $S > 2.1$) also broad facet spots appears and overlaps with the diffuse peaks at $\Delta\mathbf{K}_{\parallel}$ / $\mathbf{K}_{\perp}$ = ± 1.4%BZ (Fig. 4.27). The occurrence of these facet spots obviously marks the range of validity for this kind of spot profile analysis close to the Bragg condition.

The positions of the maximum of the facet spot and the maximum of the diffuse intensity is plotted is Fig. 4.31. The motion of the facet spot along the (557) facet rod could be clearly distinguished from the constant position of the diffuse intensity at $\Delta\mathbf{K}_{\parallel}$ / $\mathbf{K}_{\perp}$ = ± 1.4%BZ. Close to the "in-phase" condition facet spots are no longer present because the size of the facets is too small for a well defined scattering condition for a facet spot. The diffuse intensity no longer represents facets but the long range roughness of the surface.

A *G*(*S*) analysis of the central spike intensity allows an independent determination of the rms. value Δ of the roughness [see Eq.(2.34)]. The resulting curve is plotted in Fig. 4.32. From the FWHM of the peak at the "in-phase" condition a roughness of $\Delta = 1.7$ in units of layer distances *d*

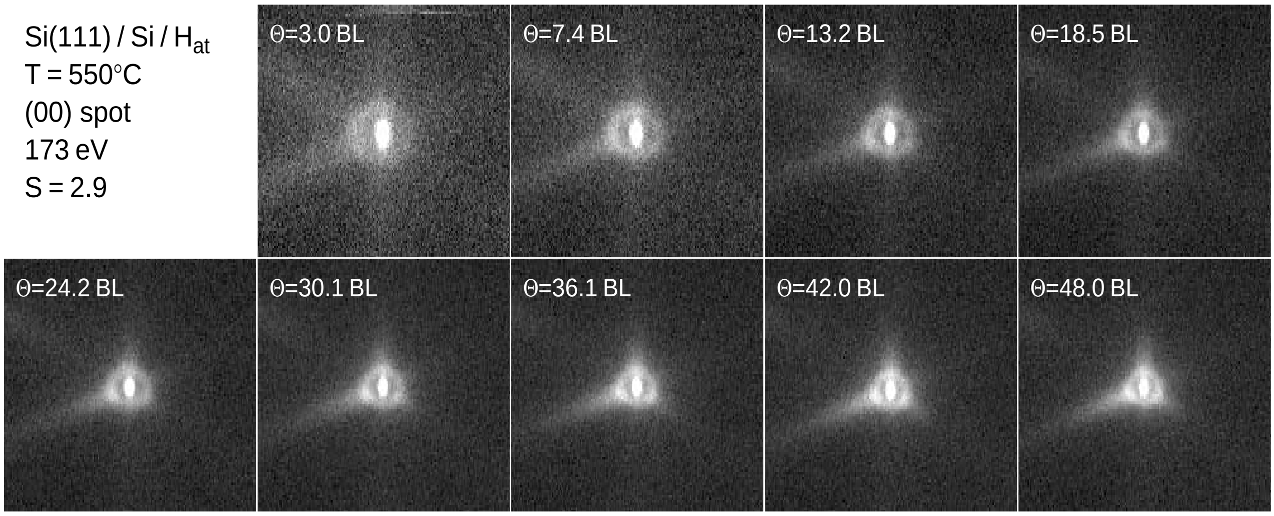

Fig. 4.34 Evolution of the fine structure of the (00) spot close to the "in-phase" condition during Si deposition and growth. With increasing coverage the diameter of the ring of diffuse intensity decreases. This reflects the coarsening process of the facets.

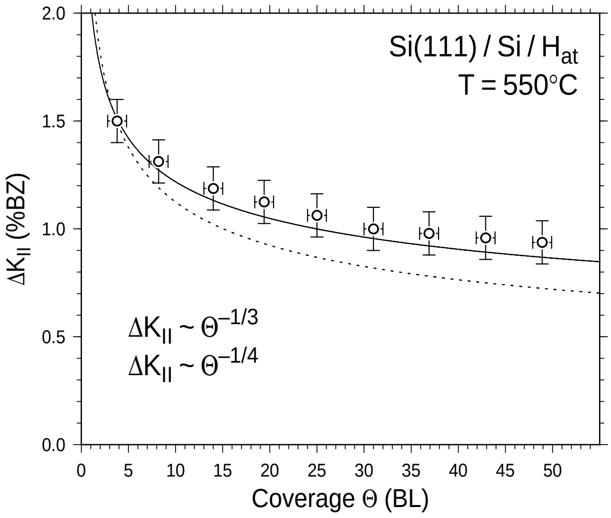

Fig. 4.35 The radius of the ring of diffuse intensity shown in Fig. 4.34 as function of coverage.

is estimated.

From the spot profile of the diffuse intensity shown in Fig 4.28 the power spectrum of the surface roughness is derived as function of correlation length (Fig. 4.33), i.e. as function of $\mathbf{K}_{||}^{-1}$. The cut-off for large values of ξ reflects the finite size of the facets or surface roughness. The cut-off for small ξ shows that the facets exhibit a minimum size.

The evolution of these large scale surface morphological features could now be monitored during growth. Figure 4.34 shows a sequence of LEED patterns of the (00) spot during Si deposition in the presence of a monolayer Hydrogen for $S = 2.9$. The same features are present as already shown in Fig. 4.27. With increasing Si coverage the ring of diffuse intensity shrinks in diameter and becomes brighter. This reflects the increasing size of the facets of the triangular pyramids with coverage. The radius of this ring of diffuse intensity is plotted in Fig. 4.35 as function of coverage.

The typical size ξ of the pyramids increases with maxiumum speed as function of the total deposited coverage θ_{total}, when their base line stays constant at the substrate:

$$\xi \propto \theta_{total}^{1/3}$$

Here we observe a weaker slope of the decay of the inverse facet size 1/ξ, indicating that the baseline of the facets increases also with coverage.

5. Ge Heterogrowth on Si(001)

5.1 Elastic Strain Relief

The growth mode in hetero epitaxial systems is mainly governed by two parameters: The lattice mismatch and the difference in surface free energies. The latter determines the possibility of wetting a substrate of element A with an hetero epitaxial film of element B. The inequality $\sigma_A > \sigma_I + \sigma_B$ with the free energy of the substrate (σ_A), the interface free energy (σ_I), and the surface free energy of the heteroepitaxial film (σ_B), sets the condition for the epitaxial film B to wet the substrate A. In this case layer-by-layer growth (Frank-Van der Merwe) may occur, changing into the Stranski-Krastanov mode beyond a critical coverage if the overlayer strain is increasing with thickness. [190] If the inequality has the opposite sign, usually Volmer-Weber growth occurs: Immediate islanding of the overlayer and formation of 3D-clusters is observed.

For the Si/Ge system, Si has the higher surface free energy, does not wet a Ge substrate and immediately start to island as sketched in Fig. 5.1. Consequently Ge is able to wet a Si surface, however, after formation of a wetting layer, islanding occurs [191] due to the accumulation of mismatch induced strain.

The inequality describes the growth mode under equilibrium conditions. Utilising kinetic limitations allows to deposit a continuous film B on a substrate A, even if this is thermodynamically unfavourable. However, growth at low temperature and/or high deposition rates usually results in poor crystal quality and rough surfaces. Increasing the temperature, or keeping the growth rate low, or even both, results in islanding of both Ge on Si and Si on Ge. However, improved epitaxy requires growth at temperatures above 500°C.

A solution out of this dilemma is the surfactant mediated

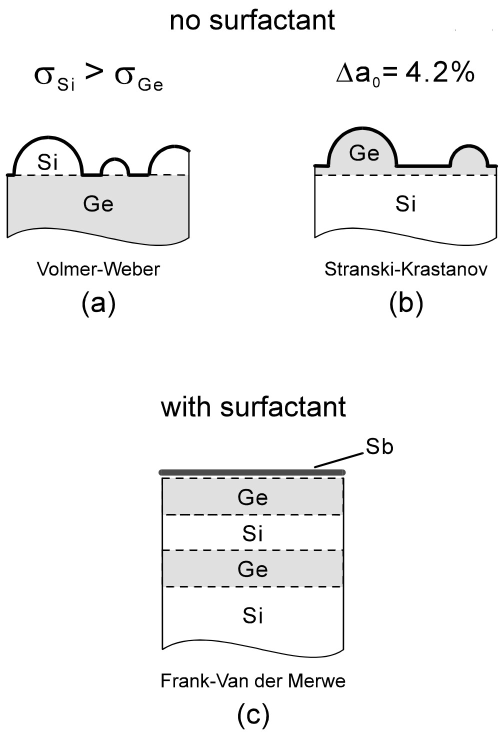

Fig. 5.1 Growth mode under thermal equilibrium is determined. by difference in surface free energy and lattice mismatch. (a) Due to its higher surface free energy, Si does not wet a Ge substrate and immediately islands in 3D clusters. (b) Ge with the lower surface free energy wets a Si substrate and forms a wetting layer of 3-4 ML thickness before islanding. The accumulation of strain in the pseudomorphic wetting layer leads to island formation. The Ge in the 3D-clusters is partially relaxed towards the bulk lattice constant. (c) Termination of the semiconductor surface by a surfactant results in layer-by-layer growth of both Ge on Si and Si on Ge. Islanding is prohibited, smooth and continuous films could be grown. The surfactant is floating on the growth front without significant incorporation.

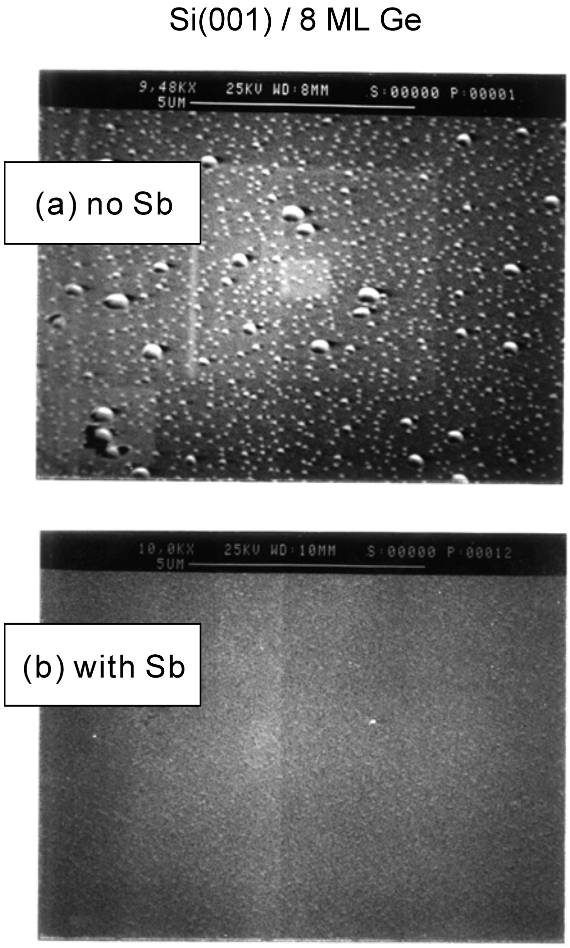

Fig. 5.2 The change of growth mode by surfactants is demonstrated with SEM top views for deposition of 8 ML Ge on Si(001). (a) Ge islanding without surfactant. (b) Smooth Ge surface with Sb as surfactant.

epitaxy: A substantial modification of the growth mode is obtained by introduction of a third element as surfactant (surface-active-species) [192]. The surfactant allows wetting of both species and prohibits formation of 3D clusters. Smooth and continuous films of element B could be grown on a substrate A and vice versa.

The surfactant (usually a group V element) saturates the dangling bonds of the semiconductor surface which results in a strong decreas [193] With the surface properties now mainly terminated by the surfactant layer, the difference in surface free energy of the Ge and Si is reduced, which already lowers the tendency towards islanding. This reduction of surface free energy is the driving force for the strong segregation of the surfactant, which floats on the growth front without significant incorporation. [194] This effect hinders high doping levels in Si-MBE [195] but is very welcome for the surfactant mediated growth. [196] The ideal surfactant modifies quasi catalytically the surface properties of the growing film without back ground doping of the film.

This change of growth mode is demonstrated in Fig. 5.2 for a 8 ML thick Ge film grown on Si(001). At temperatures of 500°C and above Ge growth on Si(001) without surfactant Fig. 5.2(a) results in formation of Ge clusters on top of a 3 ML thick pseudomorphic and strained Ge film . The so-called Stranski-Krastanov film is flat and smooth and relieves strain by a (1x8) missing dimer structure. Two different types of Ge islands form for coverages exceeding 3 ML [197]: first the strained and pseudomorphic hut clusters [198] with a width of typically 200-300Å and second 3d-clusters with a size larger than 1000Å, which are strain relieved by defects [199-201]. Hut clusters and (1x8)-structure are also observed with LEED [202].

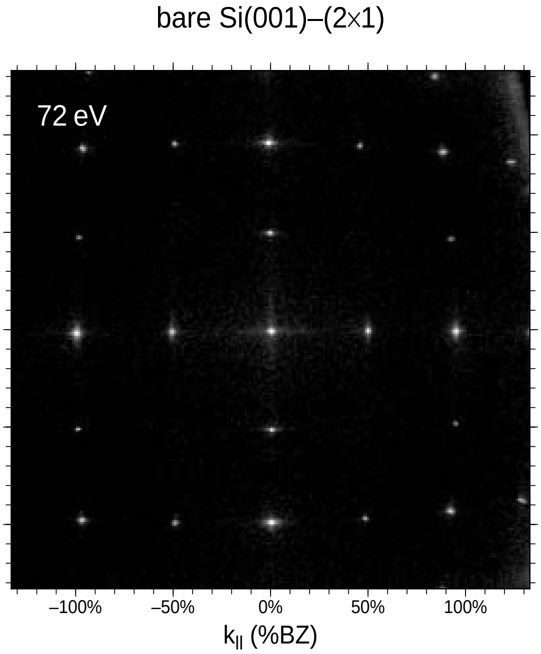

Fig. 5.3 LEED-pattern of the Si(001)-(2x1) surface without Ge. A logarithmic intensity scale with a dynamic of 1:50000 has been used. No contamination induced reconstruction is detectable.

Use of Sb or As as surfactant completely changes the growth mode: the formation of 3d-clusters is inhibited [192,203], and continuous Ge films of arbitrary thickness could be grown, as demonstrated in Fig. 5.2(b). As an additional effect the intermixing between Ge and Si is strongly suppressed [204]. The bulk morphology and defect structure of these films has been investigated by means of ion scattering [192], transmission electron microscopy [203,205] and xray-diffraction [206]. Here we will focus on the surface morphology of the Ge film during the initial stage of growth up to a thickness of 40 ML [94,95,202].

5.1.1 Micro Roughness

The Si substrate is cut from a (001)-wafer, with an orientation better than 0.2° in the ideal (001)-plane. The LEED pattern shows a brilliant (2x1) reconstruction as shown in Fig. 5.3 with a peak to background dynamic of 50000:1 as shown in Fig. 5.4 in a scan through the pattern (both scans along [100] and [110] direction are displayed with a logarithmic intensity scale). The complete lack of a (1x8) superstructure reflects a highly perfect surface.

The LEED-patterns after deposition of an 8 ML Ge-film are shown in Fig. 5.5(a,b) for two different scattering conditions. Visible are the (00)-spot in the center, the (10)- and (11)-spots as well as few (2x1)-superstructure spots.

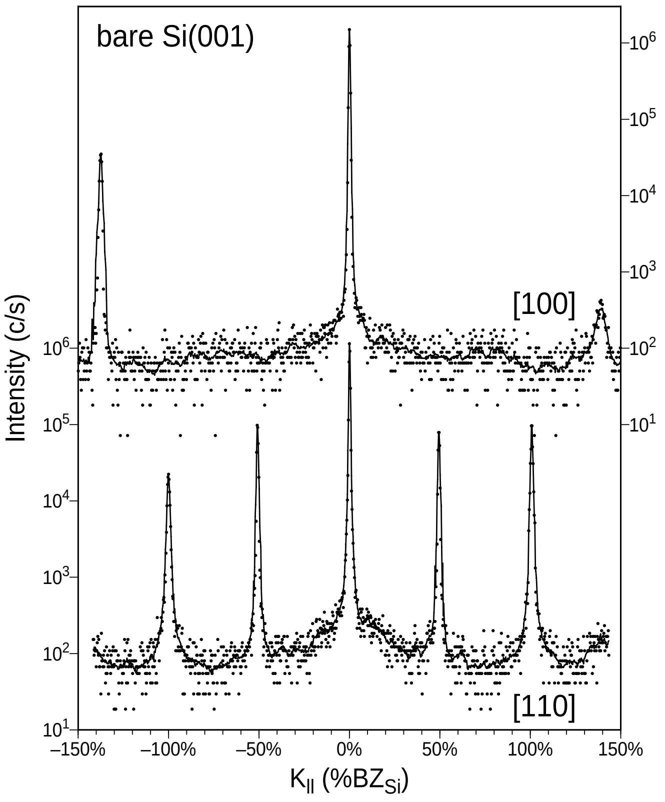

Fig. 5.4 Linear scans through the LEED-pattern shown in Fig. 5.3 in [100]- and [110]-directions. The peaks are the (00)-spot in the centre, the (11)-spots along [100] direction, and the (10)-spots and (2x1) superstructure spots along [110] direction.

Depending on the electron energy the spots are more or less broadened. The structures close to the right border are artefacts caused by the limited detection area of the SPA-LEED.

At an electron energy of 72eV the (00)-spot is very sharp without any broadening as seen in Fig. 5.5(a). This very pronounced "in-phase" condition of scattering reflects the perfect epitaxial growth of the Ge-film with all atoms on lattice sites. Decreasing the electron energy to 41eV only the broadening is observed; the sharp central spike is vanished since neighboured terraces interfere destructively due to the "out-of-phase" condition of scattering. The other integer order spots behave in a similar manner, only the energies for their "in- and out-of-phase" conditions are different. The pronounced broadening already points to a laterally and vertically very rough Ge-film which, however, is perfectly epitaxial.

Driving force for this pronounced roughness on an Ångstrom scale is the strain in the Ge film. From ion scattering [192,203] and x-ray results [200,206] it is known, that the Ge film is still pseudomorphic with the Si substrate. This very rough and open film morphology allows the elastic deformation of the strained Ge towards its bulk lattice constant [207-216]. This is accompanied by an increase of surface area and surface free energy which is out balanced by the strong decrease of strain energy.

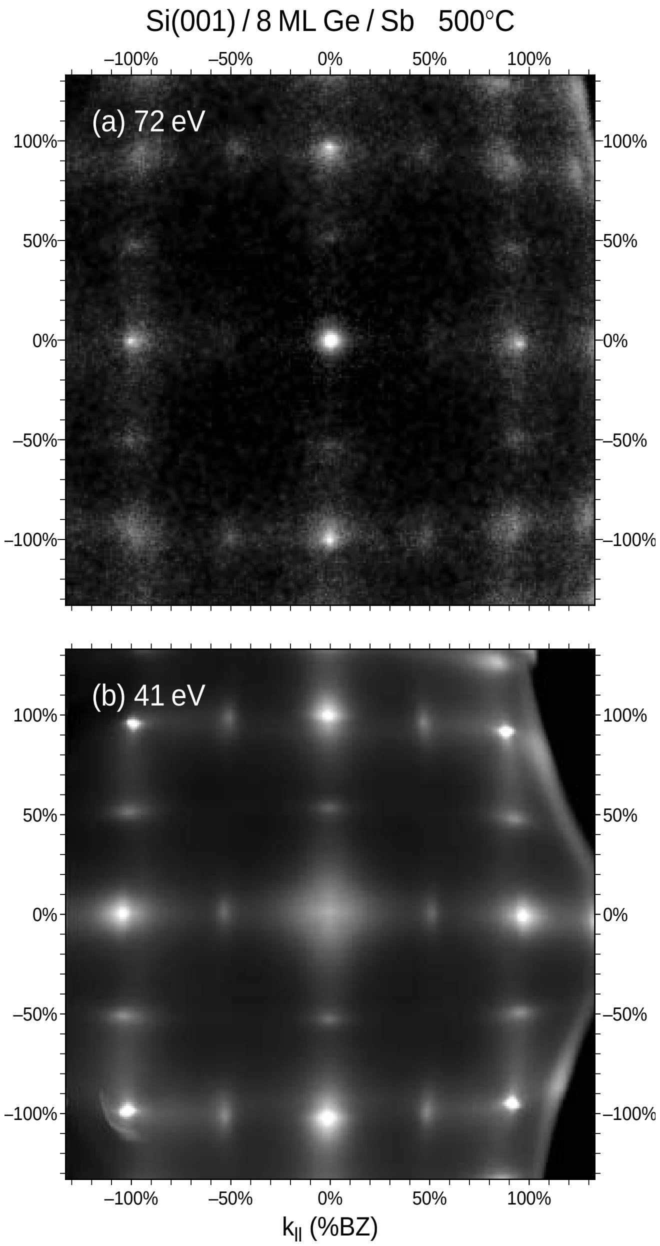

Fig. 5.5 LEED-patterns of 8 ML Ge grown at 500°C with Sb as surfactant. **(a)** Close to the "in-phase" condition for the (00)-spot at 72eV (Bragg condition). A very bright spot is observed. The (11)-spots are strongly broadened. **(b)** "out-of-phase" condition for the (00)-spot at 41eV which is therefore strongly broadened (Anti-Bragg condition). Now the (11)-spots are very bright and sharp. The (2x1)-spots show an anisotropic broadening.

The broadening of the (00)-spot at 41eV is not isotropic but shows a fourfold symmetry with increased intensity towards the [110]-directions. This is because on a (001)-surface the islands or terraces respectively preferentially grow along the dimers [217,218] which causes a larger extension of the islands in this direction. The diffraction pattern of such a narrow island reflects also this anisotropy. The fourfold symmetry of the broadening in the LEED-pattern is caused by superposition of two by 90° rotated LEED-patterns due to the two possible perpendicular dimer orientations [108]. From the shape of the broadening an aspect ratio of the terraces of 1 to 2-3 is estimated.

In order to analyse the film morphology in a quantitative way the behaviour of the spot profile has been determined for a larger range of energies (usually at least from one "in-

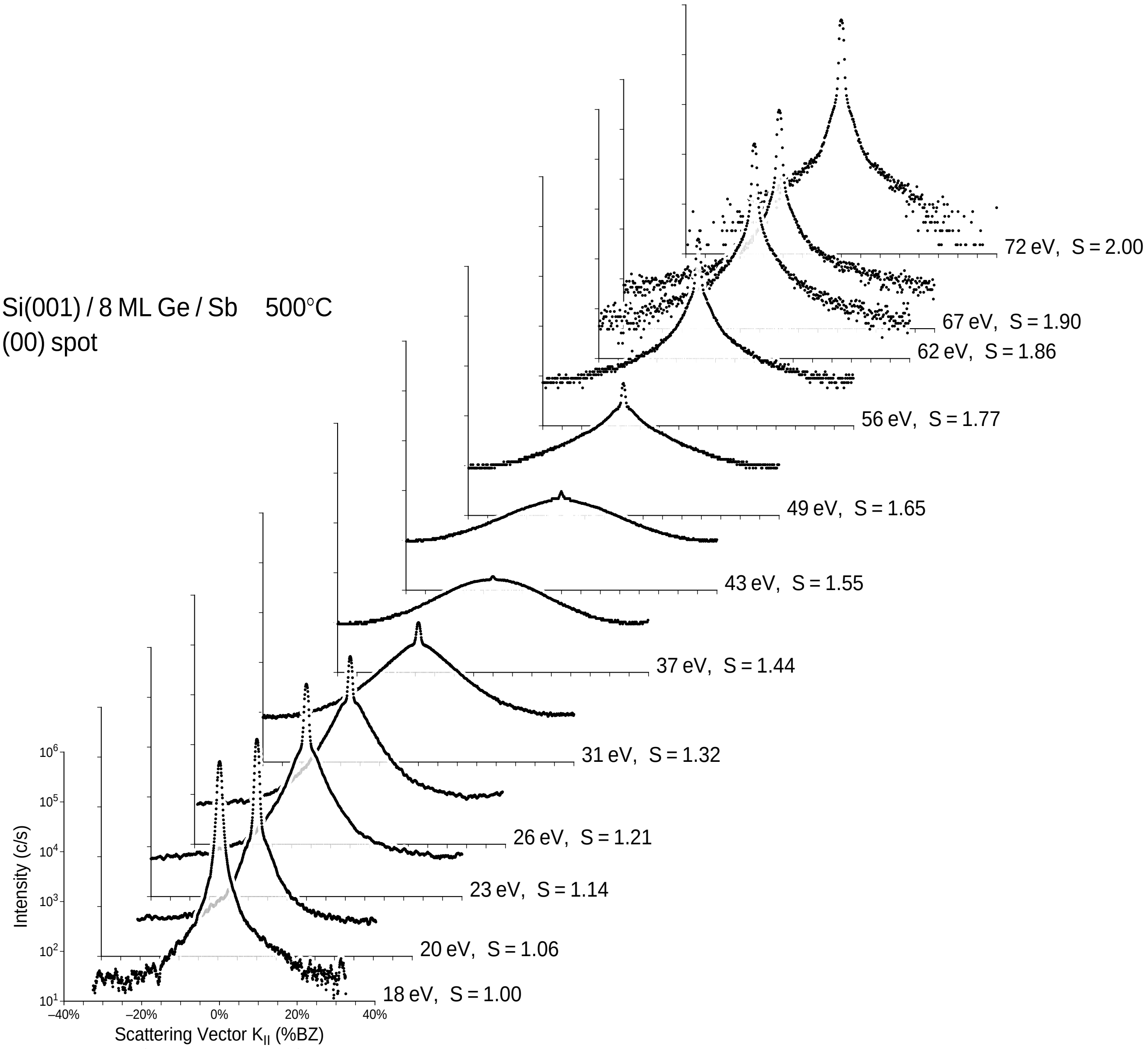

Fig. 5.6 Variation of the (00)-spot profile with electron energy or scattering phase *S* respectively. The scans are plotted in a logarithmic intensity scale. The x-axis is labelled in values of the distance to the next integer order spot (i.e. the width of the Brillouinzone). At the "in-phase" condition with S = 1.00 the spot shows only the instrumental broadening. With increasing energy the electrons which are scattered from terraces at different levels interfere more and more destructively. This is observed in the broadening below the central spike which gains more intensity and gets broader towards the "out-of-phase" condition at S = 1.5. Raising the energy further the central spike becomes again more intense with a maximum at the second in-phase condition.

phase" condition to the next). This is done by recording linear scans through the (00)-spot which are shown in Fig.5.6 as a function of lateral scattering vector $k_{||}$ with a logarithmic intensity scale and the electron energy or scattering phase *S* respectively as parameter.

At the "in-phase" condition with S=1.00 the (00)-spot is very narrow (instrumental resolution) with a peak to background ratio of 50,000:1. This shows explicitly that all atoms are on lattice sites and that the kinematic approximation is perfectly valid for the evaluation.

With increasing electron energy or scattering phase *S* respectively a broadening appears below the central spike. The broadening becomes more intense at the expense of the intensity of the central spike which nearly vanishes close to the "out-of-phase" condition at S=1.5. The width of the broadening also increases when changing the electron energies from the "in-phase" towards the "out-of-phase" condition. Increasing the electron energy further, the width of the broadening decreases again and also the central spike gains intensity with a maximum at S=2.00.

In contrast to the "in-phase" condition at S=1.00 a narrow broadening is still visible for the second "in-phase" condition at S=2.00. This deviation from the perfect behaviour is caused by the relaxation mechanism of the strained Ge-film: parallel to the surface the Ge-atoms in the lowest levels of the pseudomorphic Ge-film have exactly the Si-lattice periodicity and react via tetragonal distortion which results in an increased layer distance (larger than the Ge-bulk value). On the other hand the Ge in the upper levels is able to partially relax laterally, since the surface is very rough (this relaxation mechanism would not be possible for a flat and continuous film). Without the need of tetragonal distortion the vertical layer distance also relaxes towards the Ge-bulk value. Therefore the vertical layer distance *d* varies depending on the level in the Ge-film. Therefore the vertical scattering condition $S=k_zd/2\pi$ is no longer well defined: if for a particular electron wavelength the "in-phase" condition in the upper levels is fulfilled, it does not exactly match the increased layer distance in the lower levels and causes the observed broadening. The shorter the electron wavelength is, i.e. the higher the energies are, the more sensitive the diffraction is on this variation of the layer distance. A detailed analysis of this behaviour will be thoroughly addressed in a forthcoming publication [219].

The vertical roughness determines the intensity of the central spike as function of the scattering phase *S*. Because the intensity of the LEED-spots is additionally influenced by the dynamic form factor of scattering, the central spike intensity has to be normalised. This is done by using the ratio of the integral intensity in the central spike to the total intensity of the spot (the sum of central spike and broadening). This procedure eliminates the dynamic form factor from the evaluation which is assumed to be only slightly varying with $k_{//}$. The background intensity is excluded from the evaluation, since it is caused by thermal diffuse scattering (Debye-Waller). Only the normalised central spike intensity remains.

This normalised central spike intensity, which is derived from the spot profiles shown in Fig. 5.6, is plotted in Fig. 5.7(a) as function of the scattering phase *S*. The in-phase conditions at S=1.00 and S=2.00 are seen as pronounced maximum of the curve. Deviating from the in-phase conditions the values decrease very fast to nearly zero at the out of-of-phase conditions which points to a large vertical roughness. At the second in-phase condition the values for the normalised central spike intensity are much lower than equal one. As explained above, this behaviour is caused by the remaining broadening due to the variation of the layer distance.

In Fig. 5.7(b) the corrected data of the normalised central spike intensity are shown, the $G(S)$-curve. This curve now is determined only by the vertical roughness of the Ge-film. The rougher the surface is, the faster the $G(S)$-curve decreases for deviations from the in-phase condition. For a perfect flat surface a constant value of one is expected for the $G(S)$-curve, since there is no broadening. For a roughness of only two layers (a two level model as described by Lent and Cohen [97]) a G(S)-curve with a $1/2(1\text{-}\cos^2(2\pi S))$ dependence is expected. Increasing roughness adds terms with higher frequencies to the shape of the G(S)-curve, i.e. $(4\pi S)$-, $(6\pi S)$-, $(8\pi S)$-terms as arguments for the cosine function. Following Wollschläger [123] the rms. value of the roughness Δ could be determined by the slope of the G(S)-curve at the in-phase condition. Assuming a Gaussian shape (solid curve in Fig. 5.7(b)) of the G(S)-curve as approximation close to the in-phase condition, see also chapter 2.2.2:

$$G(S) \approx e^{-\Delta^2(2\pi\delta S)^2}$$

with δS as deviation of the scattering phase S from the next integer value, allows the easy estimation of the roughness to Δ=1.1 (in values of the layer distances d) via the full width at half maximum of the Gaussian. Assuming for the occupation of the levels a standard distribution around the mean level the roughness extends over 4-5 levels as shown in the small inset in Fig. 5.7(b).

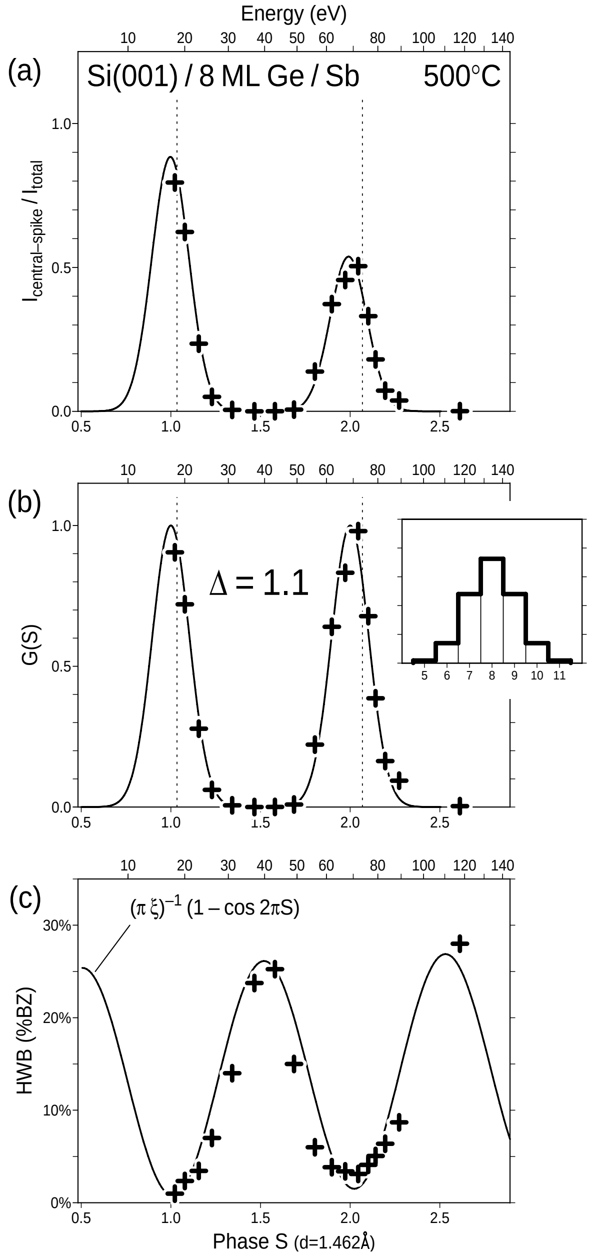

Fig. 5.7 Determination of the vertical roughness for a 8ML thick Ge-film grown at 500°C. **(a)** The central spike intensity is plotted as function of the vertical scattering vector, i.e. the scattering phase *S*. The dynamic form factor of scattering is eliminated by a normalisation. **(b)** The $G(S)$-curve is obtained by eliminating the influence of the varying layer distance which is caused by the strain relief mechanism. The maximum of the curve corresponds to the Bragg-conditions of scattering: neighboured terraces scatter in phase. The narrow width of the maximum of the $G(S)$-curve indicate a rough surface with a rms. value of Δ = 1.1 layer distances (d = 1.462Å). The inset displays the distribution of visible layers at the surface. A standard distribution has been assumed. The shift of the maximum to lower electron energies (the dotted lines indicated the bulk Bragg positions) is caused by an increased layer distance in the Ge-film due to tetragonal distortion. **(c)** The width of the broadening also varies with the scattering phase *S*. The solid line is the expected behaviour for a multi level model.

At this point we want to emphasise that the value of the vertical roughness stays the same after the correction of the data: the FWHM of the Gaussians at the in-phase conditions is the same for the curve in Fig. 5.7(a).

The $G(S)$-curve provides another important information: the vertical layer distance d could be derived from the distance ΔS between the in-phase conditions:

$d = 2\pi\ \Delta S / k_z$.

This information could only be obtained for a rough surface, since it is necessary to accurately determine the in-phase or "out-of-phase" conditions of scattering. Here we indeed observe a slight shift of the in-phase conditions to lower electron energies compared with the bulk Bragg conditions (dashed lines). The extension of the layer constant (Ge-bulk: 1.414Å) is caused by the tetragonal distortion of the strained Ge-film and is in the order of 0.048Å ± 0.02Å for this 8 ML Ge film which is smaller than the expected extension of 0.060Å for a Poisson ratio of ν_{111}=0.249 [220]. This is reasonable because part of the lattice strain is already relieved by the elastic relaxation of the Ge towards its bulk lattice parameter.

For such a rough surface a variation of the width of the broadening is expected as a function of the phase S [117]. This has been observed in the experiment (Fig. 5.6) too. The FWHM´s of the broadening of the (00)-spot are plotted in Fig. 5.7(c) as function of S. Close to the in-phase conditions the width has its minimum value and increases towards the "out-of-phase" condition. The solid curve displays the expected behaviour assuming a multilevel model described by Pukite and Cohen [117]. From the width of the broadening at the "out-of-phase" condition the average terrace width is estimated to Γ_{av}=2.6 u.c. (unit cell, 1 u.c. = $a_{0,Si}/\sqrt{2}$ = 3.84Å). Thus the Ge-film is not only very rough vertical to the surface but shows also a strong lateral roughness, i.e. the terraces have a width of only a few atoms. The Lorentzian profile of the broadening reflects a geometric distribution of the terrace widths.

5.1.2 Temperature Dependence

The influence of the deposition temperature on the Ge film morphology is of special interest to prove the micro roughness as energetically driven strain relief mechanism. The growth temperature has been changed from 420°C up to more than 700°C. Above 700°C the LEED patterns completely change its behaviour in a qualitatively way: all spots show a ring like shape which is caused by equilibrium formation of small pseudomorphic Ge-cones at the surface [94,202] and will be discussed in one of the next sections.

The main features of the LEED patterns after deposition of 8 ML of Ge at temperatures between 420°C and 640°C are very similar to the one shown in Fig. 5.5 which has been grown at 500°C. The (00)-spot is always strongly broadened for all temperatures. The width of the broadening stays approximately constant and does nearly not depend on the temperature. Only the shape of the broadening changes with temperature and reminds of a Maltese cross for the Ge-film grown at 640°C. At the lowest temperature of 420°C the (00)-spot lacks any features and is isotropically broadened. For all temperatures sharp (11)-spots reflect the epitaxial growth of the Ge-films.

The spot profiles of the (00)-spot are compared in Fig. 5.8 for the different growth temperatures. At the lowest temperatures the profile could be described by a Lorentzian which reflects a geometric terrace width distribution (see chapter 2.2.1). At higher temperatures the profile shows more features, however, the width of the broadening is approximately the same for all temperatures: The lateral roughness, i.e. the average terrace length, is almost independent on the deposition temperature. The additional broad peaks results from a missing dimer structure at the Ge surface [221].

At all growth temperatures the spot profile of the (00)-spot varies strongly with electron energy. This happens in the same manner as already observed at 500°C and reflects a very rough surface, too. The $G(S)$-curves for 420°C, 570°C and 640°C are shown in Fig. 5.9 (a-c) and are quite similar to the $G(S)$-curve for 500°C. Surprisingly the Ge-film gets rougher with increasing temperature as observed in the decreasing width of the $G(S)$-curve at the "in-phase" conditions. At 420°C a rms. value for the roughness of Δ = 0.9 is observed. At 640°C the value has raised to Δ = 1.3.

The use of surfactants during heteroepitaxial growth of Ge on Si inhibits the formation of 3d-clusters. The mechanism is the selective change of some of the activation energies for diffusion and place exchange and is discussed in detail elsewhere [194]. Another obvious result for Sb

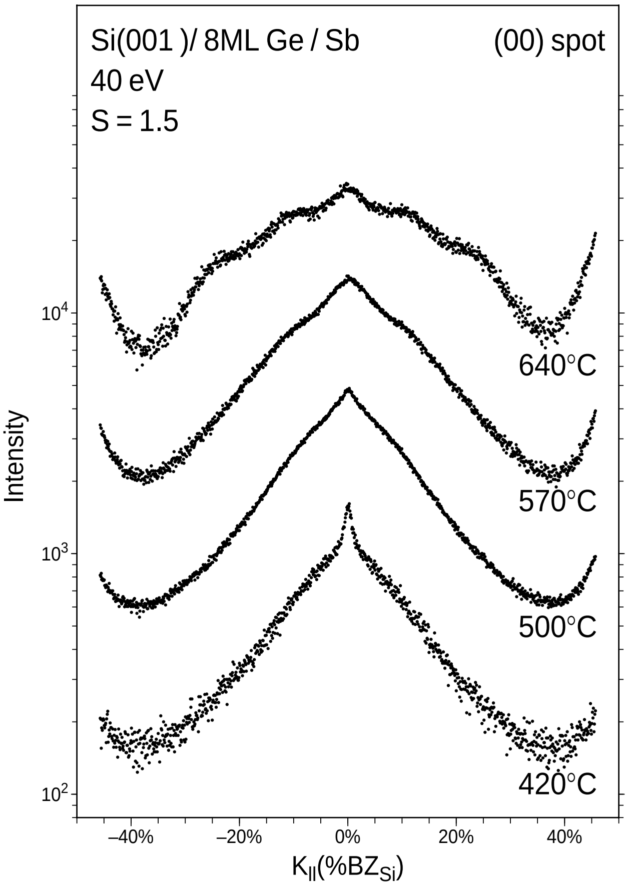

Fig. 5.8 Spot profiles of the (00)-spot at the "out-of-phase" condition at 42 eV (Anti Bragg condition) for 8 ML Ge films grown at different substrate temperatures. The broadened part of the spot profile has almost the same width independent on the growth temperature.

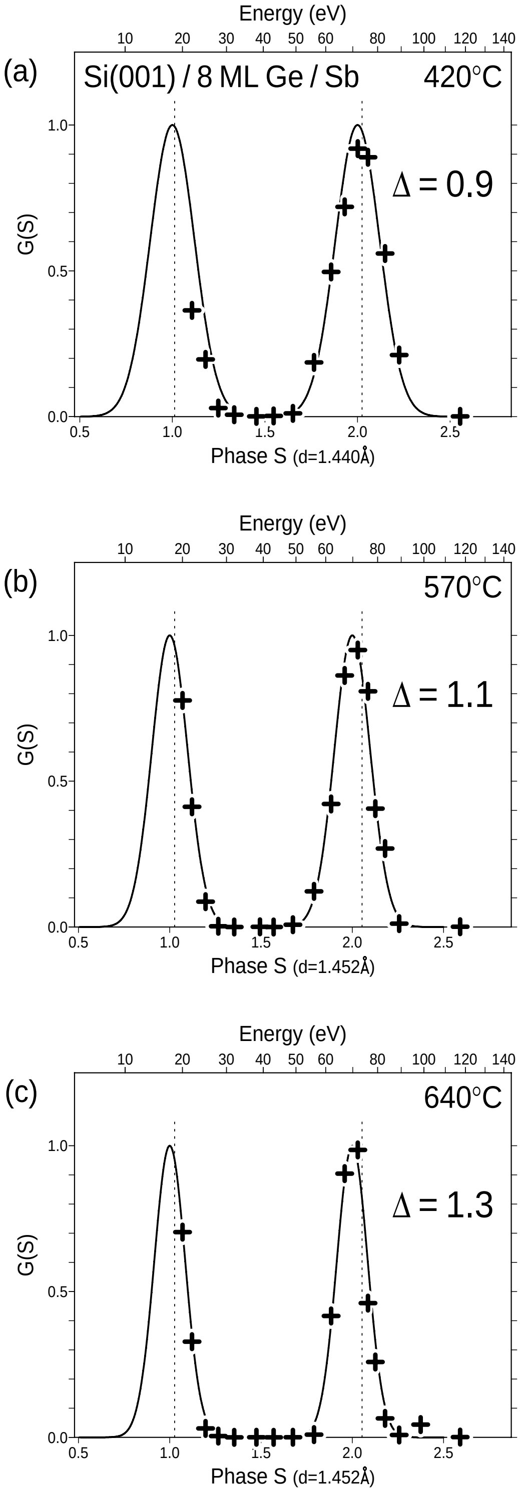

Fig. 5.9 $G(S)$-curves for 8 ML thick Ge-films grown at different temperatures. The rms value Δ of the roughness increases slightly with temperature. **(a)** Growth at 420°C results in the smoothest surface with a roughness of Δ = 0.9 layer distances. **(b)** Growth at 570°C results a roughness of Δ = 1.1 layer distances. **(c)** Growth at 640°C shows the roughest surface with Δ = 1.3 layer distances.

(a) smooth, flat heterofilm:
- pseudomorphic
- tetragonal distortion
- layer distance largely increased

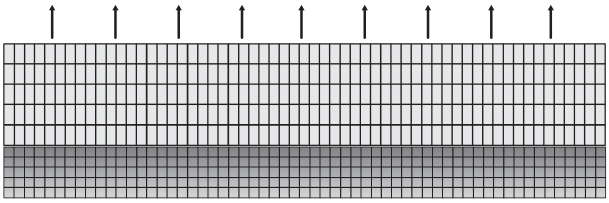

(b) microrough heterofilm:
- pseudomorphic
- elastic relaxation towards bulk lattice constant
- surface area increased
- strain energy strongly decreased
- variation of layer distance

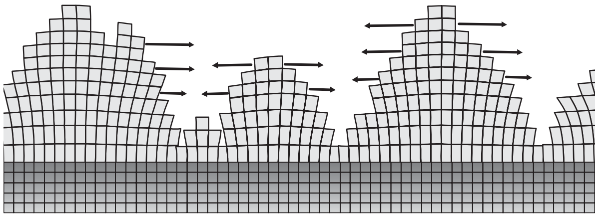

Fig. 5.10 **(a)** A smooth and flat hetero layer is highly strained and relieves strain only by tetragonal distortion: i.e. an increase of the layer distance: the Bragg condition is strongly shifted. The lateral lattice constant is determined by the substrate. **(b)** A rough and open Ge surface allows the partial elastic relaxation of the Ge film towards the bulk lattice constant. The increased surface area and surface free energy is out balanced by the strong decrease of strain energy. A smaller tetragonal distortion and a variation of the layer distance is expected: The Bragg condition is no longer well defined!

surfactant mediated growth of thin pseudomorphic, strained Ge-films is a pronounced micro roughness which is observed for all growth temperatures. Even more: the vertical roughness increases slightly with temperature. This result seems to contradict all expectations of the influence of the kinetics on growth. However, we will show that the observed phenomena could be consistently explained in terms of thermodynamics and kinetics.

The formation of the micro roughness of the pseudomorphic Ge-film allows the partial elastic relaxation towards the bulk lattice constant as sketched in Fig. 5.10: A flat and continuous film would not allow for this kind of strain relaxation mechanism (without surfactant the Ge adatoms are that mobile that they are all collected in the 3D clusters). Therefore a rough surface allows a lower strain energy of the system .

This explains why the surface becomes rougher with increasing temperature. The Ge-atoms are more mobile and occupy the most favourable lattice sites. The resulting morphology is closer to equilibrium than for growth at lower temperatures when the kinetics hinders the formation of the surface morphology with the lowest energy. Now also unfavourable lattice sites are occupied, i.e. those which actually smoothen the surface.

The result only seems to be strange: the increase of mobility with higher temperatures (smaller influence of the kinetics) forces the formation of the surface with the lowest energy which (no longer surprisingly) is a rough surface! As a consequence the surface morphology of the Ge-film is essentially governed - over the whole temperature range - by the lattice misfit and not by the kinetics.

5.1.3 Surfactant induced stress

The question arises, if the observed effects are unique to the use of Sb as surfactant. With As as surfactant the formation of a rough surface during the initial stage of growth has already been reported by Köhler et al. [222]. The surface was composed of long elongated Ge terraces each only one to a few dimers wide. This findings are also confirmed by our investigations: Fig. 5.11 shows the LEED pattern of 8 ML of Ge grown at 570°C using As as surfactant. The intensity distribution, however, has strongly changed: a very large, but sharp cross is now observed. This reflects very long terraces, which are only a few dimers broad. The width of the spot profile in the broad direction is comparable to the results shown in Fig. 5.8.

The vertical roughness has again been determined by varying the electron energy. The results are shown in Fig. 5.12. Surprisingly a relatively flat surface with a rms. value of only Δ = 0.55 for the roughness is found. The shift of the Bragg condition from 75 eV (expected value for bulk Ge) to 67 eV reflects an increase in the layer distance of 6% to 1.50Å (the Ge bulk value is 1.414Å). This films are still pseudomorphic since strain relieving defects are generated only beyond a coverage of ~18 ML [192,203].

This is also confirmed by the intensity oscillations of the (00)-spot shown in Fig. 5.13 during Ge deposition. The oscillations show a bi-layer mode caused by the difference in form factor of the (2x1) and (1x2) terrace due to the non-normal incidence of the electron beam [223]. With Sb as surfactant (a) the oscillations die out at ~11 ML indicating the formation of strain relieving dislocations. With As as surfactant (b) the oscillations are observed up to ~19 ML indicating the later onset of defect formation.

The reason for the relatively flat surface and the delay in defect formation may be the smaller size of the As compared with Sb. Adsorption of As on a Si(001) surface results always in a tensile stress [224,225] which is opposite to the

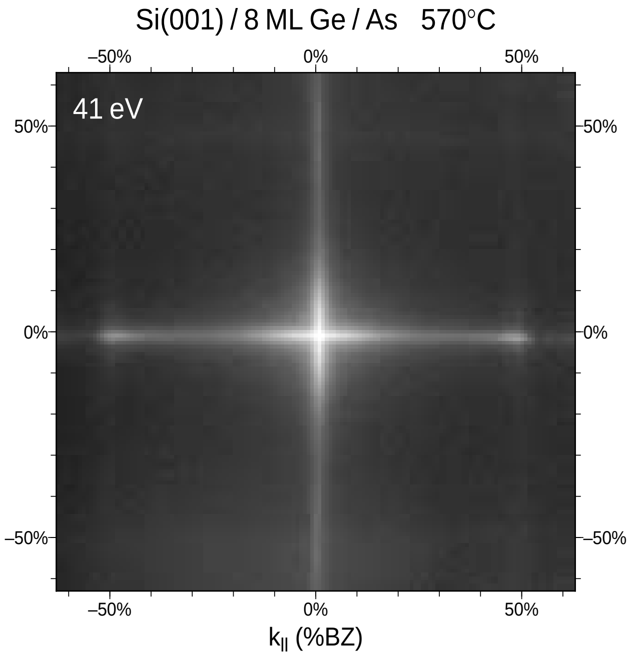

Fig. 5.11 LEED-pattern after growth of 8 ML Ge at 570°C using As as surfactant. The (00)-spot is broadened in a shape of a very large sharp cross. This reflects needle like terraces which are very long but only a few dimers wide. An aspect ratio of at least 1:10 is found for the terraces.

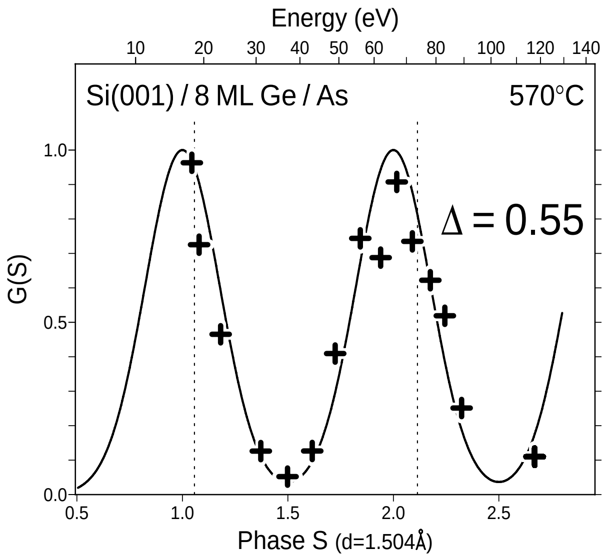

Fig. 5.12 *G*(*S*)-curve for a 8 ML thick Ge-film grown at 570°C using As as surfactant. A roughness of only Δ = 0.55 layer distances is observed. The layer distance of the Ge film has increased to 1.50Å due to tetragonal distortion.

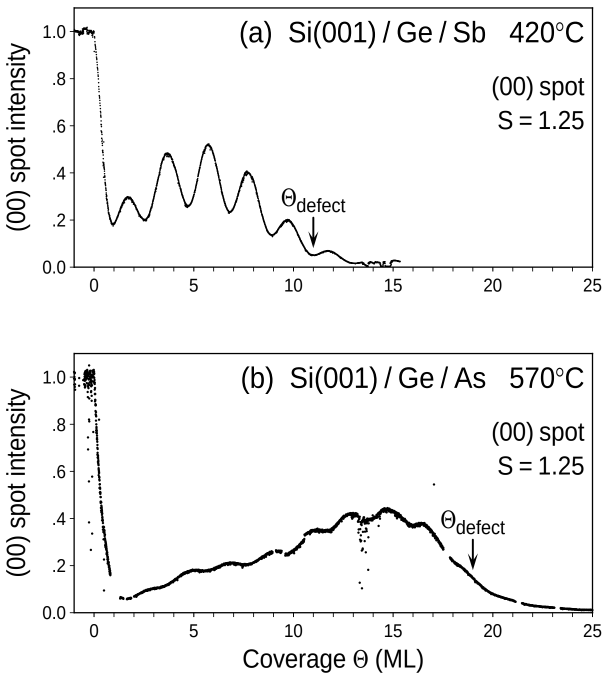

Fig. 5.13 (00) spot intensity oscillations as function of Ge coverage. Due to different form factors of the alternating (2x1) and (1x2) terraces a bilayer mode is observed. (a) With Sb as surfactant the intensity decreases strongly beyond 11 ML, indicating the formation of strain relieving defects. (b) As as surfactant with a tensile surface stress compensates part of the compressive stress of the G film and allows the growth of thicker strained Ge films. The onset of defect formation occurs beyond 19 ML.

compressive stress of the evaporated Ge-film. This balances the total energy without relieving the strain in the pseudomorphic Ge film. In contrast to this, adsorption of Sb results for higher coverages in a compressive stress because the Sb is larger than the As. With Sb as surfactant the compressive stress of the Ge film could not be compensated.

Because the lattice strain of the 8 ML thick film is not relieved by micro roughness, the Ge layer distance is increased due to a larger tetragonal distortion. From our results a Poisson coefficient of $\upsilon \sim 0.35$-0.40 could be estimated.

5.1.4 Surfactant stabilized Ge cones

With a growth temperature above 700°C the LEED patterns after deposition of 8 ML of Ge on S(001) with Sb as surfactant changes in a surprising way. Instead of broadened spots the LEED patterns show rings of intensity at the positions of the integral order spots [94]. This is shown in Fig. 5.14 for different scattering conditions.

The diameters of these rings depend on electron energy and the order of the LEED-spots. At the in-phase condition of scattering the spots are sharp and bright. This reflects the perfect epitaxial growth of the Ge with all atoms on lattice sites. At 43eV the (11)-spots are bright and sharp due to their in-phase-condition. The (10)-spots show a ring as well as the (00)-spot. At 62eV the (10)-spots have their in-phase-condition. The (11)-spots show a ring as well as the (00)-spot. The size of the ring around the (00)-spot has decreased. At 76eV the (00)-spot is close to the in-phase-condition. The intensity of the rings is determined by the surface morphology and the form factor which depends also on the electron wave vectors. This causes the asymmetric intensity distribution for all spots except the (00)-spot in the centre of the patterns. This is also the reason for the half moon shaped form of the (10)-spots at 76 eV.

The nature behind these strange LEED-patterns is enlightened by a closer look at the behaviour of the (00)-spot. The diameter of the ring decreases with decreasing deviations from the in-phase condition at 72eV as shown in Fig. 5.15 in a series of 2D-scans at different electron energies. By decreasing the energy even more the diameter increases again. Above 82eV the ring shows a fourfold symmetry with slightly increased intensity towards the (11)-spots. Below 54eV a behaviour rotated by 45° is observed. The LEED-patterns of a stepped surface (i.e. all atoms on lattice sites) must have a point symmetry with respect to the bulk-Bragg-conditions [226], which are the in-phase-conditions for surface scattering. Since the azimuthal intensity dependence is rotated by 45° above and below the in-phase-condition this effect is caused by a change in the form factor of scattering for the different azimuthal directions for different electron energies. The uniform intensity distribution around the perimeter of the ring is more evident close to the in-phase-condition, where the dynamic form factor, which is only slowly varying with $k_{||}$, stays more and more constant for different azimuthal orientations.

Figure 5.16 shows the positions of the ring around the (00)-spot in reciprocal space for electron energies ranging from 20eV to 160eV (the k_z-axis is compressed by a factor

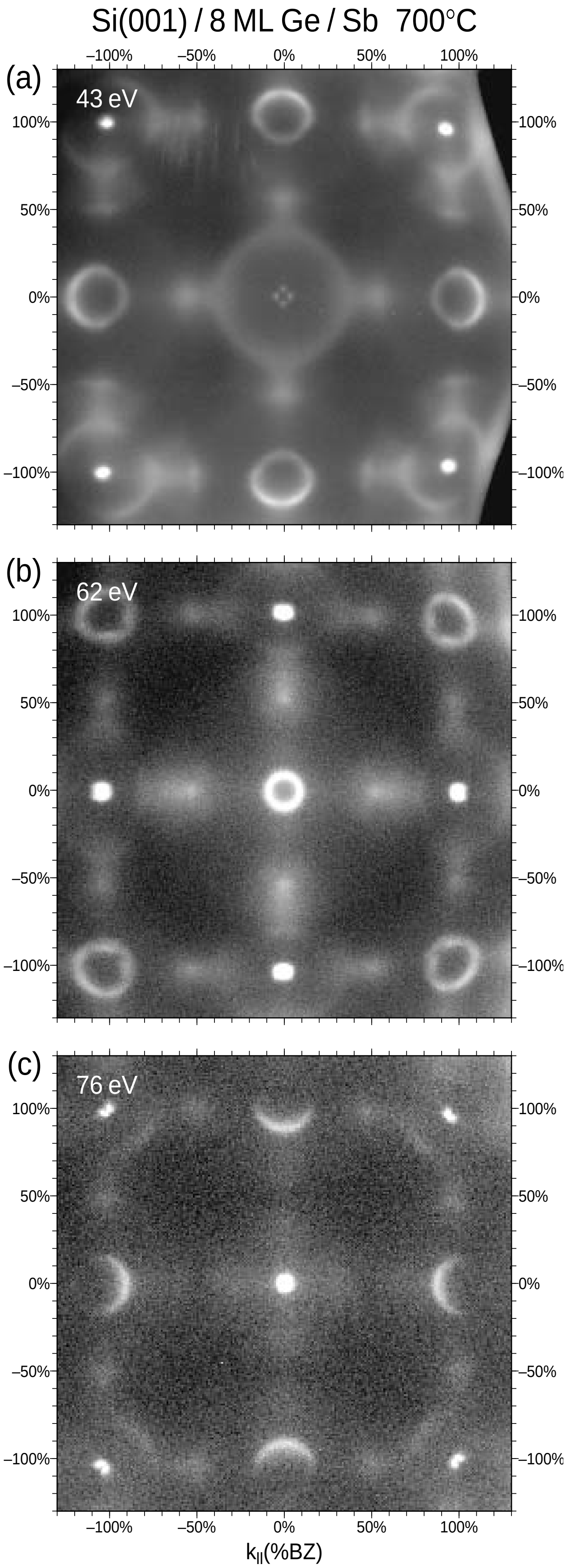

Fig.5.14 LEED patterns of 8 ML thick Ge-films grown at 700°C on Si(001) with Sb as surfactant. All spots show a ring like intensity structure. The diameter of the rings depend on the scattering condition.

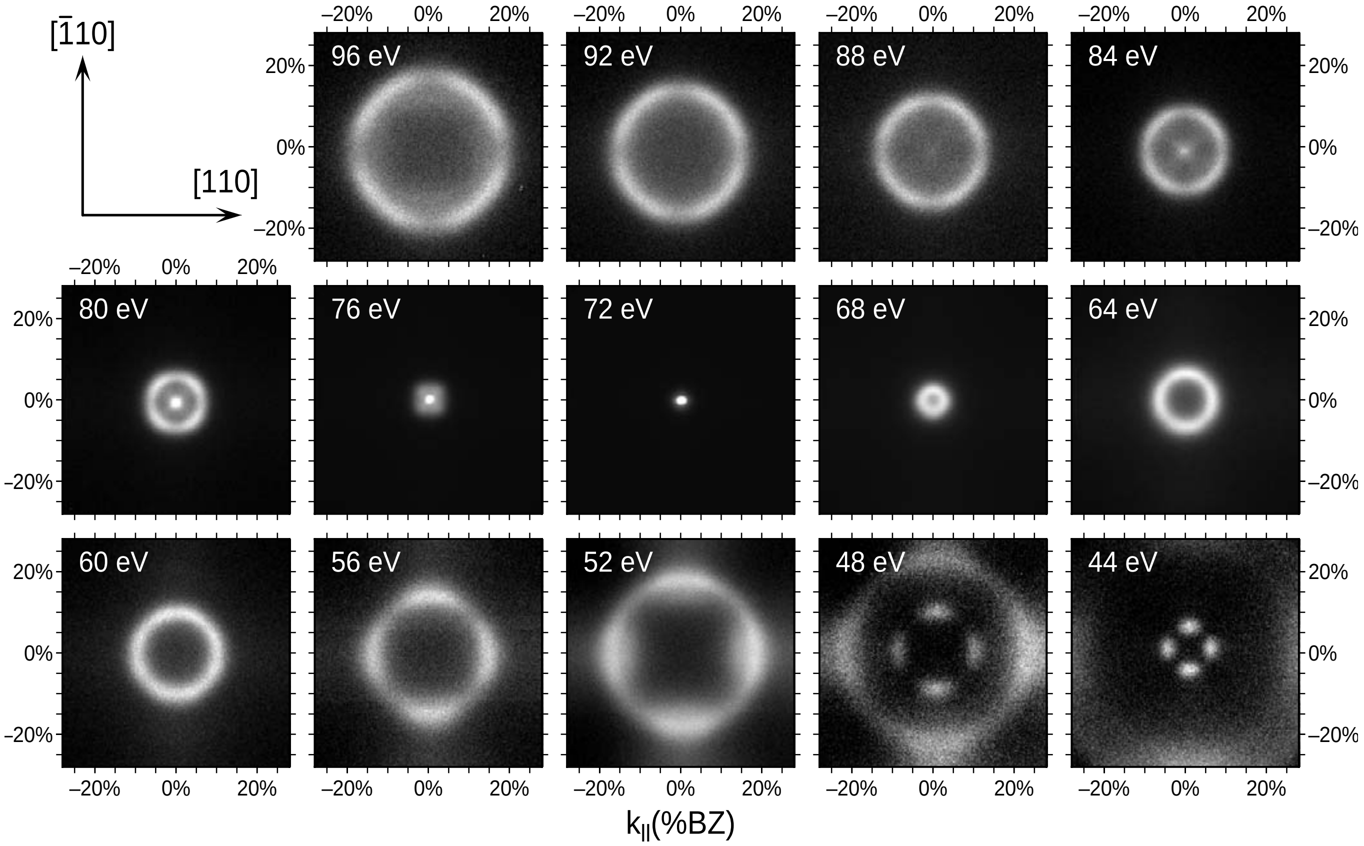

Fig. 5.15 The diameter of the ring around the (00)-spot depends on the electron energy as shown in this series of 2D-scans. The in-phase-condition at 72eV is clearly seen in the presence of the sharp central spot. The intensity of the ring is four-fold modulated by dynamic effects: at high energies weak maxima occur in [100]-directions, at low energies in [110]-directions. The four distinct intensity peaks at 48eV and 442eV are caused by the [117]-facet, which has a double periodicity. Those peaks coalesce at the out-of-phase condition for single steps at 39eV.

of two). The k_x-axis is scaled in percent of the Brilloiun-zone (%BZ), i.e. in fractions of the distance to the next integer order spot, which corresponds to 100%BZ. The length of the ovals corresponds to the full width of half maxima of the rings; the width describes the intensity of the ring.

Changing the electron energy all spots move on inclined rods with a tilt-angle of ~12° corresponding to a [117]- or [105]-direction, which is the typical behaviour of the LEED-pattern of a faceted surface. But in this special case all possible azimuthal facets with an inclination angle of ~12° occur at the surface. No azimuthal orientation of the facets is favoured, the ring shows (apart from the dynamic effects) a uniform intensity distribution. This LEED pattern is caused by circular shaped Ge cones with an inclination of 12°.

The diffraction pattern of such a 12°-cone is in reciprocal space again a cone which, however, is shaped like an ice-cream cone with an aperture angel of 24° (two times 12°) as shown in Fig. 5.17. This reciprocal space cones are opened upwards and downwards and located at any in-phase-condition of scattering (open and closed dots in fig.4). On the left side of Fig. 5.17 a cut in [100]-direction of the reciprocal space, on the right side a cut in [110]-direction is shown. The in-phase conditions for scattering are marked by closed dots. Due to the two different step geometries for the two [110]-directions on a (001) diamond lattice [227] the in- and out-of-phase conditions are not well defined for the (10)-rod and marked by the open dots. Because the translation-vector for crossing an A-type and B-type step are different no reciprocal vector exists for the (10)-rod to satisfy a complete destructive interference for both step geometries. Either the A-type step has a out-of-phase condition and the B-type step an in-phase condition or the other way around. In the [100]-directions alternating steps have the same geometry and therefore a reciprocal vector exits for the complete destructive interference for all steps.

From intersection of the facet rods in Fig. 5.17 (Bragg conditions) a slightly increased layer distance in the Ge cones is estimated. Compared with the Ge bulk lattice constant of 1.414Å the 12°-cones have a 1.6% increased layer distance of 1.438Å. This tetragonal distortion of the 12 °-cones is caused by the pseudomorphic growth with the lateral lattice positions of the Ge atoms determined by the Si substrate.

This is also confirmed by a measurement of the positions of the (10)-, (00)-, and (-10)-spots of the 12°-cone shaped surface showing exactly the same spot-positions (accuracy ± 0.003Å) compared with a Si-surface (Fig. 5.18). The in-phase-condition for the (10)-spots with an electron energy of 94 eV has been chosen as scattering condition, as also sketched in Fig. 5.17. The intensity ring of the (00)-spot can be seen in the lower curve at ±20% BZ. This data additionally confirms that the 12°-cones are still

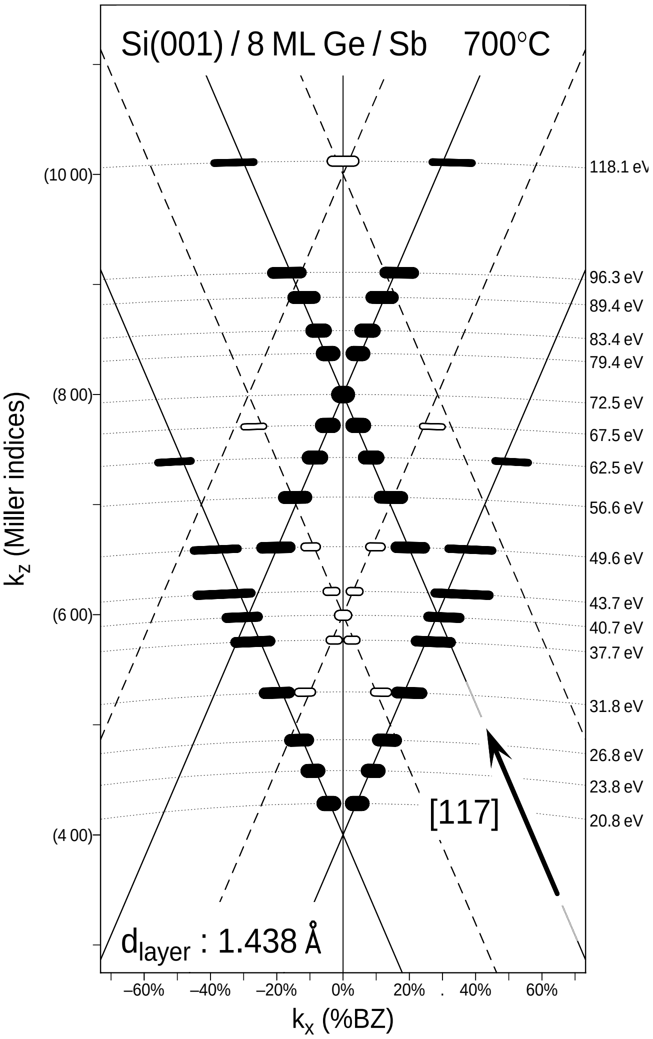

Fig. 5.16 The position of the intensity ring around the (00)-spot is plotted as ovals in reciprocal space as a function of k_Z, indicated with the Bragg-conditions. The length of the ovals corresponds to the width of the rings, the width roughly to the intensity of the rings. Open ovals denote the [117]-facet spots which only occur in the [110]-directions. The spots move on rods, which are inclined by ~12°, indicating a facet behaviour. From the in-phase conditions, which are determined with very high accuracy from the intersections of the facet rods with the (00)-rod, a layer distance of 1.438Å is estimated, which is about 1.6% larger than the Ge-bulk value.

pseudomorphic without any strain relieving defect generated up to that coverage.

The whole surface is covered by 12°-cones as seen in the almost complete lack of intensity at the (00)-spot position for scattering conditions other than the in-phase-condition (see Figs. 5.14, 5.15 and 5.18). A large flat surface area would produce intensity confined around $K_{||}= 0$.

The low intensity observed in broad (2x1)-spots at some energies may be caused by small areas, which are more or less flat, as expected between the 12°-cones or on top of the 12°-cones (from general energetical reasons rounded tops of the 12°-cones are favoured due to the high temperatures [228]).

The size of the 12°-cones could also be estimated from the LEED analysis. A finite size effect in the diffraction has to be expected for the cones if they are smaller than the

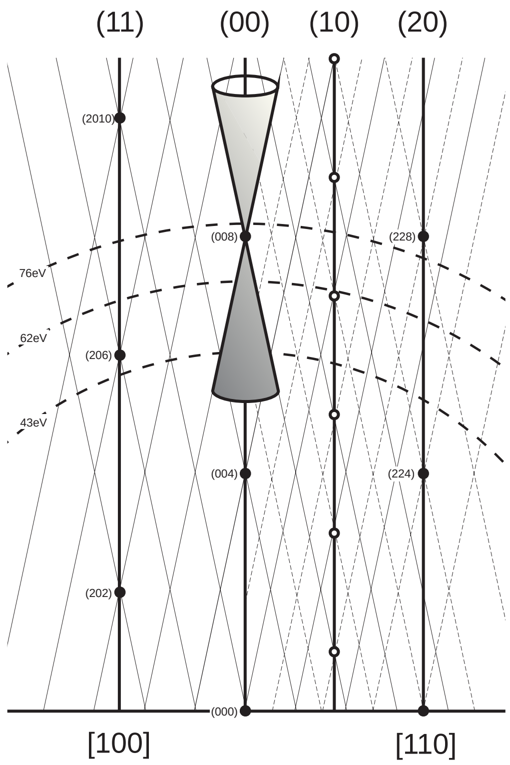

Fig. 5.17 Reciprocal space plot of the facet rods of the 12°-cones on the (001)-surface for two different azimuths. The in-phase-conditions (the Bragg-conditions) are shown by dots and open circles. The two non equivalent steps in the [110]-direction cause an inherent double periodicity (dashed lines) on the facets in this orientation. The 2D-scans of Fig. 5.14 are shown as dashed circle segments. The diffraction pattern of a 12°-cone in reciprocal space is also a cone which, however, is shaped like an ice-cream cone with an aperture angel of 24°.

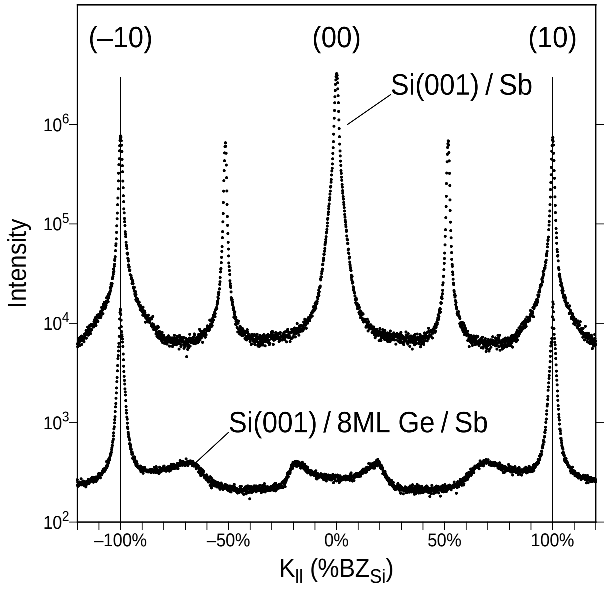

Fig. 5.18 The 12°-cones are pseudomorphic and show the same lateral lattice constant as the Si substrate as measured with identical positions of the (-10)- and (10)-spot of the bare surface and the 12°-cone covered surface. The in-phase-condition for the (10)-spots with an electron energy of 94eV has been chosen as scattering condition, producing the sharp spots necessary for the comparison.

transfer width of the instrument (~1000Å). The width of the intensity ring depends on the scattering phase S which on the other hand linearly corresponds to the diameter of the ring (see Fig. 5.19). At the out of phase condition the size distribution of the single terraces of the facets is observed in the width of the ring (the diameter of the ring, however, is determined by the facet angle).

Changing the scattering condition more and more towards the in-phase-condition reduces the width of the intensity distribution of the ring due to the larger lateral distances necessary to cause a phase shift of π. At the in-phase-condition the spot-profile is determined by the distance between the 12°-cones.

Unfortunately the broadened part of the spot disappears for this condition, since all atoms scatter constructively without any phase-difference (Bragg condition). However, the distance distribution of the 12°-cones still determines the spot-profile for scattering phases very close to the in-phase-condition. The range of validity depends on the maximum height difference Δh of the structures and is roughly given by $S \pm \Delta S$ with $\pm\Delta S = 1/\Delta h$ and S equals the integer number given by the in-phase-condition.

The width of the ring decreases linearly to lower values with decreasing diameter of the ring as shown Fig. 5.19 but shows an asymptotic behaviour towards a constant value of 2.2 %BZ. This behaviour reflects the finite size of the 12°-cones. An average distance of the 12°-cones of about 300-400Å is estimated. This is a reasonable value since an average diameter of 330Å results by assuming the whole surface covered with cones which have a tilt angle of 12° and are built up by a total coverage of 8 ML of Ge.

This finite size behaviour has also been observed in a LEED pattern of the (00) spot at the in-phase condition (Fig. 5.20). A weak intensity ring encircles the central (00) spot. The diameter of this ring stays constant for small variations of the scattering condition and reflects the power spectrum of the long wave length components of the surface morphology (see also chapter finite size in theory and Si(111)/Si/H). From the diameter a typical size of the cones of ~300Å is derived.

The results obtained by the LEED analysis are also confirmed by STM. Figure 5.21 shows the 12° cones are in a perspective STM image with a size of 1000×700Å. The whole surface is covered by 12°-cones, no flat areas are visible, not even between the cones, those space is filled up with smaller islands. The majority of the surface is covered with 12°-cones of 300Å typical size. No islands larger than 400Å are present.

The atomic structure of the 12°-cones shows a [117]-type facets with a regular pattern of atomic steps. The [105]-type facet, which is in the figure parallel to the border of the image, is irregular shaped with a high number of kinks.

The top of the 12°-cones is rounded and not sharply peaked. A convolution effect with the shape of the tip in the STM is ruled out since the arrangement of the atoms on top of the 12°-cones is different from cone to cone. The rounded top of the 12°-cones is more likely caused by the non-zero-temperature effect [228], allowing other facets than those with the lowest energy.

The island size distribution is strongly peaked at a diameter of about 300Å. This indicates that all 12°-cones have nearly the same size, therefore reducing the strain in the film to the smallest possible value without generation of defects. Larger cones would be unfavourable since they accumulate more strain energy, smaller cones may be strain relieved to a higher degree. This, however, will only happen under equilibrium conditions during growth of the film. The Ge atoms must be mobile until they find the most favourable lattice site, they even must be able to detach again from a lattice site which they already had occupied. This, however, is usually prohibited by a surfactant at lower temperatures:

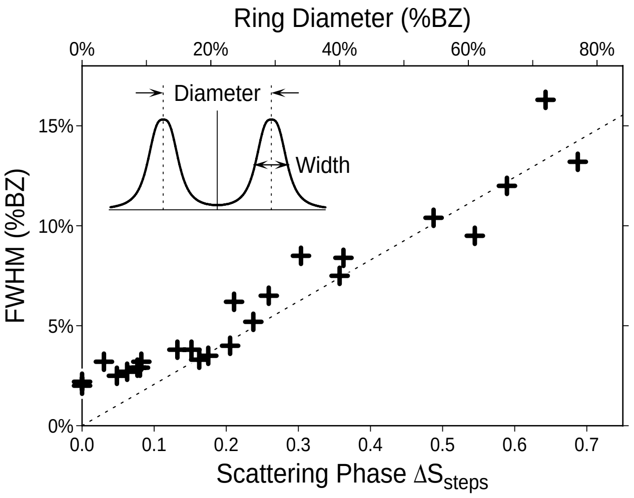

Fig. 5.19 The full width of half maxima of the rings increase linearly with the diameter of the ring or the scattering phase S (both parameters are coupled by the inclined facet rods). From the asymptotic behaviour of the width towards a constant value of 2.2%BZ close to the in-phase condition is estimated as a finite size effect a size of the 12°-cones of roughly ~300-400 Å.

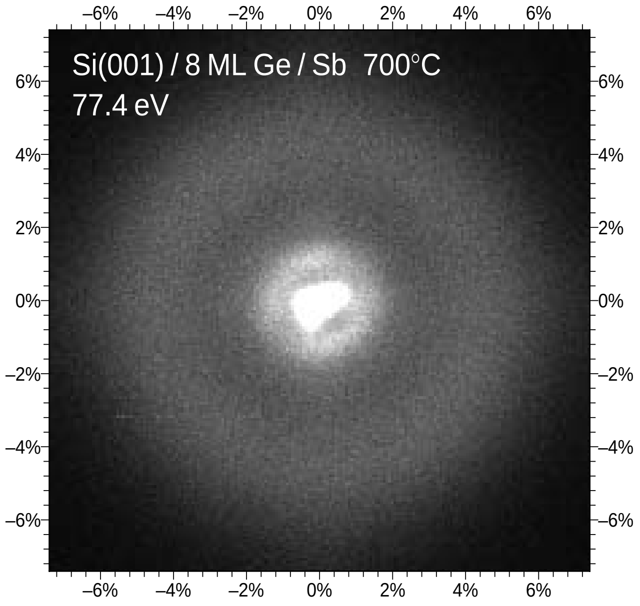

Fig. 5.20 (00) spot high resolution LEED pattern close to the Bragg condition. The small intensity ring around the central spike is caused by the distance distribution of the 12° cones. From the diameter of 1.3%BZ an average distance of 300Å is obtained. The second ring results from the inclination of 12° cones.

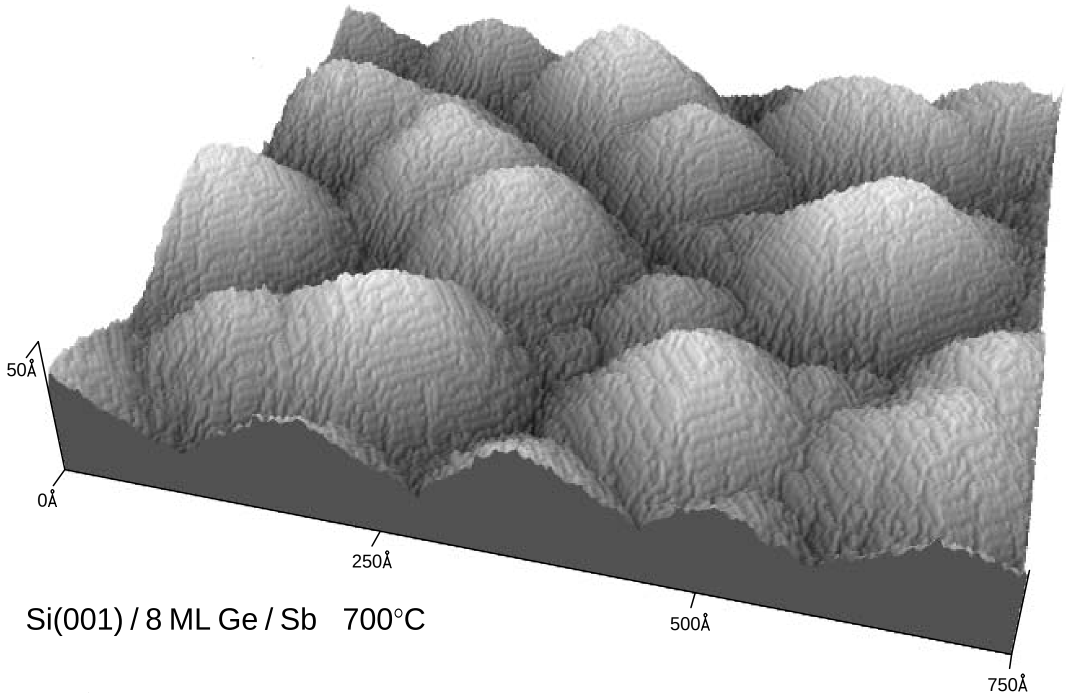

Fig. 5.21 1000 x 700 Å wide STM image of 12° cones with atomic resolution (height scale exaggerated by a factor of two). The cones are composed of (117)- and (105)-type facets. Average size is 300 Å. The entire surface is covered.

an atom is no longer mobile and is trapped, as soon as it is bonded in a lattice site. This selective change of the kinetics is just the way a surfactant forces layer-by-layer growth [194].

Similiar structures are the metastable hut clusters reported by Mo et al. [198] and related selforganised multilayer dot structures [229,230]. "Surface rippling" or "cross hatching" are film instabilities observed in the GeSi alloy system [231-235]

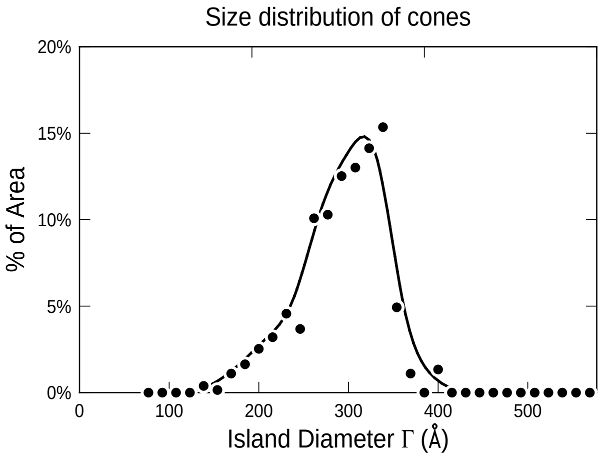

Fig.5.22 The size distribution of the cones show a sharp maximum at 300Å diameter with a complete lack of 12°-cones larger than 400Å. These peaked distribution results from the equilibrium formation process.

5.1.5 Reversible change of island shape

The shape of the Ge-cones depends on the Sb-coverage during growth [202]. At substrate temperatures above 700°C the desorption of Sb (binding energy 2.4eV [235,236]) is already significant and must be compensated by a steady flux of Sb from the effusion cell during Ge deposition. The stationary Sb coverage on the surface is then adjusted by the impinging Sb flux.

Growth of 8 ML Ge at different Sb-fluxes results in the LEED pattern shown in Fig. 5.23. An electron energy of 63 eV has been chosen to clearly show the splitting of the (00)- and (11)-spots into facet-spots, whereas the (10)-spot is close to its Bragg condition and thus sharp. At low Sb flux only [105]-type facets are present with the facet spots moving towards the [100]-directions. Now the entire surface is covered by Ge micro clusters which are solely composed of only [105]-type facets as sketched in the inset of Fig. 5.23(top).

Growth of 8 ML Ge at very high Sb-flux (~100 times larger, ~0.5 ML/sec) also leads to facets on the Ge-film which are now rotated by 45° and are [117]-type facets as shown in Fig. 5.23(bottom). The faint and broad extra spots between the integer order spots are additional facet-spots caused by an inherent double periodicity along the [117]-facets [94,237].

For medium Sb-flux (~1 ML/min, the stationary Sb-coverage has been estimated by Auger to be ~0.5 ML) the diffraction pattern of the circular shaped Ge-cones is observed again. The inclination angle of ~12° is the same as the inclination of the [117]- and [105]-facets. The cones are not simply composed of [105]- and [117]-facets, but include also all other intermediate azimuthal orientations as reflected by the uniform intensity along the perimeter of the ring. We like to point out again, that for all the shapes of the clusters the Ge is always epitaxial grown. Not the entire cluster is rotating by 45°, but diffusion of Ge atoms causes the change in island shape.

Reversibility is the crucial observation needed to confidently interpret these changes of the island shape in terms of thermodynamics. This has been proved using the second electron gun (with gracing incidence) for LEED-observations at 700°C during deposition and after film growth with a Sb-flux to maintain the Sb-coverage. The LEED-pattern is distorted due to the grazing incidence of 30° as sketched in Fig. 5.24(a) in a cartoon of the reciprocal space. The up- and downward opened cones result from the 12°-cones on the surface. The observed LEED pattern could be constructed by the intersection of the cones in reciprocal space with the Ewald-sphere (area of 2D-scan) [94].

Growth of 8 ML of Ge with medium Sb-flux results again in the formation of cones. Those are apparent as distorted ellipses in Fig. 5.24(b). At elevated temperatures this structure is only stable by keeping the Sb-flux constant (compensating losses of Sb due to desorption). Increasing the Sb-flux changes the 12°-cones towards islands with [117]-facets as shown in Fig. 5.24(c). With the reduction of the flux to the old value, the intensity rings form again as visible in Fig. 5.24(d). This transition has been repeated a couple of times as shown in Fig. 5.24(e-h). Reducing the Sb flux to even lower values results in the formation of [105]-facets as shown in Figs. 5.24(i,l). However, this transition is no longer perfectly reversible. An increased Sb-flux still results in the formation of [117]-facets but which are broader and more fuzzy than in the transitions before (Fig. 5.24(j). The generation of strain relieving defects or a change of the aspect ratio of the islands which is also observed for the hut clusters (aspect ratios of 1:5 or more are found [198] may hinder the reversible transition.

The change in the shape of the islands is associated with a diffusion of Ge atoms. Because the [105]-clusters, the 12°-cones, and the [117]-clusters all have the same facet inclination, diffusion along one level around the clusters would be sufficient for the transition of shape. This process may be mediated by the diffusion of kinks and is limited by kinetics.

The dynamics of this transition were observed by a measure of the intensity of a [117]-facet spot during changes of the Sb-flux (using a shutter) from ~1 ML/sec to zero and vice versa (Fig. 5.25}). The data points have been recorded every 500 ms. The rapid changes of the intensity in less than a second points to a very fast ad- and desorption of the Sb and the accompanied conversion of the island shape.

The change of island shape is obviously induced by a difference in Sb-coverage of the [105]-facet with the lower Sb coverage and the [117]-facet with the higher. At medium Sb flux both facets coexist. Due to the high temperatures the edges between the facets are rounded [189], all orientations between the facets are stable and form circular shaped 12°-cones.

The [105]-facets show no reconstruction spots in the LEED-pattern, and therefore, must have a unit cell size of

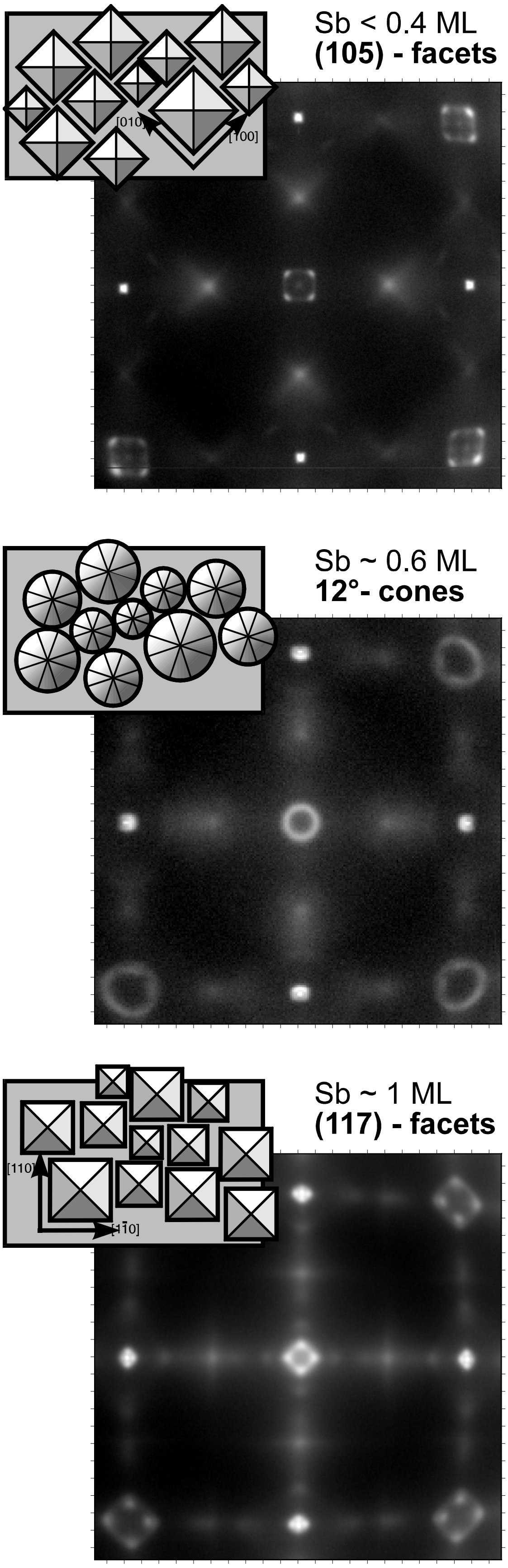

Fig. 5.23 LEED patterns of Ge nano clusters for different Sb coverages. The shape changes from islands composed of [117]-facets for high Sb-coverage (bottom) via circular, flat cones with an inclination of 12° (middle) towards islands rotated by 45° and composed of [105]-facets for low Sb-coverage (top).

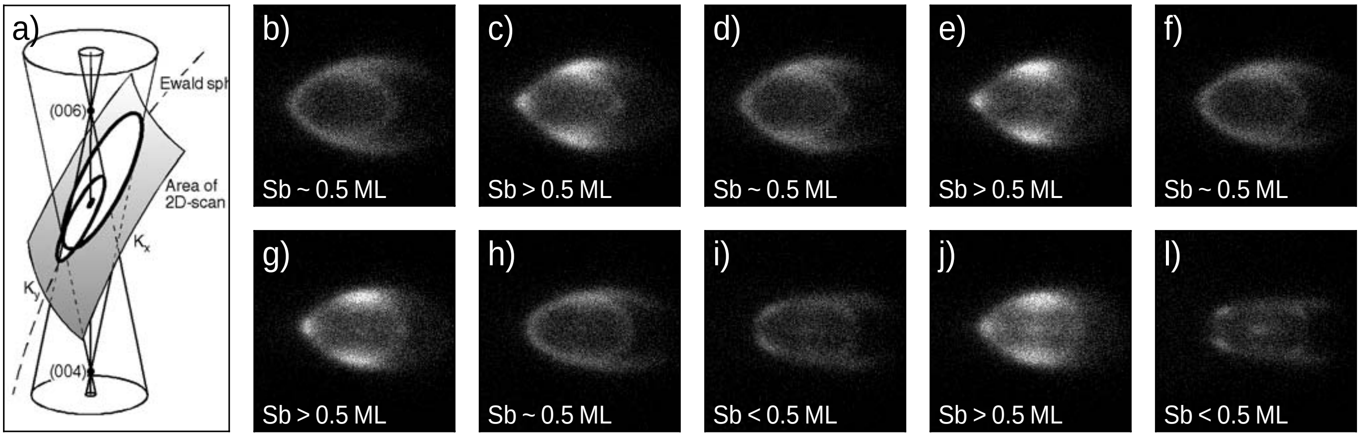

Fig. 5.24 Reversibility of the island shape as function of the Sb coverage has been proved by variations of the Sb flux. The cones (b) are transformed into [117]-pyramids (c) and vice versa (d) a couple of times (e-h). Reducing the Sb-flux to very low values [105]-facets form (i,l). The LEED pattern is distorted (a) due to the gracing incidence scattering geometry used.

$a_0\times2.5a_0$ (a_0 is the lattice constant). Without further assumptions, two Sb atoms are the minimum coverage necessary per unit-cell, which is a coverage of 0.4 ML. The two Sb atoms are bonded each with three electrons to a kink site of the [100]-step of the [105]-facet, thus saturating six of ten dangling bonds per unit cell as shown in Fig. 5.26.

The [117]-facets have a double periodicity along the facet [95,237] with an unit cell size of $a_0/\sqrt{2}\times7a_0/\sqrt{2}$. Assuming the saturation of all dangling bonds by Sb (strongest decrease of surface free energy) together with the missing reconstruction perpendicular to the facets result in the model shown in Fig. 5.26. The single A- and B-type [110]-steps form double steps as also observed for Si(001)-faces inclined more than 4°. The saturation coverage of Sb is 6/7 of a monolayer.

These simple structure models explain the observed change of island shape with coverage. The driving force is the difference in surface free energy which is strongly dependent upon the number of dangling bonds. Upon high Sb flux (compensation of desorption) all dangling bonds could be saturated and the [117]-facets form. Following our structure model, it is not possible to saturate all dangling bonds of the [105]-facet at even very high Sb-fluxes. Per [105]-unit cell two dangling bonds would be unsaturated. Therefore, the [117]-facet allows the *largest decrease of surface free energy*. With decreasing Sb flux Sb desorbs (probably from the sites where it forms Sb-dimers). In this situation the decrease of surface free energy per Sb-atom becomes the relevant value. This value is obviously larger for the [105]-facets because one single Sb atom can saturate three dangling bonds. On the [117]-facet one Sb atom is, on average, only saturating 7/3 dangling bonds. Thus, in the low coverage regime the *energy gain per Sb atom* is larger for the [105]-facets.

Of course the facet- or 12°-cone covered surface is not the true equilibrium surface which forms independent of the history of the sample. If large 3D-clusters are created during growth, they could not be dissolved by applying Sb; they remain stable. However, the formation of 12°-cones is also observed and results obviously from the transformation of hut clusters and the 3 ML thick coherent wetting layer.

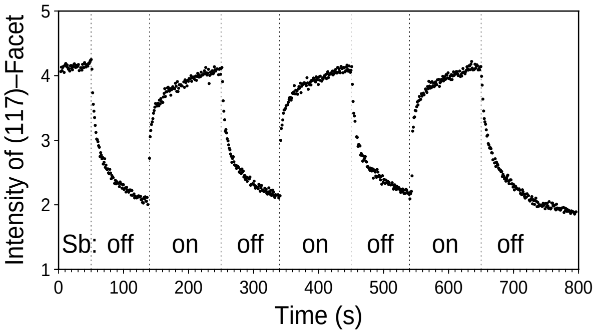

Fig. 5.25 The island shape changes reversible from [117]-facets towards 12°-cones. Plotted is the intensity of a [117]-facet spot during changes of the Sb flux from ~1 ML/sec to zero and vice versa by a shutter. The intensity has been recorded every 500 ms.

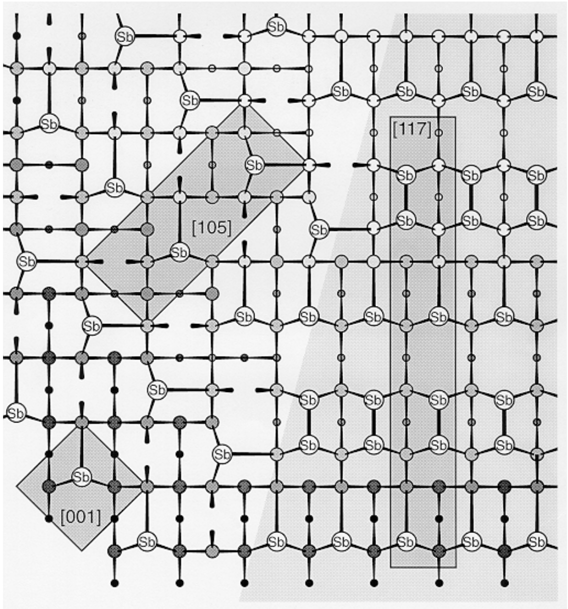

Fig. 5.26 Simple structure model for the cones. [105]-facet (left side) with Θ_{Sb} = 0.4 ML and [117]-facet (right side) with Θ_{Sb} = 6/7 ML. The [117]-facets show their saturation coverage: no dangling bonds remain. Unit cells are plotted as grey rectangles. Grey shades of the Ge atoms indicate the level of the atoms.

5.2 Plastic strain relief - defect formation

The use of surfactants hinders the formation of 3D-clusters but it could not could compensate the increasing strain energy in the growing Ge film. Finally the strain must be relieved by the formation of defects and dislocations. This plastic relaxation is also observed for the growth of Ge on Si(001). The Ge films show a defect density of up to 10^{12}cm^{-2} [199].

Strain relieving defects are generated at a coverage around 11 ML for a growth temperature of 520°C [95] as also already shown in Fig. 5.13. The strong decrease of the intensity at a Ge-coverage of ~10-12 ML reflects the generation of defects and the mosaic spread of the spot. This value for the critical coverage agrees well with observations by x-ray measurements [206]. Those measurements also show that the Ge-film is not at all relaxed to the Ge-bulk lattice constant. In addition to this the (20)-Ge Bragg peak (observed during the x-ray study) was also strongly broadened which reflects the occurrence of a variety of different lattice spacing, i.e. defects in the film.

Using As instead of Sb as surfactant the lattice strain is relieved at a coverage of ~16-18 ML by the generation of V-shaped defects [192,203,205]. This value of the critical coverage is also confirmed by the LEED results shown in Fig. 5.13.

The LEED-pattern of a 40 ML thick Ge-film grown at 500°C with Sb as surfactant is shown in Fig. 5.27. All superstructure and integer order spots are strongly broadened for all observed electron energies. This is in contrast to the LEED-patterns of the 8 ML Ge-films where the in-phase conditions of scattering have been observed in very narrow spots, as seen in Fig. 5.3(b) which has been recorded at the same scattering condition as Fig. 5.27. The pronounced in-phase conditions have reflected the perfect epitaxial growth for the 8 ML films.

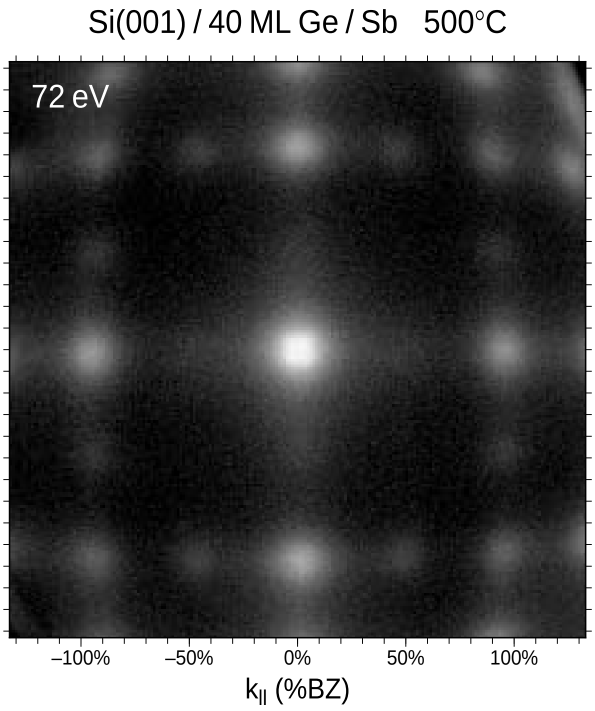

Fig. 5.27 LEED-pattern at 72 eV of a 40 ML thick Ge film grown at 500°C using Sb as surfactant. All spots are strongly broadening independent on the scattering condition.

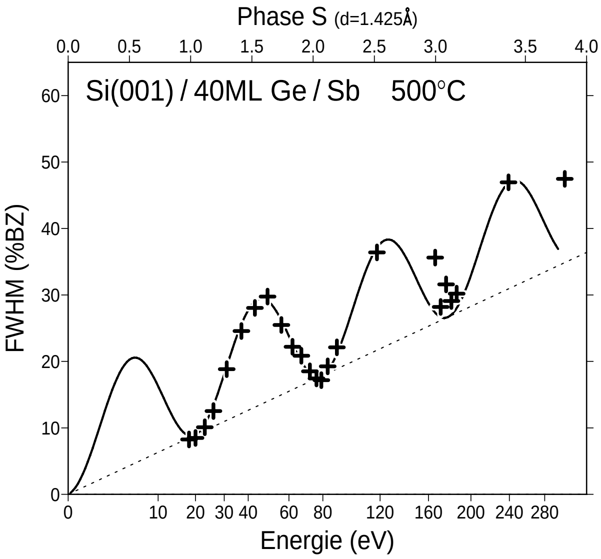

Fig. 5.28 Mosaic spread and vertical roughness of the 40 ML thick Ge film grown at 500°C. The width of the (00)-spot at the in-phase conditions increases linear with the scattering phase *S*. The variation of the width due to vertical roughness of the surface is superpositioned which is observed as (1-cos 2π*S*) curve.

For the 40 ML thick Ge-film the spots are always strongly broadened, even at the in-phase conditions. The FWHM of the (00)-spot is plotted in Fig. 5.28 as function of the scattering phase *S*. The width at the in-phase conditions (integer values for *S*) increases linear with *S*. Additionally to this the width varies periodically with *S* due to surface roughness.

The linear increase of the width (at the in-phase conditions) points to a broadening caused by mosaics in the Ge-film. The Ge-film is no longer one single crystal but consists of small single crystal areas, which are tilted randomly by small angles against the (111)-surface. Each of the small mosaics cause its own diffraction pattern. Incoherent addition of these diffraction patterns causes the broad LEED-spots. The width of the spots increases linearly with the vertical scattering vector k_z or the scattering phase *S* respectively. This behaviour in reciprocal space is shown in Fig. 5.29 for the (00)-, (1/2 0)-, (10)- and (11)-spot. The k_z-axis is compressed by a factor of two. The width of the spots are plotted as broad bars. The thin solid lines envelope the FWHM of the spots caused by the mosaics. We estimated a standard deviation of the tilt angle of $\alpha \sim 0.9°$ of the mosaics. The dotted lines show the modified Ewald spheres. Especially for the (00)-spot the additional variation due to the surface roughness could be observed.

The use of the normalised central spike intensity for the evaluation of the vertical roughness is no longer possible because most of the intensity of the central spike is of course also broadened by the mosaic spread. However, from the additional increase of the FWHM at the out-of-phase condition at $S = 1.5$ an average terrace width of 4.0 u.c. is derived. This value is larger than for the 8 ML thick Ge-films because the generation of defects has relieved most of the strain which has been the driving force for the micro-roughness of the pseudomorphic films.

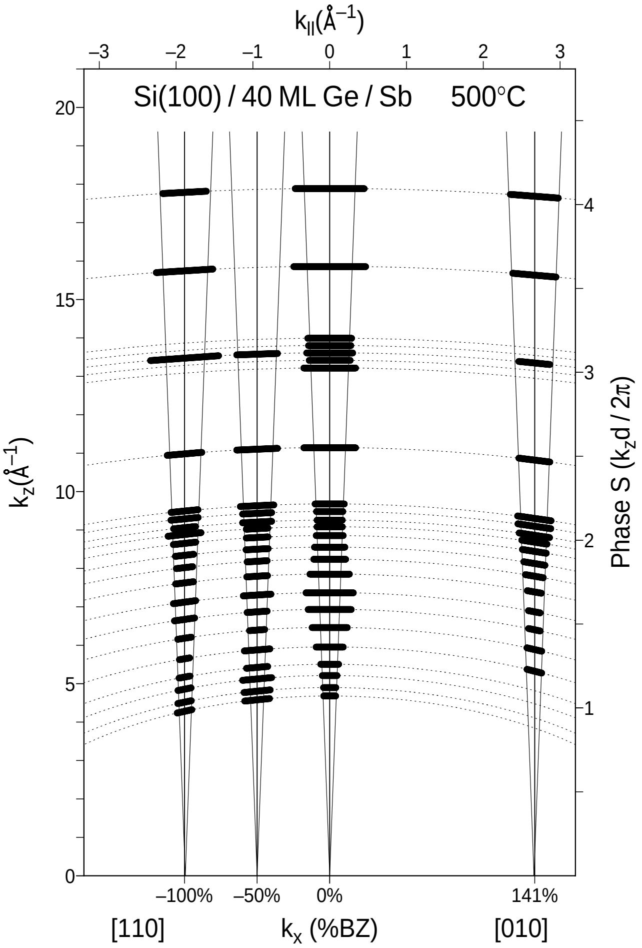

Fig. 5.29 Mosaic spread of the 40 ML thick Ge film grown at 500°C. The FWHM of the (00)-, (1/2 0)-, (10)- and (11)-spot are plotted as thick bars in reciprocal space. The width increases linearly with the vertical scattering vector k_z or the scattering phase *S* respectively. Surface roughness produces the additional increase of the width at the out-of-phase conditions. The k_z axis is compressed by a factor two.

6. Surfactant mediated growth of Ge on Si(111)

With Sb surfactant mediated hetero growth of Ge on Si(111) defect free and relaxed Ge films of arbitrary thickness could be grown [194, 238, 239]. A drastic improvement of the quality of the Ge films is achieved: islanding is prevented and smooth and continuous Ge films can be grown. The lattice mismatch of 4.2% is adjusted in a peridoic array of dislocations entirely confined to the interface between the Si substrate and the Ge film [93, 151]. The dislocation network is generated at a Ge coverage of 8 ML (monolayer, 1 ML = 7.8×10^{14} atoms/cm^2) as determined by means of medium energy ion scattering and high resolution transmission electron microscopy [238, 239].

Details on the experimental setup and sample preparation could be found elsewhere [93]. In brief, the Si surface has been precovered with a Sb adsorbate layer prior to the Ge deposition at 600°C. Sb forms a well ordered $(\sqrt{3}\times\sqrt{3})R30°$ trimer reconstruction on the T_4 site. A small Sb flux compensates Sb desorption and maintaines the surfactant coverage [240]. The Ge is deposited from an e-beam heated carbon crucible. The Sb segregates to the surface and floates on top of the growth front with extremely low incorporation [241].

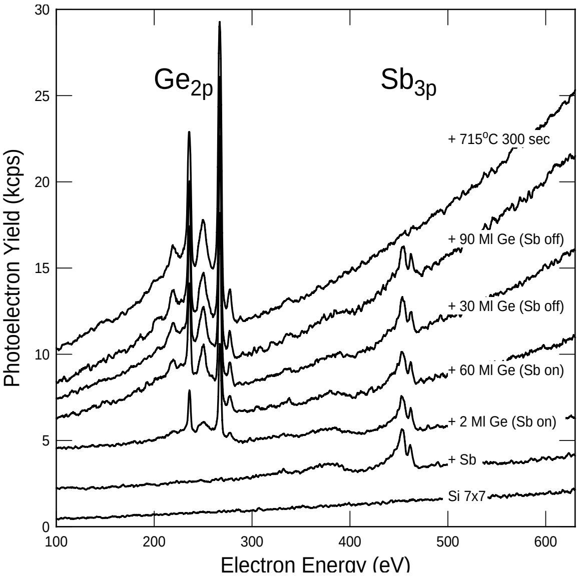

Fig6.1: X-ray photo electron spectroscopy spectra show with the Ge 2p- and the Sb 3p-signal the efficient segregation of the surfactant Sb to the surface. 60 ML of Ge have been grown with co-deposition of Sb, only 1~ML Sb adsorbs at the surface. Additional 120 ML of Ge have been grown without co-deposition of Sb. The constant height of the Sb peak reflects complete segregation. A maximum incorporation concentration of less than 2 × 10^{19}cm^{-3} i is estimated. Flashing the sample to 715°C for 5~minutes removes the surface Sb

The efficient segregation has been proved by in situ x-ray photoelectron spectroscopy (XPS). Photoelectrons have been detected normal to the surface.The XPS spectrum of the Ge 2p- and the Sb 3p-signal is shown in Fig. 6.1 for the bare Si-surface (only background), after Sb-adsorption at 600°C (only Sb-peak visible) and after subsequent deposition of Ge at the same temperature (Sb- and Ge-peak). Up to a Ge coverage of 60 ML Sb has been coevaporated during growth. Only one monolayer Sb (the saturation coverage) sticks at the surface. Excess Sb desorbs immediatley.

Additional 120 ML of Ge have been deposited without Sb-flux. The constant height of the Sb peak reflects complete segregation. A maximum incorporation concentration of less than 2 × 10^{19}cm^{-3} is estimated. Flashing the sample to 715°C for 5 minutes removes the surface Sb. Unfortunately, the Ge film is now rough, as can easily be established by visual inspection.

Recent results obtained by secondary ion mass spectroscopy and electrical characterization shows that the incorporation level is three orders of magnitude below the solid solubility of Sb in Ge: doping levels below 10^{16} have been found for high temperature SME at 700°C [241]. The high quality of the Ge films manifests also in the highest electron mobilities ever found for relaxed Ge films on Si substrates [241, 241].

6.1 Elastic relaxation

SPA-LEED has been used to determine the change of surface morphology and lattice parameter *during* the different stages of growth and strain relief. Of special importance will be the interplay between the elastic and plastic strain relief mechanism (dislocations): The lattice constant of the Ge layers has to change from pseudomorphic and strained to the bulk value of relaxed Ge.

Evidence of epitaxial and non islanding growth is seen in Fig. 6.2 (a) in the intensity oszillations of the central spike of the (00)-spot during Ge deposition. The oszillations are also evidence for a layer-by-layer growth mode. The electron energy has been set close to the out-of-phase condition. During layer-by-layer growth the incomplete layer at half a layer coverage results in minimum central spike intensity, whereas electrons diffracted from the complete flat layer causes strong central spike intensity [101, 169].

The occurrence of the smooth pseudomorphic Stranski Krastanov layer of 3~ML Ge thickness is clearly seen in the strong intensity maximum. With higher coverage the intensity drastically decreases reflecting an increasingly rough surface. Surprisingly the oscillations return after growth of 10~ML Ge with regaining intensity, indicating a more and more flat and smooth surface. After growth of 100~ML Ge a sharp and brilliant (2x1)-LEED pattern reflects layer growth of Ge, with a terrace width larger than 100 atoms and only kinetically limited. The period of the later oscillations corresponds to a bilayer growth mode of the Ge-film (1 period = 14.4×10^{14}atoms cm^{-2}).

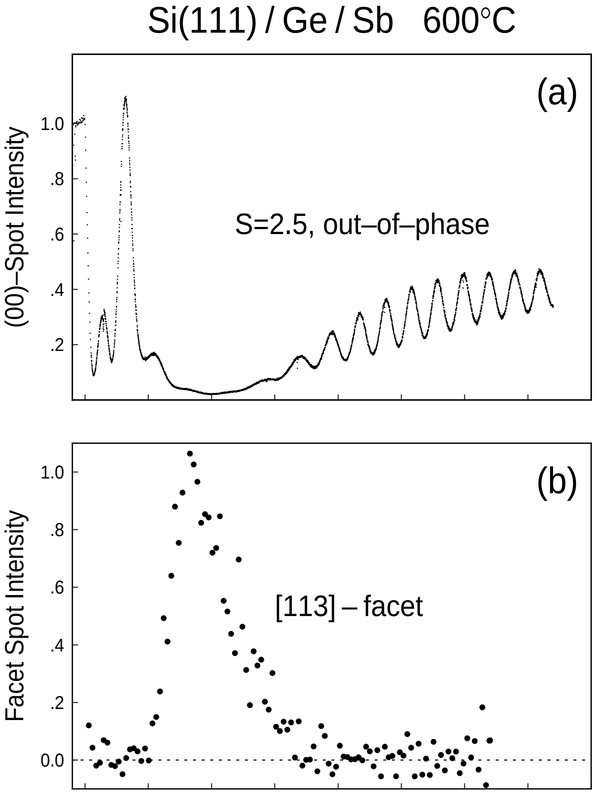

Fig. rev_g20.exg: (a) Central spike intensity oscillations of the (00)-spot during growth. The maximum at 3~ML coverage results from the Stransk-Krastanov layer. The later oscillation shows a bilayer (14.4×10^{14}atoms cm^{-2}) period. (b) The [113]-facet spot intensity shows a peak at 8~ML coverage where also the strain relieving defects are generated. Without the strain as driving force the micro roughness smoothens out resulting in a decreasing facet intensity

The surface morphology in the rough stage becomes apparent after interruption of Ge deposition at 6~ML. The LEED-pattern is shown in Fig. 6.3 as a 2d-scan at 40~eV with the (00)-spot, the nearest integer order spots and a few (2x1)-spots. Very broad and elongated spots are additionally visible between the integer order spots. The position of these broad spots varies strongly with the electron energy indicating facets at the surface. The components of all the facet spots move with increasing energy into one of the three [11-2] directions. Therefore the surface contains facets tilted in only three directions - as a triangular pyramid.

From the dependence of spot position with scattering vector k_z the orientation of the facets has been derived. The positions in reciprocal space of the facet spots are plotted in Fig. 6.4 with oval dots. The extension corresponds to the width of the spots, the thickness roughly to the intensity. The most intense facet spots agree well with a [113]-type orientation. The in-phase conditions of scattering are clearly observed with sharp intensity maxima of the (00)-spot as a function of energy. Those Bragg positions are marked by bold circles at the (00)-rod and reveal a layer distance d of 3.27±0.02Å, exactly matching the Ge lattice constant. This vertical relaxation surprises, since the Ge film is still pseudomorph and a tetragonal distortion would be expected with an increase of the vertical layer distance.

The very elongated form of the spots in reciprocal space reflects a similar but rotated structure of the facets in real space as sketched in Fig.m.eps.The narrow width of the facet spot corresponds to a long extension of the facet at the surface. The broad direction of the spot corresponds to the narrow extension of the facet. From the width in reciprocal

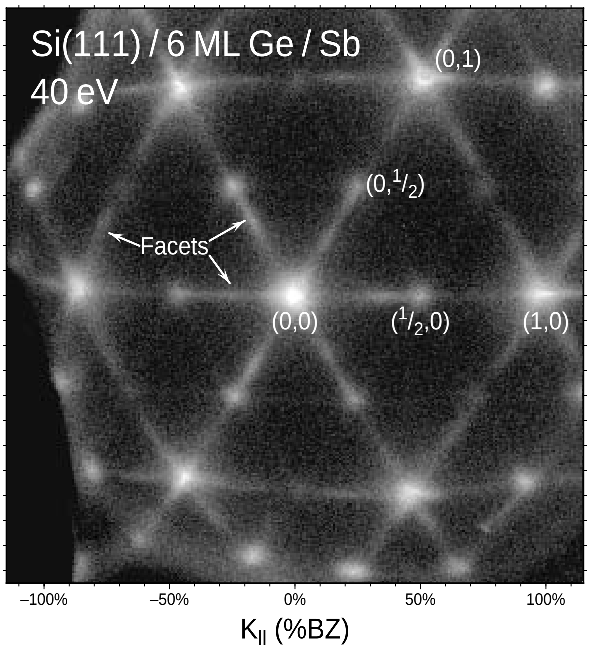

Fig. rev_g30.exg: LEED pattern after growth of 6 ML Ge with the integer order spots, (2×1)- superstructure spots and broad and elongated spots resulting from [113]-type micro facets. High background reflects a very rough surface.

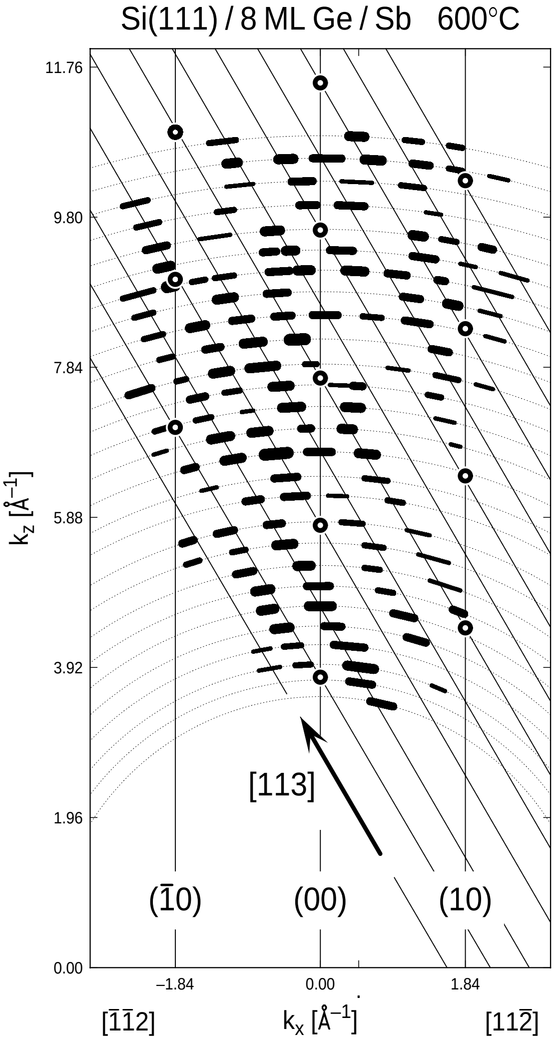

Fig. 6.4. Facet spot position in reciprocal space. The length of the ovals corresponds to the width of the spots, the thickness to the intensity. The most intense facet spots agree well with a [113]-type orientation. The facets exhibit a (2$\times$2)-reconstruction, doubling the number of facet rods. The position of the Bragg conditions are marked with bold circles and reveal a layer distance of 3.27\AA, exactly matching the Ge bulk lattice constant

space a size of the facets of 15-25Å times 60-100 Å is estimated. The elongated form of the facets could easily be understood assuming triangular pyramids constructed of three facets showing the three possible [113]-type orientations. The entire surface is covered with facets, since most of the intensity of the Brillouin zone is confined to the facet spots.

STM investigations by Meyer et al. [243] show these pyramids irregularly arranged over the surface, with different sizes and heights. The STM shows most of them truncated with a flat top for coverages below 8 ML. The typical size of one of the micro pyramids is in very good agreement with the LEED analysis.

This formation of the micro rough surface is again an efficient way to relieve part of the strain in the Ge film during the pseudomorphic growth regime. The small pyramids allow the Ge in the upper layers to relax nearly completely towards the bulk lattice constant. This mechanism also explains, that the layer distance in the pyramids is not increased: the driving force for a tetragonal distortion, the strain, is nearly completely relieved by this lateral relaxation.

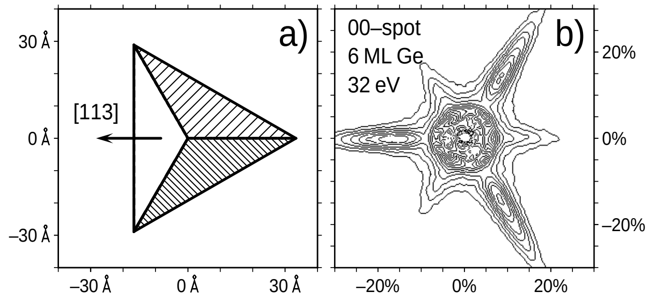

Fig. 6.5. The elongated from and size of the facet spots in reciprocal space reflects the shape and size of the micro facets. Three of the [113]-type facets could be arranged to a micro pyramid

The formation of the facets during growth could be studied by recording the intensity of one facet spot as function of coverage as shown in Fig. 6.2(b). The intensity steeply arises after 5 ML of Ge, with a maximum at 8 ML, i.e. the coverage, where misfit relieving defects were introduced [238], and vanishes at 20 ML. The growth of the pyramids is limited by their distance to each other and their facet orientation. A maximum volume is reached after the total amount of 8 ML Ge, corresponding to a base length of 20-30 unit meshes and a height of 8-12 ML. At this coverage the pyramids start to coalesce by filling the trenches between them.

Those lattice sites, however, exhibit the highest stress and are the most unfavourable growth sites. Therefore it is not surprising to find the nucleation of misfit adjusting defects in this stage of growth. As soon as defects are generated and relieve strain, the driving force for the roughening of the growth front (the stress) has vanished and

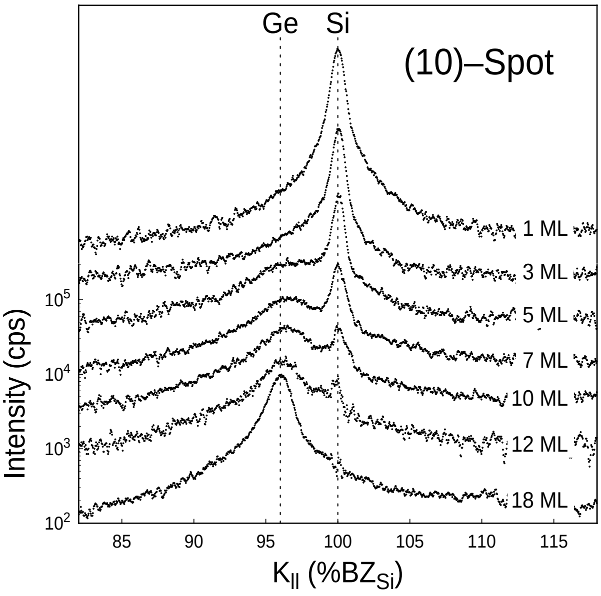

Fig. 6.6. Radial scans through the (10)-spot show the change of the lateral lattice constant from Si- towards Ge-bulk value. A shift is already apparent in the pseudomorphic regime below 8~ML, reflecting the partial lateral relaxation of the Ge in the micro pyramids towards the Ge bulk lattice constant

the surface starts to smooth. However, the pyramids could *not* dissolve by diffusion of the atoms since those are trapped in sub-surfactant sites. The stable pyramids are overgrown by filling the trenches between the pyramids [93] as also observed in Fig. 6.2(b) in the slowly decreasing intensity of the facet spots. .

The increase of the distances between the Ge atoms towards the bulk value (due to the elastic strain relaxation) is observed in a shift of the position of the (10)-spot towards the (00)-spot. In Fig. 6.6 radial scans through the (10)-spots are plotted as function of coverage. The position of the Si and Ge(10)-spot position is marked by dashed lines. With increasing Ge coverage the intensity of the Si (10)-spot decrease strongly to zero. Already during the pseudomorphic growth regime a very broad spot arises at 97.5%BZ slowly moving closer towards the (00)-spot. This broad peak is caused by Ge atoms with atomic distances already increased towards their bulk value. The lateral lattice parameter of the Ge atoms on top of the pyramids is 2.5% larger than the Si lattice constant of the substrate. The elastic strain relief mechanism resulting in the micro roughness could be directly observed.

At 12-18ML the Ge-(10)-spot appears at the position expected for the Ge-bulk lattice constant. This reflects the relaxed Ge-film which shows almost the Ge bulk lattice constant. The misfit is adusted by strain relieving dislocations.

6.2 Dislocation network

Also the next step of strain relief, the generation of misfit relieving dislocations, is observed with SPA-LEED as shown in Fig. 6.7. Of course the dislocations below a 20 ML thick Ge film could not be detected directly due to the finite penetration depth of the electrons. Each dislocation, however, is surrounded by a strain field which elastically distorts the crystal lattice. These strain fields propagate up to the surface and result in a periodic height undulation with a corrugation of up to 1 Å. Such a height undulation due to a burried dislocation network has also been observed by STM [243-245].

Low energy electrons with an energy in the range of 10eV up 400eV corresponding to a wavelength of 4Å to 1Å

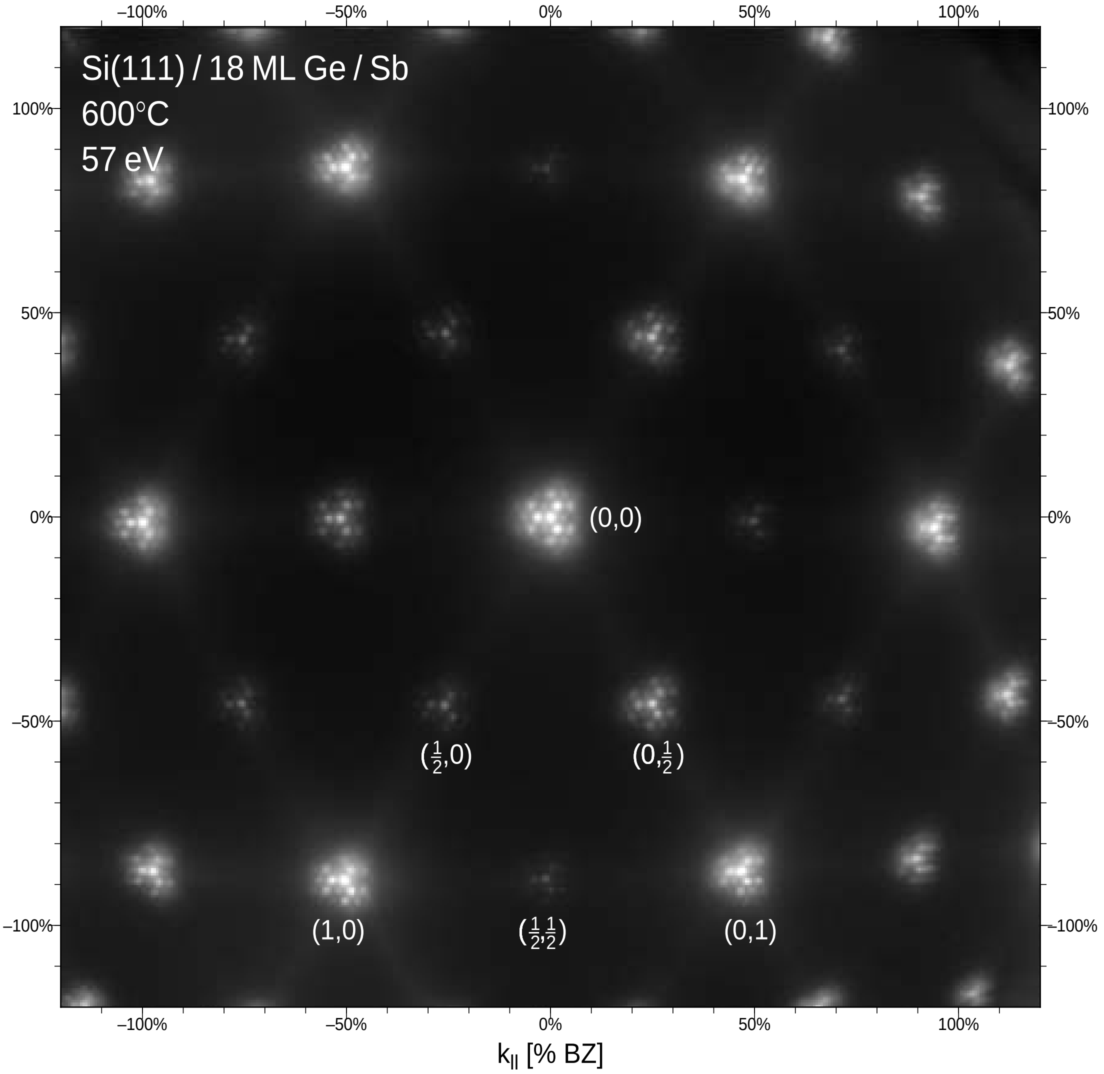

Fig. 6.7. LEED pattern after growth of 18~ML Ge with Sb as surfactant. All integer order and (2×1)-superstructure spots are split into a hexagonal array of satellites. The satellite spots have a separation of 3.20\% of the Brillouin zone, i.e. reflecting an extra periodicity of 31 lattice units at the surface. The strain fields of the interfacial dislocation network give rise to a periodic height undulation at the surface acting as 2-dimensional phasegrid for electrons

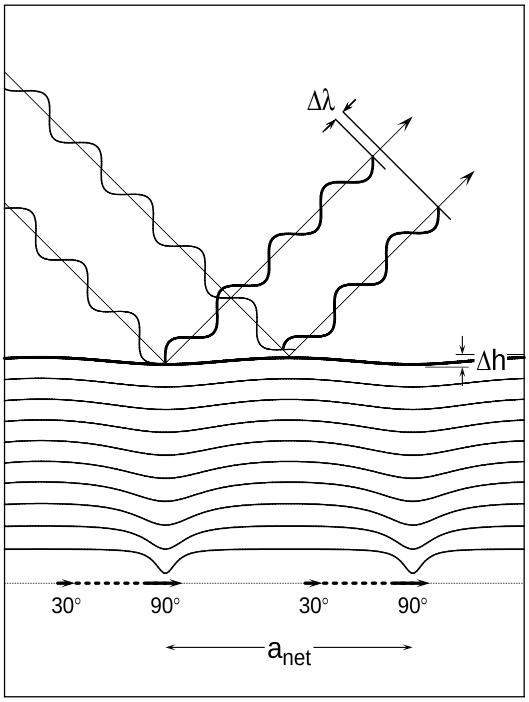

Fig. 6.8. A vertical cut of the surface shows the Shockley partial dislocations (arrows) and the corresponding stacking faults (dotted lines) in the interface plane. The elastic deformation of the lattice planes in the film and the resulting surface undulation is shown in an exaggerated height scale. The electrons scattered from the surface undergo a small path length difference resulting in a phase difference. The surface acts as a phase grid.

are sensitive to this height modulation of the surface. They undergo an additional path length difference causing a phase difference as sketched in Fig. 6.8. The periodic height undulation acts as a 2 dimensional phase grid for electrons which, of course, results in a splitting of each LEED spot into a hexagonal array of satellites as shown in Fig. 6.7 for a Ge film of 18~ML thickness.

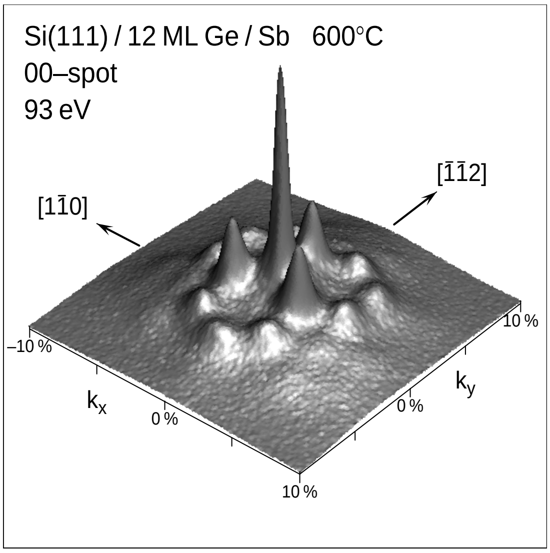

Fig. 6.9. Up to 5 orders of satellite spots are visible in this 3D-plot of the LEED intensity reflecting the periodic arrangement of the interfacial dislocation network. A linear intensity/height scale has been used. Most of the intensity is confined in the satellite spots on the expense of the central spot

Not only the integer order spots show the satellites but also the (2×1)-superstructure spots. The same pronounced threefold symmetry is observed for all spots. Up to five orders of satellites are visible as shown in the semi 3D-intensity plot in Fig. 6.9 which reflects the periodic arrangement of the dislocations at the interface.

The separation of the satellite spots of 3.2±0.1%BZ corresponds to a periodicity length of 104Å of the dislocation network. The satellite spot separation agrees perfectly with the theoretically expected value of 3.20%BZ [93, 151] assuming strain relief by 60° dislocations [238, 239].

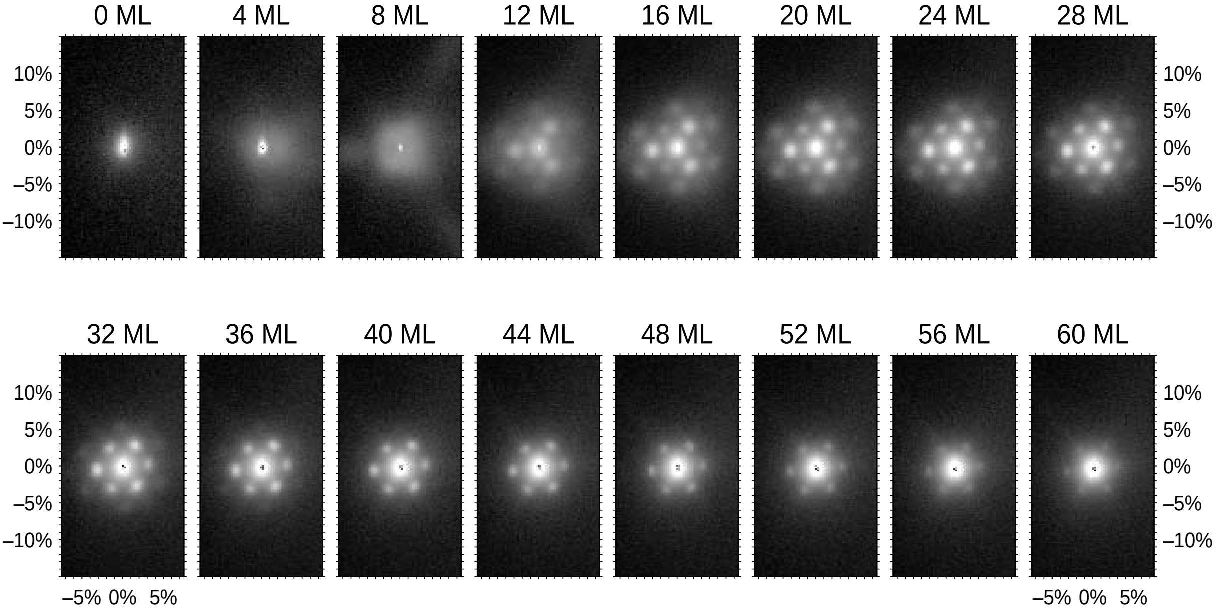

Fig. 6.10. The evolution of the dislocation network is observed in this series of 2d-scans of the satellite spots during deposition. The network starts to form at 8 ML and is completed at 18 ML. The surface undulation vanishes with increasing coverage. Nearly no variation of the spot distance is observed. The spots get sharper with increasing coverage (compare 12 Ml with 44 ML, a logarithmic scale has been used to demonstrate all features).

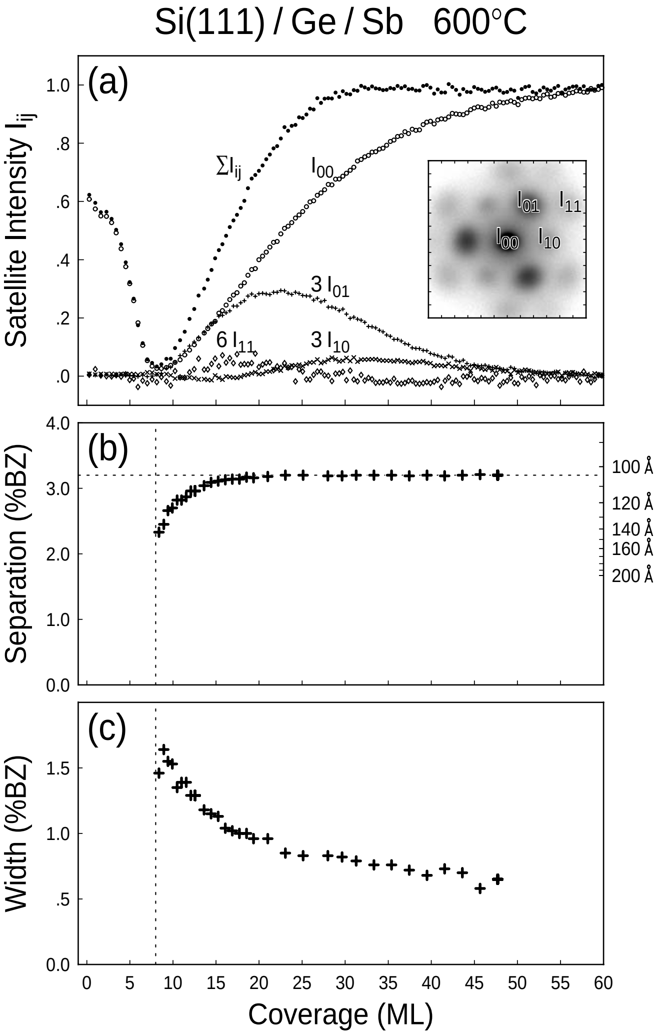

Fig. 6.11: (a) Integral intensity of the strongest satellite spots during deposition. Plotted is the sum of intensity in equivalent spots. The formation of the dislocation network starts at 8 L, as seen at the steep rise of I01. The satellites are detectable up to 60 ML film thickness. The change in shape of the surface undulation shifts the maxima of I10, I01 and I_11 to different values. (b) The satellite spot separation is determined by the average distance of the dislocations in the network. The Ge-film is immediately relaxed to 70% at the onset of disloction formation. A complete adjustment of the lattice constants is achieved after 18 ML, resulting in a spot splitting of 3.20%BZ, i.e. an average distance of the dislocations of 104Å. (c) The decrease of the FWHM of the (01)-satellite spot reflects the process towards higher regularity in the dislocation network caused by the increasing interaction of the dislocations due to the increasing interaction of their strain fields.

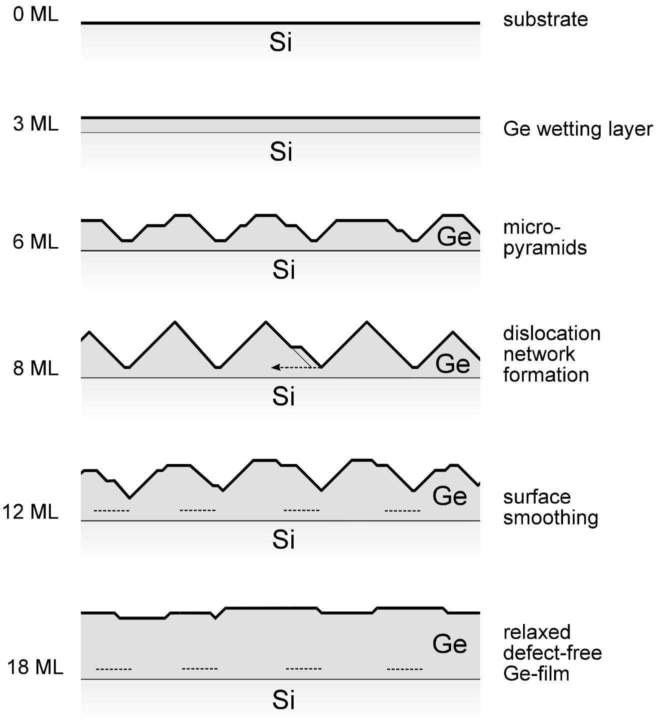

Fig. 6.12: Principal sketch of the surface structure during the different stages of growth. The Stranski-Krastanov layer is completed at 3 ML. With increasing coverage the strain in the Ge-film is relieved by the formation of micro pyramids, which are completed at 8 ML. As soon as the pyramids start to coalesce, strain relieving defects are created at their base, finally arranging to the interfacial dislocation network, composed by areas without and with stacking fault: dashed lines. Without the strain as driving force for the roughness the surface smoothens again (12 ML), finally leaving the Ge-film relaxed and defect free at 18ML}

The process of strain relaxation by introduction of dislocations is now easily observed by recording the satellite spots during deposition as shown in Fig. 6.10. The first satellites are already observed at 8~ML of coverage. They are seen best around 20~ML and are detectable up to 60~ML of coverage.

The intensity of the central spike and the most intense satellites is plotted as function of coverage in Fig. 6.11(a). The steep decrease of intensity around 8~ML again reflects the formation of the micro rough surface with all intensity confined in facet spots. The varying relative intensities between the different orders of satellites is understood and reflects the changing shape of the surface undulation with film thickness [151.]With increasing film thickness the strain fields of the disloctions overlap more and more and finally the surface height undulaton is smoothed out [93, 151].

The most important information concerning the strain relief process is the separation of the satellite spots which is determined by the average separation between the dislocations. In Fig. 6.11(b) the separation in reciprocal lattice units is plotted as function of the deposited coverage. The right scale gives the average distance of the dislocations in Å.

Surprisingly the Ge film is already at a coverage of 8 ML strain relieved within 70% of the Ge bulk value. Within only 10 additional monolayers the distance between the dislocations reaches its final value of 104 Å and the Ge film is completely strain relieved to the bulk lattice constant.

During the generation the dislocations are irregular arranged. This results in a broadening of the satellite spots. With increasing thickness of the Ge film the network becomes more regular as observed in the decreasing width of the satellites plotted in Fig. 6.11(c). The strain fields of the dislocations interact more and more with increasing film thicknessc. This results in an increasing effective repulsive force between the dislocations which is finally the reason for the regular arrangement into a network

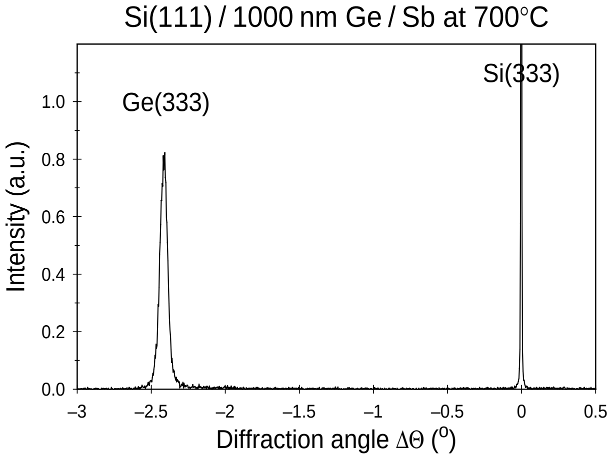

Fig. 6.13. X-ray diffraction spectra of the (333)-Bragg peak of a 1000 nm thick Ge film. At lower angles the Ge peak is seen. The vertical lattice constant is in perfect agreement with bulk Ge.

The introduction of the first dislocations for a flat and continuous hetero-film is expected for a *critical thickness* [246] of about 10 ML for the GeSi-system. After generation of the first dislocation, strain has to be accumulated again until the next dislocation could be introduced. A slowly exponential strain relaxation of the Ge film is expected - always with some residual strain, because always enough strain has to accumulated to generate the next dislocation loop.

In contrast to this we observe the complete relaxation of the Ge film to the bulk lattice constant already at a thickness of 20 ML.

This very efficient strain relief process is attributed to the interplay between the micro rough surface in the pseudomorphic regime and the generation of dislocations. Instead of a smooth and continuous surface we observe a rough surface in the coherent stage of growth due to the formation of micro-pyramids in order to relieve strain as sketched in Fig. 6.12.

As soon as the pyramids start to coalesce, dislocations are introduced at their base. Those are the lattice sites with the largest stress. The dislocation glides in the (111)-plane below the micro-pyramid. Because the Ge film is quite open and rough the strain relaxation due to a dislocation below a micro-pyramid keeps localized and could not disperse further than this single pyramid.

With the next deposited Ge atoms all the other pyramids are also strain relieved by generation of dislocations. The micro rough Ge-film provides innumerous nucleation sites for dislocations which is a requirement for the effective formation of the dislocation network. Due to the high growth temperature the dislocations are mobile enough to rearrange themselve into the well ordered network.

After the complete relaxation Ge films of arbitrary thickness could be grown. The surfactant is principally no longer necessary because there is no driving force for islanding anymore. However, the Sb sticks at the surface at the growth temperature of 600°C. Flashing the sample to

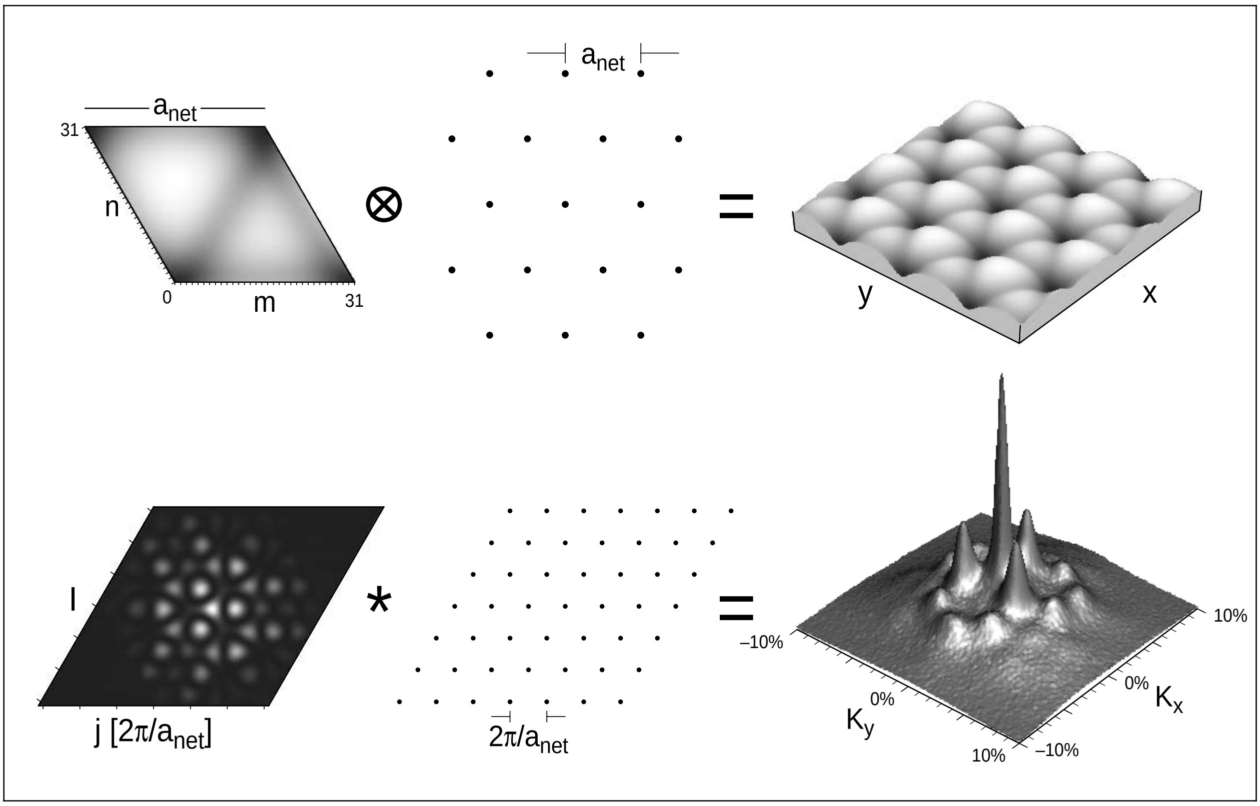

Fig. 6.14. The convolution of the undulation in the dislocation unit cell (upper left) with a six fold grid with a periodicity a_{net} (upper middle) forms the surface undulation (upper right). The The geometry of the periodic surface undulation has been determined by a kinematic SPA-LEED analysis using the intensities of the satellite spots as function of electron energy, i.e. scattering vector. LEED intensity is evaluated following the convolution theorem. The square of the Fourier-transform of the dislocation unit cell (lower left) multiplied with the Fourier-transform of the six fold grid, which is again a six fold grid with the mesh of $2\pi/a_{net}$ by 30° rotated (lower middle), results in the intensity (lower right).

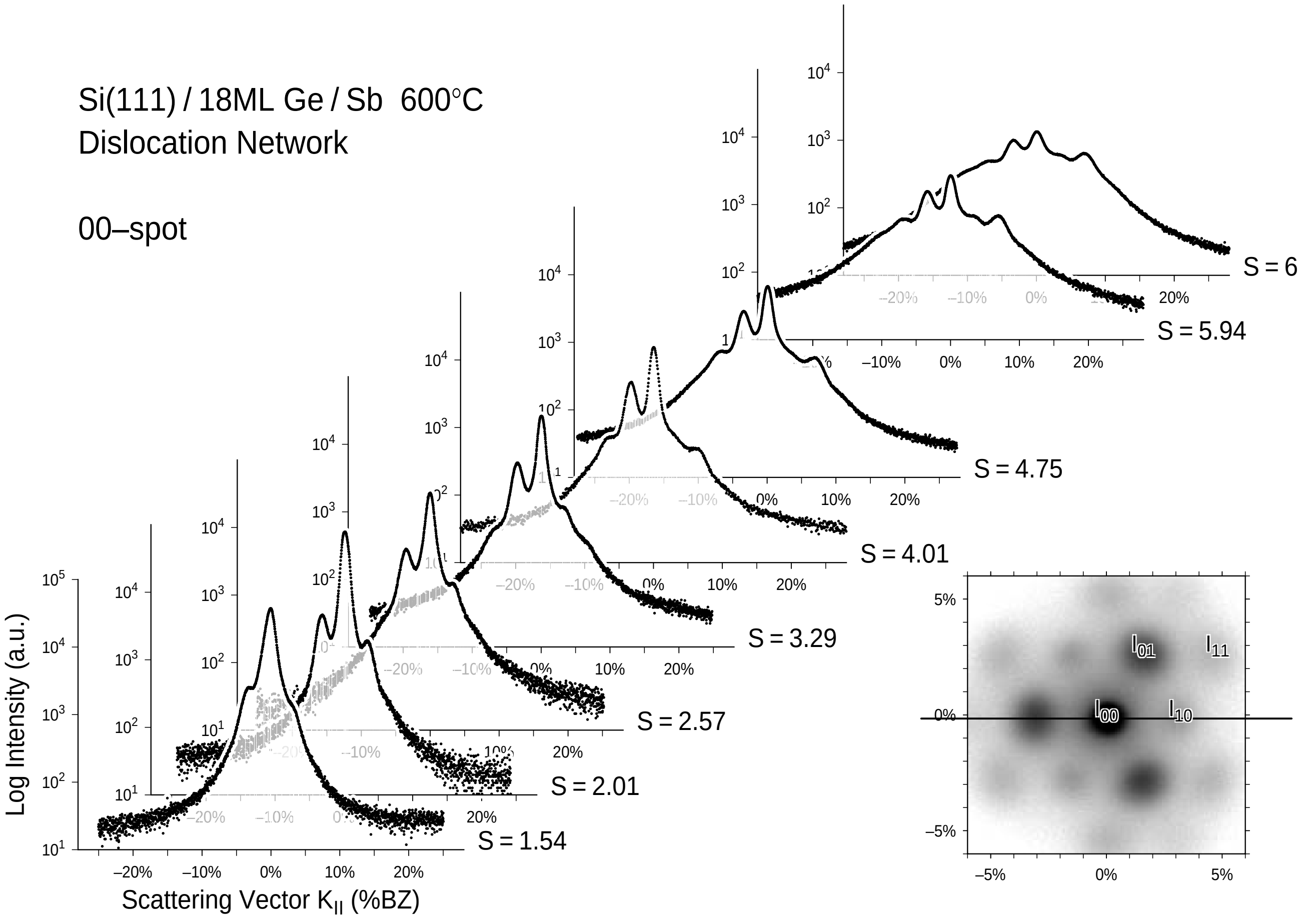

Fig. 6.15 Spot profiles of the (00) spot for a Ge film with 18 ML coverage. The intensity of the (00) spot is redistributed into satellites. With increasing electron energy or scattering phase *S* the satellites become more intense. The thick solid line in the inset shows the orientation of the linear scans

720°C desorbs the surfactant. Unfortunately the Ge film has islanded now. Strain driven intermixing between Ge and Si at the interface and looping of dislocations from the interface to the surface is probably responsible for the breakdown of the Ge film.

An X-ray diffraction analysis with a double crystal setup has been used to accurately determine the lattice parameter of surfactant grown Ge films and thus the degree of strain relaxation. Figure 6.13 shows the (333)-Bragg peak of the Si substrate and the (333)-Bragg peak of a 1000 nm thick Ge film. From this the vertical layer distance of the Ge is estimated to 3.266Å±0.0015Å which agrees perfectly with the Ge bulk value of 3.2664Å.

6.3 Geometry of interfacial dislocation network

From the separation between the satellite spots the average distance of the dislocations could be determined. The measured value of 3.2%BZ corresponds to an average distance of 31 u.c. (unit cell, 1 u.c. = 3.33 Å) or ~104 Å. Exactly this value is expected for the complete relaxation of the Ge-film towards the Ge-bulk lattice constant:

$$\Delta k_{sat} / k_{10} = \Delta a / a_0 \cdot dim / n \sin 60° = 3.20\ \%\mathrm{BZ}$$

with the separation $\Delta k_{sat}/k_{10}$ of the satellite spots, the lattice mismatch $\Delta a/a_0$, the number of identical dislocation nets *n* (depending on the kind of symmetry of the surface orientation, here threefold, thus three identical dislocation nets), the sine of the angle of the Burgers vector of the dislocation to the dislocation line (the full dislocation formed by the Shockley partials is a 60° dislocation [xx]) and the number *dim* of dimensions to be relaxed (here the two directions of the surface). Due to the three rotated dislocation nets the average distance $\Delta k_{sat}/k_{10}$ = 3.20 %BZ between the dislocations is lower than the value expected from the lattice mismatch of 4.2 %.

The intensity is calculated following the schedule shown in Fig. 6.14. The surface undulation is described as the convolution of the height function *h(x,y)* in one dislocation-unit-cell with a periodic 2-dimensional lattice (with a mesh length of a_{net}) as sketched in Fig. 6.14.

The kinematic approximation has to be used for the evaluation for simplicity reasons due to the rather complex diffraction pattern and the large dislocation unit cell. Since the undulation of the surface does not change the local arrangement of atoms the form factor of the individual unit cell is almost unchanged. Usually the form factor depends not strongly on $K_{||}$ [90], that is why it stays nearly constant in the area of the reciprocal space where satellites are observed ($K_{||}$ ± 10%BZ). Using the convolution theorem the intensity $I(k_{||},S)$ as shown in the lower right part of Fig. 6.14 is simply given by the square modolus of the product of the Fourier transforms of the height function and of the dislocation lattice.

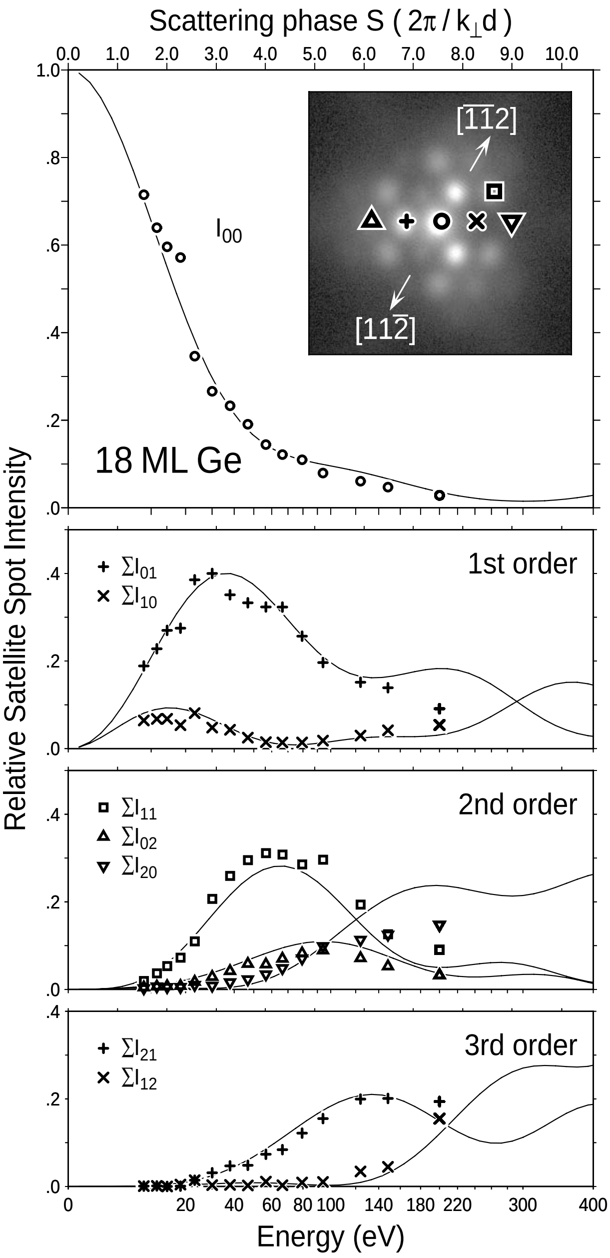

Fig. 6.16 Relative intensity of the non equivalent satellite spots as function of scattering phase *S* for a 18 ML Ge film. The solid lines show the expected behaviour for the surface undulation shown in Fig. 6.17. The height variation is Δh = 0.93Å

This data evaluation process will be demonstrated for a Ge film with a coverage of 18 ML. A detailed analysis for different coverages could be found elsewhere [93,151,165].

The spot profile of the (00)-spot has been measured for energies from 8eV up to 150eV as shown in Fig. 6.15. At low energies almost the entire intensity is concentrated to the central spot. With increasing energy more and more intensity is distributed into the satellite spots.

The profile of each spot of the network of satellites could be described by a Lorentzian with exponent 3/2

$$I(K) \propto (1+\xi^2_{net}K^2)^{-3/2}$$

which describes the spot broadening resulting from an isotropic geometric distance distribution with correlation length ξ_{net} [123]. The width of the satellites increases with the order of the spots and also with the scattering phase *S*. The broadening of the satellite spots results from varying distance between the dislocations and will be addressed later.

The profiles have been fitted by a sum of Lorentzians for scans in K_x-direction. It was very important for the description of the profiles to include not only the intensity of the satellites on that straight line but also all other spots of the satellite network, since the slow decreasing tails of the Lorentzians still add up a lot of intensity far away from their maximum.

For further evaluation only the integral of each satellite spot (integration of the Lorentzian functions in two dimensions) normalised with the sum of central spot and all satellites is used. For the evaluation within the kinematic approximation only these ratios are needed. The total sum of intensities describes the arrangement within a column of atoms and may be therefore only evaluated with the full dynamic theory. Due to the low intensity of the 4th order of satellite spots only the satellites up to the third order have been used.

The sum of the integral intensity of equivalent satellite spots (for example: $\Sigma I_{10} = I_{10} + I_{0\text{-}1} + I_{\text{-}11}$), normalised to the total intensity of all satellite spots, is shown in Fig. 6.16 as a function of electron energy *E* or scattering phase *S*. All the intensities show a very weak dependence on the energy. There is no periodicity with k_z (especially not with integer values of scattering phase *S*) visible, thus this effect could not be explained by any special arrangement of steps or islands or facets.

Now all data points add up to the normalised intensity of one. The most intense satellite spots are $I_{0,1}$ and $I_{1,1}$. Their intensity increase on the expense of $I_{0,0}$ up to energies of 40eV resp. 60eV. For electron energies higher than 100eV the second order spots $I_{2,0}$ and $I_{0,2}$ gain more and more intensity.

Because the intensity distribution of this network of spots varies with energy it has to be caused by a vertical displacement of the unit meshes of the surface. No periodic behaviour of the intensity with the energy is seen, especially not with the scattering phase *S*, thus excluding any special arrangement of a stepped surface, which shows a periodic behaviour with respect to integer values of *S*.

The displacement has to be much smaller than the step height $d_{(111)}$, since remarkable changes of the intensity of the satellites are seen only for large changes in the scattering phase *S* ($\Delta S > 4$). The smaller the vertical displacements are, the shorter the electron wave length has to be, to cause a considerable phase difference for electrons (to make the displacements visible). Therefore the intensity of the satellite spots increase with the electron energy, since the slowest electrons with their long wave length are most insensitive to this small height variations.

By applying a simple elastic theory for an isotropic, elastic continuum [247], a dislocation causes a vertical displacement of the Ge film, described by a Lorentzian function. The full width at half maxima of the Lorentzian expected theoretically is twice the thickness of the expitaxial layer. Applying this form of surface corrugation results in the solid lines for the satellite intensities in Fig. 6.16. Fig. 6.17 shows the reconstructed surface undulation of a

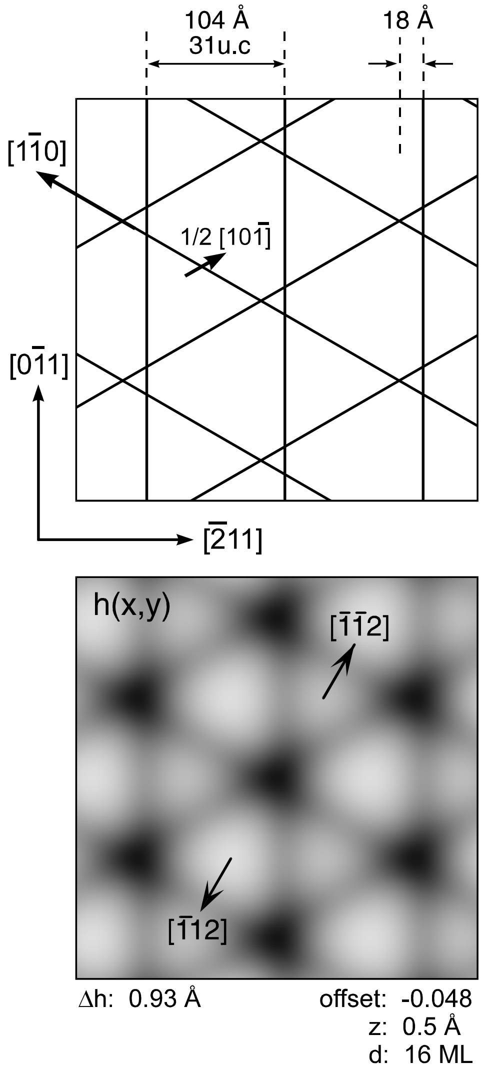

Fig. 6.17 Surface height undulation reconstructed from the LEED intensities shown in Fig. 6.16. Each dislocation at the interface is surrounded by a strain field which is observed as broad depression line with an amplitude of 0.5 Å. The dislocations do not intersect in one point but form a extended node with a width of 18 Å. The total amplitude of the undulation is 0.93Å.

threefold network of plane waves, each with the shape of a Lorentzian with the FWHM of 35.4 Å (18ML / 2 · $d_{(111),\mathrm{Ge}}$) and an amplitude of 0.50 Å.

Creating such a 2-dimensional network of dislocations by the superposition of three rotated arrays of parallel dislocations allows an additional free parameter. Each parallel dislocation array could be shifted perpendicular to the dislocation line by an *offset* relative to the other arrays. An *offset*≠0 results in an extended node instead of an intersection of the dislocations in one point. The intensity of the different satellites is strongly affected by the *offset* [151]. For an *offset* equal zero a six fold symmetry of the satellite pattern (and identical intensities for I_{10} and I_{01}) is expected, since the surface undulation also shows a six fold symmetry for this case. Here, however, we observe a pronounced threefold symmetry reflecting an extended node with a size of 18 Å as shown in Fig. 6.17. The strong influence of the *offset* on the satellite intensity allows to determine precisely this value from the experimental data.

7. Au induced faceting of Si(001)

The diffraction from vicinal surfaces and from facets will demonstrated using as example noble metal induced faceting of regular stepped Si(001).

The LEED pattern of the initial vicinal Si(001) surface (4° miscut towards [110]) is shown in Fig. 7.1. The electron energy was 82eV and corresponds to a scattering phase S = 2, i.e. the 2nd Bragg condition (008). At this condition electrons from neighboured terraces interfere constructively (in-phase-condition).

The regular arranged step train becomes apparent in the spot splitting of all integral order spots [248,249]. The array of perfectly arranged steps acts as phase grid for electrons which results in a splitting of all spots. The separation is reciprocal to the separation between the double steps. The spot splitting of 10% of the surface Brillouinzone (here the distance to the next integral order spot) indicates a terrace width or step separation of 4 nm, i.e. the existence of double height steps.

Other step morphologies have been obtained by other adsorbates: As induces fourfold steps on vicinal Si(001) [250,251]. Adsorption of H, Bi and Sb causes a single step structure [252]. Upon Ag adsorption step bunching on 4° vicinal Si(100) is observed [253-255]. Au induced faceting of Si(111) has already been studied with STM [256]. Silver induces faceting on vicinal Ge(111) surfaces [257]. Indium causes {310} faceting of a Ge(001) surface [258]. Vicinal Si(113) shows faceting even without adsorbates [259]. An overview about the phenomena and driving forces for modifications of step morphology could be found in the

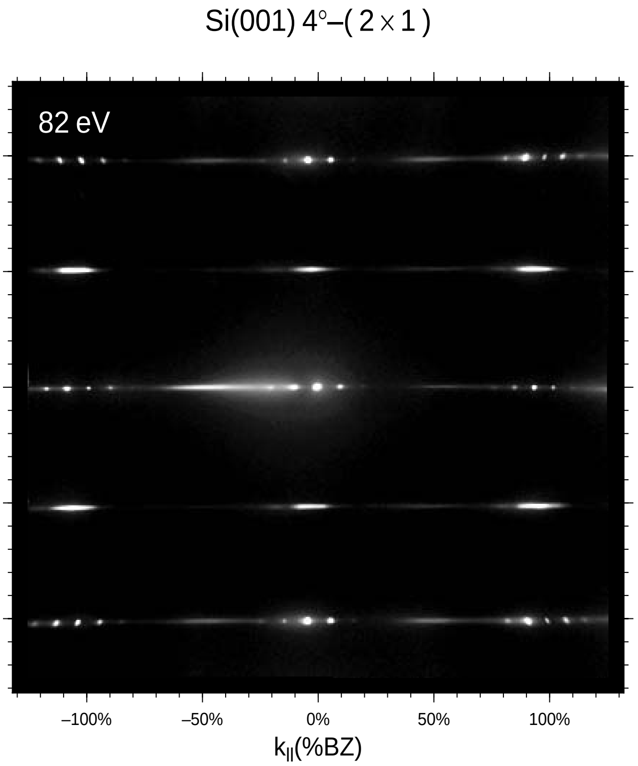

Fig. 7.1 The spot splitting of all fundamental spots in the LEED pattern of the initial 4° vicinal Si(001) surface reflects the presence of a perfect double step train with a long range order >1000Å. From the spot splitting a terrace width of 4 nm is derived.

literature [260,261]. Faceting of Si surfaces has been extensively studied by Yagi et al. [262] and Whitman et al. [263].

The (00) spot shows a splitting in up to six sharp spots. This reflects the perfect long-range order of the double step train with a correlation length of more than 1000Å. The appearance of a splitting into more than two spots is direct evidence for a stronger structurefactor of scattering at the step edge. Using simple kinematic theory with a constant formfactor for the entire terrace would result in only a splitting into two spots.

Superlattice spots from the (1×2) reconstruction indicated by (0 1/2) and (0 -1/2) are also clearly seen. The weak intensity of the (2×1) spots reflects the formation of an almost perfect single domain structure with the dimer rows of the major (2×1)-domains parallel to the miscut direction and D_B type double steps.

The miscut of the sample becomes apparent in the motion of the spots when changing the electron scattering condition, i.e. by variation of the electron energy.

The facet orientation could easily be derived by LEED: In Fig. 7.2 linear profiles along the (-10), (00), and (10) spots of Fig. 7.1 are plotted in a grey scale representation as a vertical cut of reciprocal space with the parallel $\mathbf{K}_{||}$ and vertical scattering vector $\mathbf{K}_{\perp}$ as x-and y-axis. For each value of the perpendicular scattering vector $\mathbf{K}_{\perp}$ the electron energy has been increased.

The rise, the uniform motion and the disappearance of the spots from the vicinal surface are now clearly visible in this plot with electron energies ranging from 80 eV to 185 eV. This diffraction rods [33] are oriented perpendicular to the macroscopic shape of the surface. From the inclination of the diffraction rods the inclination of the surface miscut could directly be determined. The intersections of the diffraction rods with the (00)-rod are the Bragg conditions of scattering and allow the determination of the step height: here we observe twice the number of diffraction rods and therefore can conclude the presence of double steps. This is also confirmed by the terrace width of 40Å as estimated from the spot separation. The long-range order of the surface step train is apparent in the constant width of the diffraction rods independent on the scattering condition [264].

Monolayer adsorption of Au at 800°C results in the complex LEED pattern shown in Fig. 7.3 which is composed of two major contributions: Most of the spots are attributed to a single domain, incommensurate (5×3.2) reconstruction of Au covered flat Si(001) areas without steps. The commensurate 5-fold direction is always oriented along the miscut direction towards [110]. The incommensurate unit vector of the surface unit cell is rotated by 5.7° from the [110] orientation along the step edges.

Most of the spots arise from multi scattering events. The electrons are diffracted from both the Si substrate and the Au-induced reconstruction: the four strong spots surrounding the (00) spot result from a multi scattering process with diffraction from the (01) spot from the Si substrate and the (0-3) spot from the reconstruction.

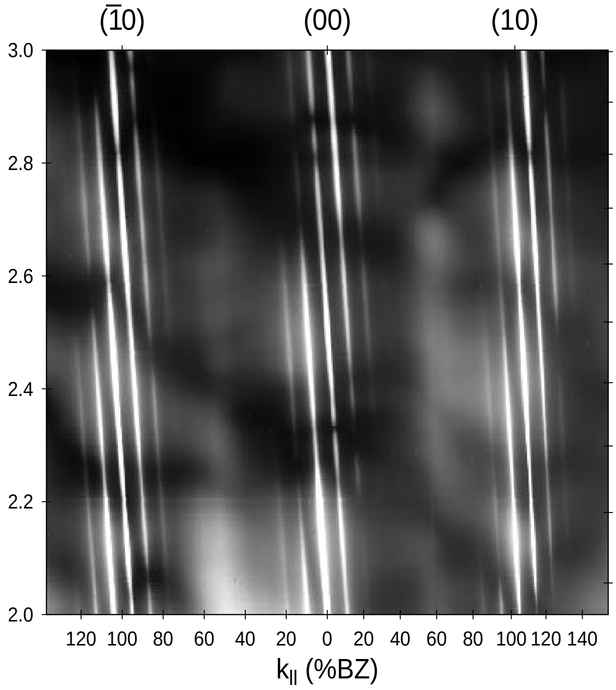

Fig. 7.2 Vertical cut of the reciprocal space along [011]-direction through the integral order spots of Fig. 7.1 . The intensity is shown in a logarithmic grey scale representation. Left scale is scattering phase *S*. On the right scale the corresponding electron energy is shown. The inclined diffraction rods from the 4° miscut vicinal Si(001) surface are clearly visible. Up to six orders of split spots could be observed. From the intersection of the diffraction rods with the Bragg conditions a double layer step height of 2.72 Å is concluded and the angle between the rods and the (001) Bragg-rod gives the miscut angle of the surface. The complete lack of vertical rods reflects the absence of flat (001) areas.

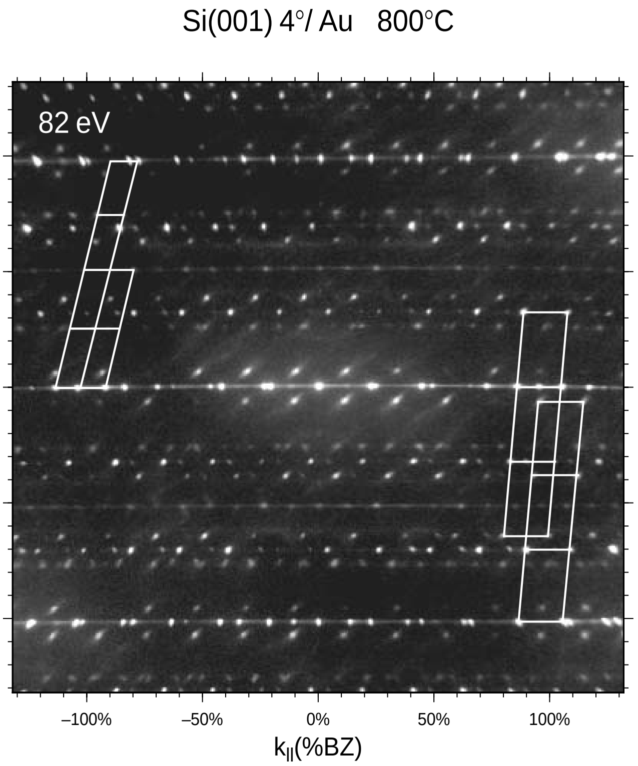

Fig. 7.3 LEED pattern after Au adsorption on 4° vicinal Si(001) at 800°C. The majority of the spots is due to a single domain, incommensurate (5×3.2) reconstruction, facet spots move along the [011]-direction between the integral order spots. The unit cells are indicated.

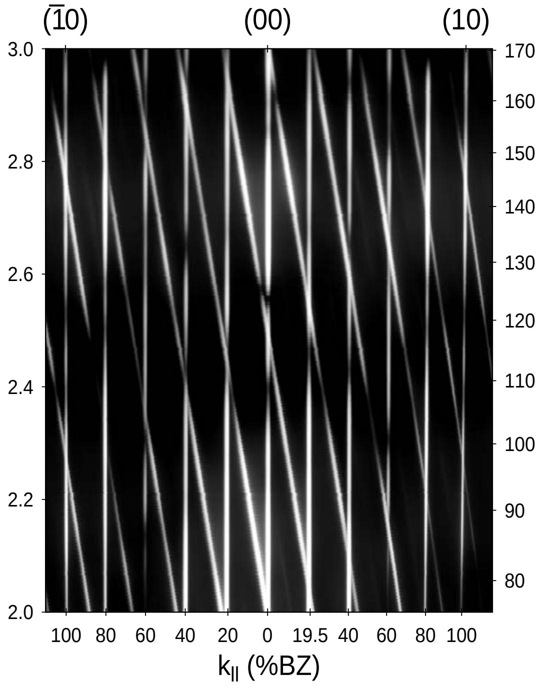

Fig. 7.4 Vertical cut of the reciprocal space after Au deposition at 800°C along [011]-direction through the integral order spots. Same conditions as in Fig. 7.2. Vertical bright lines represent the (-10), (00) and (10) rods and the 5-fold periodicity of the (5×3.2) reconstruction. The tilted rods are [119]- and [117]-facets.

The width of the spots is only limited by the instrument response function, reflecting a size of the flat areas which exceeds the transfer width of 1000Å. The 4° macroscopic miscut of the sample is conserved by steps or facets. The corresponding facet spots are observed in the LEED pattern along the [110]-direction between the integral order spots.

The facet orientation is again easily be derived by LEED: In Fig. 7.4 linear scans between the integral order spots of Fig. 7.3 are plotted in the same way as Fig. 7.2 The vertical bright lines represent the rods of the (-10), (00) and (10) spots as well as the spots reflecting the 5-fold periodicity of the (5×3.2) reconstruction. Those spots do not move in reciprocal space upon change of electron energy because they arise from the (001) faces.

The tilted rods represent facets with a steeper inclination than the initial surface shown in Fig. 7.2. The facet orientation - here a [119]-facet -- is easily derived from the intersections of the integral order rods with the facet rods. Those are the Bragg conditions. For lower adsorption temperatures also [117] and [115] facets have been observed.

The regular double step train from the initial vicinal surface has decomposed in a phase separation in to a "hill-and-valley" structure of large (001) terraces and (119) facets. The facets are necessary for the conservation of the total number of steps. Reflection electron microscopy [265], light diffraction [266,267], low energy electron microscopy [268,269], and atomic force microscopy reveal the huge size of the structures. Super terraces of a length in the millimeter range and a width of 1-2 µm are observed. This corresponds to facets consisting of bunches of 500 to 1000 steps!

The large scale morphological transformation of the regular stepped (1×2) reconstructed vicinal Si surface into this "hill-and-valley" structure composed of alternatively arranged (001)-terraces and (119)-facets has been studied by in-vivo SPA-LEED measurements using an second external electron gun with a grazing incidence of 25°. Continuous recording of spot profiles along [110] direction during Au adsorption allows to follow the change of step morphology in detail. An electron energy of E=96eV corresponds to a phase condition of S=0.95. At this condition the spots from facets with different orientations, flat (001)-areas, and differently inclined step bunches could easily separated. This would not be possible for the in-phase-condition at S=1, where all spots collapse at the (004) Bragg condition.

The change of spot profile during Au adsorption is shown in Fig. 7.5 in a grey scale representation with the x-axis for $K_{||}$ and the downward axis corresponding to the deposition time. Changes of the intensity distribution, in other words, changes of the surface morphology during Au deposition can be devided into 4 stages as follows:

Stage 1: from t_0 to t_1. The split (00) spot originating from the 4° vicinal surface is seen before Au deposition and denoted by spot A and B. The intensity of spot A increases

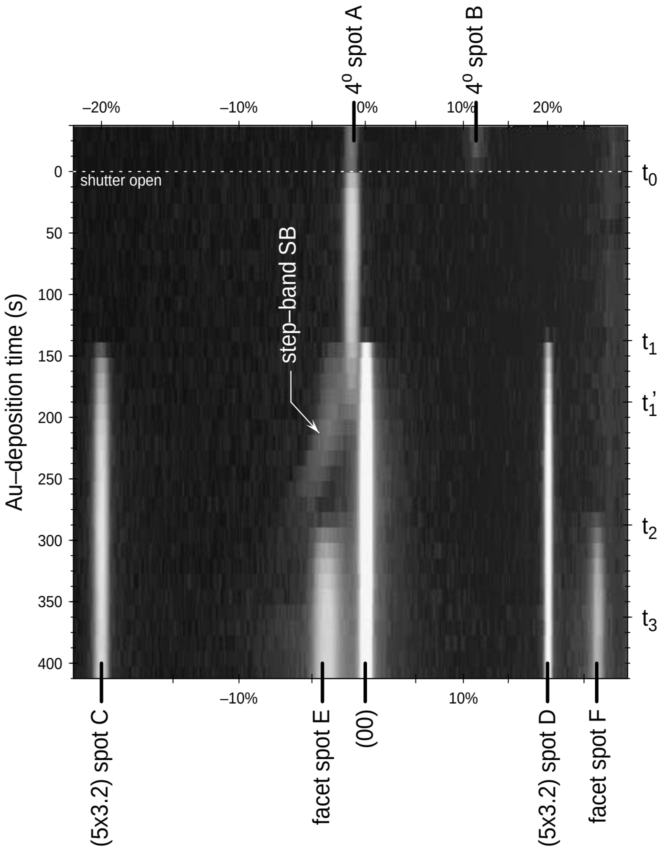

Fig. 7.5 The kinetics of the faceting process is studied during Au adsorption by recording LEED intensity profiles along [110] direction. The profiles are shown as a function of adsorption time in a logarithmic grey scale representation. The top line represents the initial 4° step train, the bottom line the formation of a "hill-and-valley" structure with various different spots originating from (001) terraces and facets. Critical Au-coverages are necessary for the morphological transformation from double steps to terraces and step bunches at t_1 and from step bunches to facets at t_2. The transformation is complete at t_3.

at the initial stage of Au deposition. This is probably caused by an increase of the reflecting power due to an increase of Au coverage on the surface. However, its position and width does not change, which indicates that changes of the surface morphology do not occur during stage 1 though the Au coverage increases almost linear.

Stage 2: from t_1 to t_1'. Above a critical Au coverage very suddenly new spots appear at t_1. Those spots could be attributed to the (00) spot from a flat (001) surface denoted as (00). At the same coverage (5×3.2) reconstruction spots from the Si(001)-Au structure arise at positions +20% and -20% of the surface Brillouin zone (%SBZ) denoted as spot C and D. The diffuse intensity indicated as step-band arises on the left side from spot A. The first nucleation of flat Si(001) terraces happens at the same coverage as the formation of the (5×3.2) structure. From the formation of the Au induced (5×3.2) reconstruction we conclude a reduction of surface free energy. This gain in energy is also the driving force for the break up process of the surface into flat (001) terraces and step bands. The diffuse intensity denoted as step-band (SB) is considered to be from bunches of steps with higher inclination angle than the initial 4° surface.

With increasing Au coverage the intensity of the (00) spot and spots C and D from the (5×3.2) reconstruction increases, while that of spots A and B originating from the 4° initial surface decay and disappears at t_1'. The position of the diffuse intensity SB does not change at this stage, which means that the average inclination angle of the step bands does not change. From the mean position of the diffuse intensity the inclination angle of the step bands is estimated to 8°. During this adsorption stage the 4° vicinal areas are still present (the initial spot A is still visible) and transform to flat wide Si(001) (5×3.2) terraces separated by step bands with higher step density.

Stage 3: from t_1' to t_2. With the disappearance of the 4° spot A, the position of the diffuse reflection (SB) gradually and continuously moved away from the (00) spot. The origin of this spot is considered not to be from distinct facets but from disordered step bands. The continuous shift of the position of SB with further Au deposition indicates the continuous increase of the average inclination angle of the step bands from 8° to ~14°. During this motion of the position of the diffuse reflection SB the intensity of the (00) and the superlattice spots slightly increases and almost saturates at t_2.

Stage 4: from t_2 to t_3. At a second critical coverage t_2 the diffuse spot from the step bands SB disappears and new spots (indicated by E and F) appear. The intensity of these new spots increases without changing their positions during further Au deposition. These new spots are identified as facet spots originating from facets with a distinct (119) orientation. It is surprising that the position of the facet spot in k-space does not coincide with the final position of the step band intensity SB. This is only explained by a decrease of the inclination angle of the stepped areas during the final stage of the faceting process. Although the step bands transform to the facets, they are much steeper (~14° inclination) than the resulting (119) facet with 8.9° inclination angle. This overshooting phenomena will be discussed later. Conservation of the macroscopic miscut of the sample requires that the flat (001) terraces shrink in size during this process, which is observed in a weak decrease of intensity of the (00) spot from t_2 to t_3.

The integral intensities of the different spots from Fig. 7.5 are plotted in a linear intensity scale as a function of Au deposition time in Fig. 7.6. Because the absolute intensity of each LEED spot is proportional to the area covered with this structure and to the structure factor of diffraction (which is not known) only relative intensities have been used. The intensities of all the reflections were scaled in arbitrary units. The different stages mentioned above could be clearly separated. The sudden onset of a linear increase of the intensity of the (00)-spot and the (5×3.2) spots with Au

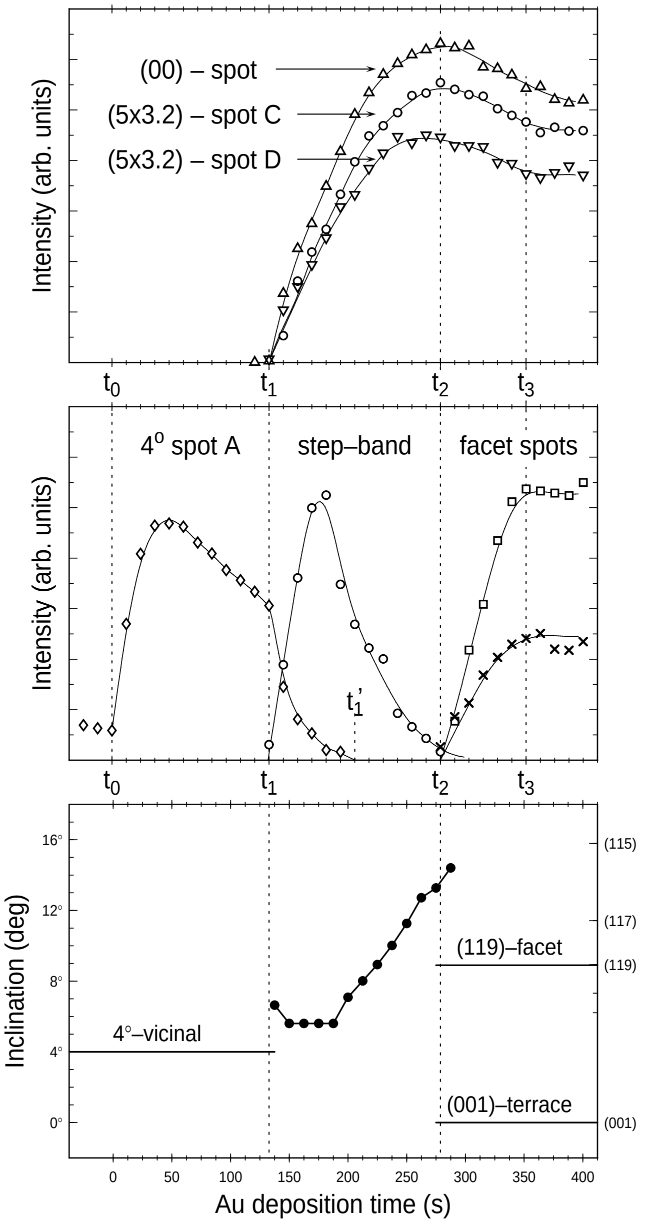

Fig. 7.6 Plot of the integral spot intensities of Fig. 7.5 as function of Au adsorption time. Formation of (001) terraces starts at a critical Au coverage t_1 at the same time as the superstructure formation. The linear increase of (001) areas with additional Au coverage is well seen. The step band intensity decrease beyond 180 s due to the step bunching process. (119) facets start to nucleate beyond a second critical coverage at t_2. At the same time the intensity of the (001) spots, i.e. the area of the (001) terraces decreases due to the increased size of the facets.

coverage starting at t_1 reflects the formation of reconstruction only above a critical Au coverage and the growth of flat (001) terraces proportional to the additional Au coverage.

The faceting process beyond t_2 can be explained by a similar process to that between t_1' and t_2: above a critical coverage the facet area increases linear with increase of Au coverage. At the same time the intensity of the (00)-spot and the (5×3.2) spots decreases slightly due to the transformation of steep step bands into smoother facets at the expense of the (001) terraces.

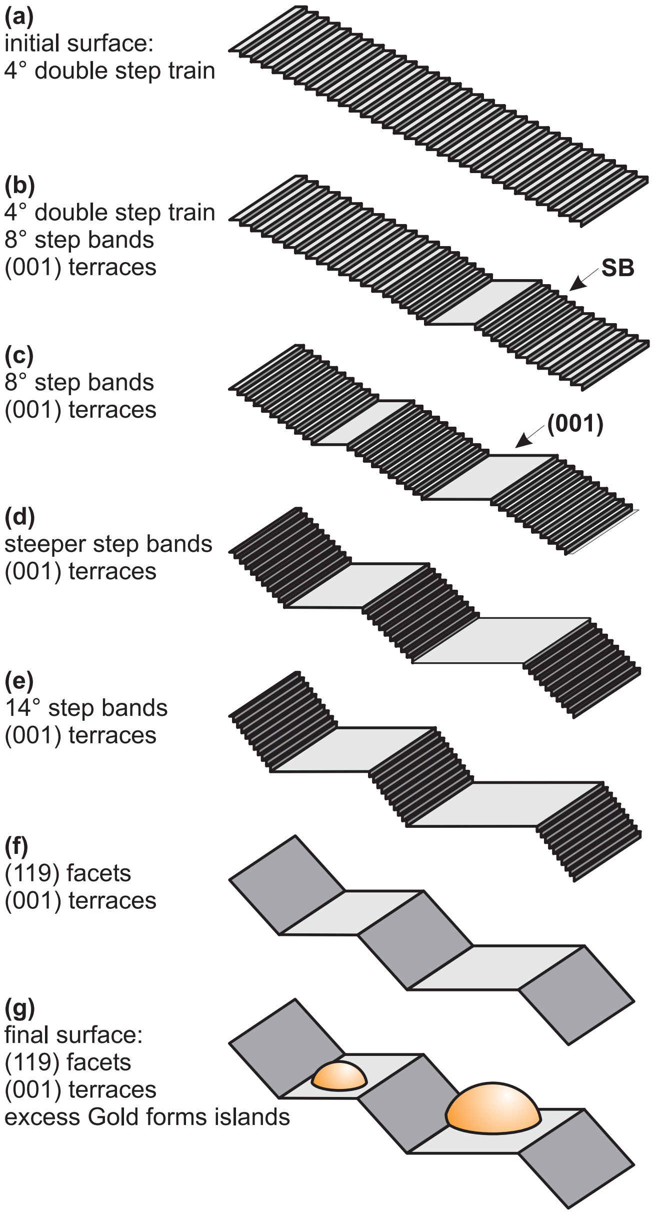

Fig. 7.7 Schematic illustrations of the different stages of surface morphology transition. (a) Initial surface with regular double step train. (b) Nucleation of the first super terrace and step bunching process. Part of the initial 4° vicinal double step train in still present. (c) The entire surface is transformed to super terraces and step bands. (d+e) The width of the super terraces increases linear with the additional Au coverage. The slope of the step bands increases. (f) The step bands transform to well ordered (119) facets. (g) Further Au accumulates in 3D clusters.

Figure 7.7 schematically illustrates the changes of surface morphology during Au adsorption. Fig. 7.7(a) shows the 4° vicinal surface at t_0. Above a critical Au coverage at t_1 Au-induced reconstructed (001) areas appear together with narrowly spaced steps (SB) as shown in (b). At t_1' 4° vicinal regions disappear due to the expansion of the (001) terraces. All steps are accumulated in step bands SB. During stage 3 the expansion of the (001) surfaces causes a further increase of the slope of the step bands as seen in (c). Finally at t_2 (119) facet planes are formed being accompanied by a slight decrease of the (001) terrace areas.

8. More and future outlook

This review about spot profile anlysing high resolution LEED must be incomplete. It highlights mainly the aspects of surface morphological defects during growth and manipulation of silicon or germanium substrates or films. Of course, SPA-LEED is for other material systems an extremely useful analytical tool, too:

The study of adsorbate induced surface equilibrium phase transitions is one of the major domains for diffraction techniques. The phase diagram of an adsorbate system is easily measured with a 4 grid LEED instrument. Critical fluctuations and the critical temperature could be obtained both with a standard low resolution LEED optics [270,271] and a high resolution SPA-LEED instrument [272-282]. The influence of impurities on the phase transition could only be studied with high resolution diffraction instruments [283,284].

The study of surface roughening transitions is an another important field for the use of high resolution diffraction instruments [285-291]. Equilibrium fluctuations of steps at elevated temperature (step roughening) has been observed for the first time with a high resolution LEED instrument by means of an autocorrelation analysis of incoherent intensity fluctuations [292,293]. High resolution LEED provides morphological information during surface melting, which is not available with other techniques [294].

Of course SPA-LEED has been used not only for the study of semiconductor growth but also for the deposition of metals on metal [295-306], metals on semiconductor [307-312], metal on thin insulators [313-315] insulators on semiconductors [316-318] and metals [319-323] and insulators on insulators [324,325].

The size of cyrstallites and mosaic spread of defected films are important informations obtained by SPA-LEED [326,327]. The change in lattice constant and lattice accomodation in hereoepitaxial systems could easily be studied with a diffraction instrument [309-311]. Lattice accommodation by periodic arrays of dislocations has also been observed for O mediated growth of Cu on Ru(0001) by spot splitting [328]. Misfit induced quasi-periodic ordering of hetero islands has been observed for Fe on Cu(311), followed by a faceting after coalescence [329,330].

A new growth mode has been found with SPA-LEED for deposition of NaCl on Ge: the carpet mode. The NaCl film covers like a bend carpet step edges of the underlying Ge substrate [331,332].

The surface morphology evolution during sublimation and sputtering has been studied by Neureiter et al. for CdTe(001) surfaces by SPA-LEED [333-335]. Reaction (or adsorbate) induced faceting has been studied also for metal surfaces as Pt [336-338], Pd [339,340], W [341], and Mo [342]. The influence of surface defects on the linewidth of surface states has been studied for Cu(111) [343].

For the near future we can expect advances in the instrumentation of the technique. The cone shaped SPA-LEED instrument will allow much better and easier access to the sample during diffraction studies. A 1-dim. or 2-dim. electron detector will speed up the data recording time by one or two orders of magnitude. A screen and video based 2-dim. detector has been set up and is already working [344].

This review will not be the end of the story as foreknowledged by M.G. Lagally: "There was diffraction before STM - and there will be diffraction again after STM..." [345].

References

[1] Davisson, C.J.; Germer, L.H.: Diffraction of electrons by a crystal of nickel. Phys. Rev. **30** (1927) 705–740.

[2] Sproull, W.T.: Diffraction of low speed electrons by a tungsten single crystal. Phys.Rev. **43** (1933) 516–526; New type of apparatus for experiments in secondary electron diffraction. Rev. Sci. Instrum. **4** (1933) 193.

[3] Ehrenberg, W.: Visual observation of diffraction of slow electrons by crystals. Philos. Mag. **18** (1934) 878.

[4] Park, R.L.; Farnsworth, H.E.: Pulsed-beam LEED system for rapid precision measurements. Rev. Sci. Instrum. **35** (1964) 1592.

[5] Caldwell, C.W.: Rev. Sci. Instrum. **36** (1965) 1500.

[6] Lander, J.J.: In: Recent progress in solid state chemistry (Ed. H. Reiss) p. 26; Vol. **2** (1965).

[7] Estrup, P.J.; McRae, E.G.: Surface studies by electron diffraction. Surf. Sci. **25** (1971) 1–52.

[8] Lagally, M.G.; Martin, J.A.: Instrumentation for Low-Energy Electron Diffraction. Rev. Sci. Instrum. **54** (1983) 1273–1288.

[9] Bauer, E.:Zum gegenwärtigen Stand der Augerelektronenspektroskopie (AES) und der Beugung langsamer Elektronen (LEED). Zeitschrift für Metallkunde **63** (1972) 437–447.

[10] Ertl, G.: Verwendung niederenergetischer Elektronen zur Untersuchung von Oberflächenstrukturen und geordneten Adsorptionsphasen. Berichte der Bunsen-Gesellschaft **75** (1971) 967–979.

[11] Pendry, J.B.: Low Energy Electron Diffraction. Academic Press, London, 1974.

[12] van Howe, M.A.; Tong, S.Y.: Surface Crystallography by LEED. Springer Series Chem. Phys., Springer, Berlin, 1979.

[13] Pendry, J.B.: LEED and the crystallography of surfaces. Surf. Sci. Rep. **19** (1993) 88–97.

[14] Pendry, J.B.: Multiple scattering theory of electron diffraction. Surf. Sci. **299/300** (1994) 375–390.

[15] Tong, S.Y.: Electron-diffraction for surface studies - the first 30 years. Surf. Sci. **299/300** (1994) 358–374.

[16] Heinz, K.: Geometrical and chemical restructuring of clean metal surfaces as retrieved by LEED. Surf. Sci. **299/300** (1994) 433–446.

[17] Van Hove, M.A.; Moritz, W.; Over, H.; Rous, P.J.; Wander, A.; Barbieri, A.; Materer, N.; Starke, U.; Somorjai, G.A.: Automated determination of complex surface structures by LEED. Surf. Sci. Reports **19** (1993) 191– 229.

[18] Landskron, J.; Moritz, W.: Anisotropic temperature factors in the calculation of LEED intensities, Surf. Sci. **337** (1995) 278–284.

[19] J.B. Pendry and D.K. Saldin, SEXAFS without X-rays, Surf. Sci. **145** (1984) 33–47.

[20] K. Heinz, D.K. Saldin, and J.B. Pendry, Diffuse LEED and surface crystallography. Phys. Rev. Lett. **55** (1985) 2312–2315.

[21] Fadley, C.S.: Diffraction and holography with photoelectrons and Auger electrons: some new directions. Surf. Sci. Reports **19** (1993) 231–264.

[22] Joly, Y.: Electronic structure analysis by low-energy positron diffraction. Phys. Rev. Lett. **72** (1994) 392–395.

[23] van Hove, J.M.; Cohen, P.I.: Development of steps on GaAs during MBE. J.Vac. Sci. Technol. **20** (1982) 726–729.

[24] van Hove, J.M.; Cohen, P.I.; Lent, C.S.: Disorder on GaAs(001) surfaces prepared by MBE. J.Vac. Sci. Technol. A **1** (1983) 546–550.

[25] van Hove, J.M.; Pukite, P.; Cohen, P.I.; Lent, C.S.: RHEED streaks and instrument response. J.Vac. Sci. Technol. A **1** (1983) 609–613.

[26] Neave, J.H.; Joyce, B.A.; Dobson, P.J.; Norton, N.: Dynamics of film growth of GaAs by MBE from RHEED observations. Appl. Phys. A**31** (1983) 1–8.

[27] van Hove, J.M.; Lent, C.S.; Pukite, P.R.; Cohen, P.I.: Damped oscillations in RHEED during GaAs MBE. J.Vac. Sci. Technol. B **1** (1983) 741–746.

[28] Cohen, P.I.; Pukite, P.R.; van Hove, J.M.; Lent, C.S.: RHEED studies of epitaxial growth on semiconaductor surfaces. J.Vac. Sci. Technol. A**4** (1986) 1251–1258.

[29] Sakamoto, T.; Kawai, N.J.; Nakagawa, T.; Ohta, K.; Kojima, T.; Hashiguchi, G.: RHEED intensity oscillations during silicon MBE growth. Surf. Sci. **178** (1986) 651–657.

[30] Henzler, M.: LEED-Investigation of Step Arrays on Cleaved Ge Surfaces. Surf. Sci. **19** (1970) 159–171.

[31] Henzler, M.: Texture of surfaces cleaned by Argon bombardment and annealing. Surf. Sci. **22** (1970) 12–18.

[32] Houston, J.E.; Park, R.L.: Low-energy-electron diffraction from imperfect structures. Surf. Sci. **21** (1970) 209–223.

[33] Henzler, M.: Atomic Steps on Single Crystals: Experimental Methods and Properties. Appl. Phys. **9** (1976) 11–17.

[34] Henzler, M.: Electron diffraction and surface defect structure. In: *Electron spectroscopy for surface analysis* (Ed. H. Ibach) pp. 117–150; Topics in Current Physics, Vol. **4**, Springer, Berlin (1977).

[35] Henzler, M.: Quantitative evaluation of random distributed steps at interfaces and surfaces. Surf. Sci. **73** (1978) 240–251.

[35a] Schulze, G.; Henzler, M.: Determination of atomic steps at Argon ion bombarded Ge(100) surfaces. Surf. Sci. **73** (1978) 553–559.

[35b] Henzler, M.: Defects in surface structure: informations with LEED. Festkörperprobleme **XIX** (1979) 193–208.

[35c] Hahn, P.O.; Henzler, M.: Influence of oxidation parameters on atomic roughness at the Si-SiO2 interface. J. Appl. Phys. **52** (1981) 4122–4127.

[36] Henzler, M.: LEED-studies of surface imperfections. Appl. of Surf. Sci. **11/12** (1982) 450–469.

[36a] Hahn, P.O.; Henzler, M.: Experimental comparison of atomic roughness and Hall mobility in p-Si inversion layers. J. Appl. Phys. **54** (1983) 6492–6496.

[37] Henzler, M.: Spot profile analysis (LEED) of defects at silicon surfaces. Surf. Sci. **132** (1983) 82–91.

[38] Henzler, M.: Measurement of surface defects by low energy electron diffraction. Appl. Phys. **A34** (1984) 205–214.

[39] Henzler, M.: Defects at semiconductor surfaces. Surf. Sci. **152/153** (1985) 963–976.

[40] Henzler, M.: A new LEED instrument for quantitative spot profile analysis. Surf. Sci. **168** (1986) 744–750.

[45] Henzler, M.: Quantitative Analysis of LEED Spot Profiles in Structure of Surfaces. In: *Structure of Surfaces* (Eds. M.A. Van Hove; S.Y. Tong) pp. 351–357; Springer Series in Surface Science **2**, Berlin (1985)

[46] Henzler, M.: The Study of Epitaxy with Spot Profile Analysis of LEED (SPA-LEED). In: *Structure of Surfaces II* (Eds. F. van der Veen, M.A. Van Hove) pp. 431–437; Springer Series in Surface Science **11**, Berlin (1988).

[47] Henzler, M.: Diffraction from stepped surfaces. In: *RHEED and Reflection Electron Imaging of Surfaces* (Eds. P.K.Larsen, P.J.Dobson) pp. 193–200; NATO ASI Ser. B Vol. **188**, Plenum Press, 1988.

[48] Henzler, M.: LEED from epitaxial surfaces. Surf. Sci. **298** (1993) 369–377.

[49] Henzler, M.: Misfit accommodation during heteroepitaxial growth, in *Semiconductor Interfaces at the Sub-nanometer scale* (ed. H. Salemink and M.D. Pashley) pp. 173–180, Kluwer Academic Publishers, (1993).

[50] Henzler, M.: Capabilities of LEED for defect analysis. Surf. Review and Letters **4** (1997) 489–500.

[51] Moritz, W.: Theory from electron scattering from defects: Steps on surfaces with non-equivalent terraces. In: *RHEED and Reflection Electron Imaging of Surfaces* (Eds. P.K.Larsen, P.J.Dobson) pp. 175–192; NATO ASI Ser. B Vol. **188**, Plenum Press, 1988.

[52] Lagally, M.G.: The present status of LEED. Applic. of Surf. Sci. **13** (1982) 260–281.

[53] Lagally, M.G.; Savage, D.E.; Tringides, M.: Diffraction from disordered surfaces: an overview In: *RHEED and Reflection Electron Imaging of Surfaces* (Eds. P.K.Larsen, P.J.Dobson) pp. 139–174; NATO ASI Ser. B Vol. **188**, Plenum Press, 1988.

[54] Pukite, P.R.; Cohen, P.I.; Batra, S.: The contribution of atomic steps to RHEED from semiconductor surfaces. In: *RHEED and Reflection Electron Imaging of Surfaces* (Eds. P.K.Larsen, P.J.Dobson) pp. 427–448; NATO ASI Ser. B Vol. **188**, Plenum Press, 1988.

[55] Hahn, P.O.; Clabes, J.; Henzler, M.: LEED-Investigations and Work Function Measurements of the First Stages of Epitaxy of W on W(110). J. Appl. Phys. **51** (1980) 2079–2088.

[56] Gronwald, K.D.; Henzler, M.: Epitaxy of Si (111) as Studied with a new High Resolving LEED System. Surf. Sci. **117** (1982) 180–187.

[57] Scheithauer, U; Meyer, G.; Henzler, M.: A new LEED Instrument for Quantitative Spot Profile Analysis. Surf. Sci. **178** (1986) 441–451.

[58] Cao, Y.; Conrad, E.: High q-resolution electron gun for LEED. Rev. Sci. Instrum. **60** (1989) 2642–2645.

[59] Martin, J.A.; Lagally, M.G.: A high-resolution LEED based on a field emission source. J. Vac. Sci. Technol. A **1** (1983) 1210–1211.

[60] Martin, J.A.; Lagally, M.G.: A high-resolution surface-sensitive scanning electron diffractometer based on a field emission source. Scanning Electron Microscopy **4** (1985) 1357–1361.

[61] Müller, B.; Henzler, M.: SPA-RHEED - a novel method in reflection high energy electron diffraction with extremely high angular and energy resolution. Rev. Sci. Instr. **66** (1995) 5232–5235.

[62] Müller, B.; Henzler, M.: Comparison of high reflection high-energy electron diffraction and low-energy electron diffraction using high-resolution instrumentation. Surf. Sci. **389** (1997) 338–348.

[63] Müller, B.; Zielasek, V.: Inelastic scattering in RHEED from Si(111). Phys. Rev. Lett. **79** (1997) 4393–4396.

[64] Claus, H.; Büssenschütt, A.; Henzler, M.: Low energy electron diffraction with energy resolution. Rev. Sci. Instr. **63** (1992) 2195–2199.

[65] Büssenschütt, A.; Claus, H.; Henzler, M.: Angular dependance of dipole scattering of low-energy electrons at thin and thick dipole active films. Phys. Rev. B **49** (1994) 7829–7832.

[66] Zielasek, V.; Büssenschütt, A.; Henzler, M.: Multiple losses in off-specular electron energy loss spectra of thin NaCl films individually resolved in energy and momentum. Appl. Surf. Sci. **90** (1995) 117–121.

[67] Moresco, F.; Rocca, M.; Zielasek, V.; Henzler, M.: Evidence for the presence of the multipole plasmon mode on Ag surfaces. Phys. Rev. B **54** (1996) 14333–14336.

[68] Moresco, F.; Rocca, M.; Zielasek, V.; Hildebrandt, T.; Henzler, M.: ELS-LEED study of surface plasmon dispersion on Ag surfaces. Surf. Sci. **388** (1997) 1–4.

[69] Moresco, F.; Rocca, M.; Zielasek, V.; Hildebrandt, T.; Henzler, M.: ELS-LEED Study of electronic excitations on Ag(110) and Ag(111). Surf. Sci. **388** (1997) 24–32.

[70] Zielasek, V.; Büssenschütt, A.; Henzler, M.: Low-energy electron thermal diffuse scattering from Al(111) individually resolved in energy and momentum. Phys. Rev. B **55** (1997) 5398–5403.

[71] Zielasek, V.: phd thesis, Hannover (1988).

[72] Binning, G.; Rohrer, H.; Gerber, Ch.; Weibel, E.: Surface studies by scanning tenneling microscopy. Phys. Rev. Lett. **49** (1982) 57–61; 7×7- reconstruction of Si(111) resolved in real space. Phys. Rev. Lett. **50** (1983) 120–123.

[73] von Laue, M.: The diffraction of an electron-wave at a single layer of atoms. Phys. Rev. **37** (1931) 53–59.

[74] Robinson, I.K.; Tweet, D.J.: Surface x-ray diffraction. Rep. Prog. Phys. **55** (1992) 599–651.

[75] Vlieg, E.; Denier van der Gon, A.W.; van der Veen, J.F.; Macdonald, J.E.; Norris, C.: Surface x-ray scattering during crystal growth: Ge on Ge (111). Phys. Rev. Lett. **61** (1988) 2241–2244.

[76] Feidenhans´l, R.: Surface structure determination by x-ray diffraction. Surf. Sci. Rep. **10** (1989) 105–188.

[77] *Surface X-Ray and Neutron Scattering* (Ed. H. Zabel and I.K. Robinson); Springer Proceedings in Physics, Springer, Berlin (1992)

[78] Wever, J.; Meyerheim, H.L.; Moritz, W.; Jahns, V.; Wolf, D.; Schulz, H.; Johnson, R.L.; Seehofer, L.: A new type of reconstruction on the InSb(111) surface determined by grazing incidence X-ray diffraction. Surf. Sci. Lett. **321** (1994) L225–L232.

[79] Moritz, W.; Meyerheim, H.L.: 3-D surface structure determination by x-ray diffraction. In: *Surface Science: Principles and Current Applications* (Eds. R.J. MacDonald, E.C. Taglauer, K.R. Wandelt) pp.12–28, Springer, 1996.

[80] Vogler, H.; Iglesias, A.; Moritz, W.; Over, H.: Ge(113) reconstruction stabilized by subsurface interstitials: An X-ray diffraction structure analysis, Phys. Rev. B **57** (1998) 2315–2320.

[81] Comsa, G.: Surface scattering of thermal energy He beams: from the proof of the wave nature of atoms to a versatile and efficient surface probe. Surf. Sci. **299/300** (1994) 77–91.

[82] Benedek, G.; Toennies, J.P.: Helium atom scattering spectroscopy of surface phonons: genesis and achievements. Surf. Sci. **299/300** (1994) 587–611.

[83] Engel, T.; Rieder, K.H.: Structural studies of surfaces with atomic and molecular beam diffraction. Springer Tracts in Modern Physics **91**, Springer, Berlin (1982)

[84] Poelsema, B.; Comsa, G.: Scattering of thermal energy atoms. Springer Tracts in Modern Physics **115**, Springer, Berlin (1989).

[85] Heinz, K.; Hammer, L.: Surface crytallography by low energy electron diffraction. Z. Kristallogr. **213**, (1998) 615–634

[86] Jagodzinski, H.; Moritz, W.; Wolf, D.: Diffuse LEED intensity of disordered crystal surfaces. Surf. Sci. **77** (1978) 233–248; Surf. Sci. **77** (1978) 249–264; Surf. Sci. **77** (1978) 265–282; Surf. Sci. **77** (1978) 283–300.

[87] Rous, P.J.; Pendry, J.B.: Diffuse LEED from simple stepped surfaces. Surf. Sci. **173** (1986) 1–19.

[88] Park, R.L.; Houston, J.E.: The effect of registry degeneracy on LEED beam profiles. Surf. Sci. **18** (1969) 213–227.

[89] Houston, J.E.; Park, R.L.: Low-energy-electron diffraction from imperfect structures. Surf. Sci. **21** (1970) 209–223.

[90] Moritz, W.: Unpublished results..

[91] Almost all experimental IV-curves show significant changes of the intensity only for variations of the scattering vectors of the order of 1/3 to 1/5 of a Brillouinzone. The reason is the finite elastic scattering lenght of the electrons.

[92] Henzler, M.; Suliga, E.: LEED measurements of a possible step atom depression at the Cu(410) surface. Appl. Surf. Sci. **25** (1986) 179– 182.

[93] Horn-von Hoegen, M.; Pook, M.; Al Falou, A. Müller, B.H.; Henzler, M.: The interplay of surface morphology and strain relief in surfactant mediated growth of Ge on Si(111). Surf.Sci. **284** (1993) 53–66.

[94] Horn-von Hoegen, M.; AlFalou, A.; Müller, B.H.; Köhler, U.; Andersohn, L.; Dahlheimer B.; Henzler, M.: Surfactant stabilized strained Ge cones on Si(100). Phys. Rev. B **49** (1994) 2637–2650.

[95] Horn-von Hoegen, M.; Müller, B.H.; Al Falou, A.: Strain relief by micro roughness in surfactant mediated growth of Ge on Si(001). Phys. Rev. B **50** (1994) 11640–11652.

[96] AlFalou, A.; Kammler, M.; Horn-von Hoegen, M.: Strain state analysis of heteroepitaxial systems. Phys. Rev. Lett. (submitted).

[97] Lent, C.S.; Cohen, P.I.: Diffraction from randomly stepped surfaces. Surf. Sci. **139** (1984) 121–154.

[98] Mamorkos, I.K.; Das Sarma, S.: Kientik simulation of MBE growth dynamics. Surf. Sci. Lett. **237** (1990) L411–L416.

[99] Cohen, P.I.; Petrich, G.S.; Pukite, P.R.; Whaley, G.J.; Arrott, A.S.: Birth-death models of epitaxy. Surf. Sci. **216** (1989) 222–248.

[100] Flynn, D.K.; Wang, W.; Chang, S.-L.; Tringides, M.C.; Thiel, P.A.: The use of LEED intensity oscillations in monitoring thin film growth. Langmuir **4** (1988) 1096–1100.

[101] Horn-von Hoegen, M.; Falta, J.; Henzler, M.: The initial stages of growth of silicon on Si(111) by spot profile analysing low-energy electron diffraction. Thin Solid Films **183** (1989) 213–220.

[102] Yang, H.-N.; Wang, G.-C.; Lu, T.-M.: Quantitative study of the decay of intensity oscillations in transient layer-by-layer growth. Phys. Rev. B **51** (1995) 17932–17945.

[103] Lu, T.-M.; Wang, G.-C.; Zhao, Y.-P.: Beyond intensity oscillations. Surf. Rev. Lett. **5** (1998) 899–912.

[104] Kang, H.C.; Evans, J.W.: Scaling analysis of surface roughness and Bragg oscillation decay in models for low-temperature epitaxial growth. Surf. Sci. **271** (1992) 321–330.

[105] Wollschläger, J.: Simple Analysis of Spot Splitting due to Diffraction at Surfaces with Atomic Steps. Surf. Sci. **383** (1997) 103–122.

[106] Lapujoulade, J.: A statistical model for the scattering of atoms from randomly stepped surfaces. Surf. Sci. **108** (1981) 526–548.

[107] Spadacini, R.; Tommei, G.E.: A Markovian approach to atomic scattering from rough surfaces. Surf. Sci. **133** (1983) 216–232.

[108] Heun, S.; Falta, J.; Henzler, M.: The initial stages of epitaxial growth of silicon on Si(100)-2 × 1. Surf. Sci. **243** (1991) 132–140.

[109] Zhao, Y.-P.; Wang, G.-C.; Lu, T.-M.: Diffraction from anisotropic rough surfaces. Phys. Rev. B **58** (1998) 7300–7309.

[110] Lu, T.-M.; Lagally, M.G.: Diffraction from surfaces with randomly distributed steps. Surf. Sci. **120** (1982) 47–66.

[111] Lu, T.-M.; Zhao, L.-H.; Lagally, M. G.; Wang, G.-C.; Houston, J. E.: Diffraction from overlayer islands with positional correlation. Surf. Sci. **122** (1982) 519–534.

[112] Presicci, M.; Lagally, M.G.; Misoriented surfaces with randomly distributed steps. Surf. Sci. **141** (1984) 233–239.

[113] Tringides, M.C.; Lagally, M.G.: The use of peak intensity in diffraction measurements of growth kinetics on surfaces. Surf. Sci. Lett. **195** (1988) L159–166.

[114] Pimbley; J.M.; Lu, T.-M., Atomic correlations of stepped surfaces and interfaces, J. Appl. Phys. **55** (1984) 182–187.

[115] Pimbley; J.M.; Lu, T.-M.: Exact one-dimensional pair correlation fucntions of a monolayer/substrate system. J. Appl. Phys. **57** (1985) 1121–1129.

[116] Pimbley; J.M.; Lu, T.-M.: Integral representation of the diffracted intensity from one-dimensional stepped surfaces and epitaxial layers. J. Appl. Phys. **58** (1985) 2184–2189.

[117] Pukite, P.R.; Lent, C.S.; Cohen, P.I.: Diffraction from stepped surfaces. Surf. Sci. **161** (1985) 39–68.

[118] Kariotis, R.; Kruger, D. W.; Savage, D. E.; Lagally, M.G.: Direct determination of the size distribution of arbitrary surface configurations from diffraction measurements: general theory. Surf. Sci. **205** (1988) 591–616.

[119] Wollschläger, J.: Diffraction from Surfaces with Randomly Distributed Structural Defects. Surf. Sci. **328** (1995) 325–353.

[120] Pflanz, S.; Moritz, W.: The domain matrix method: A new calculation scheme for diffraction profile. Acta Cryst. A **48** (1992) 716–727.

[121] Busch, H.; Henzler, M.: Quantitative evaluation of terrace width distributions from LEED measurements. Surf. Sci. **167** (1986) 534–548.

[122] Horn, M.; phd thesis, Hannover (1988).

[123] Wollschläger, J.; Luo, E.Z.; Henzler, M.: Thermal roughness of the homogeneous and inhomogeneous Cu(311) surface studied by high-resolution LEED. Phys. Rev. B **44** (1991) 13031–13041.

[124] Zhao, Y.-P.; Wang, G.-C.; Lu, T.-M.: Diffraction from non-Gaussian rough surfaces. Phys. Rev. B **55** (1997) 13938–13952.

[125] Liew, Y.-F.; He, Y.-L.; Chan, A.; Wang, G.-C.: A simple method to determine the step heights on ultrathin heteroepitaxial films. Surf. Sci. Lett. **273** (1992) L461–L466.

[126] Bedrossian, P.; Poelsema, B.; Rosenfeld, G.; Jorritsma, L.C.; Lipkin, N.N.; Comsa, G.: Electron density contour smoothing for epitaxial Ag islands on Ag(100). Surf. Sci. **334** (1995) 1–9.

[127] Poserow, B.; Jiang, Q.; Wang, G.-C.: Vertical layer distribution and atomic step height of ultrathin Co films on Cu(001) determined by lattice G-factor analysis. Surf. Sci. **388** (1997) 103–109.

[128] Martin, J.A.; Aumann, C.E.; Savage, D.E.; Tringides, M.C.; Lagally, M.G.;Moritz, W.; Kretschmar, F.: Atomic steps on Si(100) surfaces. J. Vac. Sci. Technol. A **5** (1987) 615–618.

[129] Wollschläger, J.; Falta, J.; Henzler, M.: Electron diffraction at stepped homogeneous and inhomogeneous surfaces. Appl. Phys. A **50** (1990) 57–68.

[130] Falta, J.; Henzler, M.: Studies of crystalline defects during the early stages of growth of Si on Si(100) at low temperatures by spot profile analysis of LEED (SPA-LEED). Surf. Sci. **269/270** (1992) 14–21.

[131] Horn-von Hoegen, M.; Falta, J.; Henzler, M.: The initial stages of growth of silicon on Si(111) by spot profile analysing low-energy electron diffraction. Thin Solid Films **183** (1989) 213–220.

[132] Kruger, D. W.; Savage, D. E.; Lagally, M.G.: Determination of the size distribution of noncrystalline regions on crystalline substrates. Phys. Rev. Lett. **63** (1989) 402–405.

[133] Horn-von Hoegen, M.; Golla, A.: Influence of H on low temperature Si(111) homoepitaxy. Surf. Sci. Lett. **337** (1995) L777–L782.

[134] Germer, L.H.; MacRae, A.U.: Surface reconstruction caused by adsorption. Ann. N. Y. Acad. Sci. **101** (1963) 599–605.

[135] Park, R.L.; Farnsworth, H.E.: The structure of clean nickel crystal surfaces. Surf. Sci. **2** (1964) 527.

[136] Ellis, W.P.; Schwoebel, R.L.: LEED from surface steps on UO2 single crystals. Surf. Sci. **11** (1968) 82–98.

[137] Perdereau, J.; Read, G.E.: LEED studies of adsorption on vicinal copper surfaces, Surf. Sci. **24** (1971) 555–571.

[138] Lang, B.; Joyner, R.W.; Somorjai, G.A.: LEED studies of high index crystal surfaces of platinum. Surf. Sci. **30** (1972) 440–453.

[139] Olshanetzky, B.Z.; Repinsky, S.M.; Shklyaev, A.A.: LEED studies of vicinal surfaces of germanium. Surf. Sci. **69** (1977) 205–217.

[140] Pukite, P.R.; Van Hove, J.M.; Cohen, P.I.: Sensitive RHEED measurement of the local misorientation of vicinal GaAs surfaces. Appl. Phys. Lett. **44** (1984) 456–458.

[141] Houston, J.E.; Park, R.L.: LEED from statistical step models. Surf. Sci. **26** (1971) 269–285.

[142] Whaley, G.J.; Cohen, P.I.: Relaxation of strained InGaAs during MBE. Appl. Phys. Lett. **57** (1990) 144–146.

[143] Bauer, E.: Interpretation of LEED patterns of adsorbed gases. Phys. Rev. **123** (1961) 1206–1208.

[144] Tucker Jr., C.W.: LEED studies of gas adsorption on platinum (100), (110), and (111) surfaces. J. Appl. Phys. **35** (1964) 1897–1905.

[145] Bauer, E.: Multiple scattering versus superstructures in LEED. Surf. Sci. **7** (1967) 351.

[146] Meyer, G.; Michailov, M.; Henzler, M.: LEED studies of the epitaxy of Pb on Cu(111). Surf. Sci. **189/190** (1987) 1091–1093; Surf. Sci. **202** (1988) 125–141.

[147] Grandjean, N.; Massies, J.; Etgens, V.H.: Delayed relaxation by surfactant action in highly strained III-V semiconductor epitaxial layers. Phys. Rev. Lett. **69** (1992) 796–799.

[148] Wollschläger, J.; Schäfer, F.; Schröder, K.M.: Diffraction spot profile analysis for vicinal surfaces with long-range order. Surf. Sci. **396** (1998) 94–106.

[149] Gradmann, U.; Waller, G.: Periodic lattice distortions in epitaxial films of Fe(110) on W(110). Surf. Sci. **116** (1982) 539–548.

[150] Ritter, M.; Ranke, W.; Weiss, W.: Growth and structure of ultrathin FeO films on Pt(111) studied by STM and LEED. Phys. Rev. B **57** (1997) 7240–7251.

[151] Horn-von Hoegen, M.; Al Falou, A.; Pietsch, H.; Müller, B.H.; Henzler, M.: Formation of the interfacial dislocation network in surfactant-mediated growth of Ge on Si(111) by SPALEED. Surf. Sci. **298** (1993) 29–42.

[152] MacRae, A.U.; Germer, L.H.: Thermal vibrations of surface atoms. Phys. Rev. Lett. **8** (1962) 489–490.

[153] Aldag, J.; Stern, R.M.: Surface thermal diffuse scattering from tungsten. Phys. Rev. Lett. **14** (1965) 857–860.

[154] Kinney, J.T.; Jones, E.R.; Webb, M.B.: Surface lattice dynamics of silver. II. Low-energy electron thermal diffuse scattering, Phys. Rev. **160** (1967) 523–530.

[155] Barnes, R.F.; Lagally, M.G.; Webb, M.B.: Multiphonon scattering of low-energy electrons Phys. Rev: **171** (1968) 627–633.

[156] Clarke, L.J.: Surface Crystallography. Whiley, New York, 1985.

[157] Wallis, R.F.; Maradudin, A.A.: Theory of surface effects on the thermal diffuse scattering of X rays or electrons from crystal lattices, Phys. Rev. **148** (1966) 962–967.

[158] Comsa, G.: Coherence length and/or transfer width. Surf. Sci. **81** (1979) 57–68.

[159] Wang, G.-C.; Lagally, M.G.: Quantitative island size determination in the chemisorebd layer W(110)p(2 × 1)-O. Surf. Sci. **81** (1979) 69–89.

[160] Lu, T.-M.; Lagally, M.G.: The resolving power of a low-energy electron diffractometer and the analysis of surface defects. Surf. Sci. **99** (1980) 695–713.

[161] Lander, J.J.; Morrison, J.: J. Appl. Phys. **34** (1963) 3517.

[162] Heidenreich, R.D. : Fundamentals of Transmission Electron Microscopy. Interscience, New York, 1964.

[163] Park, R.L.; Houston, J.E.; Schreiner, D.G.: The LEED instrument response function. Rev. Sci. Instrum. **42** (1971) 60–65.

[164] Lu, T.-M.; Lagally, M.G.; Wang, G.-C.: The effect of instrumental broadening on LEED intensity-energy profiles. Surf. Sci. **104** (1981) L229–L233.

[165] Horn-von Hoegen, M.; Henzler, M.: Lattice matching periodic interfacial dislocation network in surfactant-mediated growth of Ge on Si(111). Phys. Stat. Solidi (a) **146** (1994) 337–352.

[166] Sakamoto, T. ; Kawai, N.J.; Nakagawa, T.; Ohta, K.; Kojima, T.; Hashiguchi, G.: RHEED intensity oscillations during silicon MBE growth. Surf. Sci. **174** (1986) 651–657.

[167] Aarts, J.; Larsen, P.K.: Monlayer and bilayer growth on Ge(111) and Si(111). Surf. Sci. **188** (1987) 391–401.

[168] Horn, M.; Henzler, M.: LEED studies of Si molecular beam epitaxy on Si(111). J. Cryst. Growth **81** (1987) 428–433.

[169] Altsinger, R.; Busch, H.; Horn, M.; Henzler, M.: Nucleation and growth during molecular beam epitaxy (MBE) of Si on Si(111). Surf. Sci. **200** (1988) 235–246.

[170] Horn-von Hoegen, M.; Pietsch, H.: Homoepitaxy of Si(111) is surface defect mediated. Surf. Sci. Lett. **321** (1994) L129–L136.

[171] Nakahara, H.; Ichimiya, A.: Structural study of Si growth on a Si(111)7 × 7 surface. Surf. Sci. **241** (1991) 124–134.

[172] Köhler, U.; Demuth, J.E.; Hamers, R.J.: Scanning tunneling microscopy study of low-temperature epitaxial growth of silicon on Si(111)-(7 × 7). J. Vac. Sci. Tech. A **7** (1989) 2860–2867.

[173] Feenstra, R.M.; Lutz, M.A.: Kinetics of the Si(111) 2 × 1 → 5 × 5 and 7 × 7 transformation studies by STM. Surf. Sci. **243** (1991) 151–165.

[174] Ichikawa, M.; Doi, T.: Observation of Si(111) surface topography changes during Si molecular beam epitaxial growth using microprobe RHEED. Appl. Phys. Lett. **50** (1987) 1141–1143.

[175] Voigtländer, B.; Zinner, A.: Influence of surfactants on the growth-kinetics of Si on Si(111). Surf. Sci. Lett. **292** (1993) L775–L780.

[176] Andersohn, L.; Berke, Th.; Köhler, U.; Voigtländer, B.: Nucleation behaviour in molecular beam and chemical vapor deposition of silicon on Si(111)-(7 × 7). J. Vac. Sci. Technol. **A14** (1996) 312–318.

[177] Venables, J.A.; Spiller, G.D.T.; Hanbücken, M.: Nucelation and growth of thin films. Rep. Prog. Phys. **47** (1984) 399–459.

[178] Bartelt, M.C.; Evans, J.W.: Scaling analysis of diffusion-mediated island growth in surface adsorption processes. Phys. Rev. B **46** (1992) 12675–12687.

[179] Evans, J.W.; Bartelt, M.C.: Irresversible island formation during deposition: separation distributions and diffraction profiles. Surf. Sci. Lett. **284** (1993) L437–L443.

[180] Köhler, U.; Andersohn, L.; Dahlheimer, B.: Time resolved observation of CVD-growth of silicon on Si(111) with STM. Appl. Phys. A **57** (1993) 491–497.

[181] Horn-von Hoegen, M.; Golla, A.: Influence of H on low temperature Si(111) homoepitaxy. Surf. Sci. Lett. **337** (1995) L777–L782.

[182] Horn-von Hoegen, M.; Golla, A.: Adsorption induced change of equilibrium surface during crystal growth. Phys. Rev. Lett. **76** (1996) 2953–2956.

[183] Owman, F.; Mårtensson, P.: STM study of Si(111)1 × 1-H surfaces prepared by in situ hydrogen exposure. Surf. Sci. Lett. **303** (1994) L367–L372; STM study of structural defects on in situ prepared Si(111)1 × 1-H surfaces. Surf. Sci. **324** (1995) 211–225.

[184] Copel, M.; Tromp, R.M.: Medium energy ion scattering investigation of homoepitaxy on H terminated Si(111). Surf. Sci. Lett. **337** (1995) L772–776.

[185] Rice, B.M.; Raff, L.M.; Thompson, D.L.: Diffusion of H atoms on a Si(111) surface with partial hydrogen coverage: Monte Carlo variational phase-space theory with tunneling correction. J.Chem. Phys. **88** (1988) 7221–7231; Dynamics of Chemisorption/Scattering of atomic H on partially covered Si(111) surfaces. Surf. Sci. **198** (1988) 360–399.

[186] Reider, G.A.; Höfer, U.; Heinz, T.F.: Desorption kinetics of H from the Si(111) 7×7 surface. J. Chem. Phys. **94** (1991) 4080–4083.

[187] Bratu, P.; Höfer, U.: Phonon-assisted sticking of molecular hydrogen on Si(111)-(7 × 7). Phys. Rev. Lett. **74** (1995) 1625–1628.

[188] Kulkarni, S.K.; Gates, S.M.; Greenlief, C.M.; Sawin, H.H.: Mechanism of disilane decomposition on Si(111)-7 × 7. Surf. Sci. **239** (1990) , 26–35; Kinetics and mechanics of Si_2H_6 surface decomposition on Si. J. Vac. Sci. Technol. A **8** (1990) 2956–2959.

[189] Williams, E.D.; Bartelt, N.C.: Surface faceting and the equilibrium crystal shape. Ultramicroscopy **31** (1989) 36–48.

[190] Bauer, E.: Phänomenologische Theorie der Kristallabscheidung an Oberflächen. Z. Kristallogr. **110** (1958) 372–431.

[191] Marée, P.M.; Nakagawa, K.; Mulders, F.M.; van der Veen, J.F.: Thin epitaxial Ge-Si(111) films: study and control of morphology. Surf. Sci. **191** (1987) 305–328.

[192] Copel, M.; Reuter, M.C.; Kaxiras, E.; Tromp, R.M.: Surfactants in epitaxial growth. Phys. Rev. Lett. **63** (1989) 632–635.

[193] Kaxiras, E: Interplay of strain and chemical bonding in surfactant monolayers. Europhys. Lett. **21** (1993) 685–690.

[194] Horn-von Hoegen, M.: Surfactants: Perfect heteroepitaxy of Ge on Si(111). Appl. Phys. A **59** (1994) 503–515.

[195] Metzger, R.A.; Allen, F.G.: Evaporative antimony doping of silicon during molecular beam epitaxial growth. J. Appl. Phys **55** (1984) 931–940.

[196] Horn-von Hoegen, M.; Falta, J.; Copel M.; Tromp, R.M.: Surfactants in Si(111) homoepitaxy. Appl. Phys. Lett. **66** (1995) 487–489.

[197] Nakayama, T.; Tanishiro, Y.; Takayanagi, K.: Heterogrowth of Ge on the Si(001)2 × 1 reconstruction. Surf. Sci. **273** (1992) 9–20.

[198] Mo, Y.-W.; Savage, D.E.; Swartzentruber, B.S.; Lagally, M.G.: Kinetic pathway in Stranski-Krastanov growth of Ge on Si(001). Phys. Rev. Lett. **65** (1990) 1020–1023.

[199] LeGoues, F.K.; Copel, M.; Tromp, R.M.: Microstructure and strain relief of Ge films grown layer by layer on Si(001). Phys. Rev. B **42** (1990) , 11690–11700.

[200] Hammar, M.; LeGoues, F.K.; Tersoff, J.; Reuter, M.C.; Tromp, R.M.: In situ ultrahigh vacuum transmission electron microscopy studies of hetero-epitaxial growth of Si(001)/Ge. Surf. Sci. **349** (1996) 129–144.

[201] Williams, A.A.; Thornton, J.M.C.; Macdonald, J.E.; van Silfhout, R.G.; van der Veen, J.F.; Finney, M.S.; Johnson, A.D.; Norris, C.: Strain relaxation during the initial stages of growth in Ge/Si(001). Phys. Rev. B **43** (1991) 5001–5011.

[202] Horn-von Hoegen, M.; Müller, B.H.; Al Falou, A.; Henzler, M.: Surfactant induced reversible changes of surface morphology. Phys. Rev. Lett. **71** (1993) 3170–3173.

[203] Copel, M.; Reuter, M.C.; Horn-von Hoegen, M.; Tromp, R.M.: Influence of surfactants in Ge and Si epitaxy on Si(001). Phys. Rev. B **42** (1990) 11682–11689.

[204] Katayama, M.; Nakayama, T.; Aono, M.; McConville, C.F.: Influence of surfactant coverage on epitaxial growth of Ge on Si(001). Phys. Rev. B **54** (1996) 8600–8603.

[205] LeGoues, F. K.; Copel, M.; Tromp, R.M.: Novel strain-induced defect in thin molecular-beam-epitaxy layers. Phys. Rev. Lett. **63** (1989) 1826–1829.

[206] Thornton, J.M.C.; Williams, A.A.; Macdonald, J.E.; van Silfhout, R.G.; van der Veen, J.F.; Finney, M.; Norris, C.: The influence of Sb as a surfactant on the strain relaxation of Ge/Si(001). J. Vac. Sci. Technol. B **9** (1991) 2146–2149.

[207] Grinfeld, M.: Sov. Phys. Dokl. **31** (1986) 831.

[208] Srolovitz, D.: On the stability of surfaces of stressed solids. Acta Met. **37** (1989) 621–625.

[209] Tersoff, J; LeGoues, F.K.: Competing relaxation mechanisms in strained layers. Phys. Rev. Lett. **72** (1994) 3570–3573.

[210] Tersoff, J.: Tromp, R.M.: Shape transition in growth of strained islands: spontaneous formation of quantum wires. Phys. Rev. Lett. **70** (1993) 2782–2785.

[211] Hansson, P.O.; Albrecht, M.; Strunk, H.P.; Bauser, E.; Werner, J.H.: Dimensionality and critical sizes of GeSi on Si(100). Thin Solid Films **26** (1992) 199–202.

[212] Androussi, Y.; Lefebvre, A.; Courboulès, B.; Grandjean, N.; Massies, J.; Bouhacina, T.; Aimé, J.P.: Elastic misfit stress relaxation im highly strained InGaAs/GaAs structures. Appl. Phys. Lett. **65** (1994) 1162–1164.

[213] Steinfort, A.J.; Scholte, P.M.L.O.; Ettema, A.; Tuinstra, F.; Nielsen, M.; Landemark, E.; Smilgies, D.-M.; Feidenhans'l, R.; Falkenberg, G.; Seehofer, L.; Johnson, R.L.:Strain in nanoscale Ge hut clusters on Si(001) studied by x-ray diffraction. Phys. Rev. Lett. **77** (1996) 2009–2012.

[214] Chen, Y.; Washburn, J.: Structural transition in large-lattice-mismatch heteroepitaxy. Phys. Rev. Lett. **77** (1996) 4046–4049.

[215] Yu, W.; Madhukar, A.: Molecular dynamic study of coherent island energetics, stresses, and strains in highly strained epitaxy. Phys. Rev. Lett. **79** (1997) 905–908.

[216] Dong, L.; Schnitker, J.; Smith, R.W.; Srolovitz, D.J.: Stress relaxation and misfit dislocation nucleation in the growth of misfittig films: A molecular dynamics simulation study. J. Appl. Phys. **83** (1998) 217–227.

[217] Hamers,R.J.; Köhler, U.K.; Demuth, J.E.: Nucleation and growth of epitaxial Silicon on Si(001) and Si(111) surfaces by scanning tunneling microscopy. Ultramicroscopy **31** (1989) 10–19.

[218] Mo, Y.-W.; Kariotis, R.; Savage, D.E.; Lagally, M.G.: Anisotropic growth and "layer-by-layer" epitaxy. Surf. Sci. **219** (1989) L551–L559.

[219] AlFalou, A.; Kammler, M.; Horn-von Hoegen, M.: Strain state analysis of heteroepitaxial systems. Euro. Phys. Lett. **69** (2005) 570–578

[220] Brantley, W.A.: Calculated elastic constants for stress problems associated with semiconductor devices. J. Appl. Phys. **44** (1973) 534–535.

[221] Köhler, U.; Jusko, O.; Müller, B.; Horn-von Hoegen, M.; Pook, M.: Layer-by -layer growth of germanium on Si(100): Strain-induced morphology and the influence of surfactants. Ultramicroscopy **42–44** (1992) 832–837.

[222] Jusko, O.; Köhler, U.; Pietsch, G.J.; Müller, B.; Henzler, M.: Trench formation in surfactant mediated epitaxial film growth of Ge on Si(100). Appl. Phys. **A54** (1992) 265–269.

[223] Horn, M.; Gotter, U.; Henzler, M.: LEED investigations of Si MBE on Si(100). In: *RHEED and Reflection Electron Imaging of Surfaces* (Eds. P.K.Larsen, P.J.Dobson) pp. 463–474; NATO ASI Ser. B Vol. **188**, Plenum Press, 1988.

[224] Schell-Sorokin, A.J.; Tromp, R.M.: Mechanical stresses in (sub)monolayer epitaxial films. Phys. Rev. Lett. **64** (1990) 1039–1042.

[225] Schell-Sorokin, A.J.; Tromp, R.M.: Measurement of surface stress during epitaxial growth of Ge on As terminated Si(001). Surf. Sci. **319** (1994) 110–118.

[226] For a stepped surface this is valid only with all atoms on exact lattice sites. For all other cases (atoms on non-lattice sites as for example the elastic deformation surrounding a dislocation) the point-symmetry of the diffraction pattern applies only for the (000)-Bragg condition.

[227] Chadi, D.J.: Stabilities of single-layer and bilayer steps on Si(001) surfaces. Phys. Rev. Lett. **59** (1987) 1691–1694.

[228] Williams, E.D.; Bartelt, N.C.: Surface faceting and the equilibrium crystal shape. Ultramicroscopy **31** (1989) 36–47.

[229] Tersoff, J.; Teichert, C.; Lagally, M.G.: Self-organization in growth of quantum dot superlattices. Phys. Rev. Lett. **76** (1996) 1675–1678.

[230] Teichert, C.; Bean, J.C.; Lagally, M.G.: Self-organized nanostructures in SiGe films on Si(001). Appl. Phys. **A 67** (1998) 675–685.

[231] Fitzgerald, E.A.; Xie, Y.-H.; Monroe, D.; Silverman, P.J.; Kuo, J.M.; Kortan, A.R.; Thiel, F.A.; Weir, B.: Relaxed Ge_xSi_{1-x} structures for III-V integration with Si and high mobility two-dimensional electron gases in Si. J. Vac. Sci. Technol. B **10** (1992) 1807–1828.

[232] Cullis, A.G.; Robbins, D.J.; Pidduck, A.J.; Smith, P.W.: The characteristics of strain-modulated surface undulations formed upon epitaxial SiGe alloy layers on Si. J. Crystal Growth **123** (1992) 333–343.

[233] Lutz, M.A.; Feenstra, R.M.; Mooney, P.M.; Tersoff, J.; Chu, J.O.: Facet formation in strained SiGe films. Surf. Sci. **316** (1994) L1075–L1080.

[234] Tersoff, J.; Phang, Y.H.; Zhang, Z.; Lagally, M.G.: Step-bunching instability of vicinal surfaces under stress. Phys. Rev. Lett. **75** (1995) 2730–2733.

[235] Barnett, S.A.; Winters, H.F.; Greene, J.E.: The interaction of Sb4 molecular beams with Si(100) surfaces: modulated-beam mass spectrometry and thermally stimulated desorption studies. Surf. Sci. **165** (1986) 303–326.

[236] Slijkerman, W.F.J.; et al.: The interaction of Sb overlayers with Si(001). Surf. Sci. **262** (1992) 25–32.

[237] For a diamond lattice all surfaces vicinal toward [110] directions are composed of two different type of steps (see also ref. [227]). Therefore also low index planes as a [117] facet show this double periodicity.

[238] Horn-von Hoegen, M.; LeGoues, F.K.; Copel, M.; Reuter, M.C.; Tromp, R.M.: Defect self-annihilation in surfactant-mediated epitaxial growth. Phys. Rev. Lett. **67** (1991) 1130–1133.

[239] LeGoues, F.K.; Horn-von Hoegen, M.; Copel, M.; Tromp, R.M.: Strain-relief mechanism in surfactant-grown epitaxial germanium films on Si(111). Phys. Rev. B **44** (1991) 12894–12902.

[240] Horn-von Hoegen, M.; Copel, M.; Tsang, J.; Reuter, M.C.; Tromp, R.M.: Surfactant mediated growth of Ge on Si(111). Phys. Rev. B **50** (1994) 10811–10822.

[241] Reinking, D.; Kammler, M.; Horn-von Hoegen, M.; Hofmann, K.R.: Enhanced Sb segregation in surfactant-mediated-heteroepitaxy:High-mobility, low-doped Ge on Si. Appl. Phys. Lett. **71** (1997) 924–926; High electron mobilities in surfactant-grown Germanium on Silicon substrates. Jap. J. Appl. Phys. Lett. **36** (1997) L1082–L1084; Surfactant-grown low-doped Germanium layers on Silicon with high electron mobilities. Thin Solid Films **321** (1998) 125–130.

[242] Reinking, D.; Kammler, Hoffmann, N.; Horn-von Hoegen, M.; Hofmann, K.R.: Fabrication of high-mobility Ge p-channel MOSFETs on Si substrates. Electronic Lett. **35** (1999) 503–504.

[243] Meyer, G.; Voigtländer, B.; Amer, N.M.: Scanning tunneling microscopy of surfactant-mediated epitaxy of Ge on Si(111): Strain relief mechanisms and growth kinetics. Surf. Sci. Lett. **274** (1992) L541–L545.

[244] Voigtländer, B.; Zinner, A.: Surfactant-mediated epitaxy of Ge on Si(111): The role of kinetics and characterisation of the Ge layers. J. Vac. Sci. Technol. A **12** (1994) 1932–1937.

[245] Stalder, R.; Sirringhaus, H.; Onda, N.; von Känel, H.: Observation of misfit dislocations in epitaxial CoSi2/Si(111) layers by STM. Appl. Phys. Lett. **59** (1991) 1960–1962.

[246] Matthews, J.W.; Blakeslee, A.E.: Defects in epitaxial multilayers. J. Cryst. Growth **29** (1975) 273–280.

[247] Nabarro, F.R.N.: *Theory of Crystal Dislocation*; Dover Publications, New York (1987).

[248] Schröder-Bergen E.; Ranke, W.: Steps on Si(001) vicinal surfaces investigated by HR-LEED. Surf. Sci. **259** (1991) 323–338.

[249] Wasserfall, J.; Ranke, W.: Azimuthal variation of the step distribution on vicinal Si(001) surfaces. Surf. Sci. **315** (1994) 227–236.

[250] Pukite, P.R.; Cohen, P.I.: Multilayer step formation after As adsorption on Si(100): Nucleation of GaAs on vicinal Si. Appl. Phys. Lett. **50** (1987) 1739–1741.

[251] Wasserfall, J.; Ranke, W.: Arsenic interaction with vicinal Si(001) surfaces. Surf. Sci. **315** (1994) 237–247.

[252] Wasserfall, J.; Ranke, W.: Step topography of Si(001) vicinals, clean and after deposition of As, Sb and Bi. Surf. Sci. **331–333** (1995) 1099–1104.

[253] Fölsch, S.; Winau, D.; Meyer, G.; Rieder, K.H. Horn-von Hoegen, M.; Schmidt, T.; Henzler, M.: Ag-induced multistep formation on Si(001). Appl. Phys. Lett. 67 (1995) 2185–2187.

[254] Fölsch, S.; Meyer, G.; Rieder, K.H.; Horn-von Hoegen, M.; Schmidt, T.; Henzler, M.: Ag-mediated step-bunching instability on vicinal Si(100). Surf. Sci. **394** (1997) 60–70.

[255] Meier, A.; Zahl, P.; Vockenroth, R.; Horn-von Hoegen, M.: Step arrangement control of vicinal SI(001) control of vicinal Si(001) by Ag adsorption. Appl. Surf. Sci. **123/124** (1998) 694–698.

[256] Seehofer, L. Huhs, S.; Falkenberg, G.; Johnson, R.L.: Gold induced faceting of Si(111). Surf. Sci. **329** (1995) 157–166.

[257] Suliga, E.; Henzler, M.: Faceting of Ge(111) and its vicinals during Ag adsorption. J. Vac. Sci. Technol. A **1** (1983) 1507–1511.

[258] Gai, Z.; Ji, H.; He, Y.; Hu, C.; Zhao, R.G.; Yang, W.S.: {310} faceting of the Ge(001) 2×1 surface induced by Indium. Surf. Sci. **338** (1995) L851–L856.

[259] Yoon, M.; Mochrie, S.G.J.; Tate, M.W.; Gruner, S.M.; Eikenberry, E.F.: Periodic faceting of a Si(113) surface miscut towards [110]. Surf. Sci. **411** (1998) 70–85.

[260] Herring, C.: Some theorems on the free energies of crystal surfaces. Phys. Rev. **82** (1951) 87–93.

[261] Williams, E.: Surface steps and surface morphology: understanding macroscopic phenomena from atomic observations. Surf. Sci. **299/300** (1994) 502–524.

[262] Shimakura, T.; Minoda, S.; Tanishiro, Y.; Yagi, K.: In-situ study of gold-induced surface structures and step rearrangements on the Si(011) surface by high temperature STM. Surf. Sci. Lett. **407** (1998) L657–L664.

[263] Baski, A.A.; Erwin, S.C.; Whitman, L.J.: The structure of silicon surfaces from (001) to (111). Surf. Sci. **392** (1997) 69–85.

[264] Wollschläger, J.; Larsson, M.: Diffraction from tow-dimensional vicinal surfaces with noncolliding meandering steps. Phys. Rev. B. **57** (1998) 14937–14949.

[265] Minoda, H.; Yagi, K.; Meyer zu Heringdorf, F.-J.; Meier, A.; Kähler, D.; Horn von Hoegen, M.: Gold-induced faceting on a Si(001) vicinal surface: SPA-LEED and REM study. Phys. Rev. B **59** (1998) 2363–2375.

[266] Horn-von Hoegen, M.; Minoda, H.;Yagi, K.; Meyer zu Heringdorf, F.-J.; Kähler, D.: Macroscopic 1-dimensional faceting of Si(100) upon Au adsorption. Surf. Sci. **402–404** (1998) 464–469.

[267] Meyer zu Heringdorf, F.-J.; Horn-von Hoegen, M.: Dynamic light diffraction studies. Phys. Rev. Lett. (submitted).

[268] Meyer zu Heringdorf, F.-J.; Kähler, D.; Horn von Hoegen, M.; Schmidt, Th.; Bauer, E.; Copel, M.; Minoda, H.: Giant faceting of vicinal Si(001) induced by Au adsorption. Surf. Rev. Lett. **5** (1998) 1167–1178.

[269] Horn von Hoegen, M.; Meyer zu Heringdorf, F.-J.; Hild, R.; Zahl, P.; Schmidt, Th.; Bauer, E.: Adsorbate induced giant faceting of vicinal Si(001). Thin Solid Films **336** (1998) 16–21.

[270] Voges, C.; Pfnür, H.: Critical properties in two-dimensional oder-disorder phase transitions: experimental determination of the exponents α and η by integrating methods. Europhys. Lett. **38** (1997) 165–170.

[271] Voges, C.; Pfnür, H.: Experimental determination of the phase-transition critcial exponents α and η by integrating methods. Phys. Rev. B **57** (1998) 3345–3355.

[272] Grzelakowski, K.; Lyuksyutov, I.; Bauer, E.: Direct observation of scaling by HR-LEED: O on Mo(110). Phys. Rev. Lett. **64** (1988) 32–35.

[273] Sokolowski, M.; Pfnür, H.: Influence of steps on the critical behavior of a two-dimensional system: $p(2 \times 2)$ oxygen on a stepped Ru(0001) surface. Phys. Rev. Lett. **63** (1989) 183–186.

[274] Dennert, R.; Sokolowski, M.; Pfnür, H.: Ordered phases and phase diagram of sulphur adsorbed on Ru(001). Surf. Sci. **271** (1992) 1–20.

[275] Sokolowski, M.; Pfnür, H.; Lindroos, M.: Structural correlations of a chemisorbate across monoatomic steps: $p(2 \times 2)$ ordered oxygen on stepped Ru(001). Surf. Sci. **278** (1992) 87–98.

[276] Sokolowski, M.; Pfnür, H.: Critical behaviour of the $p(2 \times 2)$ and $(\sqrt{3} \times \sqrt{3})R30°$ order-disorder phase transitions of S/Ru(001). Surf. Sci. **287–288** (1993) 831–836.

[277] Schwenger, L.; Voges, C.; Sokolowski, M.; Pfnür, H.: Critical scattering at a marginally first order phase transition in two dimensions: the order-disorder transition of O/Ni(111)-$p(2 \times 2)$. Surf. Sci. **307–309** (1994) 781–788.

[278] Sokolowski, M.; Pfnür, H.: Continuous order-disorder phase transitions of the $p(2 \times 2)$ and $(\sqrt{3} \times \sqrt{3})R30°$ superstructures of sulfur on Ru(001): Effective critical exponents and finite size effects Phys. Rev. B **49** (1994) 7716–7728.

[279] Sokolowski, M.; Pfnür, H.: Phase transitions of the striped domain-wall phases of S on Ru(0001). Phys.Rev. B **51** (1995) 15742–15751.

[280] Pfnür, H.; Voges, C.; Budde, K.; Schwenger, L.: Phase transitions and critical phenomena in strongly chemisorbed adlayers: influence of defects. Progress in Surf. Sci. **53** (1996) 205–215.

[281] Baraldi, A.; Dhanak, V.R.; Comelli, G.; Prince, K.C.; Rosei, R.: O/Rh(100) $p\ (2 \times 2) \leftrightarrow c(2 \times 2)$ order-disorder phase transition. Phys. Rev. B **53** (1996) 4073–4077.

[282] Pfnür, H.: Thermal fluctuations in equilibrium and theit modification by surface defects. In: *Surface diffusion: atomistic and collective processes* (Ed. M.C. Tringides) pp. 529–542, Plenum Press, New York (1997).

[283] Zuo, J.-K.; Wang, G.-C.: Effects of impurities on the phase transition and critical phenomena of a chemisorbed overlayer. Phys. Rev. B **41** (1990) 7078–7087.

[284] Budde, K.; Schwenger, L.; Voges, C.; Pfnür, H.: Effect of oxygen impurities on the critical properties of the (2×2)-2H/Ni(111) order-disorder phase transition. Phys. Rev. B **52** (1995) 9275–9282.

[285] Yang, H.-N.; Lu, T.-M.; Wang, G.-C.: Collapsing of thermally induced steps on the Pb(111) surface. Phys. Rev. Lett. **62** (1989) 2148–2151.

[286] Yang, H.-N.; Lu, T.-M.; Wang, G.-C.: HR-LEED study of Pb(110) surface roughening transition. Phys. Rev. Lett. **63** (1989) 1621–1624.

[287] Yang, H.-N.; Lu, T.-M.; Wang, G.-C.: HR-LEED analysis of the Pb(110) roughening transition. Phys. Rev. B **43** (1991) 4714–4727.

[288] Wollschläger, Luo, E.Z.; Henzler, M.: Thermal roughness of the homogeneous and inhomogeneous Cu(311) surface studied by HR-LEED. Phys. Rev. B **44** (1991) 13031–13041.

[289] Fang, K.; Yang, H.-N.; Wang, G.-C.: Modification of surface structures and roughening phase transition in Pb(110) by impurities. Surf. Sci. Lett. **284** (1993) L399–L404.

[290] Fang, K.; Lu, T.-M.; Wang, G.-C.: Roughening and faceting in a Pb thin film growing on the Pb(110) surface. Phys. Rev. B **49** (1994) 8331–8339.

[291] Dey, S.; Kiriukhin, S.; West, J.; Conrad, E.H.: Entropic step doubling on W(430). Phys. Rev. Lett. **77** (1996) 530–533.

[292] Conrad, E.H.; Menzel, A.; Kiriukhin, S.; Tringides, M.C.: Observations of surface temporal fluctuations by LEED. Phys. Rev. Lett. **81** (1998) 3175–3178.

[293] Kammler, M.; Horn-von Hoegen, M.; Voss, N.; Tringides, M.; Menzel, A.; Conrad, E.H.: Si(001) step dynamics: a temporal low energy electron diffraction study. Phys. Rev. B **65** (2002) 075312

[294] Büssenschütt, A.; Vlieg, E.: Unpublished results.

[295] Flynn, D.K.; Wang, W.; Chang, S.-L.; Tringides, M.C.; Thiel, P.A.: Use of LEED intensity oscillations in monitoring thin film growth. Langmuir **4** (1988) 1096– 1100.

[296] Albrecht, M.; Fritzsche, H.; Gradmann, U.: Kinetic faceting in homoepitaxy of Fe(110) on Fe(110). Surf. Sci. **294** (1993) 1–9.

[297] Nyberg, G.L.; Kief, M.T.; Egelhoff, W.E.; SPA-LEED study of the epitaxial growth of Fe, Co, and Cu on Cu(100). Phys. Rev. B **48** (1993) 14509–14519.

[298] Ammer, Ch., Meinel, K., Klaua, M., High quality Ag crystal surfaces for investigating the initial stages of Ag homoepitaxy. Phys. Stat. Sol. (a) **150** (1995) 507–519.

[299] Zuo, J.-K.; Wendelken, J.F.: Evolution of mound morphology in reversible homoepitaxy on Cu(100). Phys. Rev. Lett. **78** (1997) 2791–2794.

[300] Swan, A.K.; Shi, Z.-P.; Wendelken, J.F.; Zhang, Z.: Flux-dependent scaling behaviour in Cu(100) submonolayer homoepitaxy. Surf. Sci. Lett. **391** (1997) L1205–L1211.

[301] Schwabenhausen, J.; Dürkop, T.; Elmers, H.J.: Morphology and indirect exchange coupling in Fe/Cr/Fe(110) trilayers. Phys. Rev. B **55** (1997) 15119–15129.

[302] Jorritsma, L.C.; Bijnagte, M.; Rosenfeld, G.; Poelsema, B.: Growth Anisotropy and pattern formation in metal epitaxy. Phys. Rev. Lett. **78** (1997) 911–914.

[303] Wulfhekel, W.; Beckmann, I.; Rosenfeld, G.; Poelsema, B.; Comsa, G.: Growth and Morphology of Ni Films on Cu(111). Surf. Sci. **395** (1998) 168–181.

[304] Fölsch, S.; Helms, A.; Steidinger, A.; Rieder, K.H.: Reconstructed pseudomorphic Co films on the Cr(110) surface. Phys. Rev. B **57** (1998) R4293–4296.

[305] Schmidthals, C.; Enders, A.; Sander, D.; Kirschner, J.: Coexistence of pseudomorphic and coincidence phases in nickel monolayers. Surf. Sci. **402–404** (1998) 636–640.

[306] Bardotti, L.; Stoldt, C.R.; Jenks, C.J.; Bartelt, M.C.; Evans, J.W.; Thiel, P.: HR-LEED profile analysis and diffusion barrier estimation for submonolayer homoepitaxy of Ag/Ag(100). Phys. Rev. B **57** (1998) 12544–12549.

[307] Roos, K.R.; Tringides, M.C.: Flux dependence of the Ag/Si(111) growth. Europhys. Lett. **23** (1993) 257–262.

[308] Roos, K.R.; Tringides, M.C.: Low-temperature, flux-independent epitaxy in Ag/Si(111). Surf. Sci. **302** (1994) 37–48.

[309] Horn-von Hoegen, M.; Schmidt, T.; Meyer, G.; Winau, D.; Rieder, K.H.: Epitaxial layer growth of Ag(111)-films on Si(100). Surf. Sci. **331–333** (1995) 575–579.

[310] Horn-von Hoegen, M.; Schmidt, Henzler, M.; Meyer, G.; Winau, D.; Rieder, K.H.: Lattice accomodation of low-index planes: Ag(111) on Si(001). Phys. Rev. B, Brief Reports **52** (1995) 10764–10767.

[311] Fölsch, S.; Meyer, G.; Winau, D.; Rieder, K.H.; Schmidt, T.; Horn-von Hoegen, M.: Reconstruction dependent orientation of Ag(111) films on Si(001). Phys. Rev. B, Brief Reports **52** (1995) 13745–13748.

[312] Zuo, J.-K.; Wendelken, J.F.: Kinetic processes in the transition from Ag(111) crystallites to $(\sqrt{3} \times \sqrt{3})R30°$ domains for Ag/Si(111)-(7 × 7). Phys. Rev B **56** (1997) 3897–3902.

[313] Libuda, J.; Sandell, A.; Bäumer, M.; Freund, H.-J.: Evidence for $Pd_x(CO)_y$ compound formation on an alumina substrate. Chem. Phys. Lett. **240** (1995) 429–434.

[314] Libuda, J.; Frank, M.; Sandell, A.; Andersson, S.; Brühwiler, P.A.; Bäumer, M.; Mårtensson, N.; Freund, H.-J.: Interaction of rhodium with hydroxylated alumina model substrates. Surf. Sci. **384** (1997) 106–119.

[315] Bäumer, M.; Frank, M.; Libuda, J.; Stempel, S.; Freund, H.-J.: Growth and morphology of Rh deposits on an alumina film under UHV conditions and under the influence of CO. Surf. Sci. **391** (1997) 204 – 215.

[316] Wollschläger, J.; Meier, A.: Diffraction spot profile analysis for heteroepitaxial surfaces applied to the initial growth stages of CaF2 adlayers on Si(111). Appl. Surf. Sci. **104/105** (1996) 392–401.

[317] Wollschläger, J.; Meier, A.: Film and Interface Morpholgy of CaF2 Grown on Si(111) at Low Temperature. Appl. Phys. **79** (1996) 7373–7375

[318] Pietsch, H.; Klust, A.; Meier, A.; Wollschläger, J.: Growth Instabilities of CaF2 Adlayers Deposited at High Temperature on Si(111). Surf. Sci. **377–379** (1997) 909–913.

[319] Henzler, M.; Zielasek, V.; Erdös, D.; Wollschläger, J.: Epitaxial Insulating Films. Surf. Rev. and Lett. **5** (1998) 675–684.

[320] Wollschläger, J.; Erdös, D.; Schröder, K.M.: The formation of mosaics during the reactive growth of MgO films on Ag(100). Surf. Sci. **402–404**, (1998) 272–276.

[321] Wollschläger, J.: Morphology and defect characterization of Epitaxial oxide films. Defect and Diffusion **164** (1998) 37–56.

[322] Ritter, M.; Ranke, W.; Weiss, W.: Growth and structure of ultrathin FeO films on Pt(111) studied by STM and LEED. Phys. Rev. B **57** (1998) 7240–7251.

[323] Blum, R.-P.; Ahlbehrendt, D.; Niehus, H.: Growth of Al2O3 stripes in NiA(001). Surf. Sci. **396** (1998) 176–188.

[324] Henzler, M.; Homann, C.; Malaske, U.; Wollschläger, J.: Misfit Accommodation in Heteroepitaxy by Inclined Stacking Faults. Phys. Rev. B **52** (1995) R17060–R17063.

[325] Grossmann, B.; Piercy, P.: HR-LEED study of flattening on the TiO2(110) surface. Phys. Rev. Lett. **74** (1995) 4487–4490.

[326] Luo, E.Z.; Heun, S.; Kennedy, M.; Wollschläger, J.; Henzler, M.: Surface roughness and conductivity of thin Ag films. Phys. Rev. B **49** (1994) 4858–4865.

[327] Ceelen, W.C.A.N.; Denier van der Gon, A.W. ; Reijme, M.A.; Brongersma, H.H.; Spolveri, I.; Atrei, A.; Bardi, U.: Domain structure, segregation and morphology of the $Pt_3Sn(111)$ surface. Surf. Sci. **406** (1998) 264–278.

[328] Meinel, K.; Wolter, H.; Ammer, Ch.; Neddermeyer, H.: Metastable misfit-induced relaxation structures of close-packed heteroepitaxial films. Surf. Sci. **401** (1998) 434–444.

[329] Fölsch, S.; Choi, B.-Ch.; Rieder, K.H.: Morphology of strained epitaxial Fe films on Cu(311). Appl. Phys. Lett. **69** (1996) 155–157.

[330] Fölsch, S.; Choi, B.-Ch.; Rieder, K.H.: Ultrathin epitaxial iron films on a highly asymmetrical substrate: Fe/Cu(331). Phys. Rev. B **54** (1996) 10855–10861.

[331] Schwennicke, C.; Schimmelpfennig, J.; Pfnür, H.: Morphology of thin NaCl films grown epitaxially on Ge(100). Surf. Sci. **293** (1993) 57–66.

[332] Schwennicke, C.; Schimmelpfennig, J.; Pfnür, H.: Ordering and phase diagrams of Xenon adsorbed on thin expitaxial NaCl(100) films and on Ge(100). Phys. Rev. B **48** (1993) 8928–8937.

[333] Neureiter, H.; Spranger, S.; Schneider, M.; Winkler, U.; Sokolowski, M.; Umbach, E.: Reconstruction, morphology, and stoichiometry of CdTe(001) and Cd0.96Zn0.04Te(001) surfaces, Surf. Sci. **388** (1997) 186–200.

[334] Neureiter, H.; Schneider, M.; Tatarenko, S.; Sokolowski, M.; Umbach, E.: New information on the sublimating CdTe(001) surface from high resolution LEED. Appl. Surf. Sci. **123/124** (1998) 71–75.

[335] Seidel, C.; Poppensieker, J.; Fuchs, H.: Real-time monitoring of phase transitions of vacuum deposited organic films by molecular beam deposition LEED. Surf. Sci. **408** (1998) 223–231.

[336] Falta, J.; Imbihl, R.; Henzler, M.: Spatial pattern formation in a catalytic surface reaction: the facetting of Pt(110) in $CO+O_2$. Phys. Rev. Lett. **64** (1990) 1409

[337] Imbihl, R.; Falta, J.; Kaletta, D.; Henzler, M.: Formation of Turing structures in catalytic surface reactions: the facetting of Pt(110) in CO+O2. J.Vac.Sci.Techn. **A9** (1991) 1749–1752.

[338] Falta, J.; Imbihl, R.; Sander, M.; Henzler, M.: Low Energy Electron Diffraction Profile Analysis of Reaction induced substrate changes on Pt(110) during catalytic CO oxidation. Phys. Rev. B **45**, (1992) 6858–6867.

[339] Dullweber, T.; Pfnür, H.: Unpublished results

[340] Godzik, G.; Pfnür, H.: Unpublished results)

[341] Guan, J.; Campbell, R.A.; Madey, T.E.: Ultrathin metal films on W(111): morphology and faceting reconstruction. Surf. Sci. **341** (1995) 311–327.

[342] Guan, J.; Campbell, R.A.; Madey, T.E.: Faceting of the Mo(111) surface by ultrathin Pd and Pt films. J. Vac. Sci. Technol. A **13** (1995) 1484–1488.

[343] Theilmann, F.; Matzdorf, R.; Goldmann, A.: High resolution photoemission studies at rough Cu(111) surfaces. The influence of defect scattering and disorder-dependent dephasing processes. Surf. Sci. **420** (1999) 33–42.

[344] Budde, K.; Pfnür, H.: Unpublished results.

[345] Lagally, M.G.: priv. comm; APS Meeting 1994.